Static properties and nonlinear dynamics of domain walls with a vortexlike internal structure in magnetic films (Review)

B. N. Filippov*

Institute of Metal Physics, Urals Branch of the Russian Academy of Sciences, ul. S. Kovalevskoĭ 18, 620219 Ekaterinburg, Russia

(Submitted January 2, 2002; revised April 22, 2002)
Fiz. Nizk. Temp. **28**, 991–1032 (October 2002)

The causes of the formation of domain walls with a vortex structure, their energy, and their static properties are analyzed as functions of the film parameters. The influence of the surface anisotropy and external fields on these properties is elucidated. It is it is shown that that both one- and two-vortex symmetric and asymmetric walls can be stable. The experimental evidence for the existence of asymmetric walls is presented. A review is given of the dynamic properties of walls with a vortex structure. The fields at which catastrophic changes of their structure occur with changing field (the bifurcation fields) are indicated. The mechanisms of dynamic transformation of the internal structure of the walls, in particular, the mechanisms involving the creation and annihilation of vortexlike wall formations, are examined, and the tunneling of these formations through the center of the wall is discussed. The transformations of the wall due to the onset of subperiodic magnetization oscillations are described. The period of the dynamic transformations and the character of its singularity near a bifurcation point are investigated. The nonmonotonic dependence of the bifurcation field on the film thickness, saturation induction, and exchange field and also the dependence of the bifurcation field on the damping parameter and anisotropy field are investigated. [DOI: 10.1063/1.1521291]

1. INTRODUCTION

The science of domain walls has a long history, during which the ideas about their internal structure and dynamic be have changed greatly.[1–8] By now it has become clear that the structure of the domain walls (DWs) in thin magnetic films is extremely complex; in particular, it is vortexlike,[9,10] radically different from the Bloch DWs whose existence was predicted by Bloch back in 1932[11] (see also Ref. 12).

Research interest in DWs remains undiminished to this day, since their properties determine many of the characteristics important in the practical applications of magnetic materials, e.g., electromagnetic losses, magnetic noise, coercive force, etc.[6,7,13–15] The DW also has an important influence on the spin-wave spectra, the ferromagnetic and gamma resonances, the propagation of sound waves, etc.[6,13] Knowledge of the DW dynamics in magnetic films is also necessary for the development of high-frequency devices for high-density reading and writing of data (see, e.g., Refs. 16–18).

Besides its practical significance, research on DWs, especially on their dynamics, is of great fundamental importance. This is because an inhomogeneous spin system such as a DW is extremely sensitive to various external influences. Often even small stimuli lead to large responses of the system. Here strong changes can occur not only in the parameters characterizing the wall as a whole but also in the parameters of its internal structure. From a dynamic standpoint a DW can be compared with a topological soliton having internal degrees of freedom. Thus a DW is a unique real object for studying nonlinear physical properties. This object is also unique in that its motion can be described by the substantially nonlinear Landau–Lifshitz equations,[12] which, in the general case, do not reduce to any of the nonlinear partial differential equations that have been well studied in mathematics (the sine-Gordon, nonlinear Schrödinger equation, etc.),[19] and, in the general case, they do not have known analytical solutions.

Thus the study of DWs is extremely difficult, and from a theoretical standpoint can be carried out only on the basis of a direct numerical solution of the Landau–Lifshitz equation. For this it is necessary to have certain information about the properties of the walls in order to determine the spatial and time scales on which the processes involving DW motion can be played out. The difficulties that arise can be overcome completely with the existing numerical techniques.

Even greater difficulties arise in the experimental study of the dynamic behavior of DWs, since studying their internal structure requires a spatial resolution of less than 10^{-6} cm and a time resolution of around 1 ns. Therefore the experimental studies done to date give basically an averaged (over spatial or temporal intervals) picture of the static and dynamic properties of DWs (see, e.g., Refs. 20–30). Granted, there has been a recent breakthrough in this area as well. In Refs. 31–35 the distribution of the magnetization within the DW itself was investigated experimentally in the direction along the surface of the film (but on the average over its thickness). We should also mention some more-recent experiments[36–39] in which indirect methods based on the DW "shaking" effect[40–42] were used to study the DW structure.

The science of DWs has many branches. DWs exist in ferro-, antiferro-, and ferrimagnets—in bulk samples,[2,3,43–47] particulates,[48–52] small thin-film elements,[53–60] and magnetic

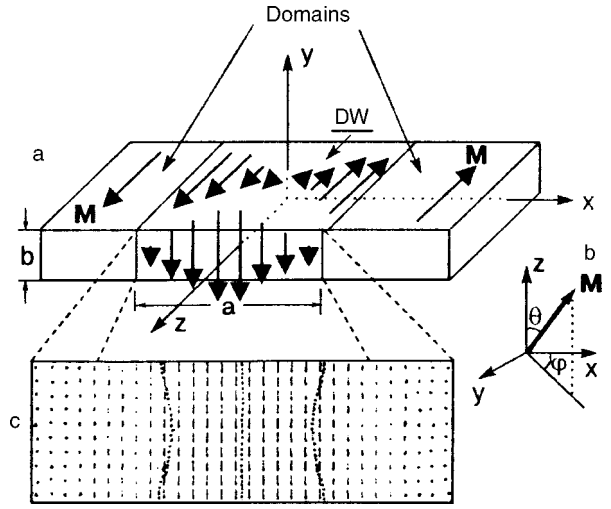

FIG. 1. Schematic illustration of the geometry of the problem and the structure of a Bloch wall on different planes of the film (a,b). Typical calculated structure of a Bloch wall on the xy plane (c).

films.[2,3,8,61] In this review we shall concentrate mainly on DWs existing in magnetically uniaxial films.

The boom in research on DWs in films with perpendicular anisotropy (see, e.g., Refs. 3 and 62–70) in connection with the magnetic writing of data is widely known. Although the main goal of this research has not been achieved, the boom itself has led to a whole new level of knowledge about the properties of DWs.

Now some completely new results have also been obtained for magnetically uniaxial films with the anisotropy axis lying in the film plane (in-plane anisotropy) and with a low quantity factor $Q=K(4\pi M_s^2)$ (K is the uniaxial anisotropy constant, and M_s is the saturation magnetization). However, those studies, in spite of their practical significance for data read heads, have only recently aroused much interest. The reason is that in films with in-plane anisotropy an extremely important role is played by magnetostatic fields, which are extremely hard to take into account because of their long-ranged character. This review is devoted mainly to presenting the data obtained in the last decade for DWs in films with in-plane anisotropy. The most important step in these studied was the prediction[9,10] of the existence of DWs with an asymmetric vortical configuration of the magnetization. The development of these studies can be found, e.g., in Refs. 71–89. Another important paper, in which for the first time it became possible to describe supercritical nonstationary behavior of the vortexlike DWs, was published by Yuan and Bertram.[90] In this review we discuss the significant amount of material that has been accumulated since the time of those papers.

2. STATIC PROPERTIES OF DOMAIN WALLS WITH A VORTEXLIKE INTERNAL STRUCTURE

2.1. Qualitative assessment of the possibility of existence of DWs with a vortexlike structure of the magnetization

Let us consider a magnetically uniaxial plane-parallel (in the xz plane) film of thickness b, with the easy axis (axis of easy magnetization) oriented along the z axis in the film plane (see Fig. 1). We assume that the magnetic state of this film corresponds to two domains with uniform saturation magnetizations $\pm M_s$, oriented along $+z$ $(-z)$ for $x<-a/2$ $(x>a/2)$. Here we assume that the DW (the transition region between domains) is completely concentrated in a region V of rectangular cross section D in the xy plane, with dimensions of a along x and b along y. The region V has the shape of a parallelepiped extended along z. The proposed simplifications are a source of error in determining the DW parameters. It is generally more correct to proceed from an analysis of a multidomain state of the film, as in Refs. 76 and 91, for example (see also Refs. 72 and 85). However, the errors mentioned can be diminished greatly through an appropriate choice of a (see below). In this Section we assume that the magnetization of the film in the region D is a function of x: $\mathbf{M}=\mathbf{M}(x)$. This corresponds to the well-known one-dimensional model of the magnetization $\mathbf{M}$. The static properties of such a model can be found in Refs. 2 and 6–8, for example (see also Refs. 92–98).

The simplest distribution of $\mathbf{M}$ in the one-dimensional model is the Bloch wall. In this case the magnetization rotates between adjacent domains while always remaining in the zy plane. Here the magnetization in the x direction (nominally in the direction perpendicular to the plane of the DW) remains continuous. This eliminates the magnetostatic fields that otherwise (in the absence of continuity) would inevitably arise. This approach is completely justified in the case when the DW is found in a crystal with $b\to\infty$. In films with a finite b, however, the situation is complicated greatly. This is clearly seen by examining Fig. 1, which shows a magnetization distribution of the Bloch type on an end surface of the film. In particular, it is seen that the magnetization distribution in the Bloch wall is symmetric relative to the plane $x=0$, and the center line of the wall (the line on which the z component of the magnetization changes sign) is a straight line perpendicular to the surface of the film.

Within the Bloch wall a resultant magnetization appears which is perpendicular to the planes of the film (see also the simplified scheme in Fig. 1a). This gives rise to magnetostatic poles, which are a source of additional magnetostatic fields and, hence, of additional domain-wall energy. With decreasing film thickness the distance between poles decreases, and the DW energy increases. In this situation, as was first pointed out by Néel,[99] it is more correct to assume that the magnetization varies from one domain to the next while remaining parallel to the plane of the surface of the crystal (see Fig. 2). This is called the Néel configuration of the DW. For convenience we shall call it the one-dimensional Néel configuration.

In the situation described, magnetostatic poles do not arise on the surface of the film, but $\operatorname{div}\mathbf{M}=\partial M_x/\partial x$ turns out to be nonzero, and this is a source of magnetostatic fields and is consequently a source of additional DW energy. At first glance there has been no energy benefit in the transition from a Bloch to a Néel wall. This is actually not the case, since it is possible for the wall thickness a to increase, leading to a decrease of the magnetostatic charges and energy of the DW. Thus at certain film thicknesses the Néel domain walls turn out to be energetically favorable. The corresponding critical thickness b_c is equal to 0.04 μm for Permalloy

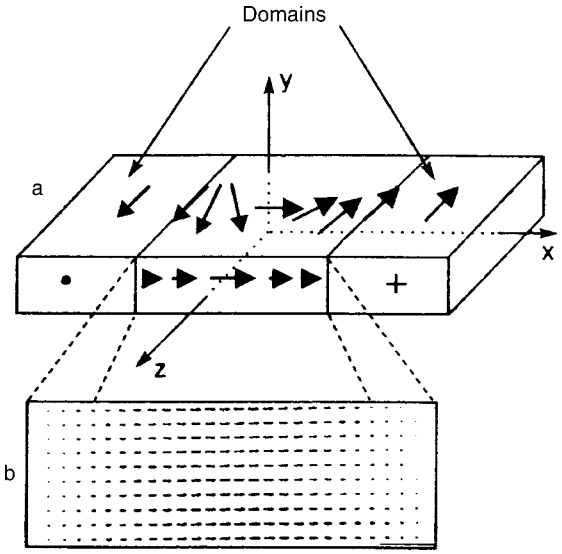

FIG. 2. Schematic illustration (a) and typical calculated structure on the xy plane of the film (b) for a Néel wall.

films. We note that, like the Block wall, the Néel wall is symmetric with respect to the plane $x=0$.

Thus it is only in comparatively thin films that one can expect to see walls in which the energy due to magnetostatic charges can be reduced by the appearance of a new configuration of the magnetization.

One would like to find a suitable configuration of the magnetization distribution in the DW such that the contribution from the magnetostatic fields to the total energy of the DW would be lowered even in films with $b>b_c$. It seems completely obvious that such a configuration might be a distribution of $\mathbf{M}$ in which the magnetization has a Néel character near the surface of the film and a Bloch character in the interior. However, for an exactly Bloch character of the rotation of the magnetization in the central plane of the film, in which case the wall would become symmetric with respect to the yz plane, the flux cannot be closed inside the film. This is clearly seen in Fig. 3a. Another possibility, involving a symmetric wall in each half of which a rotation of the Bloch type occurs in a different direction; although this leads to closing of the magnetic flux, it gives a sharp increase in the inhomogeneous part of the exchange energy (see Fig. 3b). The only possibility of closing the magnetic flux and avoiding a sharp increase in the exchange energy is to abandon the quest for symmetric configurations. The possibility of an asymmetric configuration satisfying these requirements is illustrated schematically in Fig. 3c. One can hope that in this case the DW energy in a film of thickness $b>b_c$ will be less than the energy of the one-dimensional Bloch wall. To prove this, let us turn to a detailed analysis of the DW structure.

2.2. Numerical approach to the description of DW structures with a two-dimensional magnetization distribution

Let the magnetization of the film in region D be a function of x and y: $\mathbf{M}=\mathbf{M}(x,y)$. This corresponds to the well-known two-dimensional model[9] of the distribution of $\mathbf{M}$.

The basic problem of the theory is to determine $\mathbf{M}(x,y)$. This problem has been solved on the basis of a strictly micromagnetic approach[100] with allowance for all of the main

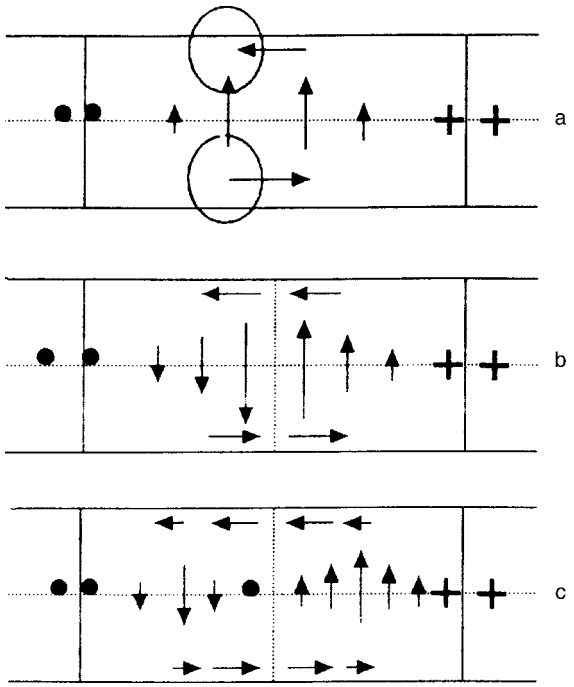

FIG. 3. Diagram explaining the asymmetric vortexlike structure of the walls (see text).

interactions: exchange, dipole (in the continuum approximation), and magnetic-anisotropy (bulk and surface). We denote these energies as ε_e, ε_m, ε_V, and ε_S, respectively, with

$$\varepsilon_e=\left(\frac{A}{M_s^2}\right)\left[\left(\frac{\partial\mathbf{M}}{\partial x}\right)^2+\left(\frac{\partial\mathbf{M}}{\partial y}\right)^2\right], \tag{1}$$

$$\varepsilon_m=-\frac{1}{2}\mathbf{M}\cdot\mathbf{H}^{(m)}, \tag{2}$$

$$\varepsilon_V=-\frac{K_V}{M_s^2}(\mathbf{M}\cdot\mathbf{c})^2, \tag{3}$$

$$\varepsilon_S=+\frac{K_S}{M_s^2}(\mathbf{M}\cdot\mathbf{n})^2. \tag{4}$$

Here A is the exchange interaction parameter, K_V and K_S are the bulk and surface magnetic anisotropy constants, M_s is the saturation magnetization, $\mathbf{c}$ is a unit vector along the easy axis, $\mathbf{n}$ is a unit vector along the normal to the film surface, and $\mathbf{H}^{(m)}$ is the magnetostatic field, which is given by

$$\mathbf{H}^{(m)}(\mathbf{r})=-\frac{\partial}{\partial\mathbf{r}}\int_V d\mathbf{r}'M_j(\mathbf{r}')\frac{\partial}{\partial x_j'}\frac{1}{|\mathbf{r}-\mathbf{r}'|}. \tag{5}$$

We note that because $\mathbf{M}$ is independent of z in the two-dimensional model under consideration, for a film which is infinite in the z direction the field $\mathbf{H}^{(m)}(\mathbf{r})$ is also independent of z, so that the DW energy per unit length along z can be written in the form

$$E_D=\int\int_D \varepsilon dxdy+\int_{D_x}\varepsilon_S dx, \tag{6}$$

where D_x is the boundary of the region D along the film surfaces, and

$$\varepsilon = \varepsilon_e + \varepsilon_m + \varepsilon_V. \quad (7)$$

The distribution $\mathbf{M}(x,y)$ must be determined under the condition $\mathbf{M}^2 = \text{const}$ and the following boundary conditions:

$$\left[\mathbf{M}, \frac{\partial \mathbf{M}}{\partial n} + q\mathbf{n}(\mathbf{M}\cdot\mathbf{n})\right]\Big|_{y=\pm b/2} = 0, \quad (8)$$

$$M_2|_{x=\pm a/2} = \pm M_s; \;\; M_x|_{x=\pm a/2} = 0; \;\; M_y|_{x=\pm a/2} = 0, \quad (9)$$

where $q = K_S/A$.

In Eq. (8) the square brackets denote the vector product. Condition (8) is obtained by the variation of E_D with respect to $\mathbf{M}$ for $\mathbf{M}^2 = \text{const}$ and equating to zero the expressions for the arbitrary and independent variations δM_x, δM_y in the surface integral.

We note that if $K_S < 0$ ($K_S > 0$), then there is a surface magnetic anisotropy of the easy axis (easy plane) type, and the axis of the surface anisotropy is oriented perpendicular to the surface of the film. Equations (8) and (9) can hold simultaneously only if

$$K_S > -b(K_V + 2\pi M_s^2). \quad (10)$$

Otherwise it is necessary to take into account the dependence of M_s on y. In this review we discuss only the situation corresponding to (10).

The above-stated problem of finding the equilibrium two-dimensional distribution $\mathbf{M}(x,y)$ in general reduces to a solution of a system of substantially nonlinear integrodifferential equations in the region D with nonsimple, in general nonlinear, conditions at the boundary of that region. The equations mentioned can be obtained by minimizing the functional (6). At the present time it is not possible to solve such a problem by analytical methods, and therefore some numerical procedure or other is usually used to minimize (6). The adaptation of numerical approaches to two-dimensional problems of the magnetization distribution has been done in a number of papers.[9,10,32,65,75,79,83,85,89,101–103] Those studies were all done using mesh methods except for Ref. 10, which was based on a variational approach. Each of the papers cited has its own specifics. For example, in Refs. 32 and 79 a numerical scheme was constructed with allowance for the contribution of the surface interactions. The scheme in Refs. 81, 82, and 85 takes into account the interlayer interaction in multilayer films. In Refs. 88 and 103 fast adaptive algorithms were used. In addition, the numerical procedure in Ref. 88 can be used to study the magnetization distribution in finite thin-film samples. Periodic structures can be analyzed with the scheme developed in Refs. 76 and 85. Finally, in Ref. 104 the problems of local minimization are investigated mathematically in a micromagnetic approach.

By minimizng the functional (6), one can find the equilibrium DW configurations and the minimum energy values E_0 corresponding to them. For convenience, we introduce the following dimensionless quantities: $\Omega = E_D/A$ and $\Omega_0 = E_0/A$.

The numerical minimization method used in this review consists in the following.[9,32,79] The computational region D is divided up by a rectangular mesh with small cells. Here V is divided up into parallelepipeds elongated along the z axis and with side walls parallel to the xz and yz coordinate planes. It is assumed that the cells are macroscopic but yet so small that the direction of $\mathbf{M}$ can be assumed constant at all points of each parallelepiped. Here $\mathbf{M}$ remains constant along each of the parallelepipeds (along z) by virtue of the two-dimensionality of the model. It is assumed that the orientation of $\mathbf{M}$ in D changes only from cell to cell. We introduce the direction cosines α, β, γ of the magnetization $\mathbf{M} = M_s(\alpha,\beta,\gamma)$. The values of these cosines in the klth cell are written as α_{kl}, β_{kl}, γ_{kl}. Finally, the functional (6) is discretized and is defined in a $P\times L\times 3$-dimensional space of variables α_{kl}, β_{kl}, γ_{kl}, where P and L are the total number of cells that fit within D along the y and x axes, respectively. The search for $\mathbf{M}$ leads to the problem of conditional minimization of the functional E on a $P\times L\times 3$-dimensional manifold under the condition $\alpha_{kl}^2 + \beta_{kl}^2 + \gamma_{kl}^2 = 1$. A concrete expression for the discretized functional can be found in Refs. 79 and 105.

The numerical calculations reported in this review were done on meshes with different numbers of cells. The maximum number of cells was 90×30. A larger number of cells would require substantially more computer time without significantly affecting the numerical results. It is important to choose correctly the computational region D, i.e., the dimensions a and b. These dimensions depend substantially on the magnetic parameters of the film. We chose certain basic parameters typical of Permalloy films: $A = 2\times 10^{-6}$ erg/cm, $K = 10^{-3}$ erg/cm^3, and $M_s = 800$ G. For such films (which will sometimes be referred to below as ''basic films'') the asymmetric structures of the walls can be stable for values of b ranging from 5×10^{-2} to 0.2 μm, for example. As to the dimension a, the calculations were done for different situations corresponding to the conditions $1 \leqslant a/b \leqslant 6$.

For doing the numerical calculation we chose a certain initial configuration of the magnetization. This could be a rough guess reflecting some symmetry properties of the distribution of $\mathbf{M}$. Here we used a mesh with comparatively large cells, e.g., with dimensions of 12×6. After a certain initial number of iterations, when the distribution $\mathbf{M}$ becomes sufficiently well developed, we switch to finer meshes, using an interpolation procedure to transfer the data from one rectangular mesh to the other.

The computation also has provisions for a procedure of introducing random disturbances of any amplitude. These disturbances can be introduced at any point in time as a check on the stability of the solutions obtained. As a criterion for terminating the numerical computation, following Ref. 106 we use the self-consistency coefficient $S_0 = \Omega_0/\Omega_{01}$, where Ω_{01} is determined by transforming Ω with the use of the Euler equation obtained as a result of the variation of Ω under the conditions $\mathbf{M}^2 = M_s^2$. It is clear that the coefficient S_0 defined in this way should approach unity as $\mathbf{M}(x,y)$ approaches the local equilibrium distribution with increasing number of iterations.

2.3. Static asymmetry of the DW structure

The first attempt to abandon the idea of a symmetric DW structure was made in Ref. 107. In this Section we present the calculated DW structure in films with the basic set of parameters (see above). Depending on the film thickness, in the absence of external magnetic field and surface anisotropy, there can exist not only classical (one-dimensional)

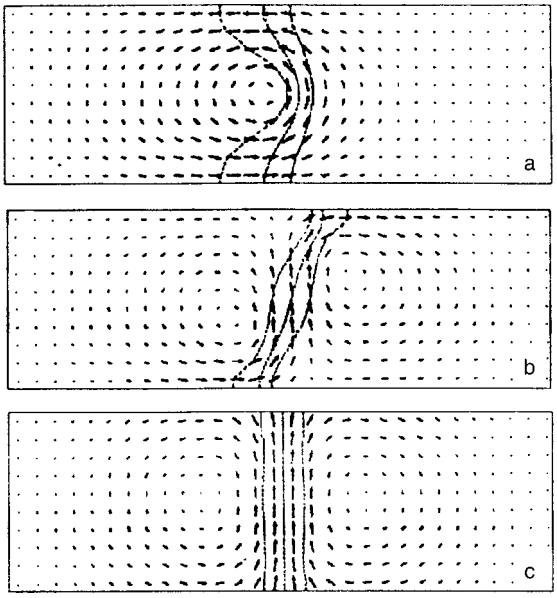

FIG. 4. Examples of vortex-like structures of DWs in films with planar anisotropy: asymmetric Bloch (a), asymmetric Néel (b), symmetric two-vortex (c); the DWs with structures b and c are metastable.

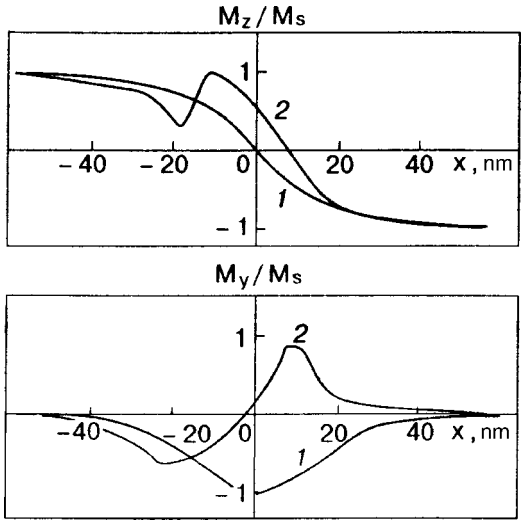

FIG. 5. Typical dependence of the z and y components of the relative magnetization in symmetric one-dimensional Bloch (*1*) and asymmetric Néel (*2*) walls.

Néel walls but also asymmetric Bloch (single-vortex) and asymmetric Néel walls. The latter can exist only as metastable. Figure 4 shows the DWs in a film 10^{-5} cm thick. We note that all of the figures in this review showing magnetization distributions correspond to a region D in the xy plane (see Fig. 1, where, in particular, the orientation of the coordinate axes is shown). The coordinate axes are not shown on the diagrams of the microstructures of the magnetization distributions. The lowest energy is possessed by the asymmetric Bloch wall (ABW) shown in Fig. 4a. This is the classical single-vortex wall first found by LaBonte[9] and independently by Hubert.[10] The figure shows the magnetization distribution in the xy plane, perpendicular to the surface and easy axis of the film. We see first of all that the projection of the magnetization **M** varies from domain to domain in such a way that a ''vortex structure'' of the magnetization is formed in the xy plane (the plane of the figure). This term was introduced by LaBonte in 1969[9] and has since been widely used, although it must be said that the topological properties of the object in question have not been analyzed by anyone. The z component of **M** also changes from one domain to the next. On the dashed center line $y=y_0(x)$ the component $\mathbf{M}_z=0$ (the center of the wall). If a straight line is passed through the two points of this line lying on opposite sides of the film, then the line $y=y_0(x)$ will lie entirely to either the right or left of this straight line. From this standpoint we shall distinguish walls with opposite curvature (right or left, respectively). Thus the center of the DW at different depths in the film corresponds to different coordinates x. The asymmetry of this line with respect to the y axis is the reason why this is called an asymmetric DW. We recall that in a one-dimensional Bloch wall the center line should be a straight line perpendicular to the surface of the film (see Fig. 1). However, calculations show that such symmetric Bloch DWs in films of the thicknesses considered, as well as the symmetric two-vortex walls of the type shown in Fig. 4c, are absolutely unstable even in the absence of surface anisotropy. It should be noted that for ABWs the component M_z of **M** turns out to be asymmetric (see Fig. 5), in agreement with the general arguments given above. A detailed analysis of the magnetization configuration shown in Fig. 4a shows that near the upper and lower surfaces of the film the change of the magnetization from domain to domain occurs in approximately the same way as for a one-dimensional Néel wall (the Néel parts of the DWs). At the same time, in the central plane of the film the variation of **M** resembles the variation of the magnetization in a one-dimensional Bloch wall. Joining these parts together leads to a vortexlike distribution of the magnetization. It is clear from what we have said that the formation of a vortexlike structure makes it possible to close the magnetic flux more completely inside the magnetic sample and thereby leads to a sharp decrease of the magnetostatic field energy. In Ref. 10 it was even assumed that the vortexlike configuration can completely eliminate the magnetostatic fields. However, these hopes have not yet been confirmed. It should be kept in mind that it is not only the magnetization components in the xy plane that vary but also the component M_z, which, in accordance with what we have said, is also asymmetric (see Fig. 5).

The vortexlike formations examined in this review are quite different from the magnetic vortices studied in a number of papers (see, e.g., Refs. 108–113 and the references cited therein). First, in the case considered here the vortices are only structural elements of other magnetization formations (domain walls). In other words, these formations, unlike those in Refs. 108–111, are localized in a field of nonuniform magnetization. In addition, these vortices are asymmetric. Their existence is is predicated on taking the dipole interaction into account, which, as a rule, other authors have not done at all or else have done in a manner inadequate for obtaining the phenomena under discussion. An exception is Ref. 111, where an extremely original approach for obtaining vortices of **M** in ultrathin films was developed. However, the geometry of the problem in Ref. 111 (as in the other papers mentioned above, by the way) is substantially different from that chosen in this review. As a

TABLE I. Calculated values of the domain-wall energies Ω_0 for a parameter $\mu_m = M_s^2 b/A = 32$, $b = 10^{-5}$ cm, and the basic values of the parameters M_s, A, and K.

Type of DW	Ω_0	Ω_e/Ω_0	Ω_m/Ω_0	Ω_V/Ω_0
Asymmetric Bloch	9.8182	0.944	0.052	0.003
Asymmetric Bloch (Ref. 6)	9.7751	0.946	0.051	0.003
Asymmetric Néel	12.5824	0.886	0.111	0.002

rule those papers (see, e.g., Refs. 108–113) considered plane-parallel magnets with a vortex lying in the easy plane. Since, with a minor exception (see, e.g., Ref. 111), the magnetostatic interaction was not taken into account in them, the whole treatment actually corresponded to an infinite magnet. In this review we investigate real magnetically uniaxial films with an easy axis lying in the film plane. Here the vortexlike formation of the magnetization arises on an end surface of the film, which is not an easy plane.

For the film parameters considered, the total energy of an asymmetric Bloch wall (dimensionless units) and the partial contributions to it from the exchange energy Ω_e, magnetic dipole energy Ω_m, and magnetic anisotropy energy Ω_V are given in Table I for a 90×30 mesh. It is seen that the contribution from the magnetic dipole energy is indeed small: approximately 5% of the total energy. The anisotropy energy is primordially small. Also shown in this table for comparison are the data of LaBonte, obtained for a 200×40 mesh. It is seen that the results agree to within a percent.

We note that the question of the influence of the dimensions of the mesh on the quantitative data for vortical DWs is investigated in detail in Ref. 84.

While, according to what we have said, the formation of a vortex **M** is due to the possibility of lowering the magnetostatic field energy, the appearance of an asymmetric structure is due to a decrease of the energy of the inhomogeneous part of the exchange interaction, as was shown in Sec. 2.1.

For the given material parameters of the film, the structure in Fig. 4a corresponds to the lowest energy at thicknesses $b \geqslant 4\times 10^{-6}$ cm. For $b \leqslant 4\times 10^{-6}$ cm walls of a different type are stable: for example, Néel (uniform) walls or DWs with necks (see, e.g., Refs. 99, 114, and 115). With increasing film thickness the Bloch segments of the vortical DW grow in extent, and it takes on the characteristic features for a classical one-dimensional Bloch wall.[12]

We note that in the wall shown in Fig. 4a the direction of rotation of **M** (the chirality of the wall) is counterclockwise. Studies show that walls with the opposite chirality have exactly the same energy (there is degeneracy in terms of chirality). In addition, walls with the opposite curvature of the center line (in comparison with Fig. 4a) also have the same energy (degeneracy in terms of curvature), and so do walls with opposite chirality and curvature both. According to what we have said, in principle one can expect the appearance of DWs having parts with one chirality and parts with the opposite chirality. The transition region between them will be a new type of Bloch line. Bloch lines separating parts of a DW with different directions of curvature of the center line, etc., are also possible.

In addition to the DW described, the DWs shown in Fig. 4b can also exist as stable in the films discussed above. However, in the absence of external magnetic field they will always be metastable. These DWs are asymmetric with respect to both the zy and xy planes. We shall call them asymmetric Néel walls, although they have a more pronounced vortical character than the corresponding DWs first considered by Hubert.[10] It is possible that the differences are due to the fact that in Ref. 10 the method of trial functions was used (see, e.g., Ref. 84, where a direct numerical method was used and, in particular, configurations like that shown in Fig. 4b are presented). The asymmetric character of the given wall is also due to the asymmetry of the center line $y = y_0(x)$. If a straight line perpendicular to the surface of the film is passed through the center of this line, i.e., perpendicular to the upper and lower lines bounding Fig. 4b, then two situations may be imagined. In the first of these the points $y = y_0(x)$ located below (above) the central plane of the film (parallel to the surface) will lie to the right (left) of this straight line. The opposite situation is also possible. We will speak of two opposite inclinations of the center line: right and left, respectively.

It is clear that the magnetostatic energy of asymmetric Néel walls is just as small as the energy of asymmetric Bloch walls. For the DWs in Fig. 4b there can also be degeneracy with respect to chirality and direction of inclination of the center line.

Because of the two-dimensional character of the distribution of **M** in asymmetric DWs, their thickness $\delta(y)$ is different at different depths in the film. Thus, in addition to the known indeterminacies, the introduction of a wall thickness with a one-dimensional distribution **M** (see, e.g., Refs. 2 and 116) raises additional questions. In connection with what we have said, for describing the structure of a DW with a two-dimensional distribution of **M** one can present the level lines $M_z = \pm \text{const}$ on the xy plane.[9] Here the regions between pairs of lines of different sign corresponding to the same $M_z/M_s = \text{const}$ will give the parts of the DWs with a definite degree of rotation of **M** relative to the full rotation in a 180° DW. These lines are introduced according to the expression

$$\gamma_k \equiv (M_z/M_s) = \pm[1-(1-|k|/8)]^{1/2}.$$

$$k = 0, \pm 1, \pm 2, \pm 3, \pm 4, \pm 5, \pm 6, \pm 7.$$

The center line (center of the DW) corresponds to $k = 0$. On this line the sign of M_z changes on going from a domain with $M_z = -M_s$ ($\gamma = -1$) to a domain with $M_z = +M_s$ ($\gamma = 1$). The two lines ($k = \pm 1$) closest to the center line correspond to $\gamma = \pm 0.484$. Consequently, the change in M_z over the distance $\delta_c(y)$ between these lines is 48.4% of the total variation of M_z at a fixed y. This gives a change of the angle between **M** and the z axis of about 67.8% of the total angle of rotation of **M** in a 180° DW. The quantity $\delta_c(y)$ is the most convenient way of characterizing the core of a DW with a two-dimensional magnetization distribution (see below).

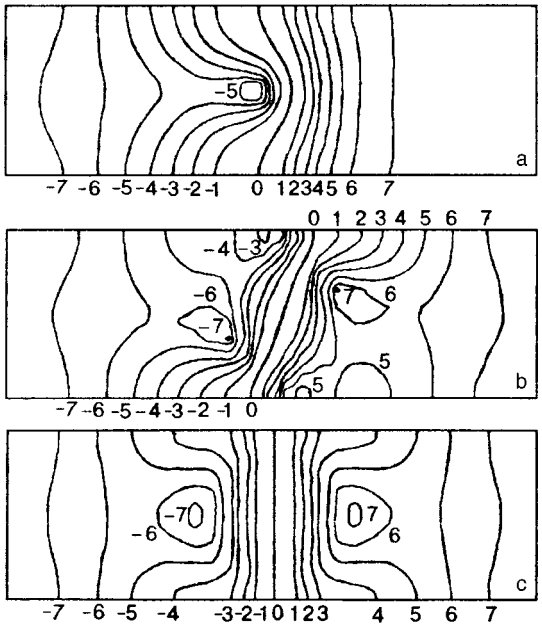

FIG. 6. Levels lines $M_z/M_s=$const corresponding to walls with the structures shown in Fig. 4a-4c.

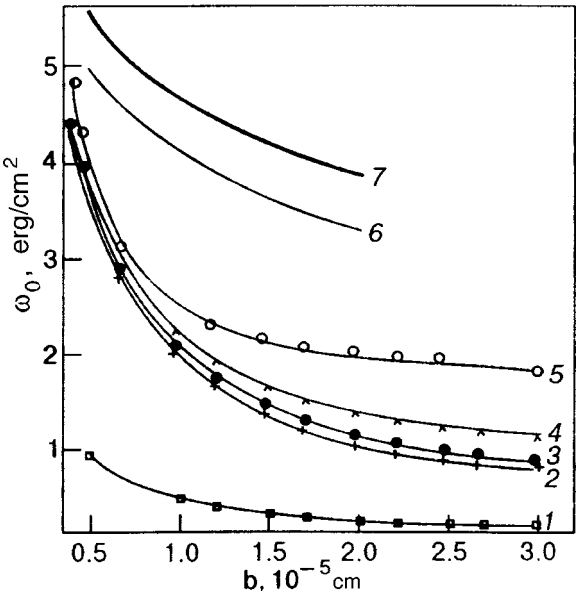

FIG. 7. Dependence of the energies of asymmetric Bloch walls (*1–5*) and one-dimensional walls (*6,7*) on the thickness of magnetic films with different parameters: $A=10^{-6}$ erg/cm, $M_s=800$ G (*1*); $A=2\times10^{-6}$ erg/cm, $M_s=800$ G (*2*); $A=2\times10^{-6}$ erg/cm, $M_s=1000$ G (*3*); $A=2\times10^{-6}$ erg/cm, $M_s=1600$ G (*4*); $K=10^5$ erg/cm^3, $A=2\times10^{-6}$ erg/cm, $M_s=800$ G (*5*); curves *6* and *7* were taken from Ref. 9 and correspond to the parameter set (*2*). For all the films except (*5*), $K=10^3$ erg/cm^3.

Figure 6 shows level lines of M_z calculated for the DW configurations illustrated in Fig. 4a. It is seen that, unlike the ordinary one-dimensional Bloch wall, where the level lines $M_z/M_s=$const are mutually parallel straight lines perpendicular to the film surface, for asymmetric walls these levels have a complex configuration. It is clear that a wall has two distinct regions: central (the core of the DW, the region between the lines $k=\pm1$) and peripheral. In each of these regions the structure of the pairs of lines corresponding to a fixed M_z/M_s is different. The core of an asymmetric Bloch wall (see Fig. 6a) has a minimum thickness at the center of the film, where its structure approaches that of the classical Bloch wall. Near the surfaces of the film the core of the DW widens out substantially and the distribution of **M** in it takes on features characteristic of the classical Néel wall.

The core of an asymmetric Néel wall has a more complex structure. As can be seen in Fig. 6b, in this case the core has two necked-down regions between the center and surfaces of the film. The distribution of the magnetization **M** in them approaches that in a one-dimensional Bloch wall. For both types of DWs the centers of the vortices lie in the peripheral parts of the wall. That is why the structure of the level lines of M_z is more complicated in the peripheral parts of the film.

2.4. Influence of the film parameters on the characteristics of an asymmetric Bloch wall

In this Section we shall show that in magnetically uniaxial films the asymmetric Bloch wall is the most favorable over a wide range of film thicknesses. The thickness dependence of the energy of an ABW was calculated for films with different magnetic parameters. Figure 7 shows the dependence of the energy $\omega_0=A\Omega/b$ (this notation is convenient for comparison with the one-dimensional model of the walls) for several sets of film parameters. It is seen first that in all cases the DW energy decreases with increasing film thickness. Such a decrease is natural, since the contribution of the magnetostatic fields to the wall energy decreases with increasing film thickness. It is seen in the figure that the wall energy changes substantially only on changes in the exchange energy, which gives the main contribution to the total energy of the wall. We note, however, that even very strong changes in the saturation magnetization and anisotropy constants of the films lead to comparatively small changes in ω_0, since these energies give a relatively small contribution to the total energy ω_0. Figure 7 also shows the one-dimensional Bloch wall energies calculated by Brown and LaBonte[95] (curve *6*) and Middelhoek[115] (curve *7*). The data were taken from Ref. 9 and correspond to the basic parameters of the films. It is seen that for films with the basic parameters, the energy of two-dimensional asymmetric walls turns out to be considerably less than the energy of one-dimensional walls at any given film thickness. Moreover, detailed calculations of the DW energies for films with parameters $A\in(0.2-2)\times10^{-5}$ erg/cm, $K\in(0.01-5)\cdot10^5$ erg/cm^3, $M_s\in(400-1600)$ G, and $b\in(0.04-0.3)$ μm show that asymmetric Bloch walls have the lowest energy for all these films. Figure 8 shows the dependence of the wall energies on the saturation magnetization according to Yuan and Bertram.[90] Shown here, along with the energy density corresponding to an asymmetric Bloch wall (circlets), are the energy densities corresponding to one-dimensional Néel (curve *3*) and Bloch (curve *2*) walls. It is seen that asymmetric walls are advantageous in films with $b\geqslant0.04$ μm. We note that one-dimensional Bloch walls are not advantageous at any M_s.

Let us consider one more characteristic of an asymmetric Bloch wall: its thickness. As we have said, for walls with a two-dimensional structure the additional difficulties of determining the wall thickness arise in comparison with the case

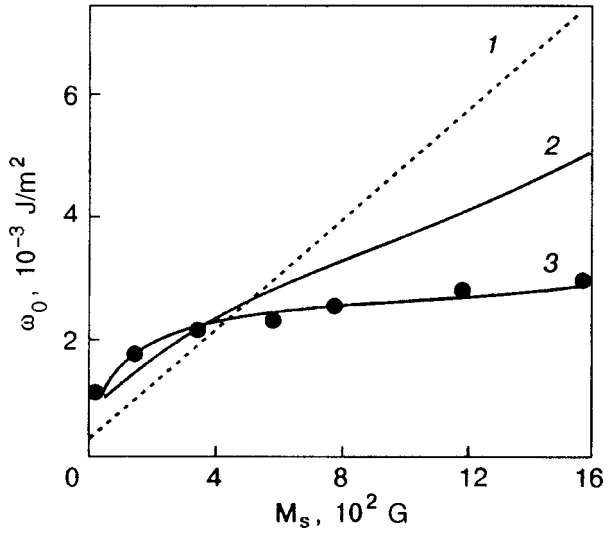

FIG. 8. Energies of asymmetric (*1*) and one-dimensional symmetric Bloch (*2*) and Néel (*3*) walls versus the saturation magnetization for films with $A=2\times10^{-6}$ erg/cm, $K=10^3$ erg/cm^3, $b=0.1$ μm.

of one-dimensional DWs; generally speaking, the wall thickness δ is different at different depths in the film.[9,10,117] Since experimentally only the value δ_w averaged over the film thickness is measured, it is reasonable to calculate this average value. Turning to Fig. 6a, we notice that it is convenient to choose δ_w as the average over the film thickness of the distance between the sixth level lines, since these lines are only slightly curved and, in addition, over the distance between them the angle θ changes by approximately 75%, which corresponds to the choice of wall thickness in the one-dimensional model.[14] Figure 9 shows the wall thicknesses for films with different parameters. It is seen that in all cases the value of δ_w increases with increasing film thickness, because of the decreasing contribution from the magnetostatic fields. However, this growth is not always linear (see also Sec. 2.8).

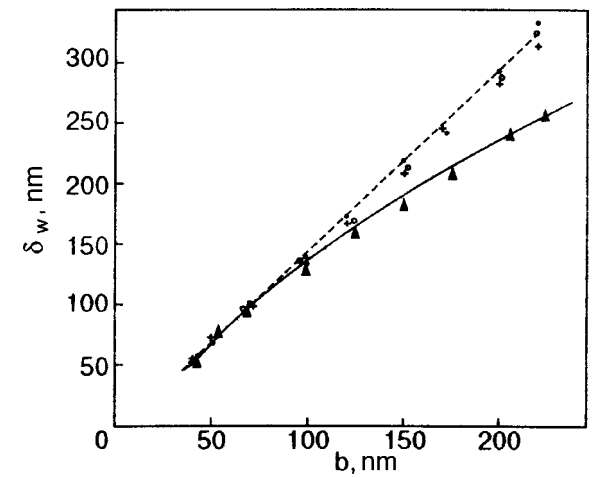

FIG. 9. Dependence of the thickness of asymmetric Bloch walls on the film thickness, for films with parameters $K=10^3$ erg/cm^3, $M_s=800$ G (+); $K=10^3$ erg/cm^3, $M_s=1000$ G (○); $K=10^3$ erg/cm^3, $M_s=1600$ G (●); $K=10^5$ erg/cm^3, $M_s=800$ G (▲).

2.5. Influence of magnetic surface anisotropy on the static DW structure

The concept of surface anisotropy was introduced by Néel.[118] Its existence has now been confirmed by experimental studies (see, e.g., Refs. 119–124). According to estimates by Néel, the surface anisotropy constant K_S can be rather large (of the order of 1 erg/cm^2). Experimental studies[119–124] lead to values of K_S smaller than 0.3 erg/cm^2. However, according to experimental spin-wave resonance data,[125] additional thin layers can be created artificially on the surface of the film, and they can result in a rather large effective surface anisotropy.

The existence of surface anisotropy can materially alter the situation with the equilibrium DW configurations, as was first pointed out in Ref. 126. In particular, in addition to the two-dimensional DW configurations given in the previous Section, a symmetric two-vortex DW appears, with the structure illustrated in Fig. 4c and the level lines shown in Fig. 6c. In the absence of surface anisotropy such a configuration is unstable. For $K_S\neq0$ it can exist as stable or metastable, depending on the film thickness and the value of K_S. In any case one should have $K_S<0$, i.e., the surface anisotropy should be of an easy-axis character. In particular, it is very important that the two-vortex symmetric DW can exist in thinner films than those in which one-dimensional Néel walls are observed. All of the features described ultimately derive from the fact that for $K_S<0$ the surface anisotropy tends to orient the magnetization perpendicular to the film surface despite the action of the magnetostatic field, which tends to rotate the magnetization into the film plane. These two tendencies are best satisfied by a symmetric two-vortex DW configuration, in which the magnetization in the core of the DW emerges on the surface of the film and is oriented along the surface anisotropy axis. In a very protracted peripheral part the magnetization in the DW lies in the plane of the film and has a distribution analogous in character to that of a simple Néel DW. All of this recalls the situation considered previously for one-dimensional walls and $K_S=0$ in Ref. 98. It was shown in Refs. 79 and 127 that there exist three different regions of values $K_S<0$ with different energy hierarchies of the DWs with variations of the film thickness. For example, if $K_S\leqslant K_{0S}$, where K_{0S} is a certain critical value of K_S which depends on the thickness and magnetic parameters of the film, the possible equilibrium configurations of the magnetization in the DWs for different film thicknesses have the form illustrated in Fig. 10. It is seen that in the thinnest films the equilibrium configuration is essentially an ordinary Bloch wall. Then, as the film thickness increases, the two-vortex symmetric wall configuration described above becomes stable. There is no specific value of the thickness b at which a transition from the first wall structure to the second would occur. Actually the simple Bloch walls goes over smoothly to a two-vortex wall with increasing film thickness, since the role of the surface anisotropy decreases with the indicated increase in b. It is seen in Fig. 10 that there exists a certain critical thickness b_{c1} above which the asymmetric single-vortex Bloch wall is stable. For the basic values of the parameters A, K, and M_s it was found that $K_{0S}=-0.8$ erg/cm^2 and $b_{c1}=4.8\times10^{-6}$ cm (for $K_S=-1$ erg/cm^2).

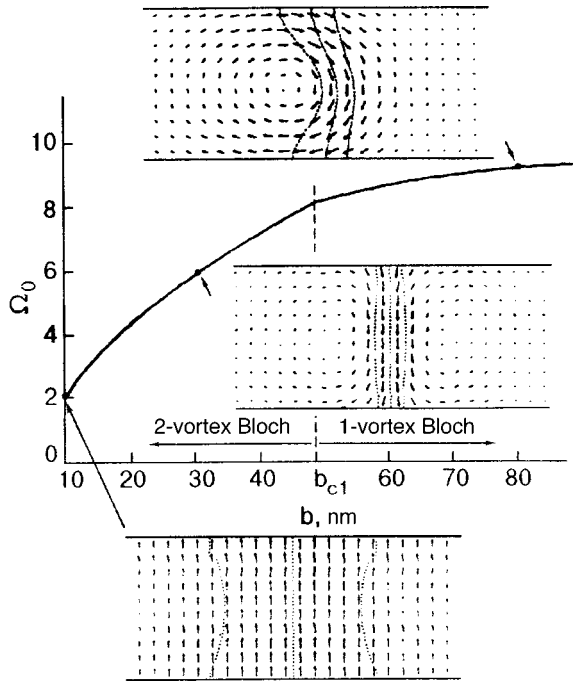

FIG. 10. Dependence of the relative energies of DWs with different structures (illustrated by fields of arrows) on the film thickness for films with the basic parameters and a surface magnetic anisotropy constant $K_S = -1$ erg/cm^2.

A different situation takes place in the interval $K_{0S} < K_S < K_{1S}$, where K_{1S} is another critical value of K_S, which also depends on the film parameters. For the basic values of the film parameters it has a value $K_{1S} = -0.2$ erg/cm^2. In this case, in the thinnest films the vortexless Bloch wall is stable. At thicknesses b greater than a certain value b_{c2} and less than b_{c3}, the classical Néel wall (with a one-dimensional distribution of **M**) is stable. As the film thickness increases further, in the interval $b_{c3} < b < b_{c1}$ the symmetric two-vortex Bloch wall is stable. Finally, for $b > b_{c1}$ the one-vortex asymmetric Bloch wall is stable. All of what we have just said is illustrated in Fig. 11. Calculations show that for the basic film parameters the values $b_{c2} = 6\times10^{-7}$ cm and $b_{c3} = 2.5\times10^{-6}$ cm, $b_{c1} = 3.6\times10^{-6}$ cm are obtained at $K_S = -0.7$ erg/cm^2.

Finally, in the region $K_S > K_{1S}$ only a transition from the equilibrium classical Néel DW to an equilibrium vortical wall can occur with changing b (see Fig. 12). In this case the surface anisotropy plays practically no role.

2.6. Influence of an external magnetic field perpendicular to the easy axis on the equilibrium configurations of the films

Let us consider a film with magnetic parameters and thickness such that an asymmetric Bloch wall is the equilibrium configuration in it. If an external magnetic field $\mathbf{H}_\perp$ is applied to such a film along the x axis, perpendicular to the easy axis, the magnetization vortex in the DW will be displaced toward the upper surface, as shown in Fig. 13c. Thus the DW becomes asymmetric relative to the xz plane as well. This transformation of the DW structure, which was first investigated by Hubert (see, e.g., Ref. 2), occurs because a

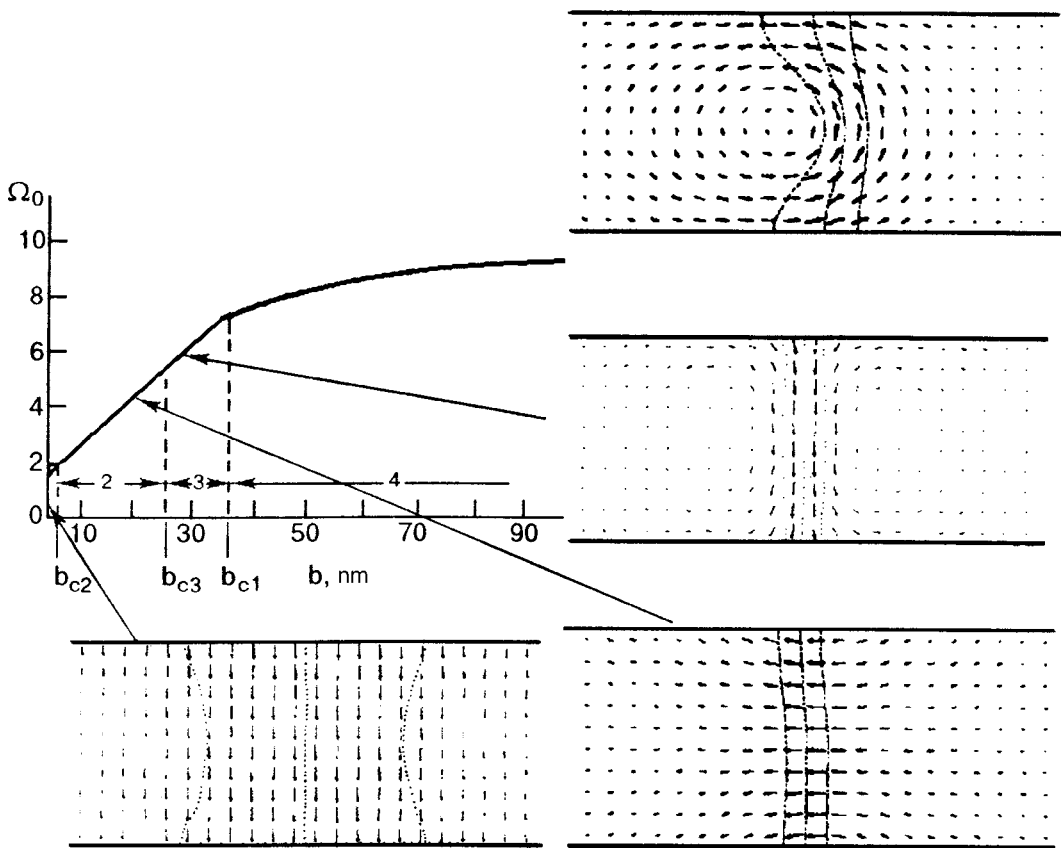

FIG. 11. Dependence of the relative energies of DWs with different structures (illustrated by fields of arrows) on the film thickness for films with the basic parameters and a surface magnetic anisotropy constant $K_S = -0.7$ erg/cm^2.

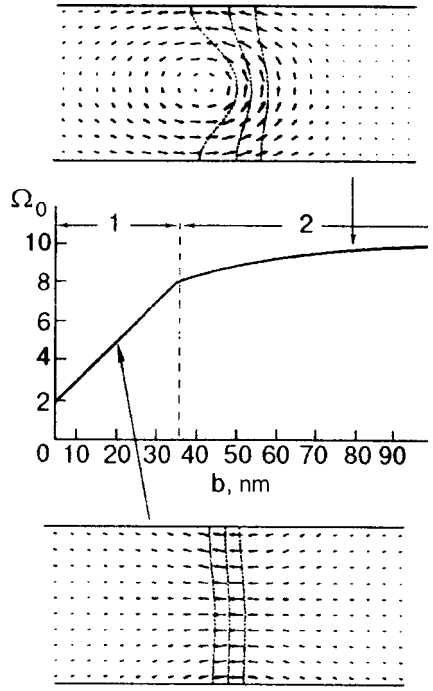

FIG. 12. Dependence of the relative energies of DWs with different structures (illustrated by fields of arrows) on the film thickness for films with the basic parameters and a surface anisotropy constant $K_S = 0.1$ erg/cm^2.

segment of DW having an average magnetization unfavorably oriented relative to the external magnetic field appears near the upper surface of the film. At the same time, near the lower surface of the film the DW segment having its average magnetization oriented along the field increases in length. As the field $H_\perp$ increases further, the **M** vortex is gradually pushed out onto the upper surface of the film. Finally, starting with a certain field $H_{\perp c}$ the wall with the asymmetric Bloch jump is transformed into an asymmetric Néel wall. These processes are clearly illustrated in Fig. 13. The field $H_{\perp c}$ depends on the material parameters of the film. For the basic values of the film parameters and a film thickness $b = 5\times10^{-6}$ cm, one finds that $H_{\perp c}$ is approximately 0.55 Oe. The influence of the surface anisotropy on the process just described was analyzed in Ref. 128. The results of this analysis are presented in Fig. 14. According to Ref. 128, for $K_S > K_{Sc} > 0$, where K_{Sc} is a certain critical field that depends on the material parameters of the film, in a field $H > H_{\perp c}$ it is not Néel walls but asymmetric Bloch walls that can exist, although the latter are metastable. This circumstance is due to the fact that the presence of surface anisotropy with $K_S > 0$ makes it difficult for the magnetization to undergo the necessary rotation at the upper surface of the film in order for the wall to transform from an asymmetric Bloch wall to an asymmetric Néel wall.

2.7. Asymmetric walls in polycrystalline films with cubic anisotropy

In Refs. 31, 33, and 129 it was shown that asymmetric Bloch walls also exist in films with cubic anisotropy. Here there is particular interest in films whose surface is oriented parallel to a crystallographic surface of the (001) type and in 180° DWs, also parallel to planes of the (001) type. In this regard we recall that in infinite crystals the 180° walls with

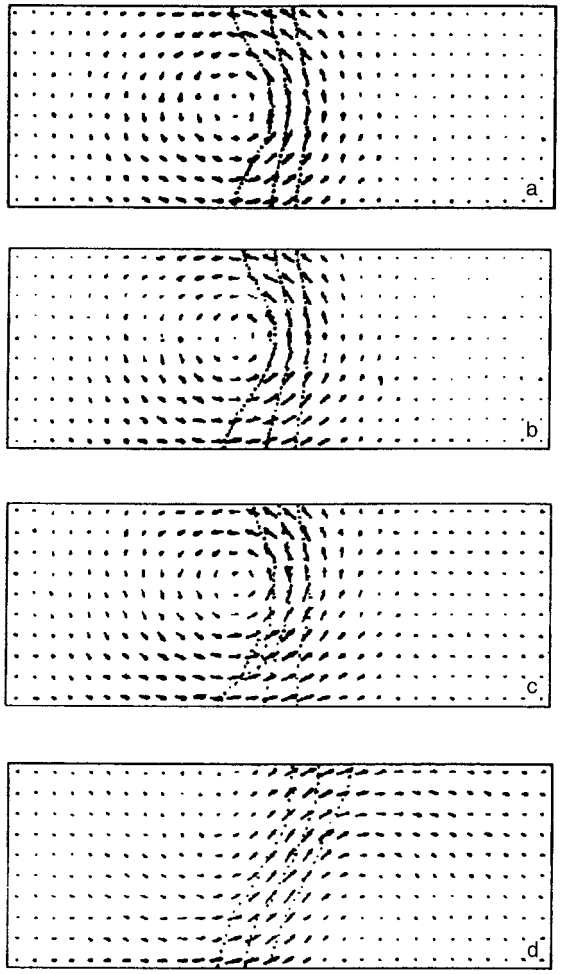

FIG. 13. Static configurations of DWs in films with the basic parameters and $b = 0.05$ μm, for different values of the external magnetic field H [Oe]: 0 (a), 0.2 (b), 0.4 (c), 0.6 (d).

such an orientation are unstable in the absence of magnetostriction, and they split into two 90° walls.[130] In Ref. 131, on the basis of qualitative considerations, it was shown that these walls can be stable in films even in the absence of magnetostriction. Rather precise calculations[31] have shown that DWs with an asymmetric two-dimensional structure exist and are stable against splitting into two 90° walls. Moreover, their energy is significantly less than the energy of the corresponding one-dimensional walls (see, e.g., Fig. 15). The possibility of the appearance of asymmetric DWs in the geometry described above and in the situation when in addition to the cubic anisotropy there is anisotropy induced in one of the directions (parallel to the surface of the film), e.g., due to magnetostriction, was also considered. It was found that the asymmetric Bloch walls are favorable even in this situation. The relative energy Ω_0 of such walls also increases with decreasing film thickness.

Asymmetric walls with a vortex structure (similar to that shown in Fig. 4a) have been observed in films with the surface plane oriented parallel to crystallographic planes of the (110) type.

In the same geometry as above, 90° DWs parallel to crystallographic planes of the (110) type (see Fig. 16) and having a two-dimensional structure were investigated in Refs. 132–134. It was found that the structure of these walls

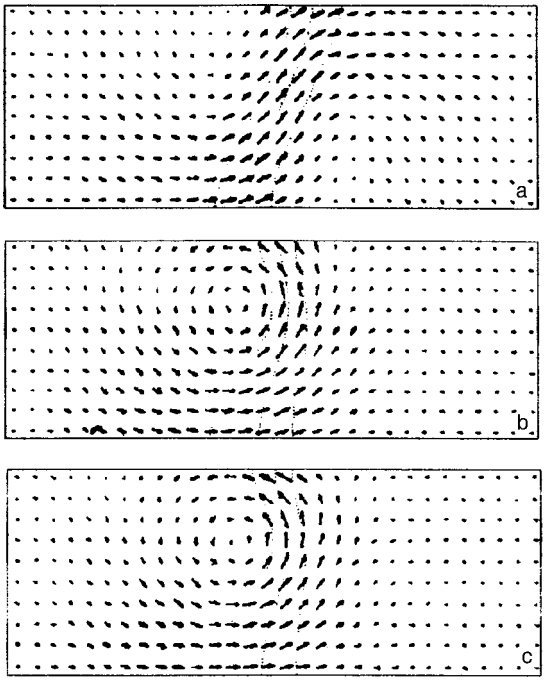

FIG. 14. Change of the static configurations of DWs in magnetic films with the basic parameters and thickness $b=0.05$ μm for $H=0.6$ Oe for different values of the surface anisotropy constant K [erg/cm^2]: 0 (a), 0.4 (b), 1.5 (c).

is asymmetric, but it is not of the asymmetric Bloch type (Fig. 4a) for any film parameters. No other stable or metastable configurations of 90° DWs of **M** have been found. This differs substantially from the situation observed for 180° DWs in magnetically uniaxial films. The two-dimensional structure of a 90° wall is shown in Fig. 17. Its asymmetry is indicated by the curved center line, which passes through the transverse cross section of the film. It is harder to make out its 90° character in Fig. 17. It is indicated qualitatively by the finite length of the arrows at the right and left ends of the figure. However, it is more convenient to judge this issue from graphs showing all the magnetization components as functions of the coordinate x (see Fig. 18). The orientation of the coordinate axes relative to the plane on which the DW structure is given (Fig. 17) is presented in Fig. 16. It is seen in Fig. 18 that M_z/M_s at the ends of the computation region along x has the values $\pm\sqrt{2}/2$. At the same time, M_y/M_s and M_x/M_s are equal to 0 and $\sqrt{2}/2$, respectively, on both ends of the computation region. From this it is clear that the magnetization **M** in the two adjacent domains lies at a 45° angle to the z axis, and that means a 90° character of the DW.

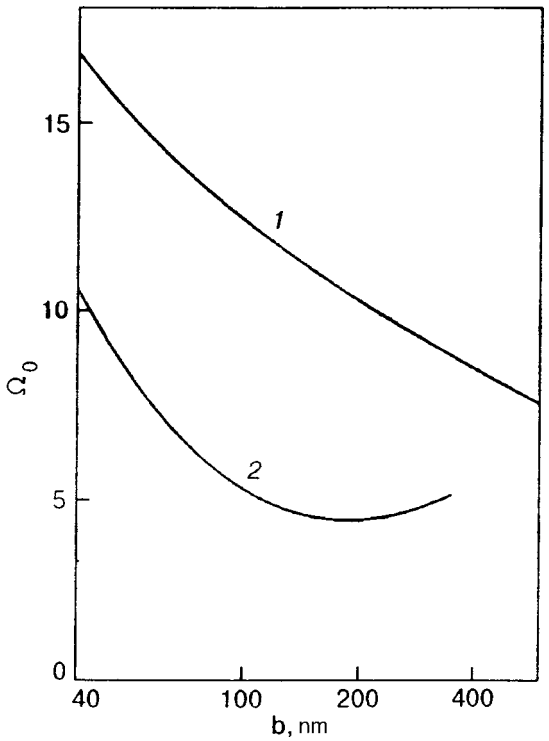

FIG. 15. Dependence of the relative energy of DWs on the film thickness in magnetic films with cubic anisotropy and parameters $A=2\times10^{-6}$ erg/cm, $K=4.2\times10^5$ erg/cm^3, $M_s=1700$ G: one-dimensional Bloch wall (*1*), asymmetric Bloch wall (*2*).[14]

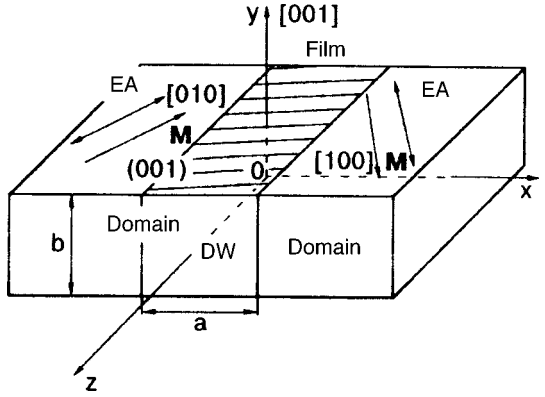

FIG. 16. Schematic illustration of a 90° domain structure in a magnetic film with cubic anisotropy and a surface plane of the (001) type and with the plane of the DW parallel to a crystallographic plane of the (110) type.

In addition to the asymmetry illustrated in Fig. 17, another substantial difference between a 90° wall and a Néel wall is that M_y in the former is nonzero, i.e., the magnetization in the film comes out of the film plane. This follows directly from a calculation of all the magnetization components and pertains to all of the films studied. The presence of M_y with the simultaneous existence of M_z does not make this a Bloch wall, since as one moves along x the rotation of **M** occurs not along a circular cone, as would be the case for a Bloch wall, but along a cone which is flattened along the y direction. Because of this, $\mathrm{div}\,\mathbf{M}\neq0$ inside the wall. In other words, both in the Néel DW, with nonzero magnetostatic volume charges due to M_x, and in the Bloch wall, with nonzero magnetostatic charges due to the presence of M_y, in

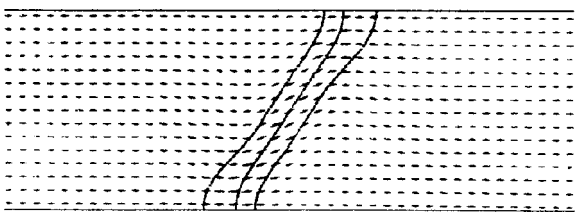

FIG. 17. Example of a 90° DW parallel to a plane of the (110) type in a film with parameters $A=2\times10^{-6}$ erg/cm, $K=4.2\times10^5$ erg/cm^3, $M_s=1700$ G, and $b=0.2$ μm. The compass arrows show the projection of the magnetization on the xy plane (see Fig. 16).

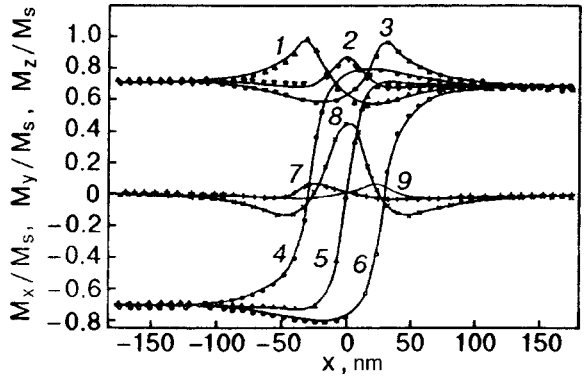

FIG. 18. Dependence of the components of the magnetization **M** on the coordinate x along the direction perpendicular to the plane of the DW for the upper (*1,2,3*), middle (*4,5,6*), and lower (*7,8,9*) layers of the film. The points correspond to a numerical simulation. The solid curves are drawn as a guide to the eye. The data were obtained for $b=0.12$ μm, $M_s=1700$ G, $K=4.2\times10^5$ erg/cm^3, and $A=2\times10^{-6}$ erg/cm.

such a wall there also exist nonzero magnetostatic charges due to the presence of M_y. Thus this wall is intermediate between the Néel and Bloch walls and, furthermore, as follows from Fig. 17, it is asymmetric (the center line of the wall is asymmetric relative to the y axis). We shall call this a quasi-Néel asymmetric wall.

Yet another feature of the 90° DW under study, and one which makes it substantially different from both the Bloch and Néel walls, is the decrease of the component M_y on going from the center of the film toward the surfaces, i.e., the oblateness of the cone mentioned earlier increases as one goes toward the film planes. In other words, near the surfaces of the film the structure of the wall becomes closer to the Néel structure, while near the center of the film it is closer to the Bloch. On the surfaces themselves the rotation of the magnetization is purely Néel. For confirmation of what we have said, Fig. 18 gives the dependence of all the components of **M** on the coordinate x for three planes: $y=0$, $\pm b/2$. The graphs agree qualitatively with those given in Ref. 132.

Figure 19 shows the total picture of the distribution of M_y inside the film region occupied by the wall.

2.8. Comparison with experimental data

Because of the small thicknesses of the films, the elucidation of their asymmetry properties requires experimental techniques with a spatial resolution of the order of a fraction of a micron. For this reason, scanning electron microscopes are usually used. Electron microscope studies of the structure of films have been reported in Refs. 31–35. In particular, in Ref. 31 a 1000 kV microscope was used. It can be considered that these experiments confirmed the existence of asymmetric vortical DWs. Let us discuss the studies of Ref. 33 in more detail. They were based on an experimental determination of $M_z(x)$ and a comparison of the results with the calculated dependence. According to Fig. 5, this dependence is asymmetric. In addition, it varies with y. However, the asymmetry remains, although less pronounced, upon averaging over the thickness of the film. What was determined experimentally was the average of $M_z(x)$ over the thickness of the film. Figure 20 shows the theoretical (dashed curve)

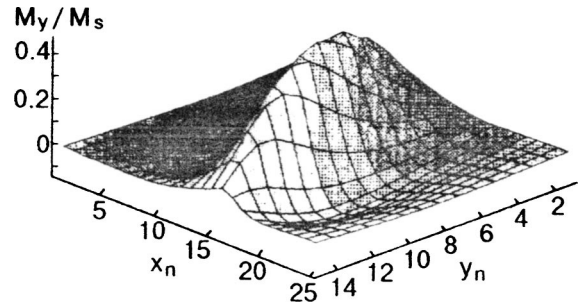

FIG. 19. Dependence of M_y/M_s on the coordinates x and y for a film with parameters $b=0.12$ μm, $M_s=1700$ G, $K=4.2\times10^5$ erg/cm^3, $A=2\times10^{-6}$ erg/cm. The numbers x_n and y_n correspond to $x=8$ (x_n-13) nm, $y=8$ (y_n-8) nm.

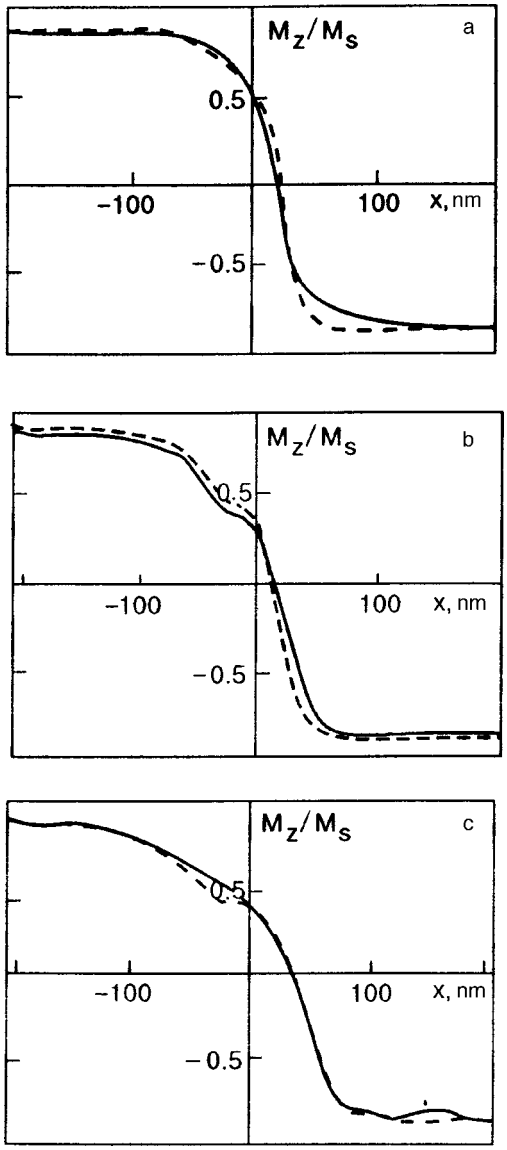

FIG. 20. Experimental (solid curve) and theoretical (dashed curve) curves of the average of the z component of the magnetization (in units of M_s) over the thickness of the film as a function of the coordinate x for films with thickness b [nm]: 100 (a), 120 (b), 200 (c). The data are taken from Ref. 33 and correspond to films of 33.8Ni–51.0Fe–14.0Co–1.2Ti (wt. %) with a saturation induction of approximately 1.5 T and with a small cubic anisotropy.

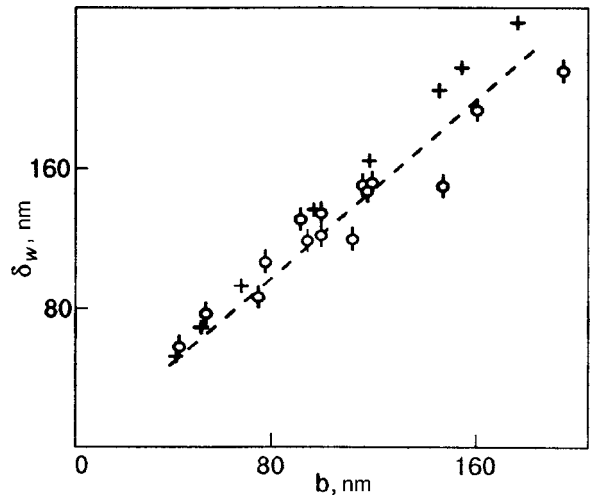

FIG. 21. Dependence of the thickness of an asymmetric Bloch wall on the film thickness for 33.8Ni–51.0Fe–14.0Co–1.2Ti films: experimental data of Ref. 33 (○, — — —), numerical simulation (+).

and experimental (solid curve) values of this function for films of various thicknesses. It is seen that the theory is in good agreement with experiment.

The experimental dependence of δ_w, which turned out to be approximately a straight line, was also obtained in Ref. 33. The data were obtained for 33.8Ni–51.0Fe–14.0Co–1.2Ti (wt.%) films, which have a saturation induction of 1.5 T and a slight cubic anisotropy. Unfortunately, the value of the anisotropy field was not given in Ref. 33. However, according to Ref. 33 and also our data (see Fig. 9), the value of δ_w depends weakly on K over a wide range of K (under the condition $K \ll 2\pi M_s$). For this reason the calculations for these films were done for $K = 10^3$ erg/cm^3. The results of a numerical simulation are also shown in Fig. 21. It is seen that the theory and experiment are in qualitative agreement. There are some quantitative discrepancies, most likely due to the aforementioned difficulties in determining δ_w.

3. DYNAMIC PROPERTIES OF DOMAIN WALLS WITH TWO-DIMENSIONAL INTERNAL STRUCTURE

3.1. Method of numerical study of the nonlinear dynamics of walls with a vortexlike internal structure

The study of DW motion was begun back by Landau and Lifshitz[12] (see also the references cited in Ref. 2). However, those studies were done at low external magnetic fields, in which the motion of the DWs occurs with practically no change in their internal structure. An important advance in this area of research was made by Döring[135] (see also Ref. 136), who predicted the existence of an effective mass of a DW. Starting with Ref. 136, the linear dynamical behavior of DWs was described by introducing some linear equations which could be justified approximately at low velocities by proceeding from the Landau–Lifshitz equations (see, e.g., Refs. 137 and 138). The DW velocities and mobilities were calculated on the basis of those equations. At sufficiently low fields (see above) those data were in good agreement with the existing experiments (see, e.g., Ref. 137).

A breakthrough in the study of nonlinear properties of DW motion came with the appearance of Refs. 139 and 140 (see also the experimental study in Ref. 141). After Ref. 140 it became clear that in a static magnetic field directed along the easy axis there exist at least two regimes of DW motion: steady and unsteady. It was explained that the unsteady regime is due to the disruption (at high fields H) of the balance of torque and the resulting precession of the magnetization about the easy axis. Unfortunately, however, those studies corresponded to the motion of a DW with a purely one-dimensional internal structure, a picture that can be applied without ''stretching'' only to infinite crystals. In films, as follows from the previous Sections, the structure of the films should be at least two-dimensional. In that case, as was mentioned in the introduction, an extremely important role begins to be played by the geometry of the problem and the values of the material parameters. In films with perpendicular anisotropy and a large quality factor $Q \gg 1$ the distribution of the magnetostatic fields plays a small role that can be taken into account in an approximate way. In particular, it is this circumstance that is responsible for the great progress that has been made in the understanding of the dynamic behavior of DWs in such films (in addition to the references cited previously[3,4,6] see also the theoretical papers[142–152] and experimental papers[153–163]).

In films with a small Q factor, including both magnetically uniaxial films with the easy axis in the film plane and also magnetically multiaxial films, as follows from the previous Section, the dipole interaction plays a decisive role and should be taken into account exactly (at least in the continuum approximation). Because of the complexity of taking this interaction into account, the dynamics of DWs with a two-dimensional magnetization distribution in films of this type can be investigated only numerically in the general case. By now a number of different numerical methods have been tried for studying the dynamical behavior of DWs with a two-dimensional structure.[90,105,164]

In the studies discussed below, the nonlinear dynamics of DWs with a two-dimensional—in particular, vortical—internal structure has been investigated on the basic of numerical solution of the Landau–Lifshitz equation, which we write in the form[165]

$$(1+\alpha^2)\frac{\partial \mathbf{u}}{\partial \tau} = -[\mathbf{u}, \mathbf{h}_{\text{eff}}] - \alpha[\mathbf{u}, [\mathbf{u}, \mathbf{h}_{\text{eff}}]], \tag{11}$$

where $\tau = \gamma M_s t$, t is the real time, α is the Gilbert damping parameter, $\mathbf{h}_{\text{eff}}$ is a dimensionless effective field

$$\mathbf{h}_{\text{eff}} = \mathbf{h}_e + \mathbf{h}^{(m)} - k_A(\mathbf{u}\cdot\mathbf{c})\mathbf{c} + \mathbf{h}, \tag{12}$$

with

$$\mathbf{h}_e = \frac{\partial^2 \mathbf{u}}{\partial \xi^2} + \frac{\partial^2 \mathbf{u}}{\partial \eta^2},$$

$$\mathbf{h}^{(m)} = \mathbf{H}^{(m)}/M_s, \quad \mathbf{h} = \mathbf{H}/M_s, \quad \mathbf{u} = \mathbf{M}/\mathbf{M}_s,$$

$$k_A = 2K/M_s, \quad \xi = x/b_0, \quad \eta = y/b_0, \quad b_0 = (A/M_s^2)^{1/2}.$$

For numerical solution of (11) with allowance for conditions (8) and (9) we choose the same spatial mesh as was used in the minimization of the functional E_D. We use the predictor–corrector method.[166] At time $\tau = 0$ the distribution

$\mathbf{u}_0$, determined by numerical minimization of the DW energy (6), is specified. In the first step of the iteration, $\mathbf{u}_{n+1}$ is determined according to the formula

$$\mathbf{u}^*_{n+1}=\mathbf{u}_n+\Delta\tau\mathbf{f}(\tau_n,\mathbf{u}_n) \tag{13}$$

(predictor), where

$$\mathbf{f}(\tau_n,\mathbf{u}_n)=-\frac{\Delta\tau}{1+\alpha^2}([\mathbf{u}_n,\mathbf{h}_{\text{eff}}(\mathbf{u}_n)]+\alpha[\mathbf{u}_n,[\mathbf{u}_n,\mathbf{h}_{\text{eff}}]]).$$

In the second step we use the procedure of final determination of $\mathbf{u}_{n+1}$:

$$\mathbf{u}_{n+1}=\mathbf{u}_n+\Delta\tau\mathbf{f}(\tau_n,\mathbf{u}^*_{n+1}) \tag{14}$$

(corrector).

The time dependence $\Delta\tau$ is chosen either constant or variable under the condition that the maximum angle of rotation of the magnetization vector in the cells is restricted to some small value.

There are provisions for introducing, at any time, random perturbations of any amplitude, and also for the possibility of starting from any configuration of **M**. This permits an assessment of the stability of the solutions obtained.

To determine the translational velocity of the DW we track the position of its center line. To rule out the escape of the wall to the boundary of the computation region V there are provisions for shifting that region as the DW moves.

The procedure described, which was originally designed to determine the equilibrium distribution of **M**, rapidly leads to stable solutions.

3.2. Steady-state DW dynamics

It was shown in Ref. 90 that, as in the case of walls with a one-dimensional structure,[140] there exists a magnetic field H_c (the bifurcation field) below which the motion of a DW with a two-dimensional structure is steady and above which it is unsteady. Let us consider the steady-state motion of the walls. According to the data of Ref. 90, when an external magnetic field $H<H_c$ is applied, after the transient processes has ended, the DW begins to move with a constant velocity (see Fig. 22a). The transient process ends in the displacement (over a certain time) of the center of the vortexlike part of the wall from the center of the film (Fig. 22c) to a new equilibrium position (Fig. 22b). Then the wall moves with a constant velocity with the displaced vortex. The value of the velocity of steady motion depends on the value of the field H and the film parameters and, as is seen in Fig. 22a, is of the order of 10^2 m/s. An important aspect is the approximately linear dependence of the velocity v on H. We note that such behavior differs strongly from the steady-state motion of walls with a one-dimensional internal structure (see, e.g., Ref. 140). According to Ref. 140, at a low Q factor the dependence of the velocity of steady motion of a wall with a one-dimensional magnetization distribution is nonlinear and even nonmonotonic. In particular, in a field $H<H_c$ the DW velocity reaches a maximum. Then as H is increased further up to H_c, the DW velocity decreases monotonically.

In Refs. 105 and 167 it was shown that the behavior of DWs with a two-dimensional structure actually does differ strongly from the steady-state motion of DWs with a one-dimensional structure. However, the region of field values in

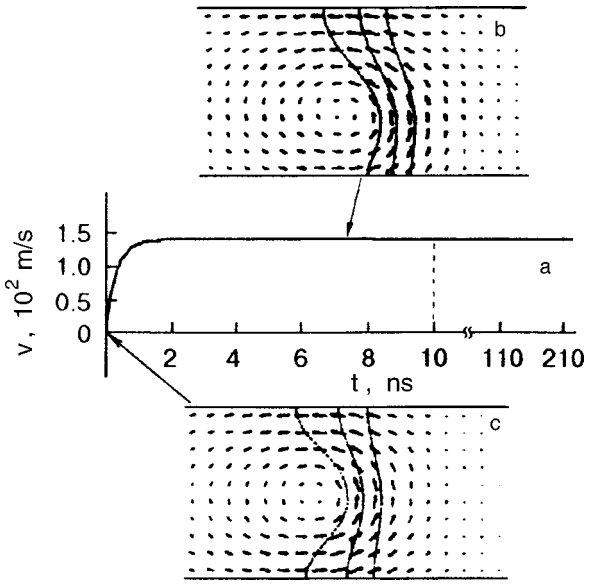

FIG. 22. Dependence of the average (corresponding to the motion of the centroid) velocity of a DW on time t (a) and the instantaneous configurations of the magnetization in the steady state of motion (b) and at the initial time (c). Basic films with $b=0.05$ μm, $\alpha=0.1$, and $H=80$ Oe.

which steady-state motion is possible, shown in Fig. 22a, differs from $(0, H_c)$: at a certain field $H=H_0<H_c$ the ABW (Fig. 23c) undergoes a transformation into an asymmetric Néel wall structure (Fig. 23b), which then moves steadily (see Fig. 23a).

Let us discuss the causes of this transformation. Remember that DW motion means a rotation of the magnetization from the direction in one domain to the direction in the other. Under the influence of a field applied along the easy axis, this rotation is made possible by the appearance of additional magnetostatic fields which lead to the precession of **M** about the x axis in the middle layers of the film or about the y axis in the layers near the surface. As they arise, these fields distort the structure of the DW, leading to an increase in the average value of the angle over the film thickness, φ_a. At a certain field $H=H_0$ the ABW structure cannot accommodate

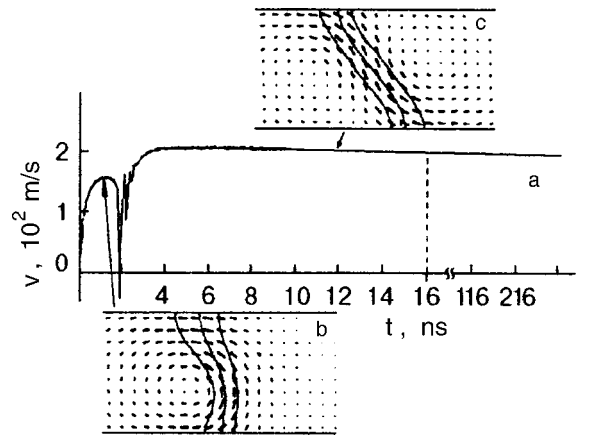

FIG. 23. Dependence of the average (corresponding to the motion of the centroid) velocity of a DW on the time t (a) and the instantaneous configurations of the magnetization in the walls: steady motion (b), transient process (c). Basic films with $b=0.05$ μm, $\alpha=0.1$, and $H=99$ Oe.

further increase in φ_a, and the wall is suitably transformed. The field H_0 depends on the film parameters and thickness.

An analogous transformation of the DW structure, but during its inertial motion, was predicted by Hubert.[2]

Thus there exists not one but two different types of steady-state motion. In one of them the wall has the asymmetric Bloch structure (in fields below $H_0<H_c$), and in the other, the asymmetric Néel structure (in fields above H_0 but below H_c). During the transformation of the structure of the wall its motion ceases to be steady, and the DW velocity increases rapidly with time until it reaches the velocity of an asymmetric Néel wall, which is always (as in the case of walls with a one-dimensional structure) higher than that of an asymmetric Bloch wall. It is clear from this that unlike the one-dimensional model, two-dimensional models of DWs (in films with a low Q factor) do not lead to the appearance of a physically incomprehensible maximum of the velocity in the region of steady-state wall motion ($H<H_c$).

At first glance it might seem that this behavior of the velocity as a function of magnetic field may be inconsistent with experiment (see, e.g., Ref. 168). However, it must be kept in mind that what is actually measured experimentally is the average DW velocity over some time interval δt. At the time of the transformation of the structure of the wall, at the transition from one steady-state motion to the other, as is seen in Fig. 23a, the velocity of the wall changes over a time interval Δt from a finite value to zero and below and then again increases to a larger positive value. Hence, in principle, a nonmonotonic H dependence of the time-averaged DW velocity, analogous to that observed in Ref. 168, for example, should arise. However, for the real samples the values of the intervals Δt are an order of magnitude shorter than δt. It is possible that at the time of the transformation of the wall structure an important role begins to be played by drag forces due to the local coercivity, which were not taken into account in the calculations. We also note that by virtue of what we have described above, it is possible that the average velocity over the time interval Δt not only decreases as a function of field H near H_0 but also subsequently increases;[168] such behavior would also agree qualitatively with experiment but does not in any way follow from the theory of the nonlinear dynamics of one-dimensional walls.[140]

3.3. Nonstationary dynamics of domain walls with a vortex domain structure

In fields above a certain critical field H_c (the bifurcation field) the steady-state motion of the wall is disrupted, and in a static magnetic field the wall begins to move with a variable velocity. In the course of time the internal structure of the DW undergoes global periodic transformations (a topological soliton with internal degrees of freedom). The program of study of the nonlinear behavior of DWs allows one to find the instantaneous configurations of the internal structure of the DW, which can be used to form freeze-frame motion sequences.[102,167]

Then by displaying those motion sequences on a monitor, one can track the dynamic transformations of the wall structure over any time intervals. It was found that the dynamic transformations of the DW structure are very sensitive both to the thickness and magnetic parameters of the film—saturation induction, anisotropy fields (in particular, the surface anisotropy field), exchange field, and damping parameter—and to the orientation and strength of the external magnetic field.

Figure 24 shows the variation of the velocity with time t and the instantaneous configurations of the magnetization characterizing the variations of the internal structure of the wall. It is seen that the velocity and structure of the wall in a field $H>H_c$ vary periodically as functions of time. Here, if at some point in time the structure of the wall is identical to that of an ABW (Fig. 24a), then in the course of time the DW vortex begins to shift toward the lower surface of the film (Fig. 24b). The direction of the displacement depends on the direction of the applied external magnetic field and the initial configuration of the wall. In this case the field **H** is directed along the positive z axis. Then the DW is transformed into the asymmetric Néel wall structure (Fig. 24c). As time goes on, the slope of the center line of this wall decreases, and the structure of the wall becomes practically similar to that of a one-dimensional Néel wall (Fig. 24d), which, in turn, is again transformed into an asymmetric Néel wall but with a different (opposite) slope of the center line (Fig. 24e). Then the lower (to the right of the center line) vortex vanishes, and the upper (to the left of the center line) shifts toward the lower surface (Fig. 24f). At that instant when the center of this vortex crosses the center of the film (Fig. 24g) the configuration of the wall is analogous to that shown in Fig. 24a but with the opposite chirality. This ends a half period of the transformation of the DW structure. In the next half period the wall undergoes exactly the same transformations as described above, and at the end of that half period the structure of the wall will be in all respects identical to the structure in Fig. 24a. The variations of the velocity in the two half periods are identical, as can be seen in Fig. 24. Thus there is degeneracy of the velocity with respect to chirality. The dynamic transformation of the DW structure described above is analogous to that which was first studied in Ref. 90. However, the resulting velocity variations presented in Ref. 90 and in Fig. 24 differ substantially from each other. The differences are due to the fact that the studies whose results are presented in Fig. 24 were done for fields only slightly different from the bifurcation field H_c, while the data of Ref. 90 correspond to fields significantly higher than H_c. It follows from a comparison of the two sets of data that the existence time of different dynamic structures are unequal, and, in particular, when **H** approaches the bifurcation field (for $H>H_c$) the existence time of the asymmetric Néel wall increases continuously. This agrees with the existence of steady motion of a DW with the asymmetric Néel structure below H_c, as described in the previous Section.

Direct numerical simulations show that the above-described dynamic transformation of the wall structure exists over a rather wide range of fields. The value of this range varies with changes in the film parameters, e.g., it decreases with increasing film thickness. In particular, as H increases, at certain values of the field the transformation can occur with the participation of three or more vortices, even in rather thin films. Figure 25 illustrates one of the stages of such a transformation at the time of formation of three vor-

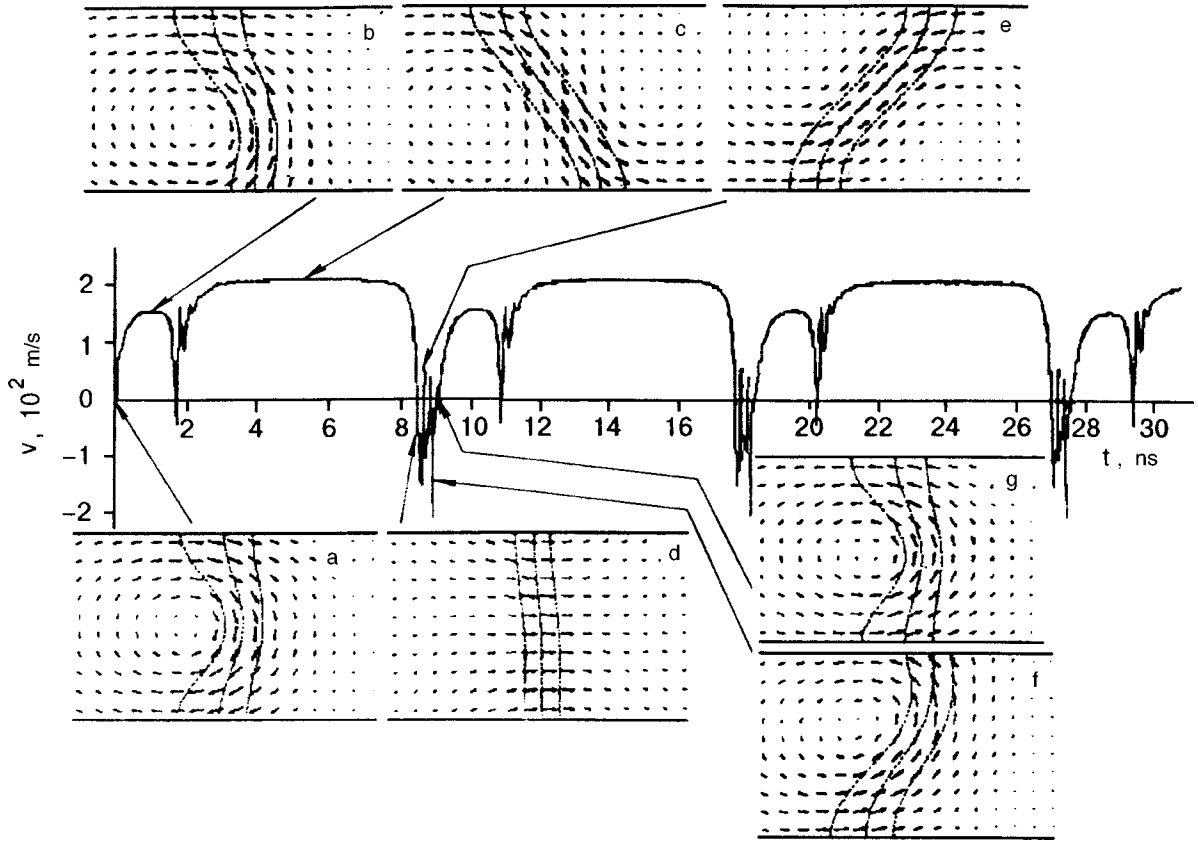

FIG. 24. Example of the time dependence of the average (corresponding to the motion of the centroid) velocity of a DW in the field region $H>H_c$ (unsteady motion) and the instantaneous configurations of the DW structure (a–g). Basic films with $b=0.05$ μm, $\alpha=0.1$, and $H=100$ Oe.

tices at $H=350$ Oe in a film with the basic parameters and a thickness of 0.05 μm. In thicker films the formation of multivortex structures occurs at considerably lower fields. Further increase of the field leads to chaotic variations of the wall structure and velocity. However, because of the complexity of the problem, this conclusion has not yet been verified successfully by the usual methods for studying the onset of deterministic chaos, which have been used, e.g., in Refs. 169–171. At the present time one can only cite Refs. 172–175, where analogous conclusions were reached for a somewhat different geometry of the problem.

As is seen in Fig. 24, in fields above H_c the variation of the wall structure is periodic. In particular, it is seen that there exist time intervals in which the wall is in retrograde motion, moving in the direction opposite to the main direction of motion determined by the given orientation of the magnetization of the domains and the external magnetic field. The causes of this surprising behavior of the wall will be discussed in Sec. 3.5. Here we only note that they have the same physical nature as in the case of the wall models with a one-dimensional distribution of the magnetization. The presence of retrograde motions does not alter the time-averaged translational motion of the walls in a definite direction (see above).

However, after the field H_c is passed the translational velocity (i.e., the average velocity over a period of the motion) should decrease with increasing external magnetic field. A certain particular case of the variation of the time-averaged velocity over a large interval of fields is shown in Fig. 26. We emphasize that this is only a particular situation, since

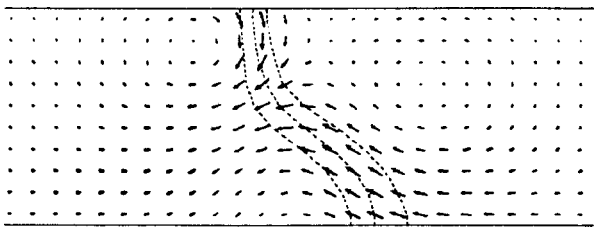

FIG. 25. Example of an intrawall three-vortex magnetization configuration arising at high magnetic fields. The data correspond to to basic films of thickness $b=0.05$ μm, $\alpha=0.1$, $H=350$ Oe.

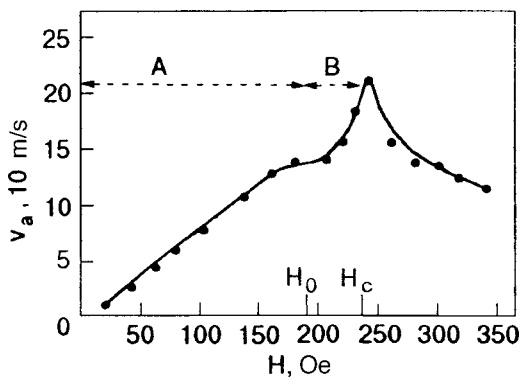

FIG. 26. Dependence of the time average (see text) velocity of a DW on the external magnetic field strength H. The data were obtained for basic films with $b=0.05$ μm, $\alpha=0.2$.

the result depends strongly on the value of the time interval over which the DW velocity is averaged. In the situation illustrated in Fig. 26, this average was done over a period of the dynamic transformation of the wall structure if $H>H_c$ and over the whole time of motion of the wall in fields $H<H_c$. As we mentioned in Sec. 3.2, if the velocity is averaged over a certain fixed time interval (as is done experimentally), the behavior of the velocity can depend strongly on the value of this interval. The two field regions (A and B) indicated in Fig. 26 correspond to different steady-state motion of the wall (see above). It is seen that for fields close to H_0 the growth of the time-averaged velocity v_a slows down, in qualitative agreement with experiments.[168]

3.4. Nature of the bifurcation process

To elucidate the causes of the onset of unsteady motion of a DW with a vortex structure, the dependence of the angle φ (see Fig. 1) on time t was investigated for three cases: 1) steady-state motion on an asymmetric Bloch wall, 2) steady-state motion of an asymmetric Néel wall, and 3) unsteady motion. We note that φ describes the deviation of the magnetization **M** from the plane of the wall (from the yz plane). The two-dimensional distribution of the magnetization in the walls is such that the angle φ is nonzero and varies from one surface of the film to the other. Here, in a state of equilibrium the magnetostatic energy of the wall becomes small compared to the magnetostatic energy of the other possible equilibrium configurations of the DW (see Sec. 2). Motion of the DW means precession of the magnetization about a direction perpendicular to the normal to the plane of the wall (about x for the central layers of the film) and about the normal to the surface of the film in the layers near the surface.

By virtue of the gyroscopic properties of the elementary magnetic moments forming the wall, an external magnetic field oriented along the easy axis cannot lead directly to such a precession but only to precession of the magnetic moments of the wall about the easy axis (about z). In the absence of damping this precession could only cause oscillations of the wall about an equilibrium position. The presence of damping can lead to a balance of the energy due to the field H and the energy due to the damping. Thus, in the simultaneous presence of damping and the precession indicated above, a stationary distortion of the wall structure, due to a stationary variation of the angle φ, can arise. Generally speaking, the situation described is analogous to that which is observed for a wall with a one-dimensional magnetization distribution[140] and differs from it only in that the departure of the magnetization from the plane of the wall which arises in the case of the two-dimensional magnetization distribution is nonuniform. This departure of **M** from the plane of the wall gives rise to an additional magnetostatic field $\Delta H^{(m)}$ oriented along x. The torque due to this field causes the precession of the magnetization (about x) necessary for motion of the wall along this axis. It is clear that the larger the torque, the higher the DW velocity. It should now be remembered that the magnetostatic field cannot exceed $4\pi M_s$ (i.e., it is finite) even in an infinitely thick film. Therefore the torque it causes will also be finite. The value of φ reaches a maximum at certain value φ_0. Consequently, as long as the angle φ remains less than φ_0 as H is increased, the torque at a fixed H remains constant. In that case the wall moves with a constant velocity. If φ increases without bound, the torque will vary periodically. This is what causes the oscillatory behavior of the velocity and structure of the DW.

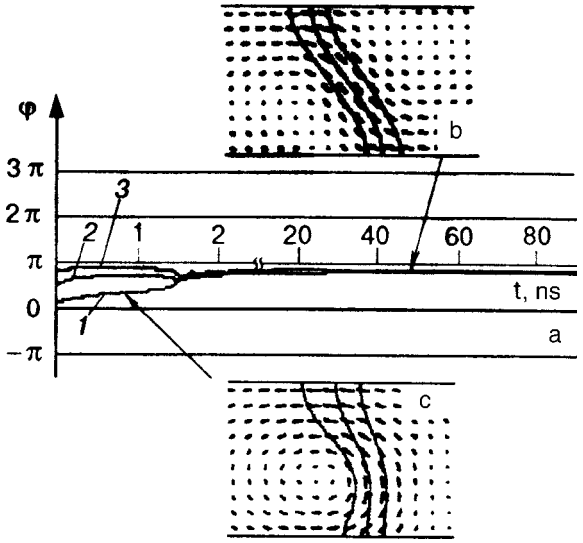

FIG. 27. Time dependence of the angle φ (a) and two instantaneous configurations of the wall (b and c) for basic films with $b=0.05$ μm and $\alpha=0.1$. Curves *1–3* correspond to φ at the lower ($y=-b/2$), central ($y=0$), and upper ($y=b/2$) surfaces of the film, respectively.

To elucidate the possibility of one situation or another arising, the angle φ was calculated[167] in three different layers of the film for three different values of the magnetic field: 1) $H<H_0$, 2) $H_0<H<H_c$, 3) $H>H_c$.

In the first case, after a transient process has taken place, the angles in all three layers approach a constant value and no longer change with time. These constant values increase with increasing H. In the second case (see Fig. 27) all three values increase with time at a fixed field and, after becoming practically identical, cease to change further. Here the wall goes to a steady state of motion, with the structure illustrated in Fig. 27b. In the third case, all values of the angle φ increase in time without bound (see Fig. 28). Here, as can be seen in Fig. 28, the structure of the wall varies periodically. From the data presented it is seen that whereas in fields below H_c only a certain finite departure of the magnetization from the plane of the wall is observed, in fields above H_c a continuous precession of the magnetization about the easy axis occurs. Thus the bifurcation field is the field starting at which the magnetization begins to precess about the easy axis as well as about the direction of motion. From what we have said it is also clear that, in contrast to a DW with a one-dimensional structure, where the nature of the bifurcation is also due to precession of **M** about the easy axis, in walls with a two-dimensional magnetization distribution the precession is also nonuniform over the film thickness.

The precession of **M** described above initially leads to a gradual increase in the average over the film thickness of the magnetization component in the direction of motion of the wall, $M_{\rm av}$. However, after reaching the maximum value of this magnetization, it again decreases to zero, and then a resultant magnetization appears in the direction opposite to the motion of the wall. This leads to retrograde motions of

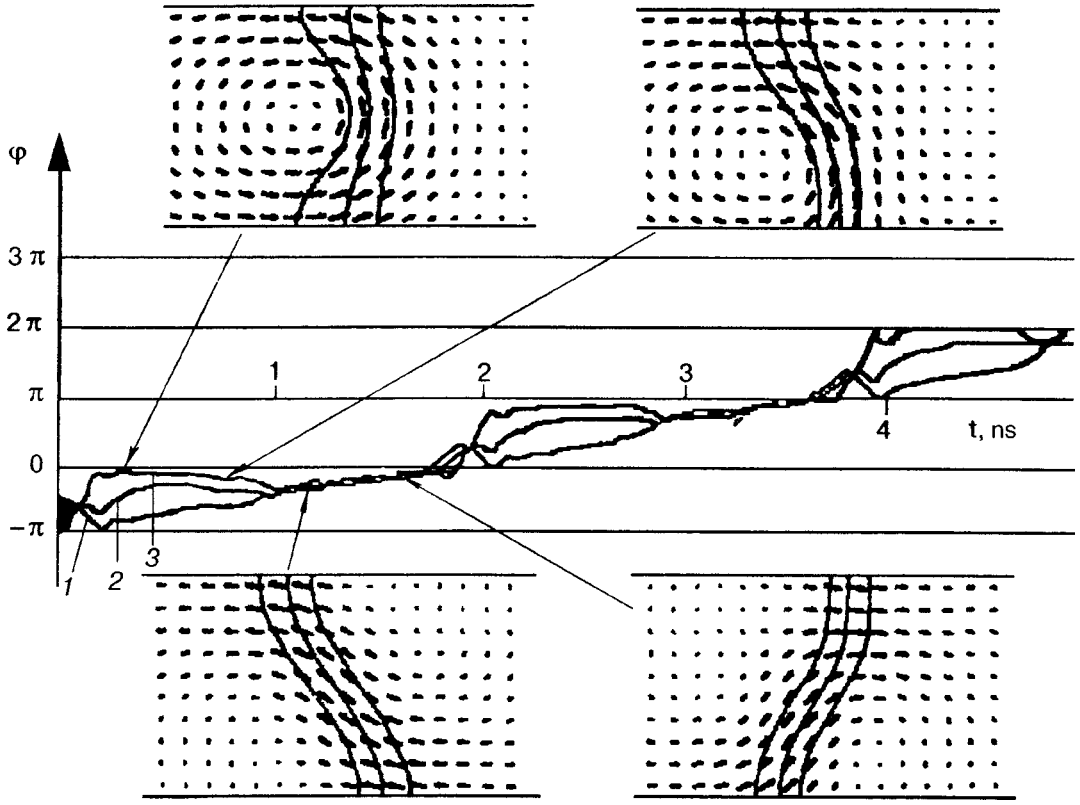

FIG. 28. Time dependence of the angle φ in three planes of the film ($y=-b/2$ (*1*), $y=0$ (*2*), and $y=b/2$ (*3*)) and instantaneous configurations of the wall at the indicated points. Basic films with $b=0.05$ μm, $\alpha=0.1$, and $H=150$ Oe.

the wall, i.e., to motions in the direction opposite to the initial direction of motion. With the change in M_{av} the internal structure of the wall should also change. In particular, it is clear that in some cases the wall should take on a one-dimensional Néel structure at the maximum value of M_{av}.

Thus the actual cause of the bifurcation is the same for DWs with one- and two-dimensional magnetization distributions. However, the specific manifestations of bifurcation in these cases are different. So far this difference has concerned only the specific transformation of the internal structure and has been natural. Below we shall indicate some radical differences of the nonstationary dynamics of two-dimensional walls from the dynamics of one-dimensional walls. In particular, we shall elucidate the important features of the dynamics of DWs with an internal structure which are impossible to describe in a one-dimensional model.

3.5. Period of the dynamic transformation of the internal structure of a wall

As we have said, in fields $H>H_c$ the motion of a wall and the dynamic variation of its internal structure in a certain region of fields occur in a periodic manner. In this regard it is of interest to study the value of this period as a function of the magnetic parameters of the film and its thickness. Such studies are not only of interest from the standpoint of the physics of the process but will also make it possible to assess the possibilities of obtaining indirect experimental evidence of the occurrence of dynamic transformation of the DW structure.

In accordance with what we have said above, the character of the dynamic transformation of the wall structure changes with distance from the bifurcation point. In Refs. 105 and 167 the dependence of the period of the dynamic transformations of the DW structure on the value of the external magnetic field was studied in the field interval (H_c, H_{c1}) directly adjacent to the bifurcation field. Here H_{c1} is the first field after H_c at which a change occurs in the dynamic transformation process. Studies were done in a wide interval of parameters M_s, K, and A. All of the $T(H)$ curves found have a qualitatively similar character. Figure 29 shows these curves for films with certain parameter values. As expected, for all the films the period of the dynamic transformation of the wall structure increases without bound as the bifurcation field is approached. This agrees qualitatively with the model of walls with a one-dimensional structure, where the period T can be obtained analytically as[140] (see also Ref. 6)

$$T=\frac{2\pi}{\omega_H}(1+\alpha^2)\frac{1}{\left(1-\dfrac{H_c^2}{H^2}\right)^{1/2}}, \tag{15}$$

where $\omega_H=\gamma H$.

The curves shown in Fig. 29 are in rather poor quantitative agreement with (15). Calculations show that instead of a critical exponent of 1/2 characterizing the behavior of the period of the dynamic transformation of the internal structure of a wall near the singular point (bifurcation point), an exponent $s\neq 1/2$, which varies with the film parameters, gives a better fit. Table II gives the data from a numerical simulation[167] for a film with the basic parameters and $b=0.05$ μm, $\alpha=0.1$. Here for comparison we also present

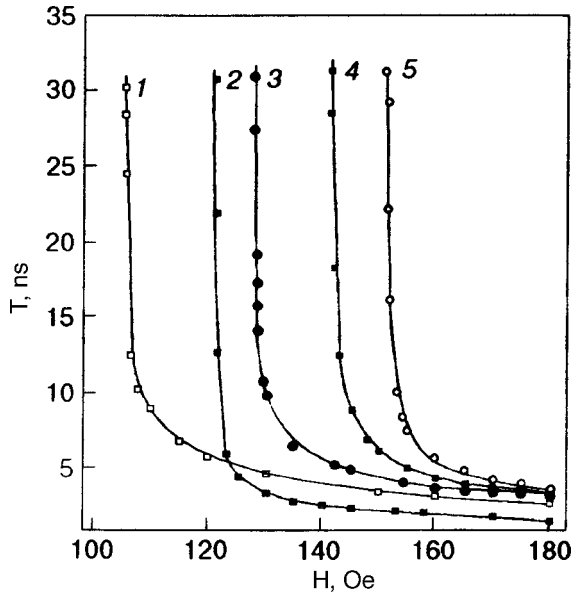

FIG. 29. Examples of the dependence of the period T of the dynamic transformation of the DW structure for films with $\alpha=0.1$ and different parameters: *1*—$K=10^5$ erg/cm^3, $b=0.05$ μm; *2*—$b=0.08$ μm; *3*—$b=0.055$ μm; *4*—$K=10^6$ erg/cm^3, $b=0.05$ μm; *5*—$M_s=900$ G, $b=0.05$ μm. The remaining parameters correspond to the basic film. The points are the data of a numerical simulation. The solid curves are drawn as a guide to the eye.

data obtained on the basis of the empirical formula proposed in Ref. 167:

$$T=\frac{2\pi}{\omega_H}(1+\alpha^2)\left(\frac{1}{\left(1-\frac{H_c^2}{H^2}\right)^s}+\frac{1}{5}\left(1-\frac{H_c^2}{H^2}\right)\right),\quad H\geqslant H_c, \tag{16}$$

and also on the basis of formula (15).

It is seen from the table that for a critical exponent $s=0.4$ and for values of the critical field $H_c=99.3265$ Oe (this value agrees with that obtained in Ref. 90), formula (16) describes the data from the numerical simulation rather accurately. The relative error is not over 5%. At the same time, the best data (at $H_c=99.3078$ Oe) obtained for T on the basis of a one-dimensional model of the magnetization distribution differs very strongly (by up to 45%) from the data of the numerical simulation.

It is clear that these discrepancies are due to the completely different character of the dynamic transformation of the DW structure in the cases of one-dimensional and two-dimensional models of the magnetization distribution. The existence of new possibilities for transformation of the wall structure in the framework of the two-dimensional model of the distribution of **M**, which are due, in particular, to the appearance, motion, and disappearance of vortexlike formations of the magnetization inside the wall, should also have an effect on the critical field (bifurcation field) itself.

3.6. Dependence of the critical field on the film parameters

To reveal most fully the features of the nonlinear dynamic behavior of DWs it is important to study the dependence of the critical field on the film parameters.[105,167] Knowledge of the critical field is also important for determining the conditions for obtaining the maximum DW velocities. The point is that in fields much below the critical field, the wall velocity can be written in terms of the mobility μ in the framework of the existing DW models as

$$v=\mu H, \tag{17}$$

where

$$\mu=\gamma\delta/\alpha, \tag{18}$$

and δ is the thickness of the DW. According to Eqs. (17) and (18), it is possible to obtain arbitrarily high DW velocities if films with low damping are used. However, in accordance with the data for one-dimensional wall models (see Ref. 140) the critical field below which the above relations are valid is

$$H_c=2\pi M_s\alpha. \tag{19}$$

We see that in films with low damping the critical field is low, and therefore the region of fields H for which Eqs. (17) and (18) are valid is narrowed in them. In that region the velocity is restricted by the limiting value $v_c=\mu H_c$. In addition, it is expected that H_c can have a different dependence of the material parameters than would follow from (19). It is therefore necessary to study H_c.

Determining H_c is a most laborious task, since finding only one value of H_c requires constructing the $T(H)$ curve for a fixed set of parameters. From those data, following Ref. 105, one can construct the $H(1/T)$ curve and then, by extrapolating it for $(1/T)\to\infty$ (see Fig. 30), find the critical value H_c. In this way we constructed the H_c curves as func-

TABLE II. Dependence of the period of the dynamic transformation of the DW structure on the external magnetic field. A comparison of the data of a numerical simulation with the data obtained from formula (15), which was obtained for a one-dimensional model, and formula (16).

H, Oe	T, ns		
	Numerical simulation	Eq. (15)	Eq. (16)
99.33	**171.684**	**171.704**	**166.244**
99.35	77.854	124.531	77.630
99.37	**59.280**	**102.569**	**60.698**
99.40	46.910	84.239	49.223
99.50	33.530	58.330	34.934
100	**19.680**	**30.698**	**20.351**
102	11.640	15.488	11.774
104	**9.524**	**11.674**	**9.434**
106	8.344	9.727	8.166
108	**7.534**	**8.494**	**7.379**
110	6.981	7.721	6.776
115	**5.906**	**6.218**	**5.787**
120	5.194	5.352	5.149
130	**4.330**	**4.298**	**4.329**

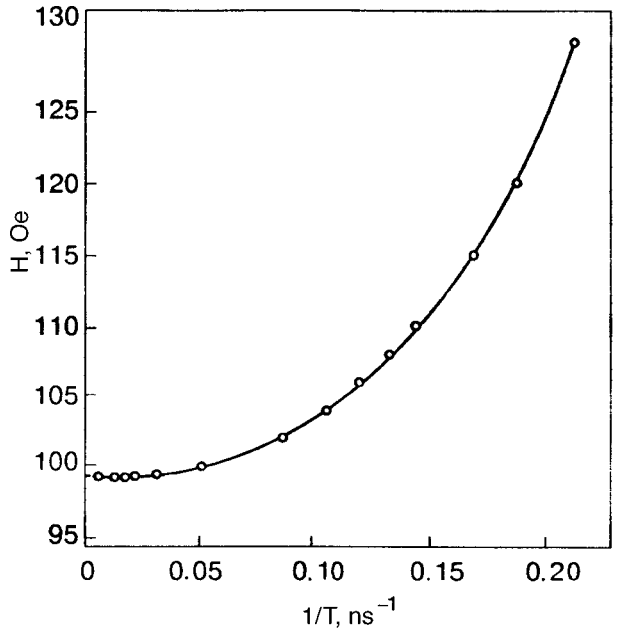

FIG. 30. Dependence of H on $1/T$. Data obtained for basic films with $b=0.05$ μm, $\alpha=0.1$.

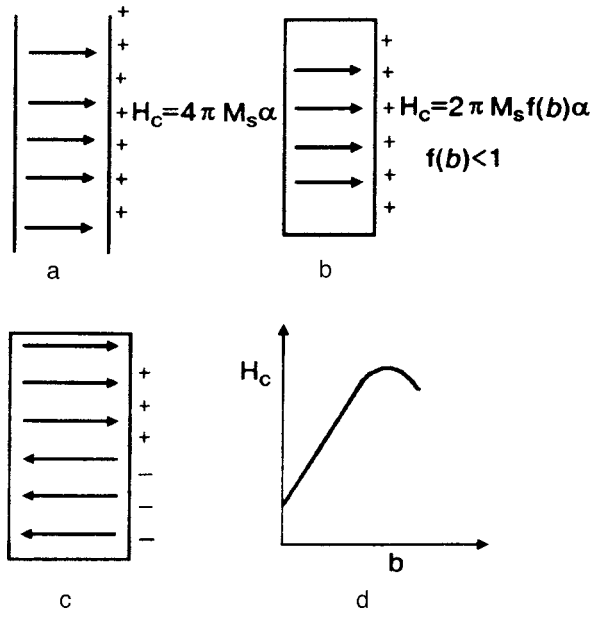

FIG. 31. Schematic illustration of the instantaneous distribution of poles on the lateral surfaces of the DWs: infinite crystal (a), film with a transformation of the wall structure by the scenario in Fig. 24 (b), film with a transformation of the wall structure by scenarios leading to fractionation of the poles (c). Schematic illustration of the decrease of H_c upon fractionation of the poles on the later surface of the film (d).

tions of the film thickness, saturation induction, anisotropy field, exchange field, and damping parameter.

Before turning to the results, let us recall that the field H_c, obtained in the framework of a model with a one-dimensional distribution of **M** in the DW is proportional to the saturation magnetization [see Eq. (19)]. This dependence of H_c on M_s is easy to explain. We recall that H_c corresponds to the field at which the torque due to the magnetostatic field component $H_x^{(m)}$ is maximum. This is reached only at the maximum of $H_x^{(m)}=H_m$. The value of H_m is realized when the configuration of **M** becomes close to the configuration of a classical Néel wall (see Fig. 24d). A DW of that type can be likened to a slab magnetized to saturation in the transverse direction. If this slab is infinite in the yz plane (see Fig. 31a), as is actually the case in the one-dimensional model,[90] then $H_m=4\pi M_{\rm av}=2\pi M_s$, which leads to Eq. (19). Here $M_{\rm av}$ is the average value of the component M_x over the thickness of the wall. In the framework of a one-dimensional Néel rotation of **M** in the wall, $M_{\rm av}=M_s/2$. In the film in Fig. 31b the wall indicated above can be represented in the form a slab with finite dimensions, and therefore the value of H_c in it, independently of the model of the **M** distribution, will depend on the thickness b in terms of some function $f(b)$,[165] i.e.,

$$H_c=2\pi M_s\alpha f(b). \tag{20}$$

With increasing b the value of $2\pi M_s f(b)$ here should approach $2\pi M_s$, i.e., the value in an infinite sample. Thus it would seem that H_c should increase with increasing film thickness. This increase has actually been observed,[165] but in a very narrow region of b. In a wider region of b, contrary to expectations, the function $H_c(b)$ is nonmonotonic (see Fig. 32). Moreover, the function $H_c(M_s)$ is also nonmonotonic (see Fig. 33). These results have nothing in common with those given by the one-dimensional model of the distribution of **M** [see Eq. (19)].[140]

To understand the cause of these unexpected results, one can trace the nonlinear dynamic transformation of the internal structure of the film in the immediate vicinity of the critical field in films of different thicknesses and with different saturation magnetizations.[176–178] It turns out that in films with the basic parameters and thicknesses roughly in the interval 0.04–0.065 μm, i.e., in the situation when H_c increases with increasing b, the transformation of the DW structure takes place according to the usual classical scenario, as is shown in Fig. 24. The most important event in this transformation is the formation of the structure shown in Fig. 24d. In films of thickness $b\geqslant 0.064$ μm the mechanism of nonlinear dynamic transformation of the DW structure is radically altered. For thicknesses roughly in the interval 0.065 μm$\leqslant b\leqslant 0.075$ μm the transformation occurs with the formation of two asymmetric vortices arranged one above

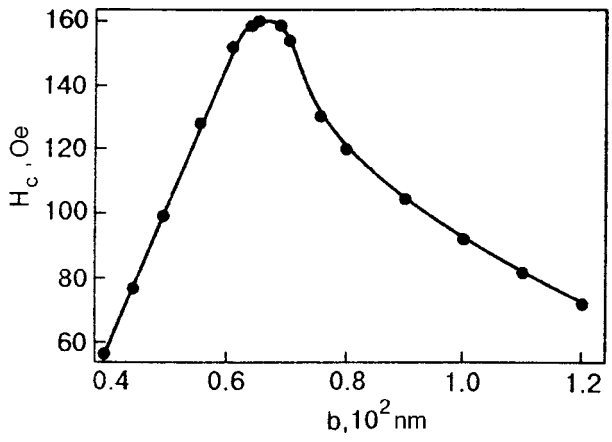

FIG. 32. Dependence of the critical field on the film thickness. Basic parameters and $\alpha=0.1$.

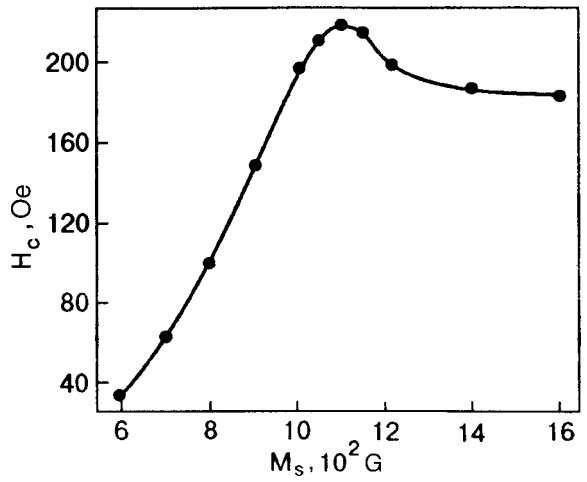

FIG. 33. Dependence of the critical field on the saturation magnetization M_s; A and K correspond to the basic parameters, $b=0.05$ μm, $\alpha=0.1$.

the other (the first type of scenario; see Fig. 34), and for $b \geqslant 0.076$ μm it occurs by the gradual penetration (tunneling) of the vortex through the center line of the wall (the second type of scenario; see Fig. 35).

Let us discuss in more detail the character of the transformation of a DW in a film with $b \geqslant 0.64$ μm, in which, according to Fig. 32, a decrease of the bifurcation field with increasing thickness occurs.

In the first case (Fig. 34) the vortex of an asymmetric Bloch wall located at the center of the film is displaced toward its lower surface (Fig. 34a). Near the upper surface a new vortex with the opposite chirality is created, so that at a certain stage of the transformation the DW consists of two vortices arranged one above the other (Fig. 34b). Then both vortices are displaced downward, and the lower vortex vanishes (Fig. 34c). The remaining, upper vortex is displaced downward. After it passes through the center of the film (Fig. 34d), a vortex configuration of **M** (see Fig. 34d) analogous to that shown in Fig. 34a but with the opposite chirality is formed. This ends a half period of the transformation of the DW. In the next half period an analogous transformation takes place, and the structure of the wall is transformed back to the initial structure.

In the second type of case (Fig. 35) the **M** vortex, having been displaced downward (Fig. 35a), begins to tunnel through the center line to the right side of the wall (Fig. 35b) so that a vortex with the same chirality as before is formed on that side (Fig. 35c). Then near the upper surface to the left of the center line another vortex forms, with a chirality opposite to the previous one. It expands, and the magnetization configuration takes the form shown in Fig. 35d. Then the vortex on the right vanishes, and the left one is displaced downward. The resulting configuration of **M** is shown in Fig. 35e,f. The latter differs from the initial configuration (Fig. 35a) only in the chirality of the vortex. This ends the half period. In the second half period analogous transformations lead back to the initial DW structure.

The most important aspect of both mechanisms of transformation is the absence of a stage involving the formation of a one-dimensional Néel wall (see Fig. 24d), as in the case of the classical scenario for the development of the the transformation of the DW structure. Besides this, a structure of the type b in Fig. 34 or type b in Fig. 35 appears. In either case, unlike the structure d in Fig. 24, a fractionation of the magnetic poles on the lateral surface of the film occurs, as is shown schematically in Fig. 31c. This leads to a decrease of H_m and, hence, to a decrease of H_c. The increase of the thickness of the film enhances the tendency toward fractionation of the poles.

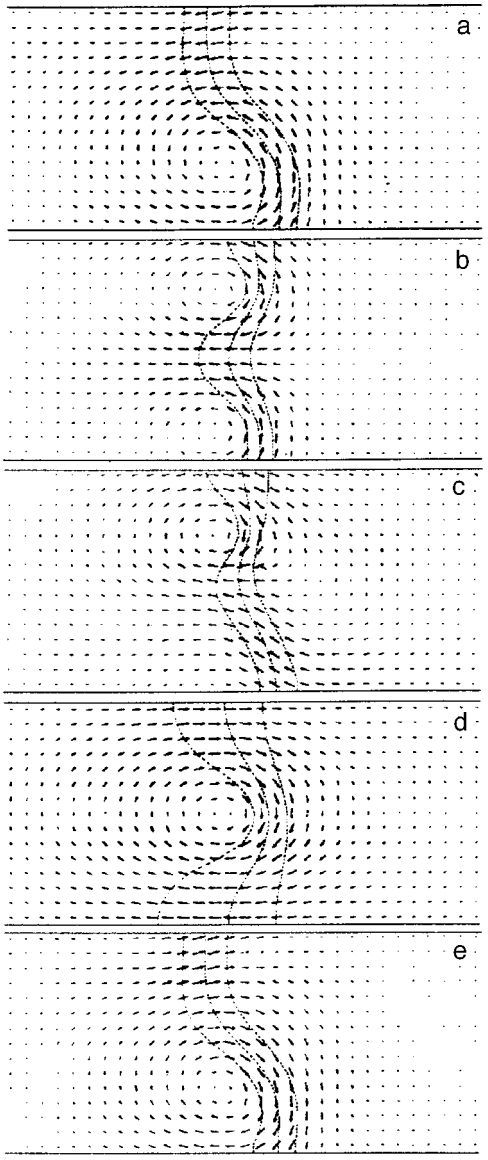

FIG. 34. Sequence of instantaneous configurations of a wall during the dynamic transformation of its structure in films with the basic parameters and $\alpha=0.1$, $b=0.07$ μm, and $H=103$ Oe.

Increasing the saturation magnetization at a given film thickness leads to an increase of the density of poles on the lateral surface of the film in the case of the classical mechanism of transformation of the DW structure. This leads to an increase of H_c. With increasing M_s, however, the exchange length b_0 decreases, so that it becomes possible for fractionation of the poles to occur on the planes of the wall which are perpendicular to x. This means that, starting at certain values of M_s, the field H_c should decrease, as is confirmed by numerical simulations (see Fig. 33). The transformations

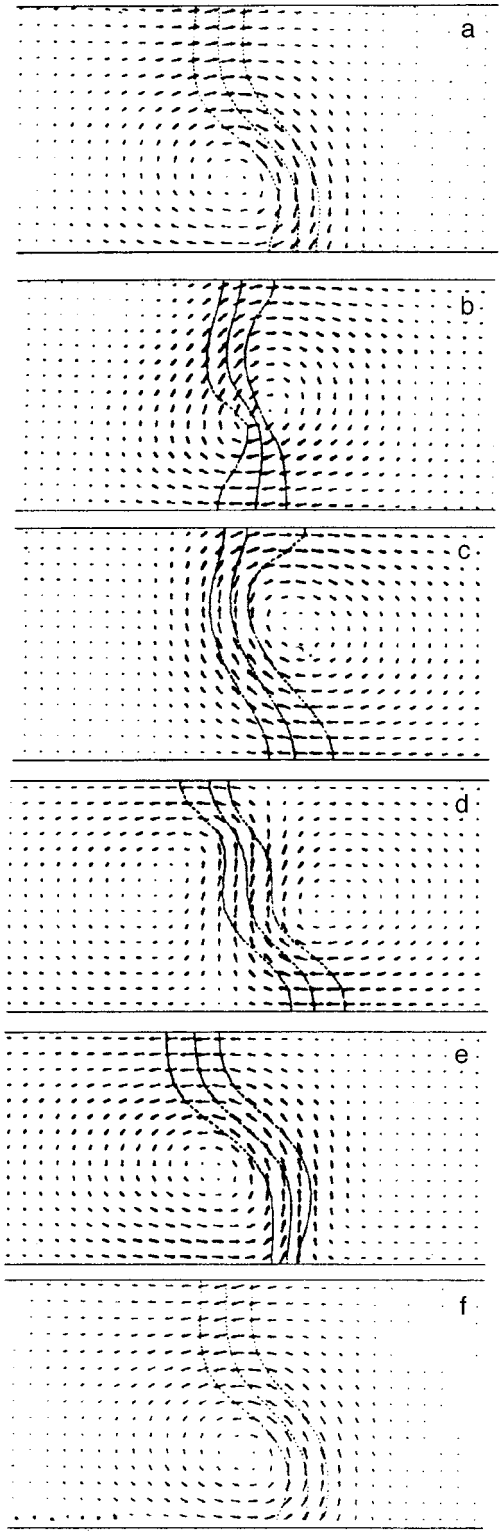

FIG. 35. Sequence of instantaneous configurations of the wall during the dynamic transformation of its structure in films with the basic parameters and $\alpha=0.1$, $b=0.1$ μm, and $H=103$ Oe.

of the DW structure that arise for this mechanism are analogous to those indicated above.

According to Ref. 20, the critical field is independent of the anisotropy field. However, this is due not to the one-dimensional character of the magnetization distribution, in the framework of which Eq. (20) was obtained, but to the assumption that the shape of the wall does not change during its motion. As we have shown, in a model with a two-dimensional distribution of **M** this as is in general incorrect. Actually, substantial distortions of the DW structure occur. This means that, in addition to the torque due to the magnetostatic fields there should also arise torques due to the exchange and anisotropic interactions. Both these contributions are finite, as is the contribution due to the magnetostatic fields. This means that, in contrast to Eq. (20), the field H_c should depend on the anisotropy field H_a and exchange field H_e. It has been observed (see, e.g., Ref. 177) that the dependence of the critical field on H_a (see Fig. 36) is close to linear, while the dependence on H_e is nonmonotonic.

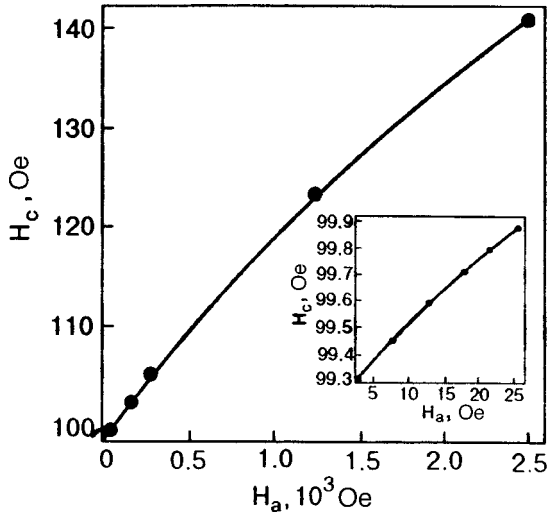

FIG. 36. Dependence of the critical field H_c on the anisotropy field H_a for films with the basic parameters and $\alpha=0.1$, $b=0.1$ μm.

3.7. Influence of damping on the dynamic transformation of the wall structure

Figure 37 shows a plot of $H_c(\alpha)$ obtained in Ref. 105 for a wide range of variation of α. It is seen that the dependence is basically close to linear, in agreement with the one-dimensional model of the magnetization distribution in the wall [see Eq. (19)]. However, the slopes of the H_c/α curves for the one-dimensional and two-dimensional models are

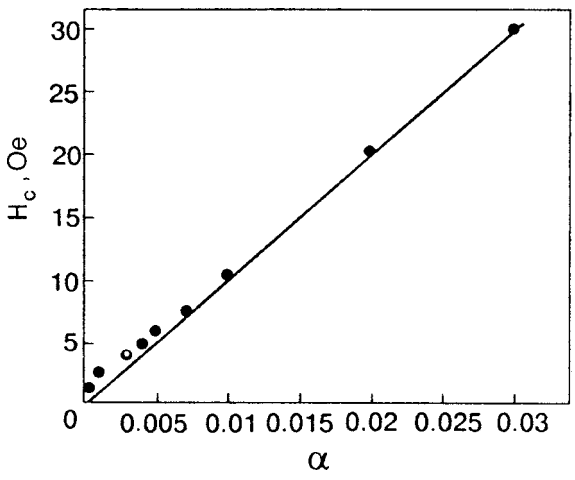

FIG. 37. Dependence of the critical field on the damping parameter α for basic films with $b=0.05$ μm.

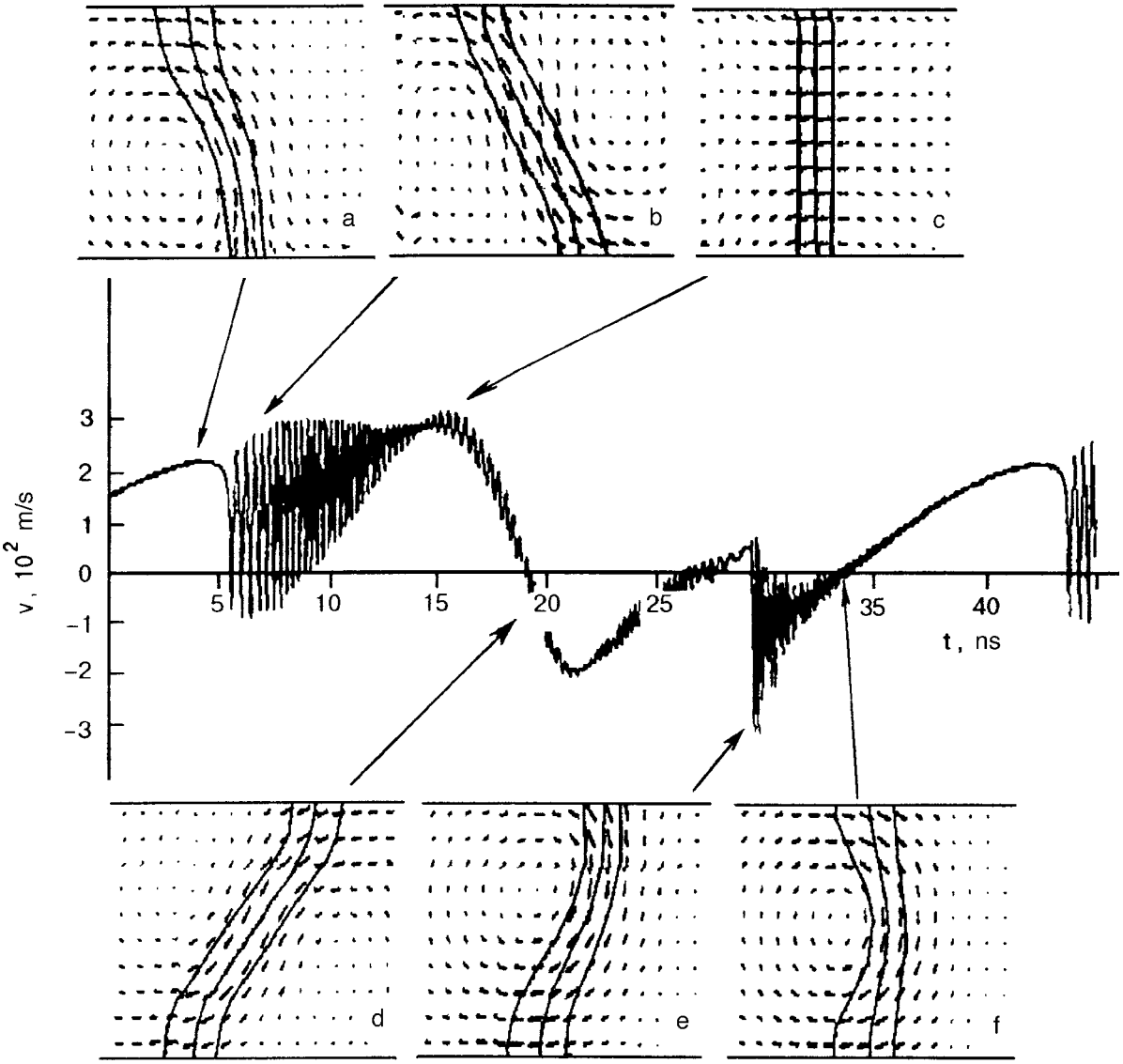

FIG. 38. Dependence of the average (corresponding to the motion of the centroid) velocity on t for a film with the basic parameters and $b=0.05$ μm, $\alpha=0.001$, $H=5$ Oe. The instantaneous configurations (a–f) correspond to the basic transformation of **M**.

strongly different, and in the case of the two-dimensional model it depends on b, in agreement with what we said in the previous Section. For example, for basic films of thickness 0.05 μm the two-dimensional model of the wall gives $H_c/\alpha=10^3$ Oe. At the same time, for a one-dimensional wall with the same value of M_s Eq. (19) gives $H_c/\alpha=5\times10^3$ Oe.

Notice the slight deviations of $H_c(\alpha)$ from linear at small α. To explain the possible causes of these deviations, let us turn to an investigation of the nonlinear dynamic transformation of the walls.[105,167,179] In Fig. 38 we show the time dependence of the DW velocity for a film with a damping parameter $\alpha=0.001$ in a field $H=5$ Oe. The critical field of these films is approximately 2.5 Oe. We see that, in addition to the usual periodic (with period T; see above) variations of the DW velocity there arise additional variations of v which occur over fractions of a period. We shall call these subperiodic oscillations of the velocity. The frequency f of these additional variations of the velocity is approximately two orders of magnitude higher than the frequency $1/T$ of the fundamental oscillations. Here, on the average over the period of the additional oscillations the $1/f$ mechanism of transformation of the DW structure remains the same as at comparatively large α, e.g., $\alpha=0.1$ (see Fig. 24). However, an examination of films that exhibit transformation of the DW structure clearly shows that when a specific configuration of the DW arises, oscillations of some parts of the wall relative to others occur without destroying the configuration itself. This is seen in Fig. 39, which shows the variation of the DW velocity for the same parameters of the film as in Fig. 38 but over a shorter time interval (for better resolution of the oscillations). Here, unlike Fig. 38, instead of the configurations of the averages over the period $1/f$ we show the DW configurations corresponding to the minima and maxima of the velocity v on different fractions of the period. These configurations demonstrate the oscillations discussed above. For example, it is seen that when an asymmetric Néel wall arises, the oscillations of the internal structure of the DW occur in such a way that the total span of the center line changes.

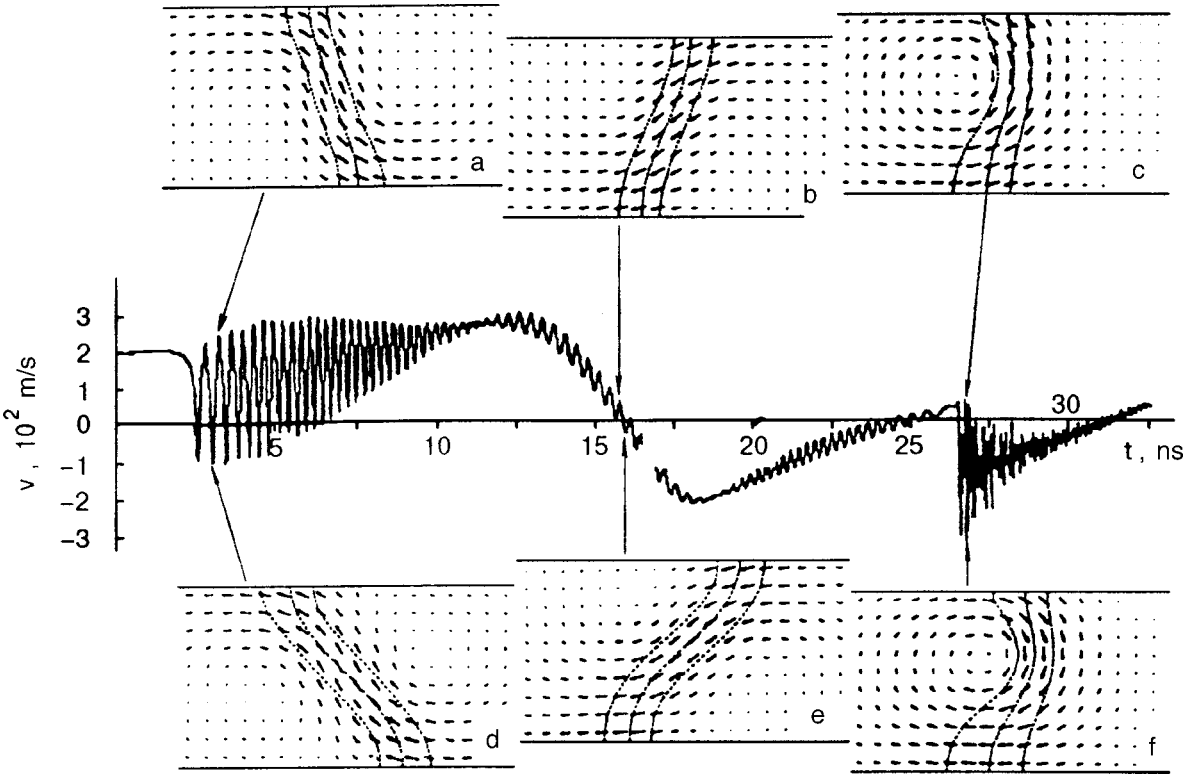

FIG. 39. The same dependence $v(t)$ as in Fig. 38 but for a shorter time interval. The instantaneous configurations (a–f) of the walls in this case illustrate the character of the intrawall oscillations during different parts of the period T.

Studies show that the subperiodic oscillations are excited every time the DW structure is radically transformed—whenever an asymmetric Bloch wall is transformed into an asymmetric Néel wall, etc. At that time sharp changes of the local magnetostatic fields occur, with inhomogeneities on a scale that is naturally commensurate with the inhomogeneities of the distribution of the magnetization in the wall.

The oscillations of the DW velocity presented above begin to arise even at rather large α, e.g., $\alpha=0.1$. However, in that case they are weakly expressed. With increasing α they become more and more substantial. Figure 40 shows that the

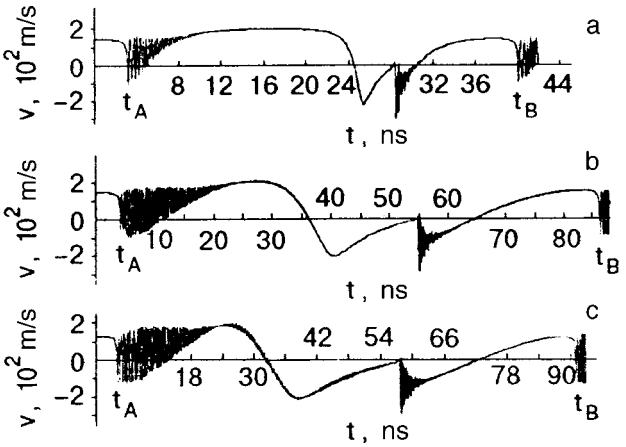

FIG. 40. Dependence on t of the average (corresponding to motion of the centroid) velocity of DWs with a two-dimensional structure of the magnetization distribution in films with the basic parameters and $b=0.05$ μm and values of α, H, and H_c, respectively: 0.01, 11 Oe, 10.5 Oe (a); 0.001, 2.6 Oe, 2.5 Oe (b); 0.0001, 2.2 Oe, 1.9 Oe (c).

corresponding oscillations arise even in fields very close to the critical. Moreover, it turns out that they also occur in the case when $H<H_c$ (see Fig. 41). Apparently, the oscillations develop even in an arbitrarily small neighborhood of H_c and influence the value of H_c itself. According to Fig. 41a, oscillations are excited at the time of the transformation of the DW structure from asymmetric Bloch (Fig. 41c) to asymmetric Néel (Fig. 41d). In Fig. 41b the oscillations are shown on an enlarged scale over a short time segment. In Figs. 41e and 41f it is clearly shown that the velocity oscillations are due to oscillations of the internal structure of the wall: the span of the center line changes. By span of the center line of an asymmetric Néel wall we mean the difference of the x coordinates of the two points of this line lying on opposite surfaces of the film.

Thus an explicit correlation is observed between the deviations of $H_c(\alpha)$ from a straight line and the onset of oscillations of the velocity and structure of the DW at small α. This is also evidenced by the data obtained for the dependence of the period T of the dynamic transformations of the wall on the strength of the external magnetic field at low dampings (see Fig. 42). It is seen in Fig. 42 that as the damping decreases, the $T(H)$ curves become less steep. The presence of this effect opens up new possibilities for experimental study of DW dynamics at high fields.

The data presented above, contrary to expectations, show that with decreasing damping the stopping of the translational motion of the wall and its transformation into vibrational motion occur as a result of not only the gradual equalizing of the times of the main and retrograde motions of the wall but also the development of high-frequency oscillations

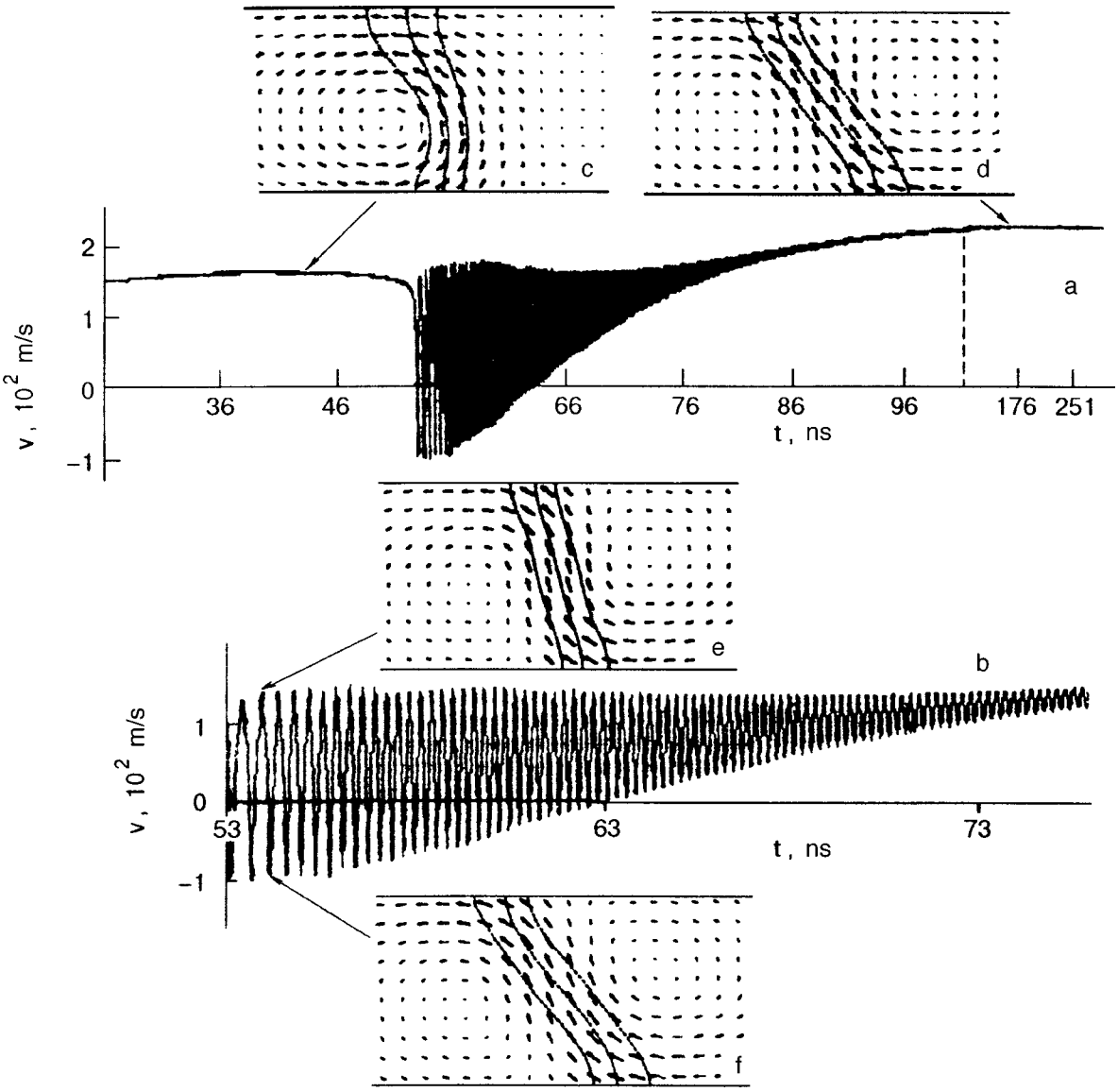

FIG. 41. Dependence of the average (corresponding to motion of the centroid) velocity of a DW on the time t (a) and a more detailed picture of its dependence over a short t interval (b), and the instantaneous configurations illustrating two types of steady-state DW motion (c and d) and the types of distribution of **M** at the maximum (e) and minimum (f) of the wall velocity.

of some parts of the wall with respect to others. Finally, we note that the oscillations described should lead to fine structure of the magnetic dipole radiation of electromagnetic waves which was predicted in Ref. 180.

3.8. Influence of surface anisotropy on the nonlinear dynamics of domain walls

The influence of surface anisotropy on the dynamics of the DWs and their dynamic transformation was studied in Refs. 181–183. The surface anisotropy of the axis type ($K_S<0$) and plane type ($K_S>0$) were considered. It was found that the surface anisotropy suppresses the unsteady DW motion.

In this Section we shall give the results of calculations of the period T of the dynamic transformation of the DW as a function of the external magnetic field strength H for different values of the surface magnetic anisotropy constant $K_S>0$. The goal of these calculations was to establish the mechanism of strong influence of the surface magnetic an-

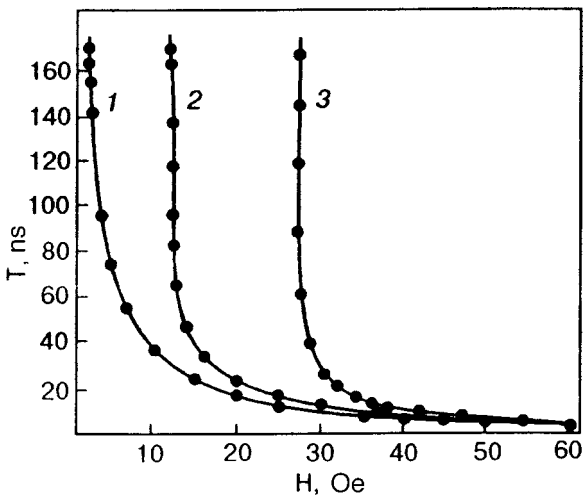

FIG. 42. Dependence of the period of the dynamic transformation of the structure of walls on the magnetic field for basic films with $b=0.05$ μm and different α: 0.001 (*1*), 0.01 (*2*), 0.03 (*3*). The data points correspond to a numerical simulation. The solid curves are drawn as a guide to the eye.

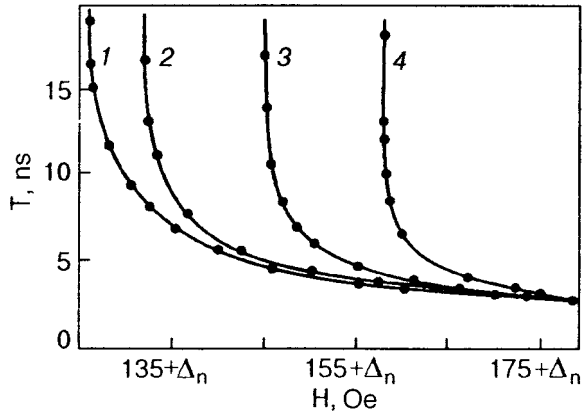

FIG. 43. Dependence of the period T of the dynamic transformation of the structure of a moving DW on the field strength H for $\alpha=0.1$ and different values of K_S[erg/cm^2]: 0.1 (*1*), 0.5 (*2*), 1 (*3*), 1.5 (*4*). The curves correspond to scales with $\Delta_n=0$ (*1*), 1 Oe (*2*), 10 Oe (*3*), 18 Oe (*4*).

isotropy on the above-described dynamic transformation of the internal structure of the DW. Figure 43 shows the corresponding graphs for a damping $\alpha=0.1$. It is seen in the figure that for any K_S the character of the $T(H)$ curves is the same—with increasing external magnetic field (in the region $H>H_c$) the period of the dynamic transformation of the DW decreases sharply. These curves turn out to be analogous to $T(H)$ for $K_S=0$.

The entire difference of the $T(H)$ curves corresponding to different K_S lies in the fact that with decreasing H ($H>H_c$) the periods T increase sharply on approach to different values H_c. In fields $H<H_c(K_S)$ the DWs move with a constant (time-independent) velocity (after the transient processes have ended). In fields $H\geqslant H_c(K_S)$ the DW motion takes place at a variable velocity and is accompanied by a change of its internal structure at a fixed H.

It is clear from what we have said and from Fig. 43 that H_c depends on K_S. Hence it is clear that the strong influence of the surface anisotropy on the character of the DW motion is due to the sharp dependence of $T(H)$ near the critical field H_c. This situation is illustrated qualitatively in Fig. 44, which shows two $T(H)$ curves for $K_S=0$ and $K_S\neq 0$. Each of these curves corresponds to its own critical field. For example, if $K_S=0$, then the critical field for the appearance of unsteady DW motion is equal to H_{c0}. The second curve does not have any significance. If $K_S\neq 0$, however, the critical field will be H_{c1}, and the first curve plays no role in the division of the regions of DW motion with variable and constant velocity at a given K_S.

It is seen in Fig. 44 that if H is chosen equal to a certain fixed value H_A from the interval (H_{c0},H_{c1}), then for $K_S=0$ we will have supercritical (unsteady) motion of the DW with a finite period of variation of the velocity and internal structure of the wall (see point A). However, one should include even a comparatively small surface anisotropy (e.g., with $K_S=0.3$ erg/cm^2), as the period T will then be described by curve *2*, and at $H=H_A$ we fall in the field region $H<H_{c1}$ where the DW undergoes equilibrium motion, i.e., it corresponds to an infinitely large T. From this it becomes clear why a sharp change of the field T arises only for some and not all H values. It will not occur, for example, in a field $H=H_B$.

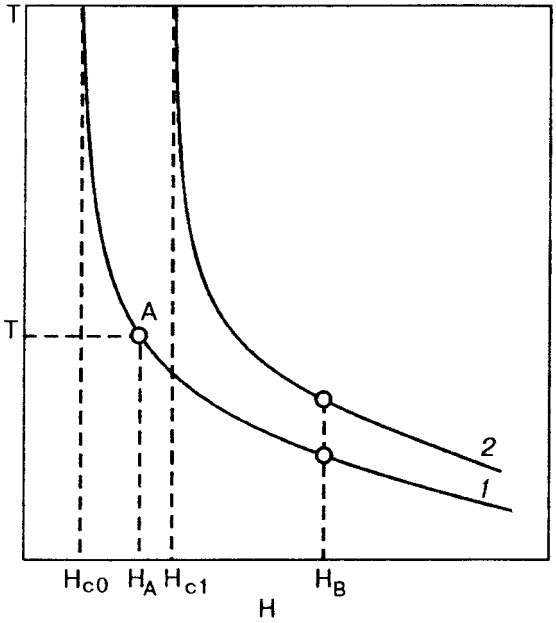

FIG. 44. Diagram illustrating the strong dependence of the period of the dynamic transformation of the DW structure in a certain region of H on a change of K_S (see text).

Since, according to Fig. 43, H_c depends on K_S, for each H there should exist a certain critical value of K_S for which the period T increases sharply, tending to ∞, as this value is approached. Figure 45 shows such a dependence for a field $H=196.5$ Oe, at which the critical value K_S turns out to be rather large (around 2 erg/cm^2). In fields ~ 100 Oe these critical values of K_S can be many times smaller (e.g., 0.3 erg/cm^2). The explanation of the behavior of $T(H,K_S)$ was given for the investigated region $K_S\sim 0.3-2$ erg/cm^2. There is reason to assume that for small $K_S<0.3$ erg/cm^2 the situation can be somewhat different. However, this region of K_S requires a more careful workup.

3.9. Influence of a field perpendicular to the anisotropy axis on the nonlinear dynamics of domain walls

As was shown in Fig. 2.6, in films with a small Q factor the internal structure of the films is substantially influenced

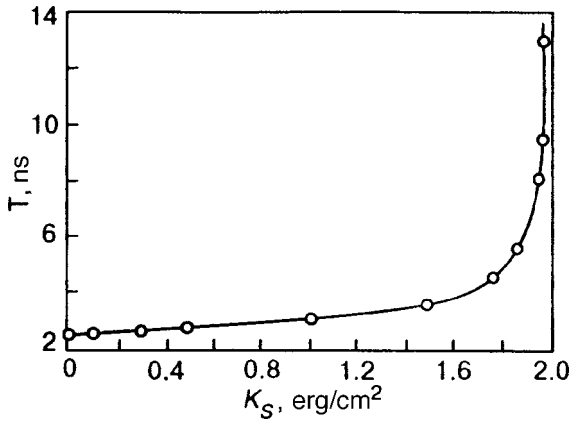

FIG. 45. Dependence of the period of the dynamic transformation of the DW structure on the value of $K_S\geqslant 0$ for $H=196.5$ Oe. The points are the data of a numerical simulation. The solid curve is drawn as a guide to the eye.

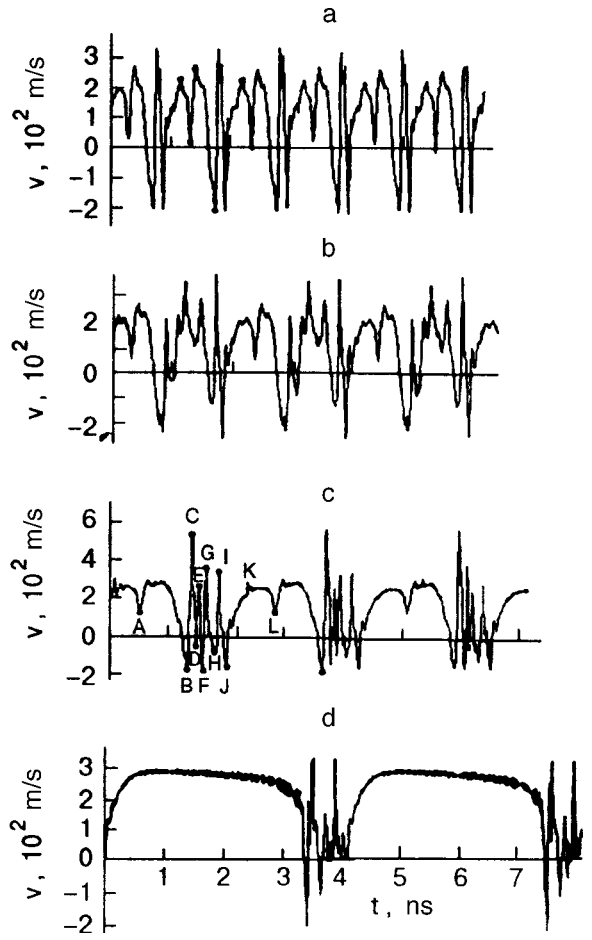

FIG. 46. Typical dependence of the average velocity (corresponding to motion of the centroid) of a DW on time t for different values of the field $H_\perp$ [Oe]: 0 (a), 0.1 (b), 0.3 (c), 0.63 (d) in a field $H=230$ Oe. The data were obtained for films with the basic parameters and $b=0.05$ μm, $\alpha=0.1$.

by an external magnetic field $\mathbf{H}_\perp$ perpendicular to the anisotropy axis and lying in the plane of the film. Here even small fields of the order of 1 Oe can radically alter the DW structure. This is due to the fact that in the films considered the only competition for $H_\perp$ is from the anisotropy field H_a, which amounts to several oersteds. In connection with what we have said, it becomes clear that if in addition to the field H that drives the motion of the DW (oriented along the easy axis) one applies a field $H_\perp$, then even a slight change in $H_\perp$ can substantially alter the character of the nonlinear DW motion. The effect is especially interesting when the main field is quite high (considerably higher than the anisotropy field). This effect is very reminiscent of that which is observed in a triode.

Numerical simulations were done in Ref. 184 over a wide range of variation of the film parameters. Figure 46 shows the data for a film with the basic parameters and thickness 0.05 μm and a damping $\alpha=0.1$ at several values of the field $H_\perp$. The field H was chosen earlier such that for $H_\perp=0$ the DW motion would be steady-state and the period of the dynamic transformations of the internal structure of the wall would be several nanoseconds.

It is seen in Fig. 46 that comparatively low fields $H_\perp<H_a$ have a very strong influence on the period T of the dynamic transformation of the wall, leading to complete suppression of the steady-state motion of the wall at a certain value $H_{\perp c}$. In particular, if $H=230$ Oe, then $H_{\perp c}\approx 0.65$ Oe.

It follows from Fig. 46 and from an analysis of the dynamic configurations of the DW that the nature of the unsteady motion of a DW and, in particular, the dynamic transformation of its internal structure in the presence of a field $H_\perp$ is the same as for $H_\perp=0$. However, for $H_\perp\neq 0$ there are specific features. Importantly, even at very low $H_\perp \ll H_a$ the value of the period $T(H_\perp)$ is at least twice as high as $T(0)$. For explanation of the physical nature of this fact it should be recalled that for $H_\perp=0$ the period $T(0)$ of the variation of the internal structure of the DW is twice as large as the period of its velocity variation. This is because the DW velocity in the geometry considered is degenerate with respect to the chirality of the DW (see Sec. 2), i.e., if an asymmetric Bloch wall with a clockwise rotation of **M** (see Fig. 24a) is considered to be the initial configuration, then, after all the transformations occurring in the DW in the half period $T(0)$, an asymmetric Bloch wall is again formed, but now with a counterclockwise rotation of the magnetization (see Fig. 24g). In the next half period all the transformations will occur as in the preceding one, but at the end there will be an asymmetric Bloch wall with the same direction of rotation of **M** as in the initial DW (clockwise, in our example), i.e., the structure of **M** will become completely identical to that shown in Fig. 24a.

If a field $H_\perp$ is applied along the x direction, it will lifts the degeneracy mentioned above, and the the transformations of the internal structure of the DW occurring in one half period will not repeat those in the other half period (see Fig. 47). This immediately leads to a doubling of the period T of the dynamic transformations of the internal structure of the DW (cf. Fig. 46a and 46b). This lifting of the degeneracy of the velocity with respect to the chirality of the DW is due to the fact that during part of the half period the relative magnetization M_r in the DW in the plane perpendicular to the easy axis is oriented in the direction of $\mathbf{H}_\perp$, while during the other part of the half period it is oriented in the opposite direction. The resulting features of the transformation of the DW structure for $H_\perp\neq 0$ differ substantially from the features of its transformation for $H_\perp=0$.

3.10. New possibilities for experimental study of the nonlinear dynamics of domain walls

Unlike the case of films with perpendicular anisotropy,[3,142,143,153–155] the nonlinear dynamics of DWs in films with planar anisotropy have not been sufficiently well studied. We also believe that the analysis of the existing experimental data is not completely correct, since it is based on the use of one-dimensional models of the walls.

The results based on the use of two-dimensional wall models indicate some new circumstances useful for interpreting the experimental data. They also present opportunities for direct study of the unsteady motion of DWs.

We note first of all that because of the presence of the two different fields H_0 (the field of the structural transformation of the DW at the transition from one type of steady-state motion to the other) and H_c (the field of the transition from steady to unsteady motion), around which the DW velocity

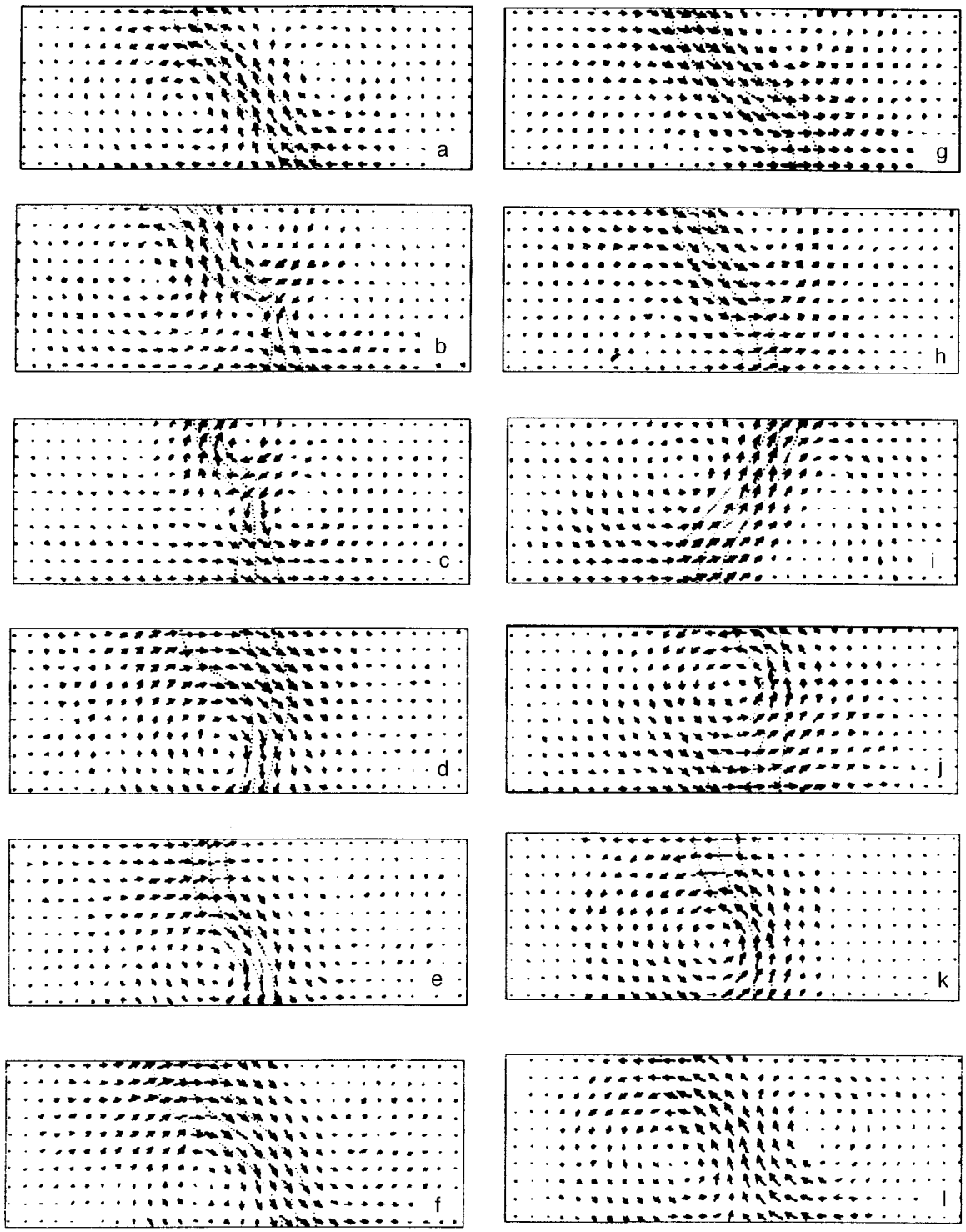

FIG. 47. Typical instantaneous configurations of DWs in fields $H=230$ Oe, $H_{\perp}=0.3$ Oe: panels a–l correspond to points A–L in Fig. 46c. The film parameters are the same as in Fig. 46.

changes sharply in time (see above), the time-averaged DW velocity can exhibit rather complicated behavior as a function of the external magnetic field. However, its actual value depends substantially on two circumstances: First, an important factor is the size of the time interval Δt_0 over which the decrease and subsequent growth of the DW velocity occurs during the transformation of the structure of the wall at the transition from one type of steady-state motion to the other. Second, experiments are usually set up so that they actually measure the average velocity over some time interval Δt (e.g., the time between two exposures). In order to reveal nonmonotonic behavior of the time-averaged velocity v_a in the region below the critical field H_c it is necessary to have $\Delta t \leqslant \Delta t_0$. If $\Delta t \gg \Delta t_0$, then as the field H is increased to H_c, the velocity v_a will increase. Above H_c, periodic motion of the DW arises, with retrograde intervals and with a period that decreases with increasing H, so that in fields above H_c the DW velocity will decrease. Thus nonmonotonic motion of the DW will arise, with a single maximum at the bifurcation point H_c. Keeping in mind that Δt_0 is equal to a few

nanoseconds (in estimating this value we have neglected several factors such as the coercivity), one can assume that the case $\Delta t \gg \Delta t_0$ is the most favorable for experimental studies. Consequently, from the aforementioned maximum of v_a it is easy to measure H_c for films with different parameters.

The studies presented above give the first indication of the real possibility of conducting experiments not only to measure the averaged characteristics of the unsteady DW motion but also to study directly the temporal transformations of the velocity of a DW during its unsteady motion. It is seen in Fig. 42 that the growth of T with decreasing H is observed at all α. Importantly, with decreasing α the dependence becomes more gradual. This circumstance, together with the comparatively small values of the fields (of the order of a few oersteds) at which the dynamic transformation of the DW structure occurs at small α is favorable for experimental studies, we believe. The point is that when the period of the dynamic transformations is large, it is not necessary to have a high time resolution. In this sense, it might seem to be sufficient to do the studies near the critical field, where the period T is rather large. However, if we take a film with $\alpha = 0.1$, the critical field in it is high (for the basic films, $H_c = 99.3$ Oe). In the direct vicinity of H_c the period T is, of course, large. For example, at $H = 99.33$ Oe the period $T = 171.7$ ns. However, the region ΔH in which T remains large is too narrow for doing experimental studies. If the field is increased only to 102 Oe, the period T decreases to about 11.6 ns. Meanwhile, at small $\alpha = 0.001$, as follows from numerical simulations, even in a field $H = 5$ Oe, which is approximately twice the critical field, the period T still remains quite large: $T = 80$ ns. As a result, in order to reveal experimentally the regions of periodic variation of the DW velocity a time resolution of the order of 10 ns is required. Furthermore, there is the possibility of increasing T by decreasing H.

Experiments can be done, for example, using high-speed photography in a double- or triple-exposure mode. At an exposure time of around 1 ns one can determine the coordinate q of the instantaneous displacement of the DW as a function of time t.

It is very important to choose the right films. Films with a low damping, e.g., with $\alpha = 0.001$, are preferable. We note that, although the conclusions presented above are based on the use of Permalloy films with the basic parameters described above, any other films with quality factors $Q < 1$ are entirely suitable. For example, variations of M_s from 400 to 1600 G and of K from 10^3 to 10^6 erg/cm^3 will lead to effects analogous to those described above. However, the films cannot be chosen too thick (for Permalloy, not thicker than 0.2 μm), since in thicker films the picture of the dynamic behavior becomes very complex.

4. CONCLUSION

Thus, in magnetically uniaxial films with easy axis lying in a plane parallel to the surface and in films with cubic anisotropy and with the surface parallel to the (100) or (110) crystallographic planes, the only equilibrium DW configuration in the region of film thicknesses $b \in 0.04-0.4$ μm in the absence of surface anisotropy is a 180° asymmetric Bloch wall. An essential element of this wall is a vortexlike distribution of the magnetization. The existence of such a distribution is due, first, to it lowering of the magnetostatic field energy, and the asymmetry of the wall is due to a lessening of the exchange interaction. Walls with a 90° structure in films with a surface of the (100) type at any thicknesses in the interval 0.02–0.4 μm do not have a vortexlike structure. Their structure is intermediate between the Néel and Bloch structures and is asymmetric.

The presence of a vortexlike structure of the DWs has a substantial impact on the nonlinear dynamic behavior of the walls. The motion is actually that of a topological soliton with internal degrees of freedom.

There exist two critical fields, H_0 and $H_c > 0$, at the transition through which the DW dynamics is radically altered. For $H < H_c$ the DW motion is steady except in a narrow region around H_0, where a transformation of the structure of the moving DW from asymmetric Bloch to asymmetric Néel occurs. Above H_c the DW motion becomes unsteady. The nature of this bifurcation is due to the fact that, starting at a field $H = H_c$ the magnetization begins to precess about the easy axis. For walls with a two-dimensional structure this precession is nonuniform over the thickness of the film. This precession is responsible for the catastrophic nonlinear dynamic transformation of the whole internal structure of the DW. It is established that the character of the dynamic transformation of the DW structure at fixed film parameters depends substantially on the strength of the magnetic field. With increasing H the character of the transformation becomes more complex: an ever increasing number of vortexlike formations become involved in the process. Most likely the DW motion ultimately becomes chaotic. However, this question requires further study.

We note that the stated cause of the transformation of the DW turns out to be the same for the different DW models: one-dimensional and two-dimensional. However, the similarity of the results ends there. In particular, it has become clear that the one-dimensional models cannot correctly describe the bifurcation process at $H = H_c$. In particular, it has been found that the bifurcation field depends nonmonotonically on the film thickness and saturation magnetization, while no such dependences exist in a consistent one-dimensional model.

The behavior of the bifurcation field is due to the newly revealed mechanisms of dynamic transformation of the wall structure. One of these involves the sequential nucleation of a vortexlike formation of the magnetization near one of the surfaces of the film, the displacement of this formation toward the lower surface, and its annihilation near the lower surface. Here each new vortexlike formation nucleated has a chirality opposite to that of the initial vortex. In the process of these transformations, states with two vortices of opposite chirality arise, one above the other. Another mechanism involves the tunneling of a vortex from one half of the wall to the other through the central surface of the wall.

A dependence of the bifurcation field on the anisotropy and exchange fields has also been found. However, this dependence is not due to the two-dimensionality of the model but is a consequence of the dynamic variation of the wall structure itself, which is not taken into account in the one-dimensional model.[140] This dynamic transformation of the

DW leads to periodic variations of the DW velocity in time. It is important to note that this transformation occurs in the presence of a static magnetic field applied along the easy axis.

It has been established that, as in the case of the one-dimensional models, when the velocity varies in time because of precession of **M** about the easy axis, retrograde motion of the wall, i.e., motion in the direction opposite to the direction prescribed by the direction of the external field, inevitably arises. The fraction of retrograde motion increases with increasing field. Consequently, in fields $H>H_c$ the DW velocity decreases with increasing H. In the general case in the region $H<H_c$, owing to the transformation of the DW structure at the point H_0, the velocity of the wall can be a nonmonotonic function of H. However, on the average over an interval Δt significantly longer than the time interval over which the transformation of the DW structure at $H=H_0$ occurs, the DW velocity increases with increasing magnetic field.

Thus it is clear that the highest DW velocity in a film of a given thickness can be attained in fields close to the critical. Here the larger the anisotropy constant K, the better, although the Q factor should remain less than unity. The saturation magnetization of the film should correspond to the value at which H_c is maximum. For Permalloy films with $K=10^3$ erg/cm^3, $A=2\times10^{-6}$ erg/cm, and $\alpha=1$, this value is $M_s\approx1150$ G. Favorable factors for increasing the DW velocity are the presence of surface anisotropy and of a small field $H_\perp$ ($H_\perp\ll H_a$) perpendicular to the anisotropy axis.

With decreasing damping parameter of the film the DW motion both for $H>H_c$ and $H<H_c$ changes substantially: besides the main periodic variation of the structure and velocity of the DW with period T there appears oscillatory behavior of the DW velocity over fractions of the period T. Here the frequencies of the subperiodic oscillations is two orders of magnitude higher than the frequency $1/T$. It has been established that the subperiodic oscillations of the DW are due to the excitation of oscillations of some parts of the DW relative to other parts.

The development of subperiodic oscillations of the wall means that with decreasing damping the stopping of the wall occurs not only on account of the increase in the retrograde motion fraction but also as a result of the development of high-frequency intrawall oscillations.

With increasing magnetic field the period T of the dynamic transformation of the DW structure increases with increasing external magnetic field. An extremely important circumstance from the standpoint of the possibilities of experimental study of the dynamic transformation of the DW structure is the fact that $T(H)$ grows slowly with decreasing damping of the precession of the magnetization in the film.

Finally, we emphasize that the data obtained indicate that the dynamic properties of DWs are substantially due to the changes of their internal structure in the course of their motion. Two-dimensional DW models provide greater opportunities for such changes. One-dimensional models cannot give an adequate description of the nonlinear dynamics of domain walls.

The author is grateful to M. G. Chernikhovskaya for comments which led to substantial improvements in the manuscript.

This study was supported by the Russian Foundation for Basic Research, Project No. 99-02-16279.

*E-mail: filbor@imp.uran.ru

[1]S. V. Vonsovskiĭ, *Magnetism*, Vols. 1 and 2 [Wiley, New York (1974); Nauka, Moscow (1971)].
[2]A. Hubert, *Theorie der Domänenwände in Geordneten Medien*, Springer-Verlag, Berlin (1974), Mir, Moscow (1977)
[3]A. Malozemoff and J. Slonczewski, *Magnetic Domain Walls in Bubble Materials* [Academic Press, New York (1979); Mir, Moscow (1982)].
[4]T. O'Dell, *Ferromagnetodynamics: The Dynamics of Magnetic Bubbles, Domains and Domain Walls* [Wiley, New York (1981); Mir, Moscow (1983)].
[5]S. Chikazumi, *Physics of Ferromagnetism* [Clarendon Press, Oxford (1997); Mir, Moscow (1987)].
[6]B. N. Flilippov and A. P. Tankeev, *Dynamic Effects in Ferromagnets with Domain Structure* [in Russian], Nauka, Moscow (1987).
[7]V. A. Zaĭkova, I. E. Startseva, and B. N. Filippov, *Domain Structure and Magnetic Properties of Electrical Steels* [in Russian], Nauka, Moscow (1992).
[8]A. Hubert and R. Schafer, *Magnetic Domains*, Springer-Verlag, Berlin–Heidelberg (1998).
[9]A. E. LaBonte, J. Appl. Phys. **40**, 2450 (1969).
[10]A. Hubert, Phys. Status Solidi **32**, 519 (1969).
[11]F. Bloch, Z. Phys. **74**, 295 (1932).
[12]L. D. Landau and E. M. Lifshitz, Phys. Z. Sowjetunion **8**, 153 (1935).
[13]B. N. Filippov, S. V. Zhakov, and Yu. G. Lebedev, IEEE Trans. Magn. **MAG-15**, 1849 (1979).
[14]C. Kittel, ''Physical theory of ferromagnetic domains,'' Rev. Mod. Phys. **21**, 541 (1949); *Physics of Ferromagnetic Domains*, edited by S. V. Vonsovskiĭ [in Russian] IL, Moscow (1951), p. 19.
[15]W. Schuppel and V. Kambersky, in *Thin Ferromagnetic Films*, edited by R. V. Telesnin [Russ. trans.], Mir, Moscow (1964), p. 105.
[16]B. Petek, P. L. Trouilloud, and B. E. Argyle, IEEE Trans. Magn. **MAG-26**, 1328 (1990).
[17]F. H. Liu, M. D. Shultz, and M. H. Kryder, IEEE Trans. Magn. **MAG-26**, 1340 (1990).
[18]R. P. Ferrier, S. McVitie, and W. A. P. Nicholson, IEEE Trans. Magn. **MAG-26**, 1337 (1990).
[19]A. M. Kosevich, B. A. Ivanov, and A. S. Kovalev, *Nonlinear Magnetization Waves. Dynamic and Topological Solitons* [in Russian], Naukova Dumka, Kiev (1983).
[20]H. J. Williams, F. G. Foster, and E. A. Wood, Phys. Rev. **82**, 119 (1951).
[21]R. C. Sherwood, J. P. Remeika, and H. J. Williams, J. Appl. Phys. **30**, 217 (1959).
[22]R. Schäfer and A. Hubert, Phys. Status Solidi A **118**, 271 (1990).
[23]S. D. Bader, J. Magn. Magn. Mater. **100**, 440 (1991).
[24]V. I. Petrov and G. V. Spivak, Usp. Fiz. Nauk **106**, 229 (1972) [*sic*].
[25]D. C. Hothersall, Philos. Mag. **20**, 89 (1969).
[26]G. R. Morrison, H. Gong, J. N. Chapman, and V. Hrnciar, J. Appl. Phys. **64**, 1338 (1988).
[27]G. V. Spivak, I. N. Prilezhaeva, and V. K. Azovtsev, Dokl. Akad. Nauk SSSR **105**, 965 (1955).
[28]G. A. Wardly, J. Appl. Phys. **42**, 376 (1971).
[29]U. Hartmann, J. Magn. Magn. Mater. **157**, 545 (1996).
[30]J. E. A. Miltat and M. Kleman, Philos. Mag. **28**, 1015 (1973).
[31]S. Tsukahara and H. Kawakatsu, J. Phys. Soc. Jpn. **32**, 1493 (1972).
[32]T. Suzuki, K. Suzuki, and Y. Igarashi, Jpn. J. Appl. Phys. **15**, 707 (1976).
[33]J. N. Chapman, G. R. Morrison, J. P. Jakubovics, and R. A. Taylor, J. Magn. Magn. Mater. **49**, 277 (1985).
[34]M. R. Sheinfein, J. Unguris, R. J. Celotta, and D. T. Pierce, Phys. Rev. Lett. **63**, 668 (1989).
[35]M. R. Sheinfein, J. Unguris, J. L. Blue, K. J. Coakley, D. T. Pierce, and R. J. Celotta, Phys. Rev. B **43**, 3395 (1991).
[36]H. Kappert and P. Schmiesing, Phys. Status Solidi A **4**, 737 (1971).
[37]D. C. Hothersall, Phys. Status Solidi B **51**, 737 (1972).
[38]C. G. Harrison and K. D. Leaver, Phys. Status Solidi A **12**, 737 (1972).
[39]T. Suzuki, Z. Angew. Phys. **32**, 75 (1971).
[40]K. U. Stein and E. Feldtkeller, J. Appl. Phys. **38**, 4401 (1967).

[41]T. Kasuda, S. Konishi, and Y. Sakurai, IEEE Trans. Magn. **MAG-3**, 286 (1967).
[42]K. Takahashi, H. Yamada, and H. Murakami, IEEE Trans. Magn. **MAG-8**, 403 (1972).
[43]M. M. Farztdinov, *Spin Waves in Ferro- and Antiferromagnets with Domain Structure* [in Russian], Nauka, Moscow (1988).
[44]M. M. Farztdinov, *Physics of Magnetic Domains in Antiferromagnets and Ferrites* [in Russian], Nauka, Moscow (1981).
[45]M. A. Shamsutdinov, V. N. Nazarov, and A. A. Khalfina, J. Magn. Magn. Mater. **214**, 139 (2000).
[46]M. A. Shamsutdinov, A. T. Bikmeyev, B. N. Filippov, and A. A. Khalfina, J. Magn. Magn. Mater. **224**, 93 (2001).
[47]M. A. Shamsutdinov and V. N. Nazarov, Fiz. Tverd. Tela (St. Petersburg) **43**, 265 (2001) [Phys. Solid State **43**, 274 (2001)].
[48]M. E. Schabes and H. N. Bertram, J. Appl. Phys. **64**, 1347 (1988).
[49]M. E. Schabes, J. Magn. Magn. Mater. **95**, 249 (1991).
[50]N. A. Usov and S. E. Peschny, J. Magn. Magn. Mater. **110**, L1 (1992).
[51]A. Aharoni and J. P. Jakubovics, Philos. Mag. B **53**, 433 (1986).
[52]M. M. Solov'ev, Fiz. Met. Metalloved. **48**, 58 (1979).
[53]H. A. M. van den Berg, J. Appl. Phys. **60**, 1104 (1986).
[54]H. A. M. van den Berg, J. Appl. Phys. **62**, 1952 (1987).
[55]H. A. M. van den Berg, J. Appl. Phys. **52**, 6830 (1981).
[56]A. Hubert and M. Ruhrig, J. Appl. Phys. **69**, 6072 (1991).
[57]M. Rührig, W. Bartsch, M. Vieth, and A. Hubert, IEEE Trans. Magn. **MAG-26**, 2807 (1990).
[58]S. Huo, J. E. L. Bishop, J. W. Tucker, W. M. Rainford, and H. A. Davies, J. Magn. Magn. Mater. **177–181**, 227 (1998).
[59]A. Hirohata, N. T. Leung, Y. B. Hu, C. C. Yao, W. Y. Lee, and J. A. C. Bland, IEEE Trans. Magn. **MAG-35**, 3886 (1999).
[60]B. N. Filippov, G. A. Shmatov, and A. B. Dichenko, J. Magn. Magn. Mater. **88**, 316 (1990).
[61]S. Huo, J. E. L. Bishop, J. W. Tucker, W. M. Rainford, and H. A. Davies, J. Magn. Magn. Mater. **177–181**, 229 (1998).
[62]Y. Nakatani and N. Hayashi, IEEE Trans. Magn. **MAG-23**, 2179 (1987).
[63]Y. Nakatani and N. Hayashi, IEEE Trans. Magn. **MAG-24**, 3039 (1988).
[64]P. Trouilloud and J. Miltat, J. Magn. Magn. Mater. **66**, 194 (1967).
[65]L. I. Antonov, S. G. Osipov, and M. M. Khapaev, Fiz. Met. Metalloved. **57**, 892 (1984).
[66]V. K. Raev and G. E. Khodenkov, *Magnetic Bubbles in Elements of Computational Technique* [in Russian], Énergoizdat, Moscow (1981).
[67]G. E. Khodenkov, Fiz. Tverd. Tela (Leningrad) **24**, 134 (1982) [Sov. Phys. Solid State **24**, 74 (1982)].
[68]A. Thiaville, F. Boileau, J. Miltat, and R. Arnaud, J. Appl. Phys. **63**, 3153 (1988).
[69]A. Thiaville and J. Miltat, J. Appl. Phys. **68**, 2883 (1990).
[70]K. Pátek, A. Thiaville, and J. Miltat, Phys. Rev. B **49**, 6678 (1994).
[71]A. Hubert, Comput. Phys. Commun. **1**, 343 (1970).
[72]A. Hubert, Czech. J. Phys. B **21**, 532 (1971).
[73]A. Hubert, Z. Angew. Phys. **32**, 58 (1971).
[74]A. Aharoni, Phys. Status Solidi A **18**, 661 (1973).
[75]L. I. Antonov, V. V. Ternovskiĭ, and M. M. Khapaev, Fiz. Met. Metalloved. **67**, 52 (1989).
[76]L. I. Antonov, S. V. Zhuravlev, E. V. Lukasheva, and A. N. Matveeva, Fiz. Met. Metalloved. **12**, 23 (1992).
[77]V. S. Semenov, Fiz. Met. Metalloved. **51**, 1175 (1981).
[78]V. S. Semenov, Fiz. Met. Metalloved. **64**, 838 (1987).
[79]B. N. Filippov and L. G. Korzunin, Fiz. Met. Metalloved. **75**, 49 (1993).
[80]B. N. Filippov and L. G. Korzunin, Pis'ma Zh. Tekh. Fiz. **20**(11), 84 (1994) [Tech. Phys. Lett. **20**, 467 (1994)].
[81]B. N. Filippov and L. G. Korzunin, Zh. Tekh. Fiz. **66**(2), 103 (1996) [Tech. Phys. **41**, 169 (1996)].
[82]B. N. Filippov and L. G. Korzunin, Fiz. Met. Metalloved. **81**, 14 (1996).
[83]M. LaBrune and J. Miltat, IEEE Trans. Magn. **MAG-29**, 2569 (1993).
[84]K. Ramstock, W. Hartung, and A. Hubert, Phys. Status Solidi **155**, 505 (1996).
[85]M. Labrune and J. Miltat, J. Appl. Phys. **75**, 2156 (1994).
[86]M. LaBrune and J. Miltat, IEEE Trans. Magn. **MAG-26**, 1521 (1990).
[87]M. J. Donahue, J. Appl. Phys. **83**, 6491 (1998).
[88]D. V. Berkov, K. Ramstöck, and A. Hubert, Phys. Status Solidi A **137**, 207 (1997).
[89]D. V. Berkov, K. Ramstöck, Th. Leibl, and A. Hubert, IEEE Trans. Magn. **MAG-29**, 2548 (1993).
[90]S. W. Yuan and H. N. Bertram, Phys. Rev. B **44**, 12395 (1991).
[91]L. I. Antonov, E. V. Lukasheva, and E. A. Mukhina, Fiz. Met. Metalloved. **80**, 5 (1995).
[92]H. D. Dietze and H. Thomas, Z. Phys. **163**, 523 (1961).
[93]R. Collet, J. Appl. Phys. **35**, 3294 (1964).
[94]W. F. Brown and A. E. LaBonte, J. Appl. Phys. **35**, 3294 (1964).
[95]W. F. Brown and A. E. LaBonte, J. Appl. Phys. **36**, 1380 (1965).
[96]R. Kirchner and W. Doring, J. Appl. Phys. **39**, 855 (1968).
[97]A. Holz and A. Hubert, Z. Angew. Phys. **36**, 145 (1969).
[98]H. Ridel and A. Seeger, Phys. Status Solidi B **46**, 377 (1971).
[99]L. M. Néel, Compt. Rend. **241**, 533 (1955).
[100]W. F. Brown Jr., *Micromagnetics*, Wiley, New York (1963).
[101]M. LaBrune and J. Miltat, J. Magn. Magn. Mater. **151**, 231 (1995).
[102]N. Hayashi, K. Sato, and Y. Nakatani, Jpn. J. Appl. Phys. **35**, 6065 (1996).
[103]S. W. Yan and H. N. Bertram, IEEE Trans. Magn. **MAG-28**, 2031 (1992).
[104]J. M. Ball, A. Taheri, and M. Winter, Calc. Var. **14**, 1 (2002).
[105]B. N. Filippov, L. G. Korzunin, and F. A. Kasan-Ogly, Phys. Rev. B **64**, 104412 (2001).
[106]A. Aharoni, J. Appl. Phys. **39**, 861 (1968).
[107]A. Aharoni, J. Appl. Phys. **38**, 3196 (1967).
[108]A. B. Borisov, A. P. Tankeev, and A. G. Shagalov, Fiz. Met. Metalloved. **60**, 467 (1985).
[109]A. S. Kovalev, S. Komineas, and K. G. Mertens, *Abstract Book of EASTMAG-2001*, Institute of Metal Physics, Urals Branch of the Russian Academy of Sciences, Ekaterinburg (2001), p. 84.
[110]A. S. Kovalev, K. G. Mertens, and J. E. Prilepsky, *Abstract Book of EASTMAG-2001*, Institute of Metal Physics, Urals Branch of the Russian Academy of Sciences, Ekaterinburg (2001), p. 101.
[111]E. Yu. Vedmendenko, A. Ghazali, and J.-C. S. Levy, Surf. Sci. **402–404**, 391 (1998).
[112]A. Bogdanov and A. Hubert, Phys. Status Solidi B **186**, 527 (1994).
[113]D. L. Huber, Phys. Rev. B **26**, 3758 (1982).
[114]E. E. Huber, D. O. Smith, and T. B. Goodenough, J. Appl. Phys. **29**, 294 (1958).
[115]S. Middelhoek, J. Appl. Phys. **34**, 1054 (1963).
[116]B. A. Lilli, in *Problems of Modern Physics. Ferromagnetism*, edited by A. P. Komar [in Russian], IL, Moscow, p. 6.
[117]L. I. Antonov, S. G. Osipov, and M. M. Khapaev, Fiz. Met. Metalloved. **55**, 917 (1983).
[118]L. Néel, J. Phys. Radium **15**, 225 (1954).
[119]U. Gradmann and J. Müller, Phys. Status Solidi **27**, 313 (1968); C. Chappert and P. Bruno, J. Appl. Phys. **64**, 5736 (1988).
[120]W. Dahle, W. Göpel, U. Gradmann, and K. Salevski, Appl. Phys. **13**, 239 (1977).
[121]U. Gradmann and H. J. Elmers, J. Magn. Magn. Mater. **206**, L107 (1999).
[122]J. Kohlhepp, E. I. Elmers, and U. Gradmann, J. Magn. Magn. Mater. **121**, 487 (1993).
[123]R. Jungblut, M. T. Jonson, and J. van de Stegge, A. Reinders, and F. J. A. den Broeder, J. Appl. Phys. **75**, 6424 (1994).
[124]B. Shulz and K. Baberschke, Phys. Rev. B **50**, 13467 (1994).
[125]Yu. A. Korchagin, R. G. Khlebopros, and N. S. Chistyakov, *Preprint IFSO-10F* [in Russian], Institute of Physics, Siberian Branch of the Academy of Sciences of the USSR, Krasnoyarsk (1973).
[126]V. A. Ignatchenko and Yu. V. Zakharov, Zh. Éksp. Teor. Fiz. **49**, 599 (1965) [Sov. Phys. JETP **22**, 416 (1966)].
[127]B. N. Filippov and L. G. Korzunin, IEEE Trans. Magn. **MAG-29**, 2563 (1993).
[128]L. G. Korzunin and M. B. Filippov, Fiz. Met. Metalloved. **85**, 30 (1998).
[129]A. Hubert, J. Phys. (Paris), **32**, C1404 (1970).
[130]E. M. Lifshitz, Zh. Éksp. Teor. Fiz. **15**, 97 (1945).
[131]B. N. Filippov, S. V. Zhakov, Yu. N. Dragoshanskiĭ, Yu. N. Startodubtsev, and E. L. Lykov, Fiz. Met. Metalloved. **42**, 260 (1976).
[132]A. Aharoni and J. P. Jakubovics, IEEE Trans. Magn. **MAG-26**, 2810 (1990).
[133]B. N. Filippov and L. G. Korzunin, in *Magnetism of Transition Metals and Alloys*, edited by Yu. A. Izyumov [in Russian], NISO UrO RAN, Ekaterinberg (2000), p. 128.
[134]B. N. Filippov, L. G. Korzunin, and L. I. Antonov, in *New Magnetic Materials of Microelectronics* [in Russian], URSS, Moscow (2000), p. 504.
[135]W. Döring, Z. Naturforsch. Teil A **3**, 372 (1948).
[136]R. Becker, Z. Phys. **133**, 134 (1952).
[137]C. Kittel and J. K. Galt, ''Ferromagnetic domain theory,'' Solid State Phys. **3**, 437 (1956); in *Magnetic Structure of Ferromagnets*, edited by S. V. Vonsovskiĭ (Russ. trans.), IL, Moscow (1959), p. 459.
[138]A. E. Borovik, V. S. Kuleshov, and M. A. Strzhemechnyĭ, Zh. Éksp. Teor. Fiz. **68**, 2235 (1975) [Sov. Phys. JETP **41**, 1118 (1975)].
[139]L. R. Walker, reported by J. F. Dillon Jr., in *Magnetism*, Vol. III, edited by G. T. Rado and H. Shul, Academic Press, New York (1963), p. 450.
[140]N. L. Shryer and L. R. Walder, J. Appl. Phys. **45**, 5406 (1974).

[141]V. V. Randoshkin and V. B. Sigachev, JETP Lett. **42**, 41 (1995).
[142]F. H. de Leeuw, van den Doil, and U. Enz, Rep. Prog. Phys. **43**, 689 (1980).
[143]V. G. Bar'yakhtar, B. A. Ivanov, and M. V. Chetkin, Usp. Fiz. Nauk **146**, 417 (1985) [Sov. Phys. Usp. **28**, 563 (1985)].
[144]A. V. Nikiforov and E. B. Sonin, JETP Lett. **40**, 1119 (1984).
[145]L. I. Antonov, A. S. Zhukarev, A. N. Matveev, and P. A. Polyakov, Fiz. Met. Metalloved. **64**, 873 (1987).
[146]V. S. Gerasimchuk and A. L. Sukstanskiĭ, Zh. Éksp. Teor. Fiz. **103**, 151 (1993) [JETP **76**, 82 (1993)].
[147]V. G. Bar'yakhtar, Yu. I. Gorobets, and S. I. Denisov, Zh. Éksp. Teor. Fiz. **98**, 1345 (1990) [Sov. Phys. JETP **71**, 751 (1990)].
[148]A. S. Abyzov and B. A. Ivanov, Zh. Éksp. Teor. Fiz. **76**, 1700 (1979) [Sov. Phys. JETP **49**, 865 (1979)].
[149]V. G. Bar'yakhtar, B. A. Ivanov, and A. L. Sukstanskiĭ, JETP Lett. **27**, 211 (1978).
[150]A. K. Zvezdin and A. F. Popkov, Fiz. Met. Metalloved. **21**, 1334 (1979).
[151]V. G. Bar'yakhtar, B. A. Ivanov, and A. L. Sukstanskiĭ, Zh. Éksp. Teor. Fiz. **75**, 2183 (1978) [Sov. Phys. JETP **48**, 1100 (1978)].
[152]S. G. Osipov, B. N. Filippov, and M. M. Khapaev, Zh. Eksp. Teor. Fiz. **98**, 2354 (1990) [Sov. Phys. JETP **71**, 756 (1990)].
[153]V. V. Volkov, V. A. Bokov, and V. I. Karpovich, Fiz. Tverd. Tela (Leningrad) **24**, 2318 (1992) [Sov. Phys. Solid State **24**, 1315 (1992)].
[154]V. A. Bokov, V. V. Volkov, N. L. Petrichenko, and M. Marysko, Phys. Solid State **39**, 1112 (1997).
[155]V. A. Bokov and V. V. Volkov, Fiz. Tverd. Tela (St. Petersburg) **39**, 660 (1997) [Phys. Solid State **39**, 577 (1997)].
[156]V. S. Gornakov, L. M. Dedukh, Yu. P. Kabanov, and V. I. Nikitenko, Zh. Éksp. Teor. Fiz. **82**, 2007 (1982) [Sov. Phys. JETP **55**, 1154 (1982)].
[157]L. M. Dedukh, V. I. Nikitenko, and A. A. Polyanskiĭ, Zh. Éksp. Teor. Fiz. **79**, 605 (1980) [Sov. Phys. JETP **52**, 306 (1980)].
[158]V. S. Gornakov, V. I. Nikitenko, I. A. Prudnikov, and V. T. Synogach, Phys. Rev. B **46**, 10829 (1992).
[159]V. S. Gornakov, V. I. Nikitenko, and I. A. Prudnikov, JETP Lett. **55**, 43 (1992).
[160]G. S. Kandaurova, Dokl. Akad. Nauk **331**, 428 (1993) [Phys. Dokl. **38**, 342 (1993)].
[161]F. V. Lisovskiĭ, E. G. Mansvetova, and E. P. Nikolaeva, and A. V. Nikolaev, Zh. Éksp. Teor. Fiz. **103**, 213 (1993) [JETP **76**, 116 (1993)].
[162]G. S. Kandaurova and A. E. Sviderskiĭ, JETP Lett. **47**, 490 (1988).
[163]M. V. Chetkin and Yu. N. Kurbatova, Phys. Lett. A **260**, 108 (1999).
[164]N. Hayashi, Y. Nakatani, and T. Unoue, Jpn. J. Appl. Phys. **27**, 336 (1988).
[165]B. N. Filippov and L. G. Korzunin, Fiz. Tverd. Tela (St. Petersburg) **38**, 2442 (1996) [Phys. Solid State **38**, 1343 (1996)].
[166]G. I. Marchuk, *Methods of Computational Mathematics* [in Russian], Nauka, Moscow (1989).
[167]B. N. Filippov and L. G. Korzunin, Zh. Éksp. Teor. Fiz. **121**, 372 (2002) [JETP **94**, 315 (2002)].
[168]D. S. Bartran and H. C. Bourne, IEEE Trans. Magn. **MAG-6**, 743 (1972).
[169]M. M. Solov'ev and B. N. Filippov, Fiz. Met. Metalloved. **81**, 49 (1996).
[170]M. M. Solov'ev and B. N. Filippov, Fiz. Tverd. Tela (St. Petersburg) **39**, 2036 (1997) [Phys. Solid State **39**, 1821 (1997)].
[171]M. M. Solov'ev and B. N. Filippov, Zh. Tekh. Fiz. **70**, 58 (2000) [Tech. Phys. **45**, 1566 (2000)].
[172]E. E. Kotova and V. M. Chetverikov, Fiz. Tverd. Tela (Leningrad) **32**, 12696 (1990) [Sov. Phys. Solid State **32**, 748 (1990)].
[173]R. A. Kosinski and A. Sukiennicki, J. Magn. Magn. Mater. **93**, 128 (1991).
[174]P. E. Wigen, H. Doetsch, and Y. Ming, J. Appl. Phys. **63**, 4157 (1988).
[175]F. Waldner, J. Magn. Magn. Mater. **31–34**, 1015 (1983).
[176]B. N. Filippov and L. G. Korzunin, Pis'ma Zh. Tekh. Fiz. **27**(58), 36 (2001) [Tech. Phys. Lett. **27**, 367 (2001)].
[177]B. N. Filippov, L. G. Korzunin, and F. A. Kasan-Ogly, Solid State Commun. **121**, 55 (2001).
[178]B. N. Filippov, L. G. Korzunin, and O. V. Sicheva, Fiz. Met. Metalloved. **91**, (2001) [to be published].
[179]B. N. Filippov and L. G. Korzunin, Fiz. Met. Metalloved. **86**, 26 (1998).
[180]A. K. Zvezdin, JETP Lett. **31**, 478 (1980).
[181]B. N. Filippov, L. G. Korzunin, and E. V. Rebryakova, Fiz. Met. Metalloved. **82**, 5 (1996).
[182]B. N. Filippov, L. G. Korzunin, and E. V. Rebryakova, Fiz. Met. Metalloved. **83**, 19 (1977).
[183]B. N. Filippov, L. G. Korzunin, and E. V. Rebrakova, Fiz. Met. Metalloved. **84**, 42 (1997).
[184]B. N. Filippov and L. G. Korzunin, Fiz. Met. Metalloved. **86**, 24 (1998).

Translated by Steve Torstveit

SUPERCONDUCTIVITY, INCLUDING HIGH-TEMPERATURE SUPERCONDUCTIVITY

Low-dose radiation effects in thin films of high-temperature superconducting $YBa_2Cu_3O_{7-x}$ irradiated by 1-MeV electrons

Yu. V. Fedotov,[a] B. A. Danilchenko, and I. S. Rogutskiĭ

Institute of Physics, National Academy of Sciences of Ukraine, pr. Nauki 46, 03028 Kiev, Ukraine
(Submitted February 1, 2002; revised March 1, 2002)
Fiz. Nizk. Temp. **28**, 1033–1040 (October 2002)

Radiation effects are investigated in thin epitaxial films of the high-T_c superconductor (HTSC) $YBa_2Cu_3O_{7-x}$ irradiated by low doses of 1-MeV electrons. The maximum radiation dose (4×10^{16} electrons/cm^2) is chosen from the condition that the defects formed as a result of electron–nucleus collisions cause a negligible lowering of the critical temperature of $YBa_2Cu_3O_{7-x}$. Under this condition the main source of radiation effects in HTSC films can be processes involving excitation of the electronic subsystem of $YBa_2Cu_3O_{7-x}$. When $YBa_2Cu_3O_{7-x}$ films are irradiated by doses of $(1-4)\times10^{16}$ electrons/cm^2 their critical temperature T_c is observed to increase (in contrast to published reports of a decrease in T_c at irradiation doses greater than 10^{18} electrons/cm^2) and then, after the irradiation has stopped, to relax over time to its original value. These effects are similar to those observed in the photoexcitation of the electronic subsystem of $YBa_2Cu_3O_{7-x}$ (photostimulated superconductivity). A decrease of the critical current density in the irradiated $YBa_2Cu_3O_{7-x}$ films is also observed, which is due to radiation-stimulated changes of the transmissivity to supercurrent of the dislocation walls in low-angle interblock boundaries. © *2002 American Institute of Physics.* [DOI: 10.1063/1.1521292]

INTRODUCTION

Acting on superconductors with radiation is one of the most convenient and controllable methods of modifying their basic parameters, such as the critical temperature T_c or the critical current density J_c. These effects are manifested most clearly in high-temperature superconductors (HTSCs), which have a substantially lower radiation stability than low-temperature superconductors.[1] A large amount of research has been done to investigate the possibility of controlling the transport and magnetic properties of HTSCs. Although this research is urgent from an applied standpoint, it does not exhaust all aspects of HTSC radiation physics. For example, the radiation-stimulated generation of a specified type of defects, leading to modification of some physical characteristic of a HTSC such as the normal-state conductivity or the value of T_c, can yield information both about the factors governing the relationship of these characteristics with features of the electronic and crystal structure of the HTSC and about the mechanism of high-temperature superconductivity. Studies of the radiation-stimulated change in the conductivity of $YBa_2Cu_3O_{7-x}$ (YBCO) films in Ref. 2 have yielded information about the symmetry of the order parameter in these compounds. Research on the effect of electron irradiation on the depression of the critical temperature of YBCO[3] has made it possible to establish a link between processes of carrier scattering on oxygen defects in the CuO_2 planes and the breaking of Cooper pairs. A study of radiation effects stimulated by irradiation with electrons having an energy of the order of 20 keV has permitted determination of the energy of formation of oxygen defects in the CuO chains of YBCO.[4]

In studies of that kind it is preferable to irradiate HTSCs either by fast electrons or by γ rays, since in those cases (especially at low temperatures) the main defects that form are Frenkel pairs. Importantly, here the resulting defect concentration, information about which is necessary in order to interpret the data, can be calculated analytically. In the overwhelming majority of cases such estimates are made on the assumption that the main mechanism of formation of radiation defects is that due to collisions of the incoming particles with atomic nuclei. For example, estimates of the suppression of T_c due to the scattering of carriers by O vacancies created in the superconducting CuO_2 planes by the irradiation of HTSC YBCO by electrons with energies in the range from 20 keV to 2.4 MeV at a dose of 10^{18} electrons/cm^2 (Ref. 3) gave results consistent with experiment. In the majority of studies of radiation effects in YBCO under irradiation by electrons of such energies it has been necessary to use irradiation doses of the order of $10^{18}-10^{22}$ electrons/cm^2 in order to achieve noticeable effects.[3] This is in good agreement with estimates of the number of defects formed at such doses by the mechanism of electron–nucleus collisions.

In the overwhelming majority of papers of this kind it has been reported that increasing the number of radiation defects in YBCO is accompanied by suppression of T_c to such an extent that the superconducting (SC) phase vanishes completely. At the same time, there have been a small number of reports of a radiation-stimulated elevation of T_c in

YBCO. For example, it was reported in Ref. 5 that the dose dependence of T_c in polycrystalline samples of YBCO irradiated by γ rays behaves as follows: there is an initial region of decreasing T_c, after which T_c increases as the dose increases further. As a rule, in such studies either the radiation doses were substantially lower than those indicated above[6] or comparatively low energies of the fast particles have been used.[4] For those conditions of irradiation it was found that other parameters of YBCO could also change. For example, a decrease in J_c by nearly a factor of two when thin YBCO films were irradiated by a beam of 4-MeV electrons in a dose of only 3×10^{16} electrons/cm^2 was reported in Ref. 7. The fact that comparatively small doses of radiation have such a large effect on the properties of YBCO and, in particular, the opposite character of the changes in T_c as compared to large doses suggests the possibility that, in addition to the formation of defects due to electron–nucleus collisions, there is an alternative mechanism of radiation effects, which is effective at low doses but has a tendency to saturate as the dose increases. The competition between these mechanisms may lead to the situation that at low doses the effects observed will be due mainly to radiation-stimulated changes of the structure of the HTSC films as a result of the alternative mechanism, which leads to an increase in T_c, but as the dose increases, the influence of defects formed as a result of electron–nucleus collisions begins to be felt. Since the formation of these latter defects leads to a lowering of T_c (Ref. 3), the radiation effects in YBCO at higher doses can mask the radiation effects from alternative mechanisms that are effective at low doses.

The goal of the present study is to investigate radiation effects in YBCO under conditions such that the number of defects formed as a result of electron–nucleus collisions is so small that the change induced by those defects in some test parameter does not exceed the measurement error in our experiments. We chose as the test parameter the value of T_c of a YBCO film subjected to increasing doses of electron irradiation. This choice was motivated by the presence of both theoretical[3] and experimental[2] papers in which a quantitative relation is established between the suppression of T_c due to the scattering of superconducting carriers by vacancies in the CuO_2 planes of YBCO and the number of such vacancies.

2. EXPERIMENT

We investigated the effect of electron irradiation on the parameters of thin (500 Å) HTSC films of YBCO with $T_c = 89.3$ K. Epitaxial YBCO films with the c axis perpendicular to the film plane were deposited on a $LaAlO_3$ substrate by the method of joint electron-beam evaporation of Y, BaF_2, and Cu, followed by annealing. The high value of the critical current density of the film ($\sim10^6$ A/cm^2) and its independence of magnetic field to fields of the order of 10^{-2} T attest to the rather high quality of the film and to the practical absence of any influences of interblock Josephson links on its properties. The irradiation was done at the Argus linear accelerator by electrons with an energy of 1 MeV. An initial dose of 10^{16} electrons/cm^2 was chosen, and the dose was increased by that amount in intervals until a total dose of 4×10^{16} electrons/cm^2 was reached. An electron beam current density of 0.1–0.2 μA/cm^2 was chosen so that the temperature of the sample would not exceed 40°C during irradiation.

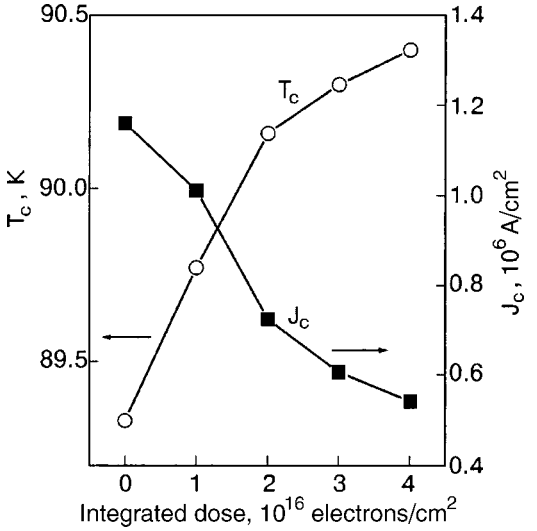

FIG. 1. Dependence of T_c and J_c(77 K) for a YBCO film on the dose of irradiation by 1-MeV electrons.

The measurements of the parameters of the HTSC films were made by the low-frequency magnetic susceptibility method at a frequency of 937 Hz in the temperature range 77–100 K in the Earth's magnetic field. The amplitude of the alternating magnetic field, perpendicular to the film plane, was varied in the range 0.001–5 mT. The registration system included an SR-830 lock-in amplifier connected to a computer via an RS-232 interface for storage and averaging of the data. The value of T_c was determined from the highest appearance temperature of the signal of the imaginary part χ'' of the complex magnetic susceptibility. The contactless technique used to measure the critical current density is based on analysis of the dependence of χ'' for the thin film on the amplitude h of the alternating magnetic field. According to Ref. 8, the value of χ'' reaches a maximum at certain values h_m of the alternating field. For a disk-shaped film the relation between J_c and h_m is $J_c = 1.013\, h_m/d$ (d is the film thickness). It was shown in Ref. 9 that this expression also describes well the experimental results for films of other isometric shapes, including squares as in our case.

3. EXPERIMENTAL RESULTS

In the electron irradiation of YBCO films by doses in the range 10^{18}–10^{22} electrons/cm^2 a continuous decrease of T_c was observed with increasing dose.[3] In our experiments, however, in which the electron radiation dose did not exceed 4×10^{16} electrons/cm^2, the situation was the reverse — the value of T_c gradually increased with increasing dose up to the maximum dose used, near which a tendency toward saturation was observed (Fig. 1).

It is noteworthy that in our experiments the value of T_c, which had increased by almost 1 K at the maximum dose (Fig. 1), began to relax after the irradiation to its original value. This process was essentially completed in around ten days (of storage of the film at room temperature). More-detailed investigations of the post-radiation relaxation are planned, and the results will be published separately.

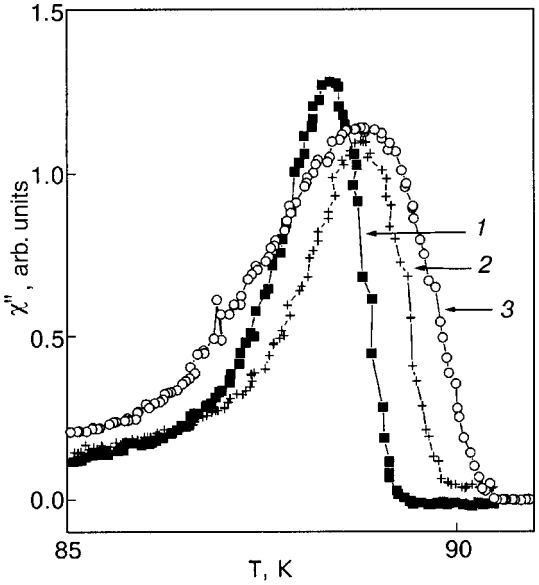

FIG. 2. Changes in the shape of the $\chi''(T)$ curve of a YBCO film with increasing dose of irradiation by 1-MeV electrons: before irradiation (*1*), and after irradiation by doses of 1×10^{16} (*2*) and 4×10^{16} (*3*) electrons/cm^2.

The critical current density of the YBCO film also exhibited substantial dependence on the electron radiation dose (Fig. 1). At the maximum dose used a decrease of J_c by nearly a factor of two was observed. It should be noted that the post-radiation behavior of J_c differs substantially from that of the critical temperature of an irradiated YBCO film. While, as we have said, the value of T_c after irradiation relaxed quite rapidly to its original value, the radiation-stimulated changes in J_c turned out to be much longer-lived — for almost six months after completion of the irradiation procedure the value of J_c for the irradiated YBCO film showed no changes within the measurement error.

Post-radiation changes which are stable in time were also observed in the temperature dependence of the real χ' and imaginary χ'' components of the complex susceptibility. With increasing irradiation dose not only did the maximum of $\chi''(T)$ shift to higher temperatures (corresponding to the increase in T_c) but an additional contribution appeared on the low-temperature part of this maximum (curve *3* in Fig. 2). This contribution, like the changes in J_c, remained stable for at least six months. Thus when, on account of the relaxation of T_c to its original value, the high-temperature part of $\chi''(T)$ had returned to its original position (in temperature), the additional residual absorption signal continued to be observed on its low-temperature part (Fig. 3). This additional contribution corresponded to a broadening (in temperature) of the region of the transition of the film to the superconducting state, as is confirmed by the character of the behavior of the $\chi'(T)$ curves shown in the inset in Fig. 3.

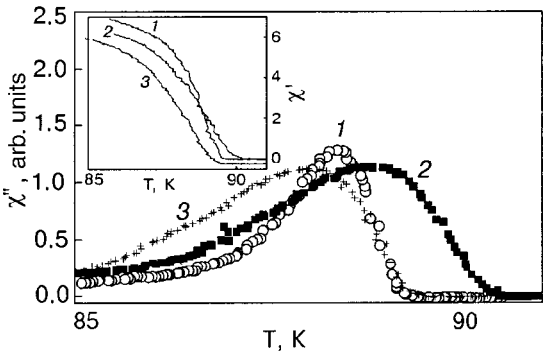

FIG. 3. Change of the imaginary part $\chi''(T)$ of the magnetic susceptibility of a YBCO film with time after irradiation by 1-MeV electrons to a dose of 4×10^{16} electrons/cm^2: before irradiation (*1*), immediately after irradiation (*2*), and 30 days after irradiation (*3*). The inset shows the corresponding data for the real part $\chi'(T)$ of the susceptibility obtained under the same conditions.

4. DISCUSSION

In Sec. 1 we stated a criterion for choosing the maximum irradiation dose at which the number of defects formed by electron–nucleus collisions in YBCO films should not (according to an extrapolation of the available estimates[3] to low concentrations of radiation-stimulated defects) lead to changes of T_c in excess of our experimental error for this quantity (±0.1 K). When this requirement is met, all of the observed radiation-stimulated changes in T_c should be due to some processes which are alternative to the formation of defects as a result of electron–nucleus collisions.

As a rule, estimates of the relation between the irradiation dose and the number of radiation-stimulated defects produced as a result of electron–nucleus collisions are made by proceeding on the assumption that the necessary condition for the appearance of a defect is the transfer to a nucleus of an energy greater than E_d, the energy necessary for the formation of a defect of a given type. Here, because of the requirement that the total energy and total momentum be conserved in such a collision and the necessity of taking relativistic effects into account, an incoming electron having energy E can transfer to the nucleus an energy not exceeding the amount

$$E_m = 2\frac{m}{M}\left(2+\frac{E}{mc^2}\right)E, \tag{1}$$

where M and m are the masses of the nucleus and electron, and c is the speed of light. The energy E_d necessary for the formation of oxygen vacancies in the CuO_2 planes and CuO chains has been determined most accurately in Refs. 4 and 10 from an analysis of the changes in the transport properties and superconducting transition temperature T_c in relation to the electron beam energy E. For an estimate of the number of defects of a given type produced in a sample under irradiation by a beam of electrons with energy E and flux density Φ, it is necessary to know the value of the effective integral scattering cross section σ for the collision of an electron with a nucleus of the given type in a process in which the energy transfer lies in the interval from E_d to E_m. For nuclei with not very high atomic numbers one may use the following approximate expression,[11] which takes into account relativistic effects:

$$\sigma=\pi\left[\frac{Ze^2\gamma}{mc^2(\gamma^2-1)}\right]^2\left[\left(\frac{E_m}{E_d}-1\right)-\frac{\gamma^2-1}{\gamma^2}\ln\frac{E_m}{E_d}+\alpha\pi Z\sqrt{\frac{\gamma^2-1}{\gamma^2}}\left(2\sqrt{\frac{E_m}{E_d}}-2-\ln\frac{E_m}{E_d}\right)\right], \tag{2}$$

where e is the charge of the electron, Z is the atomic number of the target nucleus, $1/\gamma = 1/\beta^2$, $\beta = V/c$ (V is the velocity of the electron), and $\alpha = Z/137$. It was shown in Ref. 10 that for oxygen atoms found in superconducting CuO_2 planes, the displacement energy E_d is ~ 8 eV, and for oxygen atoms in the CuO chains this energy is only around 2 eV. When these values are taken into account, the use of expressions (1) and (2) for the effective scattering cross section of electrons with energy $E = 1$ MeV on ^{16}O nuclei in CuO_2 planes gives a value $\sigma(O_{pl}) = 5 \times 10^{-23}$ cm^2, and for ^{16}O nuclei in CuO chains, $\sigma(O_{ch}) = 2.5 \times 10^{-22}$ cm^2. The number of defects N_i of a given type per unit cell is related to the irradiation dose Φ by the relation

$$N_i = n_i \sigma_i \Phi, \tag{3}$$

where n_i is the number of nuclei of the ith type in the unit cell, and σ_i is the effective scattering cross section for nuclei of the ith type. The results obtained in Ref. 3 on the basis of a comparison of a large number of experimental data with the theory describing the lowering of T_c in YBCO due to the scattering of carriers on defects in superconducting CuO_2 planes shows that for a decrease of T_c by 1 K it is necessary to create approximately 10^{-4} such defects per unit cell. As was shown in Ref. 12, the necessary concentration of oxygen defects in CuO chains for the same decrease in T_c in YBCO is at least an order of magnitude larger. With these results, one can conclude on the basis of relation (3) together with the scattering cross sections given above for the ^{16}O nuclei that in order for T_c in YBCO to be lowered not more than 0.1 K (the error of the temperature measurement in our experiments) on account of defects produced in electron–nucleus collisions, the maximum irradiation dose should not exceed 5×10^{16} electrons/cm^2. These considerations motivated the choice of both the initial (10^{16} electrons/cm^2) and maximum (4×10^{16} electrons/cm^2) doses of electron irradiation used in our experiments.

The fact that, even though this requirement was met, the electron irradiation led to an increase in T_c in the YBCO films (Fig. 1) allows us to conclude that, in addition to defect formation in electron–nucleus collisions, accompanied by depression of T_c, there exists another mechanism of radiation effects on the properties of YBCO, which is effective at comparatively low irradiation doses. It seems likely that such a mechanism may involve the radiational excitation of the electronic subsystem of YBCO. Since the cross section for electron scattering on the electronic shell of an atom or ion is many orders of magnitude greater than the cross section for scattering on the nucleus, the main part of the energy of a fast electron incident on an irradiated object is expended on the excitation of its electronic subsystem. It is possible that here there exist mechanisms by which the energy of excitation of the electronic subsystem is not dissipated as thermal energy but is converted to energy of displacement of an atom from its equilibrium position and its transfer to another cell (radiation-stimulated diffusion). Evidence for the reality of such mechanisms of radiation effects on crystals is the possibility of creating defects such as vacancies and interstitial atoms and ions and their different associations through the excitation of the electronic system in alkali–halide crystals[13] and certain semiconductors.[13,14] More-direct evidence of the possible role of effects due to the excitation of the electronic system of HTSCs comes from the observation of photoinduced conductivity (PIC) and photoinduced superconductivity (PISC) effects in YBCO.[15] Although the specific mechanism leading to PISC has not yet been reliably established, the energy of the photons used in such experiments (1.5–3.5 eV) unambiguously indicates that this mechanism involves the excitation of the electronic subsystem of YBCO, according to the data of Ref. 17. After irradiation all the photoinduced parameters relax to their original values in a matter of days at room temperature. The main features of the PISC — an increase of T_c for underdoped YBCO films, a tendency for it to saturate, and its relaxation to the original value — are analogous to the changes which we observed in YBCO films irradiated by low doses of fast electrons. Here, judging by the typical data for YBCO epitaxial films obtained by the same technology, our film samples should be regarded as underdoped. An analogy between PISC and the effect observed here (the increase of T_c with dose) confirms the conjecture made that a substantial role in the radiation-stimulated changes of the parameters of YBCO is played by processes of excitation of the electronic system.

The substantial decrease of the critical current in irradiated YBCO films and the rather long lifetime of this effect can be interpreted on the basis of the mechanism proposed in Refs. 18 and 19 for the limiting of the critical current in rather perfect HTSC epitaxial films, which, as a rule, consist of slightly misoriented single-crystal blocks. The interfaces between such blocks are periodic chains of edge dislocations, the distance between which depends on the angle of mutual misorientation θ of the blocks and is given by the well-known Frank formula: $d(\theta) = b/2\sin(\theta/2) \approx b/\theta$, where b is the modulus of the Burgers vector, which is equal in order of magnitude to the lattice constant. Arising around each edge dislocation is a region with an elevated concentration of point defects (a Cottrell atmosphere). The growth of the region occupied by the Cottrell atmosphere as a result of radiation-stimulated diffusion of both pre-existing and radiation defects into the region of the edge dislocations leads to a decrease in the width of the SC channels and suppression of the value of J_c, as was discussed in Ref. 19. Since the edge dislocations are extremely efficient trapping centers for point defects, the region near edge dislocations can acquire long-term stability as the concentration of these dislocations increases. This agrees with the observed long-term stability of the post-radiation changes of J_c in YBCO films. The rather long-lived changes of the value of J_c in YBCO films irradiated by fast electrons was also noted in Refs. 19 and 20, where it was reported that the critical current returned to its original value only after 1.5 years.

We note that the given mechanism acts in a rather wide interval of values of the angles θ, up to values for which the dimensions of the Cottrell regions become equal to $d(\theta)$, which will lead to the complete loss of superconductivity of the interdislocation channels and to a transition to a regime of passage of the supercurrent through interblock boundaries of the superconductor–insulator–superconductor type. Since the dependence of $J_c(\theta)$ has a quasi-exponential character, at sufficiently large angles θ (over 20°) the value of J_c decreases by several orders of magnitude.[18] From this we can

conclude that the high value of the critical current density of the particular film ($\sim 10^6$ A/cm^2 at 77 K) attests to the absence of large-angle boundaries between blocks. These radiation-stimulated change in the structure of YBCO films correlate with the observed post-radiation changes of the temperature dependence of the imaginary part $\chi''(T)$ of the susceptibility. As is seen in Fig. 2, the $\chi''(T)$ curve after irradiation is not only shifted to higher temperatures (because of the radiation-stimulated increase of T_c) but is also substantially broadened, mainly in the low-temperature region, and this broadening increases with increasing irradiation dose. The appearance of the additional absorption signal $\chi''(T)$ in the low-temperature region is naturally attributed to an increase in the size of the regions around edge dislocations in which the ordering is suppressed and, hence, T_c is depressed. Ultimately this leads to an increase in the degree of inhomogeneity of the film and a resulting broadening of the SC transition. The growth of the low-temperature ''tail'' of χ'' with increasing dose (Fig. 2) is consistent with the decrease of the critical current density (Fig. 1). This correlation confirms the hypothesis made above that the observed radiation-stimulated decrease of J_c is due to a decrease in the size of the superconducting channels formed by dislocation walls (as a result of the diffusion of defects into the region of the cores of the edge dislocations).

Unlike the critical temperature of the irradiated YBCO film, which returned to its original value in about ten days, the low-temperature ''tail'' of $\chi''(T)$ appearing after electron irradiation and reflecting the broadening of the superconducting temperature with respect to temperature remained essentially unchanged during the entire observation period (Fig. 3). This stability of radiation-stimulated change in the character of $\chi''(T)$ can serve as additional confirmation of the hypothesis that these changes are due to the growth of the region occupied by the cores of edge dislocations.

Since the edge dislocations are efficient sinks for point defects,[21] the defects that have diffused into the region of the dislocation cores are quite stably trapped in this region. As a result, the decrease of the effective width of the SC channels formed by the dislocation walls (decrease of J_c) and the additional appearance of regions with depressed T_c (the ''tail'' of $\chi''(T)$, i.e., broadening of the SC transition) are stable effects.

5. CONCLUSION

In thin epitaxial films of HTSC $YBa_2Cu_3O_{7-x}$ irradiated by 1-MeV electrons to a maximum dose of 4×10^{16} electrons/cm^2 we have observed an increase in the critical temperature by about 1 K and a decrease in the critical current density by almost a factor of two. These effects were described on the basis of ideas as to the possible role of mechanisms of defect formation in YBCO upon excitation of the electronic subsystem. In contrast to the reversible radiation effects observed for T_c, which involve regions of the film far from the interblock boundaries, the radiation-stimulated changes in the interblock boundaries themselves had an irreversible character and led to a stable decrease of the critical current density of YBCO and a stable broadening of the superconducting transition in temperature. This may be the result of a stable narrowing of the SC channels in the dislocation walls as a result of radiation-stimulated growth of the Cottrell atmospheres of the cores of edge dislocations in the interblock boundaries.

The authors thank S. M. Ryabchenko for steady interest in this study and for a fruitful discussion of its basic ideas.

This study was supported in part by CRDF Grant UP1-306 and was carried out under Topics 1.4.1.V/77 and V 63/34 of the National Academy of Sciences of Ukraine.

[a)]E-mail: fedotov@iop.kiev.ua

[1] B. D. Weaver, E. J. Jackson, G. P. Summers, and E. A. Burke, Phys. Rev. B **46**, 1134 (1992).
[2] J. Giapintzakis, D. M. Ginzberg, M. A. Kirk, and S. Ockers, Phys. Rev. B **50**, 15 967 (1994).
[3] E. M. Jackson, B. D. Weaver, G. P. Summers, P. Shapiro, and E. A. Burke, Phys. Rev. Lett. **74**, 3033 (1995).
[4] S. K. Tolpygo, J. Y. Lin, M. Gurvitch, S. Y. Hou, and J. M. Phillips, Physica C **269**, 207 (1996).
[5] B. I. Belevtsev, I. V. Volchok, N. V. Dalakova, V. I. Dotsenko, L. G. Ivanchenko, A. V. Kuznichenko, and L. I. Logvinov, Phys. Status Solidi A **181**, 437 (2000).
[6] F. M. Sauerzopf, Phys. Rev. B **57**, 10959 (1998).
[7] Yu. V. Fedotov, S. M. Ryabchenko, and A. P. Shakhov, Fiz. Nizk. Temp. **26**, 638 (2000) [Low Temp. Phys. **26**, 464 (2000)].
[8] J. R. Clem and A. Sanchez, Phys. Rev. B **50**, 9355 (1994).
[9] M. Wurlitzer, M. Lorenz, K. Zimmer, and P. Esqunazi, Phys. Rev. B **55**, 11816 (1955).
[10] S. K. Tolpygo, J.-Y. Lin, M. Gurvitch, S. J. Hou, and J. M. Phillips, Phys. Rev. B **53**, 12462 (1996).
[11] M. Lanno and J. Bourgoin, *Point Defects in Semiconductors I*, Springer-Verlag, New York (1981), Mir, Moscow (1985).
[12] R. J. Cava, B. Batlogg, C. H. Chen, E. A. Reitman, S. M. Zahurak, and D. Werder, Phys. Rev. B **36**, 5719 (1987).
[13] M. I. Klinger, Ch. B. Lushchik, T. V. Mashovets, G. A. Kholodar', M. K. Sheĭnkman, and M. A. Élango, Usp. Fiz. Nauk **147**, 523 (1985) [Sov. Phys. Usp. **28**, 994 (1985)].
[14] M. S. Yunusov, M. A. Zaikovskaja, and B. L. Oksengendler, Phys. Status Solidi A **35**, K145 (1976).
[15] V. I. Kudinov, I. L. Chaplygin, A. I. Kirilyuk, N. M. Kreines, R. Laiho, E. Lahderanta, and C. Ajahe, Phys. Rev. B **47**, 9017 (1993).
[16] M. Kall, M. Osada, M. Kakihana, L. Borjesson, T. Frello, J. Madsen, N. Andersen, R. Liang, P. Dosanjh, and W. Hardy, Phys. Rev. B **57**, R14072 (1998).
[17] J. Zaanen, A. Paxton, O. Jepsen, and O. Andersen, Phys. Rev. Lett. **60**, 2685 (1988).
[18] A. Gurevich and E. A. Pashitskii, Phys. Rev. B **57**, 13878 (1998).
[19] É. A. Pashitskiĭ, V. I. Vakaryuk, S. M. Ryabchenko, and Yu. V. Fedotov, Fiz. Nizk. Temp. **27**, 131 (2001) [Low Temp. Phys. **27**, 96 (2001)].
[20] Yu. V. Fedotov, A. V. Bondar', S. M. Ryabchenko, V. V. Safronov, and A. P. Shakhov, Ukr. Fiz. Zh. **46**, 211 (2001).
[21] J. P. Hirth and J. Lothe, *Theory of Dislocations*, McGraw-Hill, New York (1967), Atomizdat, Moscow (1972).

Translated by Steve Torstveit

LOW-TEMPERATURE MAGNETISM

Elastic-strain mechanisms for the influence of temperature, magnetic field, and pressure on the resistive and magnetic properties of magnetic semiconductors

P. I. Polyakov[a] and S. S. Kucherenko

A. A. Galkin Donetsk Physicotechnical Institute, National Academy of Sciences of Ukraine, ul. R. Lyuksemburg 72, Donetsk 83114, Ukraine

(Submitted April 18, 2002; revised June 10, 2002)
Fiz. Nizk. Temp. **28**, 1041–1047 (October 2002)

An analysis is made of the results of studies of the variation of the resistivity of a bulk polycrystalline sample of $La_{0.56}Ca_{0.24}Mn_{1.2}O_3$ under the influence of temperature (T), pressure (P), and magnetic field (H) and a study of the variation of the magnetostriction in single-crystal $LaMnO_3$ as a function of T and H. It is found that the peaks of the magnetoresistive, baroresistive, and baromagnetoresistive effects occur at the same temperature, which is independent of magnetic field and pressure and corresponds to the temperature T_{ms} of the metal–semiconductor phase transition in the absence of magnetic field and pressure. ''Cooling'' and ''heating'' effects of pressure and magnetic field are detected, and an equivalency of the influence of T, P, and H on the resistivity of the polycrystalline sample and of T and H on the magnetostriction of the single-crystal $LaMnO_3$ is observed. The linearity of the shifts of the $T_{ms}(P)$ and $T_{ms}(H)$ peaks in the resistive properties of $La_{0.56}Ca_{0.24}Mn_{1.2}O_3$ is demonstrated and also the linearity of $H_g(T)$ in the magnetic properties for the example of the changes in the hysteresis of the magnetostriction in the $LaMnO_3$ single crystal. The role of the regularities that obtain for an elastic-strain mechanism for the influence of T, P, and H on the magnetic and resistive properties and phase states is revealed and explained. The sign-varying nature of the influence of T, P, and H is established, and its role in the variation of the resistive and magnetic properties is found (magnetic phase transitions). The relationship of the structural, elastic, resistive, and magnetic properties in magnetic semiconductors is established. © *2002 American Institute of Physics.* [DOI: 10.1063/1.1521293]

INTRODUCTION

The colossal magnetoresistive effect has made rare-earth manganites with the perovskite structure some of the most intensively studied functional materials.[1,2] Unfortunately, the study and interpretation of the properties do not permit one to make a conclusive determination as to the nature of the unique interrelationship of the magnetic and electric properties.

In Refs. 3–5 the resistive properties of these compounds under the influence of temperature (T) magnetic field (H), and pressure (P) were investigated. The authors of Refs. 6–11 found that with increasing hydrostatic pressure and magnetic field the resistivity decreases and the metal–semiconductor phase transition temperature T_{ms} increases; it was found that the resistivity has a linear pressure dependence at a fixed temperature and that T_{ms} depends linearly on pressure and magnetic field strength.

In Ref. 12 a linear pressure dependence of T_N was demonstrated, and in Ref. 13 a linear pressure dependence of T_{ms} was revealed by studies of the magnetic susceptibility of the semiconductors $La_{0.875}Sr_{0.125}MnO_3$ under hydrostatic pressure. In Ref. 14 data on the thermal expansion and magnetostriction at phase transitions of single-crystal $La_{1-x}Sr_xMnO_3$ were presented, and it was proposed that the strictive stresses causing the elastic strains in the structure are due to the change in the magnetic field strength.

The main goal of this paper is to establish how the elastic mechanisms are related to the resistive and magnetic properties and to explain how the temperature, pressure, and magnetic field influence the properties of magnetic semiconductors.

EXPERIMENTAL RESULTS AND DISCUSSION

The polycrystalline sample of $La_{0.56}Ca_{0.24}Mn_{1.2}O_3$ investigated here was obtained by the conventional technique of a two-stage synthesizing anneal with a subsequent sintering of powders pressed in a metallic press form by the technology described in Refs. 10 and 15.

The resistance was measured by the four-probe method in direct current in the absence and presence of magnetic fields of various strengths ($H=0$, 2, 4, 6, and 8 kOe). The temperature was determined from the resistance of a bifilarly wound copper coil. A high hydrostatic pressure in the interval $P=0-1.8$ GPa was produced in the high-pressure chamber of Ref. 16.

1. The temperature dependence of the resistivity of a bulk sample under the influence of magnetic field and pressure is presented in Fig. 1. Also shown are curves of an analogous nature for the thermoresistive $\rho_0(T)$ (curve *1*), magnetoresistive $\rho_H(T)$ (*2*), baroresistive $\rho_P(T)$ (curves

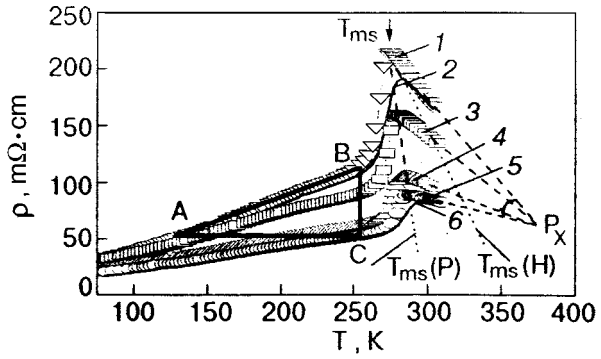

FIG. 1. Temperature dependence of the resistivity of a bulk polycrystalline sample of $La_{0.56}Ca_{0.24}Mn_{1.2}O_3$: *1* — $P=0$, $H=0$; *2* — $P=0$, $H=8$ kOe; *3* — $P=6$ kbar, $H=0$ kOe; *4* — $P=12$ kbar, $H=0$; *5* — $P=18$ kbar, $H=0$; *6* — $P=18$ kbar, $H=8$ kOe. (The conventional designation P_X implicitly relates to the parameter of the perovskite structure and to the magnetic ion Mn.)

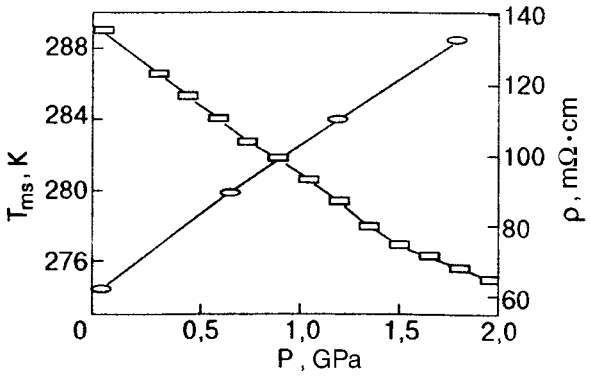

FIG. 3. Dependence of the phase transition temperature T_{ms} and of the resistivity of a bulk polycrystalline sample of $La_{0.56}Ca_{0.24}Mn_{1.2}O_3$ on the hydrostatic pressure at room temperature.

3–5), and baromagnetoresistive $\rho_{PH}(T)$ (*6*) regimes. With increasing pressure or magnetic field the position of the resistivity peak is shifted to higher temperatures and its intensity is lowered.

In Fig. 2 the temperature dependence of the magnetoresistive effect at $H=8$ kOe is shown by curve *6*, which demonstrates that the peak has become insignificant in height, amounting to 30%.[17] The baroresistive effect $(\rho_0-\rho_P)/\rho_0$ and baromagnetoresistive effect $(\rho_0-\rho_{PH})/\rho_0$ in the phase transition region (curves *1–5* in Fig. 2), which were first discovered by the authors, reach 70%.[18] It is important to note that the peaks of the magneto-, baro-, and baromagnetoresistive effects have the same temperature, T_{PP} (Fig. 2). It should be emphasized that T_{PP} remains constant independent of magnetic field and pressure acting either individually or jointly. The constancy of the temperature T_{PP} of these effects permits the assertion that the mechanisms taking part in their formation conform to the same regularities. An extremely important finding is that in these effects the temperature T_{PP} coincides in value with the metal–semiconductor phase transition temperature T_{ms} in the absence of magnetic field and pressure (see curve *1* in Fig. 1). To explain the nature of these mechanisms and the constancy of T_{PP} we were led to a more thorough analysis of the results presented in Fig. 1.

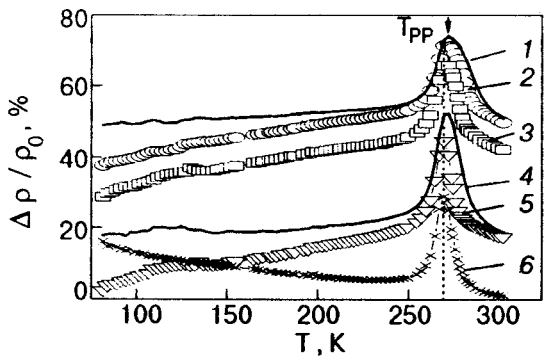

FIG. 2. Temperature dependence of the characteristics of a bulk polycrystalline sample of $La_{0.56}Ca_{0.24}Mn_{1.2}O_3$: baroresistive effect $(\rho_0-\rho_P)/\rho_0$: *2* — $P=18$ kbar; *3* — $P=12$ kbar; *5* — $P=6$ kbar; the baromagnetoresistive effect $(\rho_0-\rho_{PH})/\rho_0$: *1* — $P=18$ kbar, $H=8$ kOe; *4* — $P=6$ kbar, $H=8$ kOe; magnetoresistive effect $(\rho_0-\rho_H)/\rho_0$: *6* — $P=0$, $H=8$ kOe.

Let us estimate the influence of T, P, and H on the dynamics of the linear dependences of $\rho_0(T)$, $\rho_H(T)$, $\rho_P(T)$, and $\rho_{PH}(T)$ up to a temperature of 250 K (curves *1–5* in Fig. 1). In the absence of H and P the resistivity increment $\Delta\rho$ per degree has a value $\Delta\rho/\Delta T=0.46$ Ω/K (curve *1* in Fig. 1). At a fixed temperature $T\approx 250$ K the change of the resistivity with pressure is $\Delta\rho/\Delta P\approx 2.83$ Ω/kbar (curves *1* and *5* in Fig. 1). It follows that changing the temperature by $\delta T=6.2$ K within the linear part changes the resistivity on account of the thermoelastic expansion by the same amount as does elastic compression by a hydrostatic pressure of 1 kbar. This correspondence (or "equivalency") demonstrates the role of the elastic properties in the variation of the resistivity. A linear part of the temperature dependence of the resistivity has also been noted for a polycrystalline sample of $La_{0.9}Mn_{1.1}O_3$ (Ref. 10).

From the character of the $\rho_0(T)$, $\rho_P(T)$, and $\rho_H(T)$ curves it can be judged that pressure and magnetic field influence the resistivity in the same sense — i.e., they shift the peaks of ρ and the transition temperature T_{ms} in the same direction — in the entire temperature interval (curves *1–5* in Fig. 1). It is seen from curves *1* and *2* that in the phase transition region the application of a magnetic field of strength $H=1$ kOe leads to a change in resistivity $\Delta\rho/\Delta H=2.1$ Ω/kOe. The baric change in resistivity in this temperature region (see curves *1* and *5*) is $\Delta\rho/\Delta P=5.27$ Ω/kbar. This correspondence shows that increasing the magnetic field by $\delta H=2.37$ kOe leads to the same change in resistivity as does a 1 kbar increase in pressure. The relationship also holds in the linear region of $\rho(T)$. The same sort of estimates can be made for the linear dependences of the shifts of the peaks $T_{ms}(H)$ and $T_{ms}(P)$. For this the effect of magnetic field on the resistivity can be compared with the commensurate influence of hydrostatic pressure. The commensurate shift of the metal–semiconductor phase transition temperature T_{ms} is another indication that the mechanisms of the magnetic field and pressure effects are identical. This allows one to assert that the giant magnetoresistance is the result of a jump in the resistivity caused by magnetoelastic deforming stresses in the sample due to the influence of high magnetic fields.

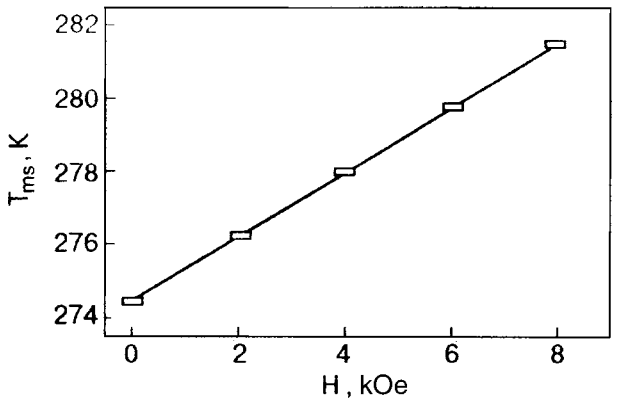

FIG. 4. Dependence of the phase transition temperature T_{ms} of a bulk polycrystalline sample of $La_{0.56}Ca_{0.24}Mn_{1.2}O_3$ on the magnetic field strength.

As confirmation of the role of the elastic properties in the behavior of the temperature of the resistivity peaks we pick $T_{ms}(H)$ and $T_{ms}(P)$ and also the linear dependence $\rho(P)$ at $T=300$ K (see Figs. 3 and 4). They are linear in the entire region of magnetic fields and pressures investigated. The same features were noted in Refs. 8 and 10. We call attention to the fact that under the simultaneous action of magnetic field and hydrostatic pressure, $T_{ms}(P,H)$ lies between $T_{ms}(H)$ and $T_{ms}(P)$. The linear behavior and the difference in these last is explained by the presence of anisotropy of the elastic and magnetoelastic properties.

2. The equivalency seen in the resistive properties under the influence of T, P, and H reveals yet another regularity. The action of pressure and magnetic field causes a ''cooling'' effect (i.e., an increase in P and H, in its effect on the resistivity of the sample via elastic mechanisms, is equivalent to a decrease in temperature) and the inverse, ''heating'' effect (a decrease in P and H, in its effect on the sample, is equivalent to a corresponding increase in temperature).

These effects in magnetic semiconductors can explain the linear dependence of $T_{ms}(H,P)$ and, undoubtedly, the underlying role of elastic properties in this process. From the standpoint of a deformation mechanism for the formation of the phase state, the metal–semiconductor transition is a consequence of thermoelastic expansion of the structure of the sample and is fixed according to the temperature T_{ms} of the resistivity peak (curve *1* in Fig. 1). The application of hydrostatic pressure and magnetic field leads to a ''cooling'' effect — the resistivity decreases to a value corresponding to the initial resistivity at a lower temperature. To bring about the phase transition in this case it is necessary to raise the temperature — the additional thermoelastic expansion compensates the compression of the structure resulting from the effects of both pressure and magnetic field; this is accompanied by an increase of $T_{ms}(H)$ and $T_{ms}(P)$. The temperature T_{PP} of the maxima of the magneto-, baro-, and baromagnetoresistive effects remains constant at different pressures and magnetic fields. This indicates that the phase transition is brought about when a certain condition is reached which is invariant for a given sample.

Looking at this process in the opposite way, we start from the $\rho(T)$ curve under the influence of P and H. Then, as these influences are reduced, the resistivity increases to a value corresponding to an initial curve taken at a higher temperature. This reveals the ''heating'' effect of P and H. To bring about a phase transition in this case it is necessary to lower the temperature — the additional thermoelastic compression compensates the expansion of the structure due to the decreasing pressure and magnetic field. This means that the removal of the external influence requires less and less overheating of the system to achieve the phase transition; $T_{ms}(H)$ and $T_{ms}(P)$ decrease.

These ''cooling'' and ''heating'' effects and also the linear dependences $T_{ms}(H)$ and $T_{ms}(P)$ attest to the compensating interaction of the elastic and magnetoelastic compression, on the one hand, and the thermoelastic expansion, on the other. Here the conditions for realization of a phase transition remain constant independent of the pressure and magnetic field within the intervals of our investigations. Confirmation of this is provided by the fact that the peaks of the baro-, magneto-, and baromagnetoresistive effects occur at the same temperature T_{PP} and by the linearity of $T_{ms}(H)$ in the magnetic properties. As a consequence, equality of the phase transition temperature T_{ms} (in the absence of P and H) and T_{PP} confirms the similar nature of the elastic strain mechanisms for the influence of T, P, and H and also attests to an invariant condition for the formation of the metal–semiconductor phase transition.

3. To establish the regularities in the variation of the magnetic properties under the influence of T and H, we analyze the results of studies of the anomalies of the thermal expansion and magnetostriction at the phase transitions of a single-crystal sample of $LaMnO_3$ and its modifications.[14] The strain-induced variations are determined by the magnetostrictive properties under the influence of a magnetic field.

Let us turn to the field dependence of the longitudinal magnetostriction for $LaMnO_{3e}$ at several fixed temperatures (Fig. 5 of Ref. 14). At low fields a nonlinear region is noticeable, and as the magnetic field is increased a linear region is observed up to and above the phase transition. It can be stated that this segment is due to the dominant effect of the magnetostriction over the temperature. We choose the part in which the influence of temperature on the magnetostriction at a fixed magnetic field is linear, and for $H\approx 130$ kOe we estimate the change in the longitudinal magnetostriction $\lambda_{\parallel}$ with temperature: $\Delta\lambda_{\parallel}/\Delta T\approx 0.013$. Such an estimate indicates that a change in magnetic field by $\Delta H=1$ kOe will have the same effect on the value of the magnetostriction as a change in temperature by $\Delta T=2.1$ K.

The linear dependence observed in Fig. 5 for the shift of the hysteresis field with temperature, $H_g(T)$, allows us to estimate the slope as $\Delta H/\Delta T\approx 0.27$ kOe/K and to determine the shift of the structural phase transition under the influence of temperature and magnetic field: $\Delta T/\Delta H\approx 6$ K/kOe. Thus the dependence $H_g(T)$ is analogous to $T_{ms}(H)$ in the dynamics of the resistive properties.

The dependence $H_g(T)$ with increasing and decreasing magnetic field also conforms to the ''heating'' and ''cooling'' effects, respectively. This is confirmed by the change in magnetostriction under the influence of T and H, which is clearly expressed in Fig. 5.

The linearity of $H_g(T)$ and the value of the shift $\Delta H/\Delta T$ permit us to link the regularities of the change in the slope of the linear parts of the $\lambda_{\parallel}(T,H)$ curves with the sign-varying

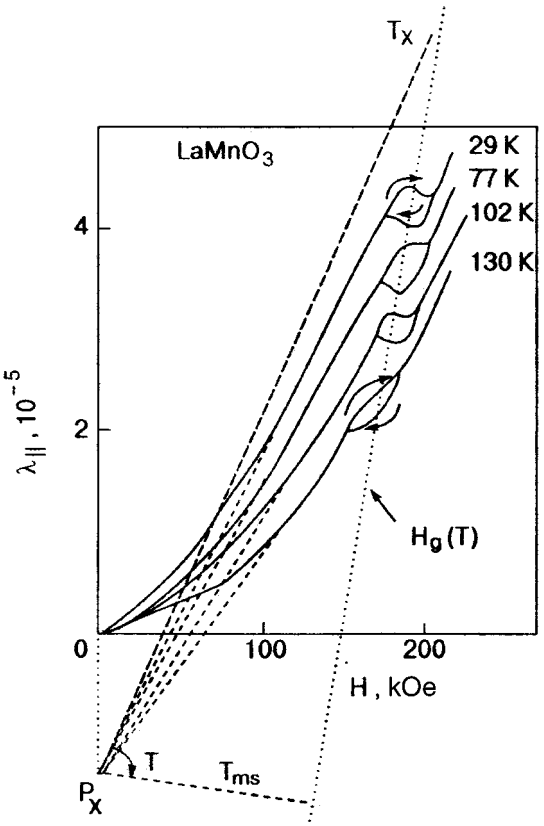

FIG. 5. Field dependence of the longitudinal magnetostriction for $LaMnO_3$ (Ref. 14).

regions on the field dependence of the longitudinal magnetostriction (Fig. 5).

4. The variation of the resistive properties under the variable influence of thermoelastic expansion and compression at fixed pressures and magnetic fields is a consequence of the ''cooling'' and ''heating'' effects. Under the influence of a variable magnetoelastic compression and expansion at fixed temperatures the magnetostrictive properties cause a change in sign of the indicated effects. Consequently, the constancy of $T_{PP}=T_{ms}$ remains in force; the linearity of the shift of the phase transition in both in the magnetostrictive and resistive properties is determined by the elastic strain equivalency (ESE) and the sign-varying nature of the influence of both the temperature and magnetic field.

The sign-varying nature is due to a competition between the ESEs of the thermoelastic expansion and magnetoelastic compression, which is manifested in a change of the peaks of the resistivity and of the colossal baro- and magnetoresistive effects while T_{PP} remains constant, and also in the linearity of the dependences $T_{ms}(H)$ and $T_{ms}(P)$. In the magnetic properties the sign-varying nature is determined by the dynamics of the variation of the magnetic susceptibility χ and is manifested in the form of magnetic phase transitions and magnetic hysteresis.

The ESE revealed here can account for the sign-varying nature under the influence of magnetic field and temperature (the nonlinearity region) observed on the initial part of the temperature–field dependence of the magnetostriction in single-crystal $LaMnO_3$ (Fig. 5), and it is manifested in variations of the resistive properties and of the magnetic phase transitions. The sign-varying nature under the influence of H and T (the change of the slope of the linear part of the curve at the corresponding T and H) gives rise to peaks in the resistive properties, magnetic hysteresis, and, as a result, a sign variation in the magnetic and resistive properties in the region of the structural phase transition.

A representative result of the ESE and the sign-varying nature is seen on the field curves of the longitudinal and transverse magnetostriction in $LaMnO_3$, which reveal two competing strain mechanisms — thermoelastic expansion and magnetoelastic compression:

a) at fixed low temperatures the initial part of the field dependence of the magnetostriction exhibits nonlinearity due to the prevailing influence of the thermoelastic strain, followed by a linear dependence as the magnetoelastic compression increases further;

b) at higher temperatures, expansion occurs because the thermoelastic strain predominates over the magnetoelastic compressibility; one observes a sharp decrease of the magnetostriction, magnetic hysteresis, and the formation of a sign-varying region for the dependence of the magnetic properties, i.e., a competing effect of the ESE for the influence of T and H; the sign-varying regions of the magnetostriction are manifested both in magnetic hysteresis and in the temperature dependences at fixed magnetoelastic compression ($H\approx 200$ kOe) of single-crystal $La_{0.9}Sr_{0.1}MnO_3$ (Ref. 14).

5. To compare the structural, resistive, and magnetic variations under the influence of T, P, and H, we turn our attention to the position of P_X (curve *5* in Fig. 1). (P_X is a conventional designation, implicitly relating to the parameter of the perovskite structure and to the magnetic ion Mn.)[14] Taking into account the correspondence in the varying properties of the magnetostriction under the influence of T and H and the linearity of the $\lambda_{\|}(T,H)$ curves, one can establish a correspondence between the structural, magnetic, and resistive properties for the example of the magnetostrictive variations under the influence of T and H. The linear parts of the field curves of the magnetostriction (Fig. 5) converge to a single point P_X. This same parameter is also represented in the family of temperature curves of the resistivity at different values of P and H (see Fig. 1).[2,5,11]

As a result of extrapolation in Fig. 5 we obtain the point T_X — a conventional designation for a variable parameter corresponding to the state of the structural phase transition in a single-crystal sample of $LaMnO_3$.

The change of the position of P_X and T_X is due to the link established in the structure between the properties and phase transitions, while the influence of T, P, and H is a regularity of the ESEs and the sign-varying nature of the changing magnetic and resistive properties and the phase transitions.

6. The characteristic parameters P_X and T_X which we have identified, the sign variations, the $H_g(T)$ dependence, analogous to $T_{ms}(H)$, and also the dependence of the magnetostriction on the magnetic field (Fig. 5) permit us to establish yet another regularity — the role of magnetostriction in the ''heating'' and ''cooling'' effects. The ''heating'' effect consists in the following: at a fixed thermoelastic expansion at $T<T_C$ the imposition of a magnetic field ''heats'' the sys-

tem as a result of the counterpressure of the magnetoelastic compression, bringing about conditions for the formation of a metal–semiconductor phase transition, and ensures the constancy of T_{PP}. The inverse, ''cooling'' effect consists in the fact that if under the same conditions the magnetic field is decreased, relieving the counterpressure, expansion occurs, corresponding to an increase in the phase transition temperature. The conditions for realization of the phase transition remain constant.

It should be noted that these same regularities , due to the influence of T and H, i.e., the ECSs, the sign variations, and the ''cooling'' and ''heating'' effects, are also manifested in magnets.

CONCLUSION

Our analysis of the experimental research on the dynamics of the change in resistivity of a polycrystalline sample of $La_{0.56}Ca_{0.24}Mn_{1.2}O_3$ under the influence of temperature, pressure, and magnetic field and of the magnetostriction curves[14] of single-crystal $LaMnO_3$ under the influence of T and H has enabled us to do the following:

— establish the linear parts of the resistivity curves $\rho_0(T)$, $\rho_H(T)$, $\rho_P(T)$, and $\rho_{PH}(T)$ and of the phase transition $T_{ms}(H)$ and $T_{ms}(P)$;

— to determine the characteristic parameters P_X and T_X;

— to assess the elastic strain mechanisms for the influence of T, P, and H on the resistivity of $La_{0.56}Ca_{0.24}Mn_{1.2}O_3$ and of T and H on the magnetostriction of $LaMnO_3$;

— to explain the different linear dependences of $T_{ms}(H)$ and $T_{ms}(P)$ in terms of the regularity of the difference of the anisotropy of the elastic and magnetoelastic striction;

— to establish that the peaks of the baro-, magneto-, and baromagnetoresistive effects have the same temperature T_{PP}, which coincides with the phase transition temperature T_{ms};

— to establish, from the dynamics of the resistivity under the influence of T, P, and H, the ''cooling'' and ''heating'' effects, which confirm the elastic strain mechanisms for the shift of $T_{ms}(H)$ and for the constancy of T_{PP} and its coincidence with the phase transition temperature T_{ms};

— to establish the regularities of the variation of the hysteresis magnetic field $H_g(T)$ and its correspondence to $T_{ms}(H)$ from the parameters of the striction and the value of the ''heating'' and ''cooling'' effects of magnetic field.

The results obtained here point to an elastic strain mechanism for the influence of temperature and magnetic field on polycrystalline and single-crystal samples of magnetic semiconductors. They are due to a competition between two forms of striction, — thermoelastic expansion and magnetoelastic compression — and are manifested in a varying sign of the properties.

Our analysis permits the assertion that the baro-, magneto-, and baromagnetoresistive, ''cooling,'' and ''heating'' effects and the constancy of T_{PP} for these listed effects and its coincidence with the phase transition temperature T_{ms} are a regularity of the elastic strain mechanism for the influence of T, P, and H on the properties and phase states of magnetic semiconductors.

[a)]E-mail: poljakov@host.dipt.donetsk.ua

[1] V. M. Loktev and Yu. G. Pogorelov, Fiz. Nizk. Temp. **26**, 231 (2000) [Low Temp. Phys. **26**, 171 (2000)].
[2] M. B. Salamon and M. Jaime, Rev. Mod. Phys. **73**, 583 (2001).
[3] F. Mascarenhas, K. Falk, P. Klavins, J. S. Schilling, Z. Tomkowicz, and W. Haase, J. Magn. Magn. Mater. **231**, 172 (2001).
[4] N. Fujii, R. Zach, M. Ishizuka, F. Ono, T. Kanomata, and S. Endo, J. Magn. Magn. Mater. **224**, 12 (2001).
[5] V. Moshnyaga, S. Klimm, E. Gommert, R. Tidecks, S. Horn, and K. Samwer, J. Appl. Phys. **88**, 5305 (2000).
[6] S. S. Kucherenko, V. I. Mikhaĭlov, V. P. Pashchenko, P. I. Polyakov, V. A. Shtaba, and V. P. D'yakonov, Pis'ma Zh. Tekh. Fiz. **27**, 38 (2001) [Tech. Phys. Lett. **27**, 638 (2001)].
[7] S. S. Kucherenko, V. P. Pashchenko, P. I. Polyakov, V. A. Shtaba, and A. A. Shemyakov, Fiz. Nizk. Temp. **27**, 761 (2001) [Low Temp. Phys. **27**, 559 (2001)].
[8] S. S. Kucherenko, V. P. Pashchenko, P. I. Polyakov, S. I. Khartsev, and V. A. Shtaba, Pis'ma Zh. Tekh. Fiz. **27**, 24 (2001) [Tech. Phys. Lett. **27**, 451 (2001)].
[9] P. I. Polyakov, V. P. Pashchenko, and S. S. Kucherenko, Fiz. Tekh. Vys. Davlenii **11**, 104 (2001).
[10] V. P. Pashchenko, S. S. Kucherenko, and P. I. Polyakov, Fiz. Nizk. Temp. **27**, 1370 (2001) [Low Temp. Phys. **27**, 1010 (2001)].
[11] I. V. Medvedeva, K. Barner, G. H. Rao, N. Hamad, Yu. S. Bersnev, and J. R. Sun, Physica B **292**, 250 (2000).
[12] A. E. Petrova, E. S. Itskevich, V. A. Ventstel', V. F. Kraĭdenov, and A. V. Rudnev, Fiz. Nizk. Temp. **27**, 1123 (2001) [Low Temp. Phys. **27**, 831 (2001)].
[13] O. Prokhnenko, Z. Arnold, I. Medvedeva, A. Kuchin, and J. Kamarad, Fiz. Nizk. Temp. **27**, 375 (2001) [Low Temp. Phys. **27**, 275 (2001)].
[14] A. M. Kadomtseva, Yu. F. Popov, G. P. Vorob'eva, K. I. Kamilov, V. Yu. Ivanov, A. A. Mukhin, and A. M. Balbashov, Fiz. Tverd. Tela (St. Petersburg) **42**, 1077 (2000) [Phys. Solid State **42**, 1110 (2000)].
[15] V. P. Pashchenko, S. I. Khartsev, and O. P. Chernekov, Neorg. Mater. **35**, 1294 (1999).
[16] A. V. Oleĭnik, P. I. Polyakov, and V. G. Synkov, Fiz. Tekh. Vys. Davlenii **4**, 88 (1994).
[17] P. I. Polyakov, V. P. Pashchenko, and S. S. Kucherenko, in *Proceedings of the International Conference "Functional Materials,"* Simferopol (2001), p. 49.
[18] P. I. Polyakov and S. S. Kucherenko, Pis'ma Zh. Tekh. Fiz. **28**, 8 (2002) [Tech. Phys. Lett. **28**, 311 (2002)].

Translated by Steve Torstveit

Effects of chaotic local crystal fields in pseudobinary rare-earth intermetallides

A. S. Ermolenko*

Institute of Metal Physics, Ural Branch of the Russian Academy of Sciences yl. C. Kovalevskoi, 18, Ekaterinburg, 620219, Russia

(Submitted February 1, 2002)
Fiz. Nizk. Temp. **28**, 1048–1055 (October 2002)

Works on the influence of local chaotic crystal fields on the magnetic properties of pseudobinary rare-earth intermetallides are briefly reviewed. Attention is focused primarily on compounds of the type $RNi_{5-x}M_x$, M=Cu, Al. Experimentally observed effects of local crystal fields, such as, the appearance of ferromagnetism in the system $Pr(Ni, Cu)_5$ and a decrease of the spontaneous magnetic moment and an increase in the anisotropy energy in the basal plane and coercive force in the intermediate pseudobinary alloys $R(Ni, Cu)_5$ and $R(Ni, Al)_5$ as compared with the limiting binary compounds, are discussed. [DOI: 10.1063/1.1521294]

1. INTRODUCTION

It is known that the interaction energy between the crystal field (CF) and the $4f$ electrons of rare-earth ions makes the decisive contribution to the formation of the magnetic states and magnetic properties of rare-earth intermetallides.[1] The CF theory is now well developed, but calculating the CF parameters for metals or metallic compounds is a quite difficult problem, since the point-charge model, which is successfully used for dielectrics, is found to be ineffective for conducting crystals. In this case the CF parameters are ordinarily determined empirically by finding a particular set of parameters which gives the best agreement between theory and experiment. Experimental methods, such as the study of inelastic neutron scattering, the temperature dependence of the specific heat, and the magnetization curves of single crystals in the direction of the principal crystallographic directions, are usually used for this purpose. For a theoretical description of these properties, the CF Hamiltonian in the form proposed by Stevens[2] is used. The interaction Hamiltonian for a rare-earth ion interacting with a hexagonal CF is

$$H_{CF}=B_{20}O_{20}+B_{40}O_{40}+B_{60}O_{60}+B_{66}O_{66}=\sum_{lm} B_{lm}C_{lm}, \tag{1}$$

where B_{lm} are the parameters of the crystal field; O_{lm} are the equivalent Stevens operators, which are tabulated in, for example, Ref. 3; $l=2, 4, 6$; $m=0,6$; $m \leqslant l$.

Sometimes, rare-earth ions in intermetallides occupy several nonequivalent positions. Then, for each position there exists a unique set of parameters B_{lm}, and if the positions with nearest-neighbors environment of different symmetry are present, even the form of the Hamiltonian (1) is different. The most difficult problem is describing CF effects in compounds with impurity atoms, for example, in disordered solid substitution or interstitial solutions. Even if the crystal lattice type in such solutions remains unchanged, the magnitudes of the charges of the nearest neighbors of a rare-earth ion and the distance between this ion and the surrounding atoms can change. For a disordered distribution of impurity atoms over crystal lattice sites, a set of various configurations of the nearest-neighbor environment of the rare-earth ions arises, and to each configuration there corresponds a different CF Hamiltonian. Obviously, it is extremely difficult to interpret CF effects in these systems. Random local crystal fields (RLCFs) and the statistical nature of their distribution must be taken into account. Thus far, there are very few works on RLCFs. In addition, the objects in which RLCFs occur are very common. They essentially include all pseudobinary, pseudoternary, and so on solid solutions based on ''pure'' binary, ternary, and so on intermetallides. It is known that investigating such solid solutions is not only an important tool for clarifying the nature of the fundamental interactions in rare-earth intermetallides but it is also a basic method for searching for new materials which are important for practical applications, specifically, materials for a new generation of permanent magnets and magnetostriction transducers.

A convenient object for studying RLCF effects are the intermetallides RNi_5 (R–rare-earth metal or yttrium), which possess a hexagonal crystal structure of the type $CaCu_5$.[4] In these objects the valence electrons of the rare-earth ions almost completely fill the $3d$ band in nickel. Consequently, the nickel subsystem has virtually no magnetic moment and YNi_5, $LaNi_5$, and $LuNi_5$ are Pauli paramagnets. Compounds with R=Nd, Sm, Gd, Tb, Dy, Ho, Er, and Tm are ferromagnets with very low Curie points (the highest value 32 K occurs in $GdNi_5$), and $PrNi_5$ is a vanVleck paramagnet, since the crystal field forms an energy spectrum of the ground J multiplet of the Pr^{3+} ion with a nonmagnetic ground state. The ferromagnetically ordered systems RNi_5 possess compounds with easy-axis anisotropy (R=Sm, Gd, and Tm) and easy-plane anisotropy. It is the latter compounds and $PrNi_5$ that are especially promising for determining the effects of RLCFs. In the present paper the results of recent investigations of RLCFs in RNi_5-based pseudobinary intermetallides are briefly reviewed.

2. CRYSTAL-FIELD EFFECTS IN $PRNI_5$-BASED COMPOUNDS

Even in the very early works it was discovered that the interaction of the Pr ions with the crystal field strongly in-

fluences the magnetic and thermal properties of the compound $PrNi_5$ (see, for example, Ref. 1). A peak near 13 K was observed in the temperature dependence of the magnetization measured in a 14 kOe field. The first attempts to explain this peak by a possible antiferromagnetism–paramagnetism transition were not confirmed by subsequent specific-heat measurements: no λ anomaly of the specific heat near 13 K was observed. But, two Schottky-type anomalies with peaks at 20 and 50 K were observed on the magnetic part of the specific heat. They were explained by a characteristic feature of the spectrum of the ground state multiplet of the Pr^{3+} ion in a CF. A hexagonal CF splits the nine-fold degenerate ground state of the Pr^{3+} ion into three singlets (Γ_1, Γ_3, Γ_4) and three doublets ($2\Gamma_5$ and Γ_6). The ground state is the nonmagnetic singlet Γ_4, so that $PrNi_5$ is a van Vleck paramagnet. The magnetic susceptibility peak observed at 13 K is due to the thermal excitation of the Γ_5 state separated from the ground state by a 38 K gap. In Ref. 5 the magnetic susceptibility was measured for a $PrNi_5$ single crystal. Substantial magnetic anisotropy was observed at low temperatures. In a field applied perpendicular to the *c* axis, a susceptibility peak was observed at 15 K, while the susceptibility along the *c* axis had no peak. On the basis of these results the authors of Ref. 6 determined the crystal-field parameters and calculated the spectrum of the levels of the bottom multiplet. In Ref. 7 the similar spectrum was obtained for a Pr^{3+} ion in $PrNi_5$ on the basis of inelastic neutron scattering data. The scheme of the lower levels of the spectrum from Ref. 7 is reproduced in Fig. 1a.

It is shown in Ref. 8 that the inelastic neutron scattering spectrum in the pseudobinary alloys $RNi_{5-x}Cu_x$ is substantially different from that in binary $PrNi_5$. The authors of Ref. 8 attribute this fact to the influence of configurational disorder arising in the nearest-neighbors environment of the Pr ions with disordered substitution of copper for nickel. We performed a systematic study of the magnetic properties of single crystals of the pseudobinary compounds $PrNi_{5-x}Cu_x$.[9] The results were unusual from our standpoint. Substitution of even a small amount copper for nickel sharply increases the magnetic susceptibility of single crystals measured at 4.2 K along the *a* and *b* axes in the basal plane (Fig. 2). The magnetization curves along the hard axis *c* is essentially independent of *x*.

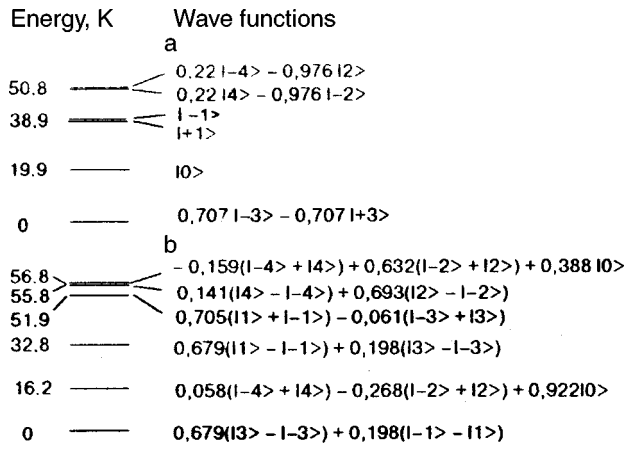

FIG. 1. Scheme of the lower levels of the ground state multiplet of the Pr^{3+} ion split in a crystal field described by the Hamiltonian (1) (a) and the Hamiltonian (1) with the term $B_{22}O_{22}$ (b). The crystal field parameters are taken from Ref. 7; $B_{22}=0.2B_{20}$.

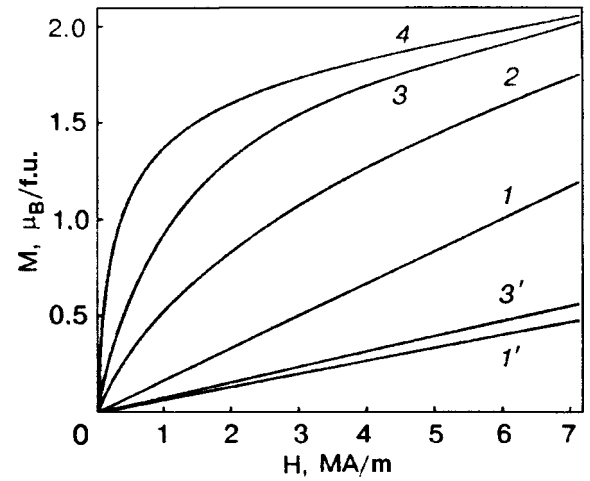

FIG. 2. Magnetization curves at 4.2 K of the single crystals of the alloys $PrNi_{5-x}Cu_x$ along the *b* (*1*–*4*) and *c* (*1′*,*3′*) axes for $x=1$ (*1 and 1′*), 0.3 (*2*), 0.7 (*3* and *3′*), and 1.6 (*4*).[9]

Figure 3 shows the temperature dependences of the magnetization $M(T)$ for the alloys $PrNi_5$ and $PrNi_{4.9}Cu_{0.1}$, obtained in external fields 1.6 and 4 MA/m applied along the *b* axis. They all possess peaks near 16 and 13 K, respectively, for the first and second alloys. As mentioned above, for $PrNi_5$ similar results were obtained previously and explained by thermal excitation of Pr^{3+} ions from a nonmagnetic singlet into close-lying magnetic states. In an alloy with a low ($x=0.1$) copper content the peak $M(T)$ is relatively much smaller, and it virtually vanishes for alloys with $x>0.1$.

As the external magnetic field increases, the absolute peak value of the magnetization for both alloys increases sharply, but the relative magnitude of the peak decreases for $PrNi_5$ and increases for the copper-doped compound. This behavior of the magnetization can be explained by a change in the position of the energy levels in the spectrum of the bottom multiplet of the Pr ions whose nearest-neighbors environment contains at least one copper ion. Indeed, a nickel

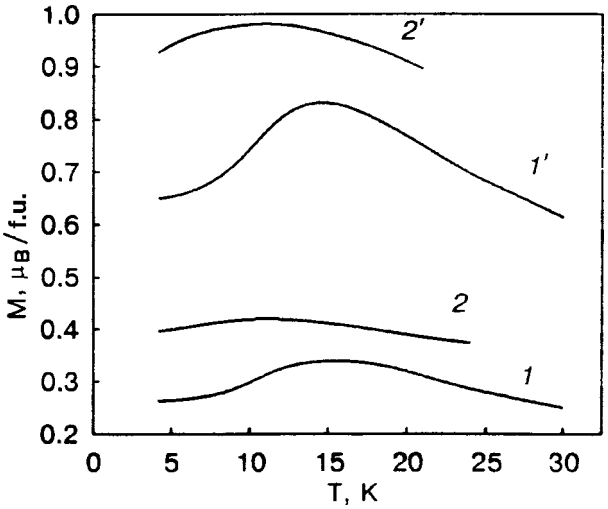

FIG. 3. Temperature dependence of the magnetization along the *b* axis for the alloys $PrNi_5$ (*1* and *1′*) and $PrNi_{4.9}Cu_{0.1}$ (*2* and *2′*), measured in an external magnetic field 1.6 (*1*, *2*) and 4 (*1′*,*2′*) MA/m.[9]

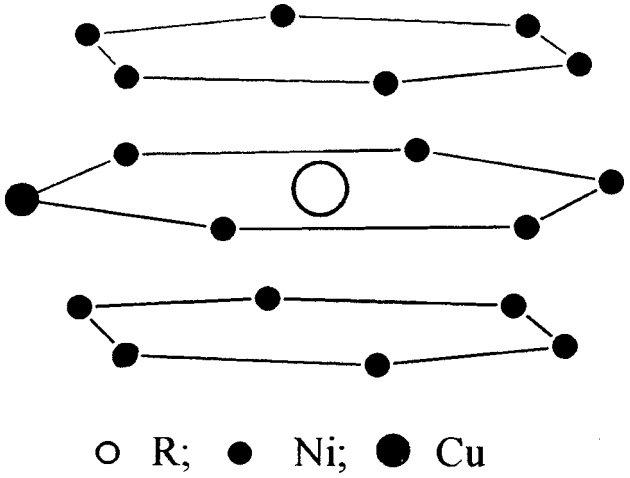

FIG. 4. The simplest nearest-neighbors configuration at the rare-earth ion in the crystal lattice of the pseudobinary alloy $RNi_{5-x}Cu_x$ for small x.

atom possesses less than one copper atom per electron, and the electric charges associated with them can be different. As one can see in Fig. 4, this can destroy the six-fold symmetry in the arrangement of the charges which create the crystal field on the central Pr ion and hence change the position of the levels of the bottom multiplet of this ion. This change can be quite large, since its nature is the same as that of the splitting itself of the multiplet. In principle, it can result in a sharply higher magnetic susceptibility and lower critical exchange interaction field required for the appearance of ferromagnetic ordering. One would expect that at temperatures $T<4.2$ K such ordering will occur in copper-doped alloys. Indeed, in alloys with $0.7\leqslant x\leqslant 2.6$ we observed peaks of the initial susceptibility for ac current at temperatures $T<4.2$ K.[10,11]

Analysis of the magnetization curves using the Arrot method gave Curie points T_C which are identical to the temperatures of the susceptibility peaks. Figure 5 displays the concentration dependence of the Curie points. It possesses a peak $T_C=3.6$ K at $x=1.1$. As x increases further, the Curie point decreases linearly down to $x=2.6$. Although we did not study alloys with a higher copper content, it can be expected that at a certain critical concentration they will become paramagnets in the ground state, since the limiting alloy $PrCu_5$ is a van Vleck paramagnet, just like $PrNi_5$. The explanation of the appearance of ferromagnetism in pseudobinary solid solutions of the two van Vleck paramagnets by the destruction of the initial configurational order in the distribution of electric charges over the crystal-lattice sites is also confirmed by the fact that in the amorphous state $PrNi_5$ is a ferromagnet.[12] As the state changes from crystalline to amorphous, the local environment of a Pr^{3+} ion changes and the spectrum of the levels in its ground state multiplet also changes. In Ref. 13 it was shown that to explain adequately this spectrum it is no less important to take account of the breakdown of local symmetry of the nearest-neighbors environment than to take account of the distribution of the nearest neighbors over distances from the central Pr^{3+} ion. Specifically, in Ref. 13 a term $B_{22}O_{22}$, describing the influence of the orthorhombic distortion of the initial hexagonal symmetry, was introduced into the Hamiltonian (1) as an attempt to take account of the influence of the breakdown of local symmetry. It was found that such a term completely removes the degeneracy of the J multiplet and changes the wave functions of the levels. Figure 1b shows a diagram of the lower levels for the multiplet of a Pr^{3+} ion in a crystal field described by the Hamiltonian (1) containing the term $B_{22}O_{22}$ with $B_{22}=0.2B_{20}$. Evidently, the spectrum is substantially different from the initial spectrum for a hexagonal crystal field (Fig. 1a).

Introducing a term $B_{22}O_{22}$ into the Hamiltonian (1) can also take into account, to some extent, the change produced in the crystal field acting on a Pr ion by the substitution of one copper atom for at least one nickel atom in its environment (Fig. 4b). We calculated the magnetization curves for Pr^{3+} in such an altered crystal field and possessing the spectrum of lower levels which is presented in Fig. 1b. The result is shown in Fig. 6, which gives for comparison the magnetization curves calculated for ''pure'' $PrNi_5$. It is evident that the magnetization curve along the easy-magnetization axis

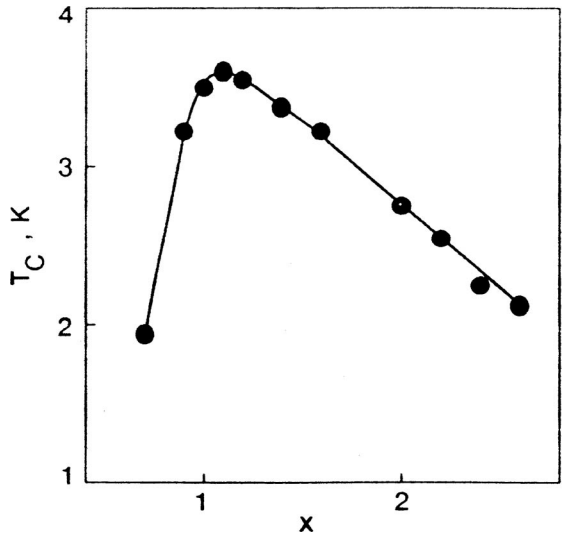

FIG. 5. Concentration dependence of the Curie point of the alloys $RNi_{5-x}Cu_x$.[10]

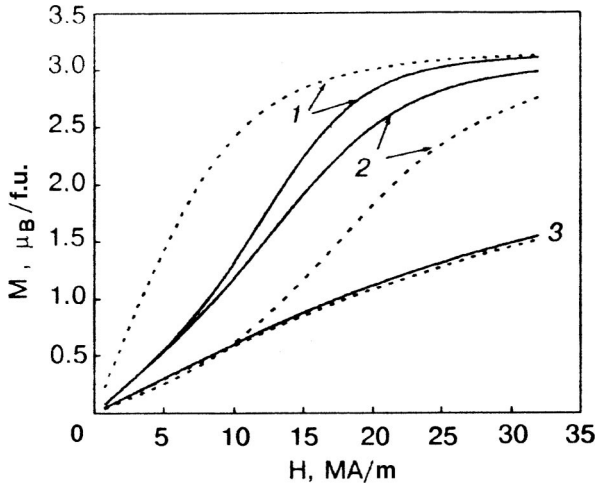

FIG. 6. Computed magnetization curves of the ion Pr^{3+} located in a hexagonal crystal field (sold lines) and in the same field but with orthorhombic distortion (broken lines) at $T=4.2$ K and magnetic field orientation along the b (*1*), a (*2*), and c (*3*) axes. The same crystal-field parameters were used for this calculation as in the calculation of the spectra presented in Fig. 1.

(EMA) (b axis) is substantially different: initially, it rises more steeply than for the binary compound $PrNi_5$ ($B_{22}=0$). Conversely, the magnetization along the a axis became more difficult, and a substantial difference between the magnetic moments with magnetization along the b and a axes remains right up to the field 40 T. The magnetization curves along the hard axis c for the two cases studied are virtually identical. Thus, the influence of the term $B_{22}O_{22}$ in the Hamiltonian (1) on the magnetization curves qualitatively correspond to the appearance of uniaxial anisotropy with the EMA lying in the basal plane. Irkhin *et al.* predicted this result theoretically back in 1980.[14]

The increase in magnetic susceptibility in pseudobinary alloys $Pr(Ni, Cu)_5$ in the presence of an exchange interaction also results in the appearance of ferromagnetic order in them. Apparently, a mechanism in which the appearance of a magnetic moment on some Pr^{3+} ions intensifies the exchange reaction and the latter, in turn, stimulates a further increase of the magnetization (the so-called bootstrap process[15] which terminates in the establishment of ferromagnetic order), occurs here. Neutron diffraction analysis confirms the presence of ferromagnetic order in the pseudobinary alloys $Pr(Ni, Cu)_5$.[16] A spontaneous magnetic moment was found in the alloy $PrNi_{3.9}Cu_{1.1}$, equal to 0.5 μ_B/f.u. at 1.5 K, lying in the basal plane and localized on Pr ions. A moment arises in a magnetic field, reaching in $H=40$ T the value 3.15 μ_B/f.u.,[17] which is essentially identical to the magnetic moment of a free Pr^{3+} ion (3.2 μ_B).

3. CRYSTAL FIELD EFFECTS IN RNi_5-BASED PSEUDOBINARY SYSTEMS

The above-described manifestations of local crystal fields in $PrNi_5$-based solid solutions have suggested that the influence of local crystal fields (LCFs) can also be observed in pseudobinary systems with different R. Appreciable LCF effects should be observed in RNi_5-based systems with easy-plane anisotropy, since the anisotropy factor k_{66} is small and, against this background, the influence of LCFon the magnetic properties can be substantial. Figure 7 displays the concentration dependence of the spontaneous magnetic moment M_s measured at 4.2 K for single crystals of the pseudobinary alloys $RNi_{5-x}Cu_x$.[18] It is evident that M_s for compounds with R=Tb, Dy, and Ho decreases quite rapidly with increasing x, while in alloys with Er it remains virtually unchanged and even increases in alloys with Gd. The LCF model discussed above easily explains this result. Indeed, the Gd ions possess zero orbital angular momentum and do not interact with the crystal field, so that the LCF in pseudobinary alloys with Gd have no effect on M_s. The small increase in M_s occurring when copper is substituted for nickel is due to a decrease in the contribution of the $3d$ subsystem to the spontaneous magnetization (the magnetic moments of the Ni and Gd sublattices are antiparallel to one another). Against the background of strong uniaxial anisotropy of the compounds $ErNi_{5-x}Cu_x$, LCFs likewise have no great effect on the magnetic moments of the Er ions, and M_s in these alloys are virtually independent of x. Alloys with Tb, Dy, and Ho possess easy-plane anisotropy. The local uniaxial anisotropy due to the LCFs predominates over the weak six-fold anisotropy in the basal plane and fixes the magnetic moments of the rare-earth ions in random directions, resulting in a breakdown of the collinear magnetic structure. This is the reason for the sharp drop of the curves $M_s(x)$ in alloys with Tb, Dy, and Ho. Results similar to those described above were obtained by doping $TbNi_5$ compounds with aluminum.[19] The minimum value of M_s in the system $TbNi_{5-x}Cu_x$ can be estimated assuming that the magnetic moments of all Pr^{3+} ions are fixed in a disordered manner by the local uniaxial anisotropy along the a axes. The value so obtained for Tb_{cal} is presented in Fig. 7. It agrees acceptably with the minimum experimental value obtained for M_s in the system $RNi_{5-x}Cu_x$.

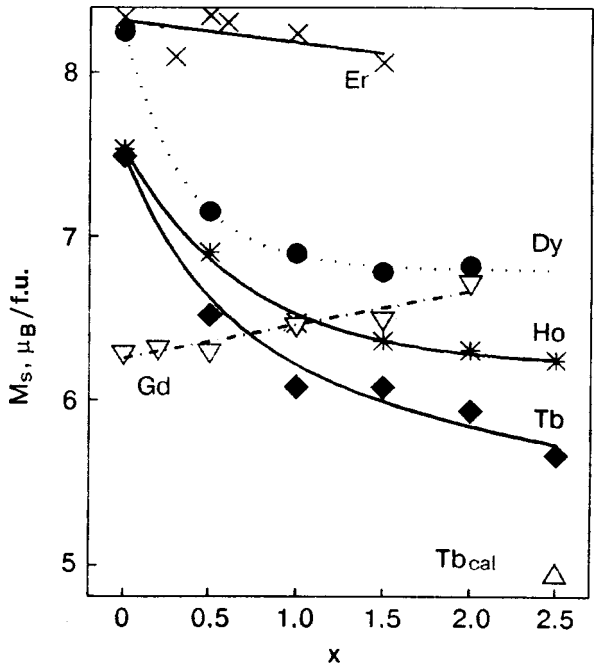

FIG. 7. Concentration dependence of the spontaneous magnetic moment, measured at 4.2 K for the alloys $RNi_{5-x}Cu_x$ with R indicated on the curve; Tb_{cal} is the computed minimum value of M_s for the alloys $TbNi_{5-x}Cu_x$ (see text).[18]

Another manifestation of LCFs in pseudobinary alloys of the type $RNi_{5-x}Cu_x$ with easy-plane anisotropy is the appearance of a quite strong anisotropy in the basal plane.[19] Figures 8 and 9 display magnetization curves for alloys with R=Tb along the a, b, and c axes. The magnetization curves along the c axis are essentially identical for alloys with $x=0$ and 1. For $x=0$ the curves along the a and b axes are essentially identical, i.e. the anisotropy in the basal plane for $TbNi_5$ is small with the EMA along the a axis; this agrees with previous results.[20,21] However, substantial anisotropy appears in the basal plane in Cu- and Al-substituted alloys. In the former alloys the easy magnetization axis is still the a axis, while in the latter the b axis becomes the EMA. This difference is probably due to the different preferences for copper and aluminum atoms in occupying crystallographic positions. Indeed, neutron diffraction data[22] show that the Al atoms occupy predominantly $3g$ sites in $LaNi_{5-x}Al_x$ compounds with $x\leqslant 1$. Conversely, Cu atoms in $PrNi_4Cu$ preferably occupy $2c$ position, as shown by neutron diffraction in Ref. 16.

Finally, we note one other fact which we believe is due to LCFs in the pseudobinary alloys $TbNi_{5-x}M_x$. Ordinarily,

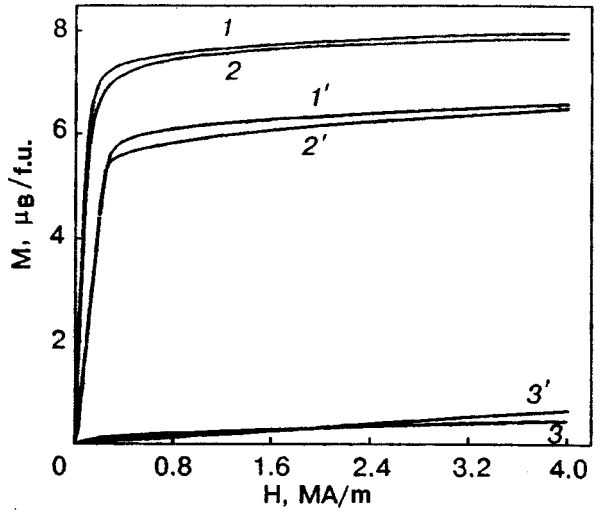

FIG. 8. Magnetization curves at 4.2 K for the single crystals of the alloys $TbNi_5$ (*1, 2, 3*) and $TbNi_4Cu$ (*1′,2′,3′*) along the *a* (*1, 1′*), *b* (*2, 2′*), and *c* (*3, 3′*) axes.[19]

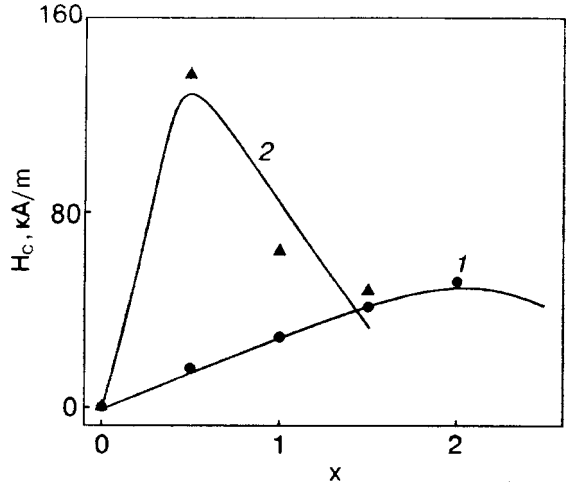

FIG. 10. Concentration dependence of the coercive force measured at 4.2 K along the easy axis of magnetization in $TbNi_{5-x}Cu_x$ (*1*) and $TbNi_{5-x}Al_x$ (*2*).[19]

a high coercive force H_c was observed in them at 4.2 K in magnetization curves along the *a* and *b* axes.[19] The function $H_c(x)$ is shown in Fig. 10 for the alloys $TbNi_{5-x}Cu_x$ and $TbNi_{5-x}Al_x$. The value of H_c reaches a maximum at $x=2$ for Cu-substituted alloys, while the maximum value of H_c for Al-substituted alloys was observed at $x=0.5$. The maximum value of H_c in the latter alloys is 2.6 times greater than in the former alloys.

According to the first calculations.[23] in the rare-earth metals Tb and Dy, which possess easy-plane anisotropy, the domain walls are very narrow. It was predicted that appreciable internal pinning of domain walls, which is due to the discreteness of the crystal lattice, is present. It can be assumed that narrow domain walls also occur in $TbNi_5$. But, we have not observed an appreciable coercive force in this compound (at least at 4.2 K). This can be explained by the negligible energy of the six-fold anisotropy in the basal plane. The situation changes in pseudobinary alloys, where the Tb ions possess strong chaotic local uniaxial anisotropy, as discussed above. The pinning of narrow domain walls on nonuniformities of the anisotropy energy in the basal plane could be the reason for the appearance of a high coercive force in the pseudobinary alloys $TbNi_{5-x}Cu_x$. This mechanism occurs in many pseudobinary rare-earth compounds (see, for example, Ref. 24).

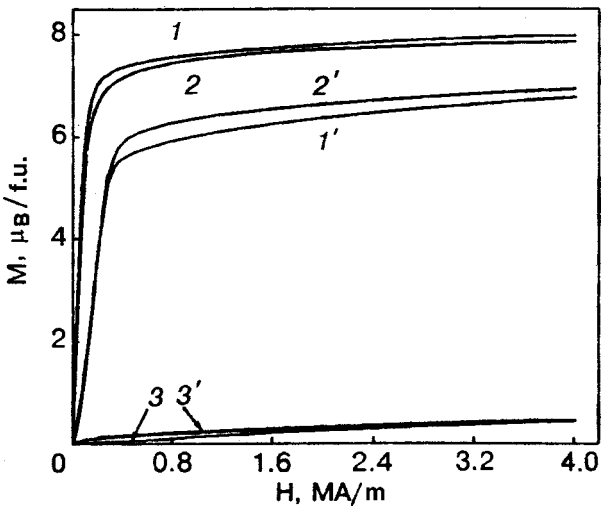

FIG. 9. Magnetization curves at 4.2 K for single crystals of the alloys $TbNi_5$ (*1, 2, 3*) and $TbNi_4Al$ (*1′,2′,3′*) along the *a* (*1, 1′*), *b* (*2, 2′*), and *c* (*3, 3′*) axes.[19]

This work was supported by the Russian Foundation for Fundamental Research and the government of the Sverdlovsk oblast', project 01-02-96420.

*E-mail: ermolenko@imp.uran.ru

[1] W. E. Wallace, S. G. Sankar, and V. U. S. Rao, "Crystal field effects in rare-earth intermetallic compounds" in *Structure and Bonding*, edited by J. D. Dunitz *et al.*, Springer-Verlag, New York (1977), Vol. 33, p. 1.
[2] K. W. H. Stevens, Proc. Phys. Soc. London, Sect. A **A65**, 209 (1952).
[3] M. T. Hutchings, "Point charge calculations of energy levels of magnetic ions in crystalline electric fields" in *Solid State Physics*, Academic Press, New York (1964), Vol. 16, p. 227.
[4] K. H. J. Bushow, Rep. Prog. Phys. **40**, 1179 (1977).
[5] K. Andres, P. H. Schmidt, and S. Darack, AIP Proc. **24**, 238 (1975).
[6] K. Andres, S. Darack, and H. R. Ott, Phys. Rev. B **B19**, 5475 (1979).
[7] P. A. Alekseev, A. Andreeff, H. Griessmann, L. P. Koun, B. Lippold, W. Matz, I. P. Sadikov, O. D. Chistyakov, I. A. Markova, and E. M. Savitskii, Phys. Status Solidi B **B97**, 87 (1980).
[8] E. A. Goremychkin, N. B. Kol'chugina, É Myule, M. Popesku, A. L. Saling, S. Saling, and O. D. Chistyakov, Fiz. Tverd. Tela (Leningrad) **28**, 3642 (1986) [Sov. Phys. Solid State **28**, 2052 (1986)].
[9] A. G. Kuchin, A. S. Ermolenko, V. I. Khrabrov, and G. M. Makarova, Phys. Status Solidi B **B197**, 447 (1996).
[10] A. G. Kuchin, A. S. Ermolenko, V. I. Khrabrov, and G. M. Makarova, Fiz. Met. Metalloved. **81**, No. 2, 54 (1996).
[11] A. G. Kuchin, A. S. Ermolenko, V. I. Khrabrov, and G. M. Makarova, J. Magn. Magn. Mater. **81**, No. 2, 54 (1996).
[12] P. A. Alekseev, V. N. Lazukov, V. G. Orlov, I. P. Sadikov, V. I. Nazhankovskii, J.-B. Suck, and H. Schmidt, J. Magn. Magn. Mater. **149–144**, 861 (1995).
[13] P. A. Alekseev, Ĭ. B. Zuk, S. N. Ishamev, V. N. Lazukov, V. G. Orlov, I. P. Sadikov, and M. N. Khlopkin, Zh. Éksp. Teor. Fiz. **99**, 1369 (1991) [Sov. Phys. JETP **72**, 765 (1991)].
[14] Yu. P. Irkhin, E. I. Zabolotskii, and E. V. Rozenfel'd, Fiz. Met. Metalloved. **49**, 1216 (1980).
[15] Y.-L. Wang and B. R. Cooper, Phys. Rev. **185**, 696 (1969).
[16] A. Pirogov, R. Shneider, A. Teplykh, A. Ermolenko, and A. Kuchin, Physica B **B276–278**, 580 (2000).
[17] A. S. Ermolenko, A. G. Kuchin, A. N. Pirogov, N. V. Muchnikov, V. I.

Khrabov, R. Schneider, and T. Goto, in *Proceedings of the Moscow International Symposium on Magnetism, Moscow 1999*, Part 2, p. 332.
[18] A. S. Ermolenko, in *Proceedings of the 8th European Conference on Magnetic Materials and Applications*, *Material Science Forum 2001*, p. 29, 373.
[19] A. G. Kuchin, A. S. Ermolenko, V. I. Khrabrov, N. I. Kourov, G. M. Makarova, E. V. Belozerov, T. P. Lapina, and Yu. A. Kulikov, J. Magn. Magn. Mater. **238**, 29 (2002).
[20] B. Barbara, D. Gignoux, D. Givord, F. Givord, and R. Lemaire, Int. J. Magn. **4**, 77 (1973).
[21] D. Gignoux, A. Nait-Saada, and R. Perrier de la Bathie, J. Phys. **40(C5)**, 188 (1979).
[22] A. Percheron-Guegan, C. Lartique, J. C. Achard, P. Germi, and F. Tasset, J. Less-Common Met. **74**, (1980).
[23] T. Egami and C. D. Graham, Jr., J. Appl. Phys. **42**, 1299 (1971).
[24] A. S. Ermolenko, A. V. Korolev, and A. F. Rozhda, Fiz. Met. Metalloved. **42**, 518 (1976).

Translated by M. E. Alferieff

Magnetic field induced phase transition in $KEr(MoO_4)_2$. Vibronic model

A. A. Loginov[a)]

B. Verkin Institute for Low Temperature Physics and Engineering, National Academy of Sciences of Ukraine, pr. Lenina 47, 61103 Kharkov, Ukraine

(Submitted February 22, 2002; revised April 3, 2002)
Fiz. Nizk. Temp. **28**, 1056–1064 (October 2002)

A vibronic model with Kramers magnetic ions is investigated in a parameter region that does not admit phase transitions on changes of the temperature T in the absence of magnetic field H. The H–T ($\theta=0$) and θ–H ($T=\text{const}$) phase diagrams (the angle θ specifies the orientation of the field relative to the symmetry axis of the crystal) are constructed in the mean field approximation. A comparison is made with the experimentally obtained phase diagrams of the $KEr(MoO_4)_2$ crystal. © *2002 American Institute of Physics.* [DOI: 10.1063/1.1521295]

1. INTRODUCTION

Double alkali–rare-earth molybdates (DRMs) are layered crystals containing magnetic ions of a (quasi) Jahn–Teller type. Therefore at low temperatures they exhibit various effects due to the interaction of the electronic and lattice subsystems. In particular, some DRMs have structural phase transitions on changes in temperature,[1,2] and these are interpreted as a cooperative Jahn–Teller effect.[3–5]

Some crystals of this class do not undergo a phase transition on changes in temperature, but a phase transition can be induced in a magnetic field[6–8] by making use of the strong anisotropy of the g factor of the rare-earth (RE) ions. For this the magnetic field H is applied in the direction of the small g factor, and at a sufficiently high field H the crystal structure can suffer an instability that tends to increase the g factor in the field direction. These compounds also have other properties of significant interest.[8–10]

The most completely studied magnetic field induced phase transition is that in potassium–erbium molybdate, for which the H–T and θ–H diagrams (T is the temperature and θ is the angle specifying the field direction) have been constructed from experimental data.[11] Other properties of this crystal have also been investigated,[9–16] so the amount of information available about it is comparatively large. Therefore $KEr(MoO_4)_2$ is a model object for theoretical analysis of the observed effects.

Although there is some understanding of the general causes of the phase transition observed in $KEr(MoO_4)_2$, the specific mechanism of the transition and some of its features remain unclear. For example, what are the lattice displacements and what interactions play the main role in the first-order phase transition and determine its temperature? Is this phase transition accompanied by symmetry breaking? What accounts for the sharp decrease of the critical temperature of the phase transition and the decrease of the transition field at a small deviation of the magnetic field direction from the symmetry axis of the crystal? These and many other questions are in need of clarification.

There are various existing models describing the phase transitions in (pseudo) Jahn–Teller crystals, but each of them can be used to examine only individual parameter regions specific to a particular compound, experimental conditions, etc.

In this paper we investigate the possibility of explaining the features of the phase transition in $KEr(MoO_4)_2$ and its phase diagrams observed when the magnetic field direction deviates from the symmetry axis of the crystal (the orientational properties of the phase transition) with the aid of a simple model that takes into account the polaronic and vibronic mechanisms of interaction of the electronic and lattice subsystems (by polaronic we mean the part of the interaction that commutes with the crystalline field, i.e., the part which is diagonal in the basis of eigenstates of this field). The model takes into account the low positional symmetry of the RE ions—the real geometry of the g tensors of the ground and excited Kramers doublets of these ions at an arbitrary orientation of the magnetic field parallel to the layers (i.e., to the cleavage planes) of the crystal. We consider a region of model parameters in which the absence of a phase transition at $H=0$ is due to the rather large energy between the ground and excited doublets in the crystalline field in comparison with the parameters of the electron–lattice interaction. The part of the Zeeman energy that does not commute with the crystalline field is taken into account, and its value and influence on the properties of the phase transition in the investigated region of parameter values are estimated. Numerical calculations in the mean field approximation (MFA) are used. The model is based on well-known concepts (see, e.g., Refs. 3–5 and 17–19).

Previously an attempt was made to describe the phase transition in $KEr(MoO_4)_2$ in a model with an effective triple-well potential (besides the main minimum there were two metastable minima for librations of the oxygen tetrahedra) on the assumption that the rotations of the tetrahedra lead to rotation of the axis of the g tensor for the Er ion.[20,21] However, this model cannot account for the orientational features of the phase transition in this compound. In Ref. 5 a model describing a system with a large vibronic interaction constant was used under a special condition of commutation of the Zeeman energy with the molecular field; this leads to a phase transition in the absence of field. The properties of the phase diagrams described in Ref. 5 do not correspond to those for potassium–erbium molybdate.

2. STATEMENT OF THE MODEL

Let us give some information about the $KEr(MoO_4)_2$ crystal and discuss the choice of parameters of the model considered. The layered rhombic crystal $KEr(MoO_4)_2$ has symmetry space group D_{2h}^{14}. The crystal lattice parameters along the *a*, *b*, and *c* axes are $a' \approx 5.063$ Å, $b' \approx 18.25$ Å, and $c' \approx 7.91$ Å, respectively. The $Er(MoO_4)_2^-$ layers are parallel to the *a* and *c* axes and alternate with K^+ layers in the *b* direction, with two neighboring layers of $Er(MoO_4)_2$ which lie a distance $b'/2$ apart and are taken into each other by a rotation of π about the *a* axis (with a shift of $a'/2$). The local symmetry of the Er ion is C_2 (about the *b* axis), and the crystalline field at this ion has monoclinic components in the *ac* plane. Therefore the axes of the *g* tensor of the magnetic ion in this plane do not coincide with the axes of the crystal, and two magnetic centers, symmetrically rotated in the neighboring $Er(MoO_4)_2$ layers, are seen in the EPR spectra. The distance between nearest Er ions along the *c* axis, which are connected by inversion symmetry, is equal to $c'/2 \approx 4$ Å.

The ionic ground term in $KEr(MoO_4)_2$ is split by the low-symmetry crystalline field into 8 Kramers doublets separated in energy by intervals of $\simeq$15, 32, 74, 185, 258, 317, and 324 cm^{-1}, the positions of which are practically the same at temperatures of 4.2 and 77 K.[14,22] it has been established from the EPR spectra[12,13] that the lower doublet has a highly anisotropic *g* factor with principal values of $\simeq$17 and 0.6; approximately the same values are found for the *g* factor of the first excited state. For the ground and excited doublets the axes of the *g* tensor in the *ac* plane are rotated by different angles relative to the axes of the crystal. For the ground doublet this deviation has not been successfully determined to sufficient accuracy, but according to the existing experimental data it should be in the range from $\pm 3°$ to $\pm 9°$ (the signs refer to the neighboring $Er(MoO_4)_2^-$ layers).[13,11] For the first excited doublet the rotation of the axes is quite clearly determined from the EPR spectra[13] for pure and impure $KEr(MoO_4)_2$ crystals and is equal to $\pm 56°$.

The first-order phase transition under discussion is obtained for a magnetic field direction along the *a* axis at temperatures below 5 K and magnetic fields up to 42 kOe (the position of the critical point is $T=5$ K, $H=41$ Oe). Here the value of the transition field *H* varies little with increasing temperature (in the interval 1.8–4.2 K it varies in the range $\simeq$38–41 kOe). An observation of the behavior of the phase transition when the magnetic field deviates from the *a* axis (in the *ac* plane) was made at $T=1.8$ K. The transition field decreases from $\simeq$37 kOe to $\simeq$30 kOe at a deviation of 4.5°, this being the critical value of the angle: the first-order transition is absent when the field deviates further from the *a* axis.

For theoretical analysis of the above-described properties of the phase transition in $KEr(MoO_4)_2$ we use a model with a Hamiltonian of the form[3–5,17–19]

$$\mathcal{H}=\mathcal{H}_e+\mathcal{H}_{\rm ph}+\mathcal{H}_{\rm int}, \tag{1}$$

where the subscripts *e*, ph, and int denote the Hamiltonians for the electronic excitations of the RE ions, the lattice vibrations, and their interaction, respectively. We assume that the direct interaction of the electronic excitations of the *f* shells of the RE ions can be neglected, and therefore

$$\mathcal{H}_e=\sum \mathcal{H}_f, \tag{2}$$

where $\mathcal{H}_f$ is the Hamiltonian of the electronic excitations of the unfilled shell of the RE ion found at site *f* of the ideal lattice in the effective field created by all the other ions in the ground state in an external magnetic field *H*. The energy in $\mathcal{H}_f$ is measured from its ground state at $H=0$. The magnetic field lies in the *ac* plane and is directed at an angle θ to the *a* axis.

For a qualitative description of the properties of the phase transition it is sufficient to consider only the nearest excited doublet, which lies at a distance of 21 K from the ground state, since it already has the necessary large *g* factor in the field direction, and its component can give a substantial contribution to the free energy of the system in the range of temperatures and magnetic fields investigated (the contribution of other states can be partially taken into account by the choice of constants of the model). We denote the ground and excited Kramers doublets formed by the crystalline field by the indices $\Gamma=0,1$ and their components by the indices $m=1,-1$.

Then in terms of the Hubbard transition operators[14] $B_f(\Gamma',m';\Gamma,m)$ the Hamiltonian $\mathcal{H}_f$ will have the form (the summation in Eq. (5) and below is over those indices which are absent in one of the parts of the equation; exceptions to this rule will be indicated explicitly)

$$H_f=\sum E_f(\Gamma',m';\Gamma,m)B_f(\Gamma',m';\Gamma,m), \tag{5}$$

$$E_f(0,m;0,m)=-mg_0(\theta_0-\theta)H/2, \tag{6}$$

$$E_f(1,m;1,m)=E_0-mg_1(\theta_1-\theta)H/2, \tag{7}$$

$$E_f(0,m;1,m)=mpH\cos\alpha_+, \tag{8}$$

$$E_f(0,m;1,-m)=-pH\sin\alpha_+, \tag{9}$$

where E_0 is the energy which in the undeformed lattice separates the ground doublet from the excited doublet at $H=0$; $g_0(\varphi)$ and $g_1(\varphi)$ are the *g* factors in the field direction for the ground and excited doublets, respectively:

$$g_j(\varphi)=[g_j^2+(G_j^2-g_j^2)\sin^2\varphi]^{1/2}, \quad j=0,1. \tag{10}$$

Here G_j and g_j are the maximum and minimum values of the *g* factor, and θ_j ($j=0,1$) are the angles of rotation of the axes of the *g* tensor relative to the crystallographic axes for the ground (0) and excited (1) doublets. The angle $\alpha_\pm$ is determined by the equations

$$\alpha_\pm=\frac{x_1+x_0}{2}+r_\pm, \tag{11}$$

$$x_j=\arccos\left[\frac{1}{g_j(\theta_j-\theta)}G_j\sin(\theta_j-\theta)\right], \quad j=0,1. \tag{12}$$

The value of *p* has the form

$$p=P\sin[(\theta_0+\theta_1)/2-\theta]; \tag{13}$$

the coefficient *P* and the phases $r_\pm$ in (11) are parameters characterizing the properties of the states of the doublets. All of the formulas given pertain to one sublattice; for the sec-

ond sublattice it is necessary to replace θ by $-\theta$ in them (this is a consequence of the C_2 symmetry about the a axis).

The Zeeman energy matrix elements (8), (9) coupling the different doublets are obtained under the following assumptions. Since the maximum values of the g factors in the doublets are close to the theoretical limit ($g=18$ for $^4I_{15/2}$)it can be assumed that the states realized when an infinitesimal field is applied along the directions of the maximum values of the g factor are close to the states

$$|0,J,M\rangle, \quad |1,J,M\rangle, \quad M=\pm J \tag{14}$$

having the maximum possible (for the given quantum number J) angular momentum projections M on the corresponding directions of the principal axes in the ground and excited doublets. The rotation between these axes in the model considered can amount to $\simeq 45$–$65°$. Since the quantum numbers $\pm J$ are 15 units apart and the Zeeman energy operator couples only the closest of their values (for the same directions of the quantization axes), it can be expected that only the matrix elements between states with projections making acute angles with each other can have an appreciable value. Therefore, those are the only elements (assuming they are real) that remain in the basis of ''states with maximum projections'' defined above Eq. (14). In writing the matrix elements it is important to take into account the symmetry with respect to time inversion. The formulas written above were obtained after going to a basis in which the Zeeman energy is diagonal within each doublet. The qualitative arguments as to the values of the matrix elements are confirmed by a calculation in a basis obtained by symmetric orthogonalization of the states (14). Here the matrix elements that have been dropped are one to two orders of magnitude smaller than the rest, which are also quite small. If in the latter we drop terms of the order of the matrix elements that have been dropped, we can obtain the following estimate for the parameters P and α_+:

$$P=9\cos^{14}[(\theta_1-\theta_0)/2]\sin^2[(\theta_1-\theta_0)/2], \quad \alpha_+=0. \tag{15}$$

We emphasize that these expressions are valid only for angles between the principal axes of the doublets in the interval 45–65°. Although this estimate is somewhat too low, we shall use these values in the subsequent calculations.

The coarsest part of the adiabatic potential of the lattice vibrations can be written as the dependence of the total energy of the system (without the kinetic energy of the nuclei) on the displacements of the ions from the sites of the undeformed lattice, $u\equiv(\ldots u_j \ldots)$. This energy is calculated for electronic states differing from the ground state at $u=0$, $H=0$ only by the shifts u_j and has the form

$$H_p=\sum\left(\frac{1}{4}A_s q_{gs}^4+\frac{1}{2}K_s q_{gs}^2\right)-\frac{1}{2}\sum{}' J_{gs,g's'}q_{gs}q_{g's'}, \tag{16}$$

where the prime on the second summation sign means to omit terms with $(g,s)=(g',s')$, and s is the index of the generalized coordinate q describing the displacements of the ions of the gth unit cell of the crystal. In Eq. (16) the anharmonicity ($A>0$) is taken into account in the simplest form in order to limit too large displacements, which are possible in the case of small elastic constants K and J (for simplicity the indices have been omitted). The quadratic form in (16) should be positive definite. We are not taking the kinetic energy of the lattice vibrations into account, since the energy of the optical lattice vibrations under consideration lie quite high in comparison with the temperature.

The finer dependence of the adiabatic potential of the lattice vibrations on the displacements, which lead to hybridization of the electronic states of the RE ions of the ideal lattice, and also the induction of displacements by the electronic excitations (the ''polaron'' effect) are taken into account in the interaction Hamiltonian $\mathcal{H}_{\rm int}=\mathcal{H}_{\rm int1}+\mathcal{H}_{\rm int2}$ in an approximation linear in the displacements, where

$$\mathcal{H}_{\rm int1}=-\sum V_{f,gs}q_{gs}B_f(1,m;1,m) \tag{17}$$

is the part of the interaction which is diagonal in the basis (Γ,m) (the polaronic part), and

$$\mathcal{H}_{\rm int2}=\sum W_{f,gs}(m,m')q_{gs}B_f(1,m';0,m)+\text{H.c.}$$

$$W_{f,gs}(m;m)=W_{f,gs}\cos\alpha_-, \tag{18}$$

$$W_{f,gs}(m;-m)=-mW_{f,gs}\sin\alpha_-,$$

is the off-diagonal (vibronic) part of the interaction. Here $V\ldots$ and $W\ldots$ are coefficients which are nonzero for the nearest-neighbor environment of the RE ion, and α_- is defined in Eq. (11). In deriving these expressions we have taken into account only the symmetry with respect to time inversion, and for simplicity the coefficients have been taken as real.

3. PHASE DIAGRAMS

To obtain the phase diagrams of the phase transitions under study we calculate the nonequilibrium free energy in the mean field approximation (MFA). We have two comments about this. It is known that if the vibronic interaction is not taken into account, one can exactly eliminate the polaronic term from this model with the aid of a unitary transformation. In that case an effective intersite interaction of the electronic excitations of the RE ions appears, and also the excitation energy E_0 is reduced to a field-independent constant.[3,4,17] Then the intersite interactions are taken into account using mean field theory. If the MFA is used immediately (without doing the unitary transformation), then one can arrive at the same results except for corrections to E_0. However, the experimentally determined value of the excitation energy Δ already contains this correction, and therefore in the MFA one can simply replace E_0 by Δ. On the other hand, when the vibronic interaction is taken into account (it cannot be eliminated exactly like the polaronic interaction) it is natural to take both interactions into account in the same MFA, and for simplicity that is what we have done in this paper. Here we limit consideration to the class of two-sublattice structures of the order parameters (the sublattices are layers with oppositely rotated axes of the g tensor).

Our second general remark concerns the direction of deviation of the axes of the g tensor (in the ac plane) from the symmetry axis of the crystal for the ground and excited states of a fixed ion. From the existing experimental data it is impossible to determine whether they are the same. It is

clear, however, that if these directions are chosen opposite, then in one of the sublattices when the field deviates from the a axis the crossover field of the lower components of the doublets under study should decrease substantially, and that may lead to the decrease of the phase transition field which was observed in Ref. 11. The calculations confirm the advantage of this choice for better agreement of the phase diagrams with the experimental characteristics. Therefore we shall from now on assume that $\theta_0 \geqslant 0$ and $\theta_1 < 0$.

We consider three versions of the model.

1. Since the nearest-neighbor environment of the RE ion consists of rigid oxygen tetrahedra of the molybdenum complex,[25] it can be assumed that their librations have the most effective influence on the monoclinic components of the local crystalline field at the RE ion, and, hence, on the rotation of the g tensors relative to the tetragonal axes of the crystal.

Introducing the average values of the corresponding generalized coordinates for each sublattice (u_1, u_2), we write the free energy in the MFA in the form (we assume that the electrons of the RE ions interact with the displacements only of their own sublattice)

$$F = \frac{A}{4}(u_1^4 + u_2^4) + \frac{K}{2}(u_1^2 + u_2^2) - K' u_1 u_2 - T \ln(\Sigma_1 \Sigma_2),$$

$$\Sigma_s = \sum \exp[-E_{sp}(H, \theta, u_1, u_2)/T], \tag{19}$$

$$s = 1,2; \quad p = 1,2,3,4.$$

Here Σ_s is the partition function of sublattice s, K and K' are the intra- and intersublattice elastic constants, which are determined by the parameters in (16), and p is the number of the energy level $E_{sp}(H, \theta, u_1, u_2) \equiv E_{sp}$ of the mean field Hamiltonian $\mathcal{H}_{\mathrm{av},s}$

$$\mathcal{H}_{\mathrm{av},s} \sum M_s(\Gamma', m'; \Gamma, m) B_s(\Gamma', m'; \Gamma, m) \tag{20}$$

where $B_s(\ldots)$ is the transition operator for an arbitrary fixed RE ion in sublattice s, and the matrix elements $M_s(\ldots)$ in the notation of Eqs. (6)–(9), (11), and (18) and with E_0 replaced by Δ are

$$\begin{aligned} M_1(0,m;0,m) &= -mg_0(\theta_0 - \theta)H/2, \\ M_1(1,m;1,m) &= \Delta - Vu_1 - mg_1(\theta_1 - \theta)H/2, \\ M_1(0,m;1,m) &= Wu_1 + mpH\cos\alpha_+, \\ M_1(0,m;1,-m) &= mWu_1 - pH\sin\alpha_+. \end{aligned} \tag{21}$$

The polaronic V and vibronic W coupling constants are obtained in the usual way for the MFA from the corresponding parameters in (16)–(18). For the second sublattice the index "1" should be replaced by "2" and θ by $-\theta$. The fourth-degree characteristic equation can be solved numerically. Changing to the dimensionless displacements x $(\lesssim 1)$, we obtain the natural parameters (in kelvins) which determine the form of the phase diagram:

$$\begin{aligned} &x = (K/V)u, \quad a = AV^4/K^4, \quad \upsilon = V^2/K, \quad w = WV/K, \\ &\upsilon' = K'V/K. \end{aligned} \tag{22}$$

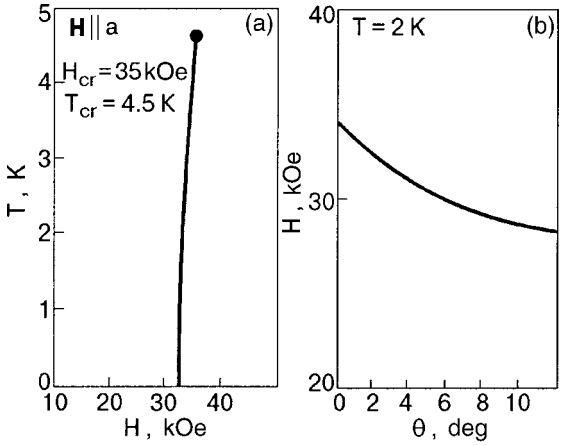

FIG. 1. Lines of equilibrium at a first-order phase transition for the first version of the model. The parameters are given in Eqs. (23) and (24a). There is no critical point on the θ–H diagram (b).

The parameters having the same values in all versions of the calculations are

$$\begin{aligned} &g_0 = g_1 = 0.6; \quad G_0 = G_1 = 17, \quad \Delta = 21\mathcal{K}, \\ &\theta_1 = -56°, \quad \theta_0 = 5°, \ 9°. \end{aligned} \tag{23}$$

The parameters (22) for the first version are chosen as

$$a = 0, \quad \upsilon = 10, \quad w = 4, \quad \upsilon' = 2(\theta_0 = 9°, r_- = 6°); \tag{24a}$$

$$a = 1, \quad \upsilon = w = 4, \quad \upsilon' = 2(\theta_0 = 5°, r_- = 11°). \tag{24b}$$

The corresponding phase diagrams are presented in Figs. 1 and 2.

2. In the second version of the model we consider one active vibrational mode, e.g., the displacements of the K^+ ion in the direction of the b axis. These displacements lead to opposite signs in the polaronic terms of different sublattices, i.e., they break the equivalence of the sublattices. In this case one should set $u_2 = -u_1$ and $K' = 0$ in Eqs. (19)–(21). The calculation is done for the following values of the parameters in (22):

$$a = 0, \quad \upsilon = 15, \quad w = 8, \quad \upsilon' = 0(\theta_0 = 5°, r_- = 11°). \tag{25}$$

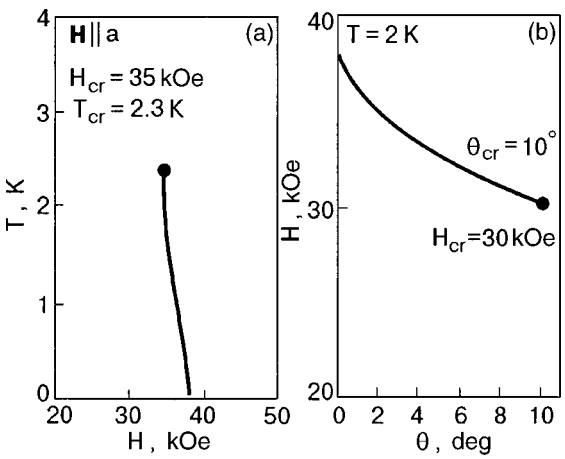

FIG. 2. Lines of equilibrium at the first-order phase transition for the first version of the model. The parameters are given in Eqs. (23) and (24b).

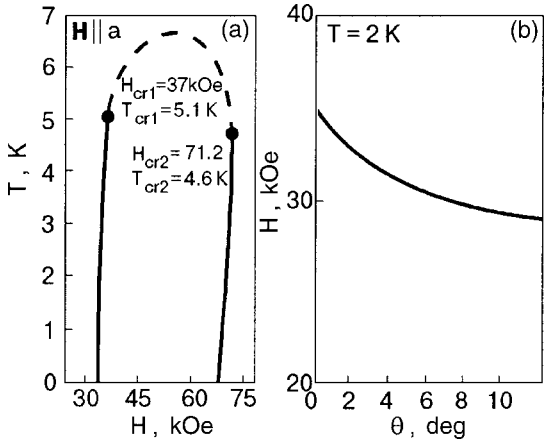

FIG. 3. Lines of equilibrium at the first-order phase transition and the line of second-order phase transitions (dashed line) for the second version of the model. The parameters are given in Eqs. (23) and (25). There is no critical point on the θ–H diagram (b); the field of the second transition is high-lying and increases with increasing θ.

The corresponding phase diagram is presented in Fig. 3. Here a tricritical point appears, since the phase transition occurs with symmetry breaking.

3. The third version corresponds to the participation of two modes in the phase transition, one of which leads only to a polaronic type of interaction with electronic excitations, while the second leads only to a vibronic displacement. In the elastic part of the Hamiltonian we neglect their interaction. In this case the expression for the free energy (19) becomes

$$F=(A_1u_1^4+A_2u_4^2)/4+(K_1u_1^2+K_2u_2^2)/2-T\ln(\Sigma_1\Sigma_2), \tag{26}$$

and Wu_1 in (21) must be replaced by Wu_2 (in the second sublattice θ is replaced by $-\theta$). The parameters analogous to (22) are chosen as ($x_1=u_1K_1/V$, $x_2=u_2K_2/W$):

$$a_1=A_1V^4/K_1^4=3, \quad a_2=4,$$
$$\upsilon=V^2/K_1=10, \quad \mathfrak{w}=W^2/K_2=4. \tag{27}$$

The phase diagram for this case is shown in Fig. 4.

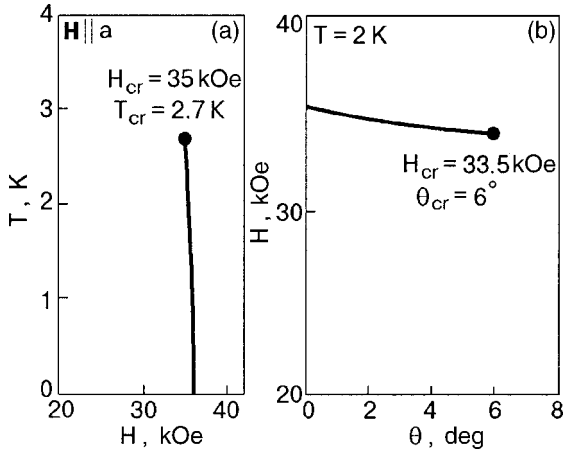

FIG. 4. Lines of equilibrium at the first-order phase transition for the third version of the model. The parameters are given in Eqs. (23) and (27). $\theta_0=5°$, $r_-=11°$.

3. DISCUSSION OF THE RESULTS

The phase diagrams presented in Figs. 1–4 correspond to a choice of parameters for which a certain similarity with the diagrams constructed in Ref. 11 could be achieved in the framework of the approximations used. The calculated phase diagrams do not reflect the whole diversity of possible forms of the phase transition diagrams, as that was not our the purpose of this study.

In all of the models considered a first-order phase transition is obtained, and there is a characteristic weak temperature dependence of the phase transition field. One also observes a decrease of the transition field when its direction deviates from the symmetry axis of the crystal. However, the most pronounced feature—the vanishing of the first-order phase transition at a small deviation of the field from the a axis at a temperature substantially below T_{cr} (the critical temperature for the symmetric field direction)—is manifested very weakly and only in some versions of the calculation, when the value of the vibronic interaction parameter can be chosen large enough. The possibility of doing this is limited by the condition that the other properties of the phase transition be preserved. For example, violation of the inequalities

$$\upsilon=2w^2/\Delta, \quad w<\Delta/2 \tag{28}$$

leads to instability of the lattice in the absence of field (the first inequality pertains to the first and second versions of the model, and the second inequality to the third version).

In addition, an increase of w corresponds to a decrease of the transition field, making it necessary to decrease the parameter υ. But then one cannot obtain a high enough temperature T_{cr}, which is determined mainly by the latter parameter.

The fact that increasing w leads to a decrease of the transition field and ultimately to a continuous transformation of the ground state to a state with a larger g factor explains the mechanism for the appearance of a critical current on the phase diagram when the magnetic field deviates from the symmetry axis a of the crystal. The point is that the vibronic interaction is determined by the independent parameters w and r_-, which determine the two matrix elements coupling the different components of the doublets, the sum of their squares being equal to w. A change in orientation of the field leads to a decrease of one of them and an increase of the other. If in the analysis of these matrix elements one uses arguments similar to those which were used in estimating the matrix elements of the Zeeman energy, then an increase in the coupling of the two lower components of the doublets should be expected upon a deviation of the field. From the form of the coefficients of the characteristic equation, however, it follows that the term containing the angular dependence of the matrix elements is proportional to the product of the Zeeman splitting in the field direction (calculated without the vibronic coupling taken into account). This reduces substantially the influence of the orientation of the field on the properties of the phase transition because of the small splitting on the ground doublet. The parameter r_- is chosen such that the largest orientation effect is achieved. This can be done rather simply thanks to the chosen form of the Hamiltonian representation. Of the different versions of the model

studied, the third apparently needs more careful study. In that version there is a possibility of explaining the observed feature by a competition between two independent mechanisms of rearrangement of the system.

Let us conclude with a discussion of the two most important facts that must be kept in mind during further optimization of the choice of the region of parameter values.

In the IR absorption spectra of $KEr(MoO_4)_2$ in Ref. 9 ($T \simeq 2$ and 4 K) a sharp break was observed in the field dependence of the g factor for excitation of the doublet in the direction of the a axis. In a field exceeding 30 kOe (i.e., still substantially below the phase transition field) the g factor was found to have practically the value attained in EPR. It can therefore be assumed that the anomalies observed in the IR absorption are due to dynamic effects and are no longer substantial in the phase transition region. Consequently, one can use the EPR data for thermally excited ions, which are manifested in the thermodynamics. However, this situation requires careful analysis and is of fundamental interest from the standpoint of choosing the model parameters.

In potassium–erbium molybdate the positions of the energy levels of the ''actual'' excited excitations of the RE ions (without an external field) remain practically constant over a wide temperature interval.[14,22] This fact was not taken into account in our choice of model, but subsequent calculations have shown that the polaronic interaction leads to temperature dependence of the energy of electronic excitation at temperatures $T \gtrsim \Delta$. This dependence may be compensated to some degree by the choice of the vibronic constant, but this way of resolving the issue is inefficient. It is not ruled out that this simple fact may be a serious argument for choosing substantially different relationships of the model parameters—with small values of both the polaronic parameter and the crystalline field Δ. However, then it would be necessary to introduce new mechanisms of ''anharmonicity'' for suppressing the phase transition in the absence of field and ensuring an induced first-order transition. These could be either anharmonicity of the ''coarse'' part of the adiabatic potential or the inclusion of quadratic vibronic terms.

4. CONCLUSIONS

The vibronic model describing the structural phase transition has been put in a form that permits taking into account the real geometry of the g tensors of the ground and excited Kramers doublets and an arbitrary orientation of the external magnetic field. The model variants considered here take into account the absence of a phase transition in the system when no magnetic field is applied and correspond to the assumption that the main role in the formation of the doublets of the RE ions and the energy Δ separating them is played by the static crystalline field.

The main factor responsible for the presence of a magnetic field induced first-order phase transition and which determines its critical temperature in this model is an interaction of the polaronic type (that part of the electron–lattice interaction which commutes with the crystalline field). The vibronic coupling of the doublets lowers the phase transition field and, because of its dependence on the orientation of the magnetic field, can lead to the appearance of critical points on the phase diagram when the field deviates from the a axis of the crystal (the axis with the small g factor).

The examples considered give a characteristic weak temperature dependence of the phase transition field and a slight decrease in this temperature when the magnetic field field deviates from the a axis. However, the most important feature—the appearance of critical points at small angles of deviation at a temperature substantially below the critical—is manifested very weakly. Other versions of the model, with the polaronic and vibronic parts of the interaction determined by independent displacements (one such displacement could be a uniform strain), merit careful study in relation to this feature.

The estimates and numerical results have shown that in our chosen region of parameter values the part of the Zeeman energy that does not commute with the crystalline field has no substantial influence on the properties of the phase transitions and features of the phase diagrams.

Analysis of the present state of affairs shows that further advances in the explanation of the microscopic mechanism of the phenomena observed in $KEr(MoO_4)_2$ will require, first, a theoretical study of the anomalies observed[9] in the behavior of the g factor of the excited doublet and the temperature stability of the level of electronic excitation.[14,22] It could be very informative to continue the experimental studies of IR absorption[9] into the magnetic field region corresponding to the phase transition.

The author is grateful to V. I. Kut'ko for numerous helpful discussions on the topic examined in this paper, and to M. I. Kobets, A. G. Anders, and A. S. Chernyi for explaining many details of the experiment.

[a)]E-mail: loginov@ilt.kharkov.ua

[1] A. I. Zvyagin, T. S. Stetsenko, V. G. Yurko, and R. A. Vaĭshnoras, JETP Lett. **17**, 135 (1973).
[2] A. I. Zvyagin, S. D. El'chaninova, T. S. Stetsenko, L. N. Pelikh, and E. N. Khats'ko, Fiz. Nizk. Temp. **1**, 79 (1975) [Sov. J. Low Temp. Phys. **1**, 39 (1975)].
[3] G. A. Gehring and K. A. Gehring, Rep. Prog. Phys. **38**, 1 (1975).
[4] I. B. Bersuker and V. Z. Polinger, *Vibronic Interactions in Molecules and Crystals* [in Russian], Nauka, Moscow, (1983).
[5] M. D. Kaplan, Fiz. Tverd. Tela (Leningrad) **26** 89 (1984) [Sov. Phys. Solid State **26**, 51 (1984)].
[6] V. I. Kut'ko, V. A. Pashchenko, and M. I. Kobets, Fiz. Nizk. Temp. **19**, 1354 (1993) [Low Temp. Phys. **19**, 962 (1993)].
[7] E. N. Khats'ko, Yu. V. Pereverzev, M. I. Kobets, V. A. Pashchenko, and V. I. Kut'ko, Fiz. Nizk. Temp. **21**, 1061 (1995) [Low Temp. Phys. **21**, 816 (1995)].
[8] M. I. Kobets, Fiz. Nizk. Temp. **26**, 96 (2000) [Low Temp. Phys. **26**, 72 (2000)].
[9] V. I. Kut'ko, Yu. N. Kharchenko, N. M. Nesterenko, and A. A. Stepanov, Fiz. Nizk. Temp. **20**, 361 (1994) [Low Temp. Phys. **20**, 228 (1994)].
[10] V. I. Kut'ko and M. I. Kobets, Fiz. Nizk. Temp. **22**, 1447 (1996) [Low Temp. Phys. **22**, 1099 (1996)].
[11] V. I. Kut'ko, M. I. Kobets, V. A. Pashchenko, and E. N. Khats'ko, Fiz. Nizk. Temp. **21**, 441 (1995) [Low Temp. Phys. **21**, 345 (1995)].
[12] A. M. Pshisukha, A. S. Chernyi, and A. I. Zvyagin, Fiz. Nizk. Temp. **1**, 473 (1975) [Sov. J. Low Temp. Phys. **1**, 233 (1975)].
[13] A. M. Pshisukha, A.I. Zvyagin, and A. S. Chernyi, Fiz. Nizk. Temp. **2**, 339 (1976) [Sov. J. Low Temp. Phys. **2**, 170 (1976)].
[14] V. I. Kut'ko, Yu. N. Kharchenko, N. M. Nesterenko, and A. A. Gurskas, Fiz. Nizk. Temp. **22**, 785 (1996) [Low Temp. Phys. **22**, 603 (1996)].
[15] A. Orendacheva, M. Orendach, V. Bondarenko, A. G. Anders, J. Phys.: Condens. Matter **10**, 1125 (1998).

[16] G. A. Zvyagina and A. A. Zvyagin, Fiz. Nizk. Temp. **26**, 482 (2000) [Low Temp. Phys. **26**, 354 (2000)].
[17] A. S. Davydov, *Solid State Theory* [in Russian], Nauka, Moscow (1976).
[18] V. M. Agranovich, *Theory of Excitons* [in Russian], Nauka, Moscow (1968).
[19] A. K. Zvezdin, V. M. Matveev, A. A. Mukhin, and A. I. Popov, *Rare-Earth Ions in Magnetically Ordered Crystals* [in Russian], Nauka, Moscow (1985).
[20] Yu. V. Pereverzev, Fiz. Nizk. Temp. **22**, 289 (1996) [Low Temp. Phys. **22**, 226 (1996)].
[21] V. G. Borisenko, Ju. V. Pereverzev, and A. A. Loginov, Condens. Matter Phys. **1**, (1999).
[22] G. I. Frolova, L. E. Reznik, and I. E. Paukov, Fiz. Tverd. Tela (Leningrad) **23**, 2160 (1981) [Sov. Phys. Solid State **23**, 1262 (1981)].
[23] A. G. Anders, S. V. Volotskii, and O. É. Zubkov, Fiz. Nizk. Temp. **19**, 731 (1993) [Low Temp. Phys. **19**, 526 (1993)].
[24] J. Hubbard, Proc. Roy. Soc. A **285**, 542 (1965).
[25] R. F. Klevtsova and S. B. Borisov, Dokl. Akad. Nauk SSSR **177**, 1333 (1977).

Translated by Steve Torstveit

Magnetic phases in $La_{0.66}Ba_{0.34}MnO_3$: effects of temperature and elastic strains

A. B. Beznosov,* V. V. Eremenko, E. L. Fertman, and V. A. Desnenko

B. Verkin Institute for Low Temperature Physics and Engineering, National Academy of Sciences of Ukraine, pr. Lenina 47, 61103 Kharkov, Ukraine

D. D. Khalyavin

Institute of Solid State and Semiconductor Physics, National Academy of Sciences of Belarus, ul. P. Brovki 17, 220072 Minsk, Belarus

(Submitted February 26, 2002)
Fiz. Nizk. Temp. **28**, 1065–1071 (October 2002)

The static magnetization M_N and dynamic magnetic susceptibility χ_{ac} of polycrystalline manganite $La_{0.66}Ba_{0.34}MnO_3$ are investigated in the temperature region $5\ \mathrm{K}<T<350\ \mathrm{K}$. Measurements are made on a sample with a demagnetizing factor $N=5.4$ in static magnetic fields H in the range 0–120 Oe and on a toroidal sample with $N=0$ in fields with frequencies of 120 and 1000 Hz and amplitudes from 8×10^{-3} to 4.1 Oe. The effect of a uniaxial pressure $P=0.1$ kbar on the static susceptibility $\chi_N=M_N/H$ is investigated in the region $5\ \mathrm{K}<T<270\ \mathrm{K}$. It is found that in the magnetically ordered state (below 314 K) χ_{ac} is independent of the field amplitude in the interval 1.5–4.1 Oe and independent of temperature between 250 and 302 K. At a temperature $T_p=250$ K a second-order phase transition (discontinuity of the derivative $\partial\chi_{ac}/\partial T$) is observed, and at $T_i=177.5$ K—a first-order phase transition (discontinuity of $\chi_{ac}(T)$). The uniaxial pressure leads to an anomalous lowering of the susceptibility in the region 160–250 K with a sharp minimum at 200 K. The temperature and field dependence of the magnetic susceptibility outside the phase transition region are interpreted in terms of ideas about the formation of a helicoidal magnetic structure in the system in low fields at a temperature below 302 K. © *2002 American Institute of Physics.* [DOI: 10.1063/1.1521296]

1. INTRODUCTION

The compound $La_{0.66}Ba_{0.34}MnO_3$ with the perovskite structure is one of the first manganese oxides to attract the attention of investigators in the past decade in connection with the search for new materials for microelectronics. Nevertheless, the La–Ba–Mn–O perovskites remain among the least studied oxides possessing colossal magnetoresistance,[1] even though they are generating great interest from both the scientific and applied standpoints. One of the characteristic features of Ba-substituted manganites is the significant disparity in the sizes of the lanthanide and Ba ions, which leads to high values of the tolerance factor t of the system, which characterizes the internal stresses in the crystal lattice.[2] In comparison with the analogous manganites doped with Ca and Sr, the substitution of barium for lanthanum leads to particularly large internal stresses in the crystal. Consequently, the tolerance factor of $La_{0.66}Ba_{0.34}MnO_3$, defined the expression

$$t=(\mathrm{A}-\mathrm{O})/\sqrt{2}(\mathrm{M}-\mathrm{O}),$$

where A–O and M–O are the bond lengths in the cubic perovskite AMO_3, turns out to the the largest among all the known isostructural compounds of the type $Ln_{2/3}A_{1/3}MnO_3$ (Ln=La, Pr and A=Ca, Sr, Ba): its value is greater than 0.99 and is close to 1.[3] As a result, $La_{0.66}Ba_{0.34}MnO_3$ is a nearly cubic perovskite with a high Curie temperature $T_C\approx340$ K.[4,5] The compound has a rather simple magnetic phase diagram: at normal pressure $La_{0.66}Ba_{0.34}MnO_3$ is a paramagnetic insulator above T_C (it is possible that the temperature-induced insulator–metal transition is slightly shifted in the single crystal[4]), a ferromagnetic conductor below T_C, and has a peak of the modulus of the magnetoresistance in the neighborhood of T_C.[4,6]

Because a system with close to critical internal stresses should be extremely sensitive to external mechanical stresses, we have used the effect of pressure on the magnetic properties of the substance to study the stability of the electronic and magnetic structures of $La_{0.66}Ba_{0.34}MnO_3$ in the magnetic ordering region.

2. EXPERIMENT

The initial bulk polycrystalline sample of $La_{0.66}Ba_{0.34}MnO_3$ investigated in this study was prepared by the standard method of solid-phase reaction in a mixture of powders of La_2O_3, $BaCO_3$, and Mn_2O_3, taken in the necessary proportions. After a preliminary two-hour annealing at 900 °C for decarbonization, the mixture was pressed into a tablet and sintered for 4 hours at 1470 °C. The sample was then cooled slowly together with the furnace at a rate of 80 °C/h. X-ray phase analysis showed the presence of a single-phase substance.

Magnetic measurements were done on samples in the form of a parallelepiped (with dimensions of $2.55\times2.31\times1.1$ mm with a demagnetizing factor $N\sim5.4$ in the direction of the short edge, along which the external magnetic field and uniaxial pressure were applied) and a toroid of rect-

angular cross section (with an outer diameter of 2.31 mm and an inner diameter of 1 mm, a thickness of 1.1 mm, and $N=0$). The static magnetization M_N (and the effective static magnetic susceptibility $\chi_N=M_N/H$) of the sample with $N=5.4$ and its dependence on the uniaxial pressure $P=0.1$ kbar were measured in the temperature interval 5 K $\leqslant T \leqslant 270$ K for magnetic fields in the range $0<H<120$ Oe with the aid of a SQUID magnetometer. The procedures and the methods of measurement are described in detail in Ref. [7]. The sample with $N=5.4$ was also used for measurements of the temperature dependence of the dynamic magnetic susceptibility in a field of frequency 120 Hz and amplitude 1 Oe in the interval 250 K$<T<$350 K. The toroidal sample ($N=0$) was used for measurements of the temperature and field dependence of the dynamic magnetic susceptibility χ_{ac} in a field of frequency $\nu_{ac}=1000$ Hz in an amplitude interval 8×10^{-3} Oe$<H_{0ac}<$4.1 Oe in the temperature region 78 K$<T<$350 K. The value $N=5.4$ is the average in the field interval 20 Oe$\leqslant H\leqslant$120 Oe, where the range of the demagnetizing factor was $5.29\leqslant N\leqslant 5.51$.

3. RESULTS

The results of the measurements and calculations made in this study are presented in Figs. 1–3. As we see from Fig. 1, the susceptibility χ_{ac} rapidly reaches saturation with increasing field H_{0ac} and maintains a value $\chi_{ac}\approx 13.7$ at $T=290$ K and $\chi_{ac}\approx 9.7$ at $T=78$ K in the interval 1.5 Oe $<H_{0ac}<$4.1 Oe. Because of the high values of the magnetic susceptibility, the magnetization

$$M_N(H)=\frac{\chi[H_i(H)]H}{1+N\chi[H_i(H)]}, \tag{1}$$

where the internal field H_i in the sample is a root of the equation

$$H_i=\frac{H}{1+N\chi(H_i)}, \tag{2}$$

is an almost linear function of the external magnetic field H. The dependence $M_N(H)$ calculated according to formulas (1) and (2) with the experimental values of the function $\chi_{ac}(H_{0ac})$ used for $\chi(H_i)$ is practically the same as in experiment. Assuming that

$$M_N(T,H)=\chi_N(T,H)H,$$

we obtain

$$\chi_N(T,H)=\chi_{0N}(T)-\xi(T)H,$$

where the parameters χ_{0N} and ξ are equal to 0.1891 and 9.55×10^{-5} for the investigated field interval and $T=4.2$ K. The value $H=120$ Oe corresponds to $H_i=2.4$ Oe at $T=78$ K. The close values of the experimental and calculated data indicate that the results of the experiments done on samples with different demagnetizing factors are consistent.

The temperature behavior of the susceptibility was also unusual (see Fig. 2). After a sharp rise below 320 K, the value of χ_{ac} remained practically constant in the interval 250 K$<T<$302 K and, as might be expected, below 80 K. At a temperature $T_p=250$ K the derivative $\partial\chi_{ac}/\partial T$ suffers

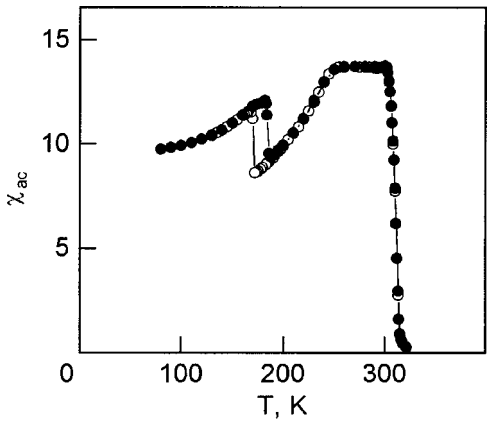

FIG. 2. Dynamic magnetic susceptibility χ_{ac} of polycrystalline $La_{0.66}Ba_{0.34}MnO_3$ in a field of frequency $\nu_{ac}=1000$ Hz and amplitude $H_{0ac}=2.2$ Oe on cooling (○) and heating (●).

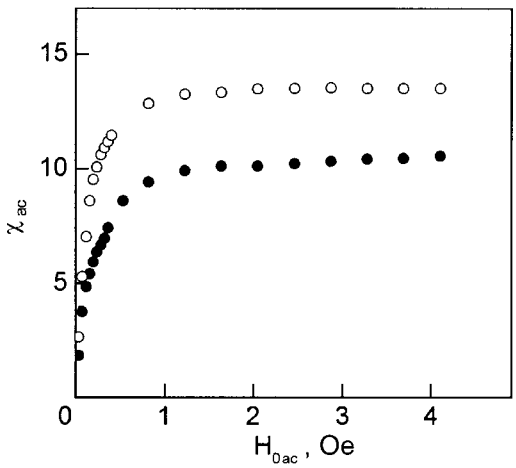

FIG. 1. Dependence of the dynamic magnetic susceptibility χ_{ac} of polycrystalline $La_{0.66}Ba_{0.34}MnO_3$ on the amplitude of the alternating magnetic field H_{0ac} of frequency $\nu_{ac}=1000$ Hz at temperatures of 290 K (○) and 78 K (●).

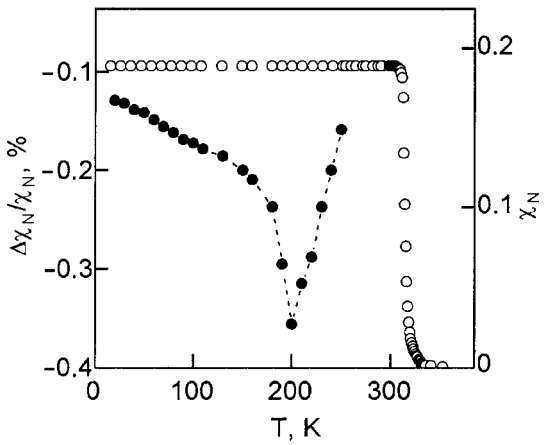

FIG. 3. The temperature dependence of the effective magnetic susceptibility χ_N (○) of a polycrystalline sample of $La_{0.66}Ba_{0.34}MnO_3$ and its relative change $\Delta\chi_N/\chi_N$ (●) under the influence of a uniaxial pressure $P=0.1$ kbar. The measurements were made on heating of the sample in a magnetic field $H=20$ Oe after it was cooled in the same field; the demagnetizing factor of the sample $N=5.4$.

a discontinuity, and at $T_i = 177.5$ K (the middle of the 15-degree temperature hysteresis loop in Fig. 2) a discontinuity of the susceptibility χ_{ac} occurs.

No less unexpected is the temperature behavior of the contribution $\Delta\chi_N$ to the susceptibility χ_N under the influence of a uniaxial pressure $P = 0.1$ kbar (Fig. 3): the function $\Delta\chi_N(T)/\chi_N$ contains three almost linear segments: $5\text{ K} < T < 160$ K, $160\text{ K} < T < 200$ K, and $200\text{ K} < T < 270$ K, on which the quantity

$$\kappa_T = \frac{1}{\chi_N P}\frac{\partial \Delta\chi_N}{\partial T}$$

has the following values at the different temperatures: $\kappa_{160} = -0.054$ Mbar^{-1} K^{-1}, $\kappa_{200} = -0.58$ Mbar^{-1} K^{-1} and $\kappa_{270} = 0.386$ Mbar^{-1} K^{-1}; the deep minimum at $T = 200$ K corresponds to a value $\Delta\chi_N(T)/\chi_N P = -36$ Mbar^{-1}.

4. DISCUSSION

4.1. The problem of the ferromagnetic state

As can be seen in Fig. 1, the magnetic susceptibility of the system has a value typical for soft ferromagnets. At the same time, the absence of a drop in χ_{ac}, which would be evidence of approaching technical saturation, shows that ferromagnetic saturation is not reached in the investigated interval of fields H_{0ac}. The magnetization curve for a multidomain system with a simple ferromagnetic structure in the low-field region should have a positive curvature $\partial^2\chi/\partial H^2$, whereas experiment gives a field-independent susceptibility χ_{ac} for $H_{0ac} > 1.5$ Oe. This means that the observed dependence $\chi_{ac}(H_{0ac})$ is not due to motion of domain walls and can be regarded as intradomain. In that case, however, if the magnetic structure of the system were a simple ferromagnetic one, the susceptibility should be substantially temperature dependent, since it should be determined by the average value over the crystal of the magnetic moment per Mn atom, the temperature dependence of which is characterized qualitatively by the Brillouin function.[8–10] A close to Brillouin temperature dependence of the magnetization has in fact been observed[11] for a thin slab of $La_{0.66}Ba_{0.34}MnO_3$, but only in magnetic fields exceeding 4 kOe. This is an unusually large value for a soft ferromagnet. The magnetic ordering temperature T_C, which is the main parameter of the Brillouin function and is found by extrapolation of the dependence $\chi_{ac}^2 = \text{const}(T - T_C)$ to $\chi_{ac} = 0$, turned out to be 314 K. According to the data of Ref. 11, this may mean that the oxygen index of the compound is less than 3 and may be equal to 2.97.

4.2. Susceptibility of a helicoidal structure

A magnetic susceptibility $\chi = M/H$ which is independent of the magnetic field and the temperature, which would in principle suit the conditions of the problem at hand, can be obtained in the model of a noncollinear magnetic structure—a canted ferromagnetic[12] or a simple helicoidal (antiferromagnetic helicoidal)[13] structure. The susceptibility of a canted ferromagnetic structure is determined solely by the exchange interactions[2] and can be estimated using the formula for the transverse susceptibility of a collinear antiferromagnet:

$$\chi_\perp = \frac{C}{2T_N}, \tag{3}$$

where C is the Curie constant and T_N is the Néel temperature. An estimate according to formula (3) gives $\chi \approx 10^{-4}$ (if $T_N = 314$ K), which is five orders of magnitude smaller than the observed value. The experimental value $\chi \approx 10$ can be given by a model of a simple long-period helicoid:

$$\chi_h = \frac{9\mu_B^2}{16 k_B V_{fu}}\left\{\left|J_2\right|\left(1 - \frac{J_1}{4|J_2|}\right)^2 \times\left[1 + \frac{J_1}{2|J_2|}\left(1 + \frac{J_1}{4|J_2|}\right)\right]\right\}^{-1}, \tag{4}$$

where μ_B is the Bohr magneton, k_B is Boltzmann's constant, V_{fu} is the volume of a formula unit of the substance, and $J_1 > 0$ and $J_2 < 0$ are the exchange integrals for the first and second coordination spheres. The susceptibility (4) can be quite high if the helicoid angle α, determined by the relation

$$\cos\alpha = -\frac{J_1}{4J_2}, \tag{5}$$

is small enough.

Since the data obtained (constancy of the magnetic susceptibility in the face of changing field and temperature over certain intervals of values) are characteristic for a helicoidal magnetic structure,[13,14] it can be assumed that the magnetic structure of $La_{0.66}Ba_{0.34}MnO_3$ is helicoidal. The interaction mechanism between Mn ions leading to the formation of a helicoidal magnetic structure may be due to various causes: 1) Ruderman–Kittel oscillations of the spin density in the magnetic conductor[15,16] (which $La_{0.66}Ba_{0.34}MnO_3$ becomes below T_C); 2) a competition of ferromagnetic and antiferromagnetic interactions characteristic for ''medium-band'' oxide magnets;[17–20] 3) the joint action of double exchange and the Dzyaloshinskiĭ–Moriya interaction.[1,21]

The main ferromagnetic interaction in the system under study is most likely non-Heisenberg (double exchange, i.e., a process of electron exchange between the $Mn^{3(4)+}$ and O^{2-} ions according to the formula

$$Mn_1^{3+} - O^{2-} - Mn_2^{4+} \leftrightarrow Mn_1^{4+} - O^{2-} - Mn_2^{3+},$$

describing a sequence of two processes: the transfer of a p electron of the oxygen to the Mn^{4+} ion and the hop of a d electron of the ion Mn^{3+} into its place), while the antiferromagnetic interaction is Heisenberg (superexchange),[1,2,12,16,20,22] so that the resulting energy parameter $J(\mathbf{Q})$ determining the wave vector $\mathbf{Q}$ of the magnetic structure and the magnetic ordering temperature T_C (Ref. 17), is of a mixed origin. Therefore an estimate of J_1 with the use of the molecular field model for a Heisenberg ferromagnet

$$J_1 \approx \frac{3k_B T_C}{2zS(S+1)} \tag{6}$$

is rather provisional (in the case of double exchange the relation between T_C and S is different[2,17]). Nevertheless, it is useful to make such an estimate in order to satisfy oneself of

the reasonableness of the values obtained in this way, which may be used for estimating the angle of the helicoid.

Assuming in (6) that the number of nearest neighbors of the Mn ion $z=6$, the spin of the Mn^{3+} ion $S=3/2$, and the magnetic ordering temperature $T_C=314$ K, we obtain $J_1 \approx 24.5$ K. An estimate of the helicoid angle using Eqs. (4), (5), and the values $\chi \approx 13.67$ and $J_1 \approx 24.5$ gives $\alpha \approx 5.8°$ ($J_2 \approx -6.16$ K), which is, in general, a physically acceptable value, but it is not very suitable for direct experimental observation: the period of the structure is approximately 62 times larger than the lattice constant and reaches 238 Å. The value $\chi=9.73$ below 80 K corresponds in this model to a helicoid angle $\alpha \approx 6.3°$ ($J_2 \approx -6.17$ K). Using the data of Refs. 11 and 23, we can conclude that the value of the magnetic field that will bring the observed magnetic structure to a simple ferromagnetic one lies in the field interval 3 kOe $<H<$ 4 kOe.

4.3. Susceptibility and pressure effects

The jump of the derivative $\partial\chi_{ac}/\partial T$ at the point $T_p=250$ K is indicative of a second-order phase transition (we take into consideration that $\chi_{ac} \approx M_{0ac}/H_{0ac}$, where M_{0ac} is the amplitude of the magnetization), while the jump of χ_{ac} at $T_i=177.5$ K, with a characteristic ''clockwise'' temperature hysteresis, is obviously a manifestation of a first-order phase transition. Since the character of the field dependence of the susceptibility at low fields is practically the same at both high (290 K) and low (78 K) temperatures (Fig. 1), we assume that the magnetic state does not change radically at these phase transitions. Probably the main changes occur in the crystal lattice: the transition at the point T_p may be related to a change of the symmetry space group of the lattice (polymorphic transition), while the transition at T_i involves a change of the atomic volume (isomorphic transition).

The effect of pressure on the magnetic properties of different doped manganites with mixed valency has been studied previously primarily near T_C. The application of pressure usually stabilizes the ferromagnetic state ($dT_C/dP \approx 10-30$ K/GPa; Refs. 2 and 22). Here the effects of ordinary pressure and chemical pressure (i.e., the pressure arising when the ions at sites A are replaced by ions of a smaller radius) are opposite. This is because the effect of pressure consists in an increase of the overlap integral of the electronic wave functions of the Mn ions and, consequently, in a widening of the bands and an increase of T_C, while a decrease of the radius of the cations in sites A will lead to a decrease of the Mn–O–Mn bond angles and, consequently, to a decrease of the transfer integral.[22] In this scheme the observed effect of a comparatively low pressure of 0.1 kbar on the magnetic susceptibility of the manganite looks rather unusual. It is maximum at $T_e=200$ K (the subscript e here reflects the presumably electronic nature of this feature), which is about $0.64T_C$, it is clearly discernable in the temperature interval 160 K$<T<$260 K, and it is negative in character (the susceptibility decreases under the influence of pressure, and in the case of a simple ferromagnetic structure that would correspond to a decrease of T_C). The observed effect of uniaxial pressure on the magnetic susceptibility of the oxide exhibits a singular point—a discontinuity of the derivative $\partial^2 M_N/\partial P\partial T$ at $T_e=200$ K, which can be interpreted as being a result of a nonanalyticity of the electronic density of states at the Fermi level—an ''electronic transition.''[24] Electronic phase transitions of this kind can precede ordinary first-order or second-order phase transitions or can occur simultaneously with them. In the given case the region identified with the anomaly accompanying the ''electronic transition'' (160 K$<T<$250 K) overlaps the region identified with the anomalies accompanying the ordinarily phase transitions in the system (170 K$<T<$250 K). Therefore it can be assumed that the nature of the latter is determined by the interaction of the electronic and lattice subsystems.

The difference in the positions of the temperature of the maximum of the pressure effect and the point of the first-order phase transition (the latter is at 185 K on heating) merits a special discussion. The data obtained in this study do not rule out the possibility that these two points coincide. The fact is that the anomalies at T_e and T_i were observed in experiments on two different samples, and it is not clear that their chemical compositions were identical: the toroidal sample was subjected to additional (in comparison with the other sample) heat treatment in that it was heated in air during the electrospark cutting of the hole. Although the two samples have the same characteristics near the Curie point, this does not guarantee that there will be no differences at lower temperatures. In such a case there is a certain probability that the temperature of the maximum of the pressure effect and temperature of the jump of the susceptibility at the first-order transition coincide in each of the samples individually.

5. CONCLUSIONS

1. We assume that the observed anomalies of $La_{0.66}Ba_{0.34}MnO_3$ (differences from the properties of $La_{1-x}Ca_xMnO_3$ and $La_{1-x}Sr_xMnO_3$) are due to features of the electronic structure of this manganite. These features stem from the complexity of the electronic structure of the Ba^{2+} ion, the $4f$ shell of which (vacant in the free ion) has a tendency toward a sharp drop in energy and a decrease in radius (collapse) at certain values of the crystal-field potential in oxide compounds.[25,26]

2. The phase transitions at the points T_p and T_i are found in a region of anomalous response of the system to uniaxial pressure. Their origin may lie in the transformation of the electronic structure of the compound. The thermodynamic feature in the system at the point T_e is determined by a discontinuity of the third derivative of the thermodynamic potential

$$\frac{\partial^3 \Phi}{\partial H \partial P \partial T} = -\frac{\partial^2 M}{\partial P \partial T}$$

and may be due to the appearance of nonanalyticity of the electronic density of states at the Fermi level when this level is crossed by the bottom of the ''sinking'' band of the previously vacant states.

3. The experimental data obtained suggest that the magnetic structure of $La_{0.66}Ba_{0.34}MnO_3$ in the investigated temperature and field region is more likely a long-period helicoid than a simple ferromagnetic configuration.

*E-mail: beznosov@ilt.kharkov.ua

[1] V. Dagotto, T. Hotta, and A. Moreo, Phys. Rep. **344**, 1 (2001).
[2] V. M. Loktev and Yu. G. Pogorelov, Fiz. Nizk. Temp. **26**, 231 (2000) [Low Temp. Phys. **26**, 171 (2000)].
[3] W. Archibald, J.-S. Zhou, and J. B. Goodenough, Phys. Rev. B **53**, 14445 (1996).
[4] S. N. Barilo, G. L. Bychkov, L. A. Kurnevich, S. V. Shiryaev, L. A. Kurochkin, J. W. Lynn, and L. Vasiliu-Doloc, J. Cryst. Growth **211**, 480 (2000).
[5] I. O. Troyanchuk, D. D. Khalyavin, S. V. Trukhanov, and H. Szymczak, J. Phys.: Condens. Matter **11**, 8707 (1999).
[6] S. V. Trukhanov, I. O. Troyanchuk, F. P. Korshunov, V. A. Sirenko, H. Szymczak, and K. Baerner, Fiz. Nizk. Temp.**27**, 385 (2001) [Low Temp. Phys. **27**, 283 (2001)].
[7] V. A. Desnenko, A. S. Panfilov, and A. I. Smirnov, Fiz. Nizk. Temp. **21**, 546 (1995) [Low Temp. Phys. **21**, 424 (1995)].
[8] E. S. Borovik and A. S. Mil'ner, *Lectures on Ferromagnetism* [in Russian], Izd. KhGU, Kharkov (1960).
[9] S. V. Vonsovskiĭ, *Magnetism*, Vols. 1 and 2, Wiley, New York (1974), Nauka, Moscow (1971).
[10] M. S. S. Brooks and D. A. Goodings, J. Phys. C **1**, 1279 (1968).
[11] H. L. Ju, J. Gopalakrishnan, J. L. Peng, Q. Li, G. C. Xiong, T. Venkatesan, and R. L. Greene, Phys. Rev. B **51**, 6143 (1995-I).
[12] P.-G. de Gennes, Phys. Rev. **118**, 141 (1960).
[13] K. P. Belov, M. A. Belyanchikova, R. Z. Levitin, and S. A. Nikitin, *Rare-Earth Ferromagnets and Antiferromagnets* [in Russian], Nauka, Moscow (1965).
[14] A. B. Beznosov, E. L. Fertman, and P. P. Pal-Val, J. Magn. Magn. Mater. **192**, 111 (1999).
[15] C. Kittel, *Quantum Theory of Solids*, Wiley, New York (1963), Nauka, Moscow (1967).
[16] É. L. Nagaev, Usp. Fiz. Nauk **166**, 833 (1996).
[17] É. L. Nagaev, *Physics of Magnetic Semiconductors* [in Russian], Nauka, Moscow (1979).
[18] J. Inoue and S. Mackawa, Phys. Rev. Lett. **74**, 3407 (1995).
[19] J. Jiang, J. Dong, and D. Y. Xing, Phys. Rev. **55**, 8973 (1997-II).
[20] M. B. Salamon and M. Jaime, Rev. Mod. Phys. **73**, 583 (2001).
[21] D. Coffey, K. Bedell, and S. Trugman, Phys. Rev. B **42**, 6509 (1990).
[22] J. M. D. Coey, M. Viret, and S. von Molnar, Adv. Phys. **48**, 167 (1999).
[23] S. E. Lofland, S. M. Bhagat, H. L. Ju, G. C. Xiong, T. Venkatesan, and R. L. Greene, Phys. Rev. B **52**, 15058 (1995).
[24] I. M. Lifshitz, Zh. Éksp. Teor. Fiz. **38**, 1569 (1960) [Sov. Phys. JETP **11**, 1130 (1960)].
[25] N. G. Stoffel and J. M. Tarascon, Phys. Rev. B **36**, 3986 (1987).
[26] V. V. Nemoshkalenko, V. Kh. Kas'yanenko, B. G. Nikitin, L. I. Nikolaev, Yu. G. Pogorelov, G. A. Klimenko, and P. V. Gel', Sverkhprovodimost' (KIAE) **2**, 41 (1989) [Superconductivity **2**, 47 (1989)].

Translated by Steve Torstvcit

LOW-DIMENSIONAL AND DISORDERED SYSTEMS

Low-temperature inversion of the magnetoresistance in charge-ordered layered superstructures

P. V. Gorskyi[a)]

Yu. Fed'kovich Chernovsty National University, ul. Kotsyubinskogo 2, 58001 Chernovtsy, Ukraine
(Submitted February 4, 2002)
Fiz. Nizk. Temp. **28**, 1072–1077 (October 2002)

The nonoscillatory (with respect to magnetic field) part of the magnetoresistance of layered charge-ordered crystals is determined under the condition that the relaxation time of the charge carriers is inversely proportional to their density of states. It is demonstrated that inversion of the magnetoresistance can occur as a function of the carrier concentration, temperature, magnetic field, and value of the effective attractive interaction that leads to the charge ordering.
 [DOI: 10.1063/1.1521297]

INTRODUCTION

Various effects due to structural phase transitions in layered structures have been studied in Refs. 1–5, for example. In those papers it is demonstrated theoretically and experimentally that both intralayer and interlayer charge ordering can occur in layered superstructures, including those with an incommensurate charge-density wave (CDW). Concrete physical characteristics have been determined mainly for crystals with interlayer charge ordering. In Ref. 2 a model of charge ordering in layered structures was proposed in which the charge ordering is treated as a simple alternation of layers which are more filled and less filled by charge carriers (e.g., electrons). The source of this ordering, as in conventional models of structural phase transitions, is assumed to be an effective attraction between carriers, which reduces, e.g., to their interaction with a phonon mode whose wave vector corresponds to the period of the CDW. The factors that oppose the structural phase transition are the Coulomb repulsion of carriers of like charge and the increase of the average kinetic energy of the electrons in the neighboring layers. A study of the oscillatory (in magnetic field) part of the magnetoresistance of charge-ordered layered crystals was the subject of Ref. 6. In the present paper we determine and analyze the nonoscillatory part of the magnetoresistance of these crystals.

It was shown in Ref. 7 that if the charge ordering consists in a simple alternation of layers more filled and less filled with electrons, i.e., the electron density on the ith layer is

$$n_i = n_0 a[1+(-1)^i \delta], \tag{1}$$

where n_0 is the volume-averaged electron density and a is the distance between neighboring layers, and δ is the relative ordering parameter $(0 \leqslant \delta \leqslant 1)$, which is such that $\delta = 1$ corresponds to an alternation of ''empty'' and ''filled'' layers and $\delta = 0$ corresponds to a uniform distribution of carriers over layers, then the energy of the carriers is given by

$$\varepsilon(\mathbf{k}) = \frac{h^2}{8\pi^2 m^*}(k_x^2 + k_y^2) \pm \sqrt{\Delta^2 \cos^2 a k_z + W_0^2 \delta^2}. \tag{2}$$

Here k_x, k_y, and k_z are the quasimomentum components, m^* is the effective mass of the electrons in the plane of the layer and for simplicity is assumed to be isotropic, 2Δ is the width of the ''bare'' miniband describing the translational motion of electrons between layers, and W_0 is the effective constant of the attractive interaction. In a quantizing magnetic field $\mathbf{H}$ perpendicular to the layers, the energy of the carriers is written as

$$\varepsilon(n, k_z) = \mu^* H(2n+1) \pm \sqrt{\Delta^2 \cos^2 a k_z + W_0^2 \delta^2}, \tag{3}$$

where n is the number of the Landau subband, $\mu^* = \mu_B m_0 / m^*$, μ_B is the Bohr magneton, and m_0 is the mass of a free electron. In formulas (2) and (3) the energy is measured relative to the center of the gap between minibands.

The self-consistency equations that determine the order parameter δ and the chemical potential ζ of the system in the absence of magnetic field have the form[7]

$$\begin{cases} 1 = \dfrac{kT}{2\zeta_0 \pi} \displaystyle\int_0^{\pi} dx \ln\left\{\left[1+\exp\left(\frac{\zeta + \sqrt{W_0^2\delta^2 + \Delta^2 \cos^2 x}}{kT}\right)\right]\left[1+\exp\left(\frac{\zeta - \sqrt{W_0^2\delta^2 + \Delta^2 \cos^2 x}}{kT}\right)\right]\right\} \\ \delta = \dfrac{kTW_0\delta}{2\zeta_0 \pi} \displaystyle\int_0^{\pi} \frac{dx}{\sqrt{W_0^2\delta^2 + \Delta^2 \cos^2 x}} \ln\left\{\left[1+\exp\left(\frac{\zeta + \sqrt{W_0^2\delta^2 + \Delta^2 \cos^2 x}}{kT}\right)\right]\left[1+\exp\left(\frac{\zeta - \sqrt{W_0^2\delta^2 + \Delta^2 \cos^2 x}}{kT}\right)\right]^{-1}\right\}, \end{cases} \tag{4}$$

where k is Boltzmann's constant, and $\zeta_0 = n_0 a h^2/4m^*\pi$.

For calculating the nonoscillatory part of the electrical conductivity in the case of spectrum (3) in an electric field perpendicular to the layers and in a strong magnetic field, when each electron remains in its own Landau subband in the scattering process, so that the relaxation time is inversely proportional to the density of states in the magnetic field,[8] one can use the formula[9]

$$\overline{\sigma}(H) = \frac{16\pi^2\tau_0 e^2 m^* a \overline{W}}{h^4 kT|\mu^* H|}\left\{ \int_{\substack{W(x)\leqslant\zeta \\ x\geqslant 0}} (W'(x))^3 dx + \sum_{l=1}^{\infty} (-1)^l h_l^{\sigma}\left[\int_{\substack{W(x)\leqslant\zeta \\ x\geqslant 0}} dx (W'(x))^3 \times \exp\left(\frac{l(W(x)-\zeta)}{kT}\right) - \int_{\substack{W(x)\geqslant\zeta \\ x\geqslant 0}} dx (W'(x))^3 \exp\left(\frac{l(\zeta - W(x))}{kT}\right)\right]\right\}, \tag{5}$$

$$h_l^{\sigma} = \frac{(\mu^* H l/kT)}{\sinh(\mu^* H l/kT)}. \tag{6}$$

Here τ_0 is a parameter having dimensions of time and characterizing the scattering intensity, and $\overline{W}$ is the half-width of the "bare" miniband. In addition, $W(x) = \pm\sqrt{W_0^2\delta^2 + \Delta^2\cos^2 x}$, so that for calculating the conductivity one should substitute this expression for $W(x)$ in (5), do the integration with allowance for the real position of the chemical potential level, and divide the result in half, since two minibands take part in the process. Formula (5) was derived on the assumption that the scattering of electrons on acoustic phonons is decisive, and $h\nu_m \ll kT$ and $h\nu_m \ll \mu^* H$, where ν_m is the maximum phonon frequency. In formula (5) the parameter τ_0 is assumed to be independent of magnetic field, although in many cases such a dependence is actually present. If the field dependence is taken into account in the way that was done in Ref. 8 for the case of scattering on acoustic phonons, i.e., if it is assumed that

$$\tau_0 = \tau_1 a^2 \frac{eH}{ch}, \tag{7}$$

where τ_1 is independent of both temperature and magnetic field, then we obtain the following expressions for the nonoscillatory part of the conductivity:

for $\zeta < -\Delta_\delta$

$$\overline{\sigma}(H) = \frac{128\pi e^2 m^{*2} a^3 \tau_1 \Delta}{h^6 kT}\sum_{l=1}^{\infty}(-1)^{l-1} h_l^{\sigma}\exp\left(\frac{l\zeta}{kT}\right) \times\left\{\frac{kT}{l}\left[(\Delta_\delta^2 + W_0^2\delta^2)\left(\sinh\frac{l\Delta_\delta}{kT} - \sinh\frac{lW_0\delta}{kT}\right) + W_0^2\delta^2\sinh\frac{lW_0\delta}{kT} - \Delta_\delta^2\sinh\frac{l\Delta_\delta}{kT}\right] + 2\left(\frac{kT}{l}\right)^2 \times\left(\Delta_\delta\cosh\frac{l\Delta_\delta}{kT} - W_0\delta\cosh\frac{1W_0\delta}{kT}\right) + \left(\frac{kT}{l}\right)^3 \times\left(\sinh\frac{lW_0\delta}{kT}\right) - \sinh\frac{l\Delta_\delta}{kT}\right) + \frac{1}{kT}W_0^2\delta^2\Delta_\delta \times\left(\mathrm{Shi}\frac{lW_0\delta}{kT} - \mathrm{Shi}\frac{l\Delta_\delta}{kT}\right) + W_0^2\delta^2\Delta_\delta\exp\frac{l\Delta_\delta}{kT} - W_0\delta\Delta_\delta^2\exp\frac{lW_0\delta}{kT}\right\}; \tag{8}$$

for $-\Delta_d < \zeta < W_0\delta$

$$\overline{\sigma}(H) = \sigma_0 + \sigma_1(H), \tag{9}$$

where

$$\sigma_0 = \frac{128\pi e^2 m^{*2} a^3 \tau_1 \Delta}{h^6 kT} \times\left[\zeta(\Delta_\delta^2 + W_0^2\delta^2) + W_0^2\delta^2\Delta_\delta^2\zeta^{-1} - \frac{\zeta^3}{3} + \frac{2\Delta_\delta^3}{3} + 2W_0^2\delta^3\Delta_\delta\right], \tag{10}$$

$$\sigma_1(H) = \frac{128\pi e^2 m^{*2} a^3 \tau_1 \Delta}{h^6 kT} \times\sum_{l=1}^{\infty}(-1)^l h_l^{\sigma}\left\{2\left(\frac{kT}{l}\right)^2\zeta + W_0^2\delta^2\Delta_\delta^2\zeta^{-1}\left(\frac{kT}{l}\right)^2 \times\left[2W_0\delta\exp\frac{l\zeta}{kT}\cosh\frac{lW_0\delta}{kT} - 2\Delta_\delta\sinh\frac{l\zeta}{kT}\exp\left(-\frac{l\Delta_\delta}{kT}\right)\right] - 2\left(\frac{kT}{l}\right)^3\left[\exp\frac{l\zeta}{kT}\sinh\frac{lW_0\delta}{kT} + \exp\left(-\frac{l\Delta_\delta}{kT}\right)\sinh\frac{l\zeta}{kT}\right] + W_0\delta\Delta_\delta^2\exp\frac{l\zeta}{kT}\cosh\frac{lW_0\delta}{kT} - W_0^2\delta^2\Delta_\delta\sinh\frac{l\zeta}{kT} \times\exp\left(-\frac{1\Delta_\delta}{kT}\right) + \frac{lW_0^2\delta^2\Delta_\delta^2}{2kT}\left[\exp\left(-\frac{l\zeta}{kT}\right) \times\left(\mathrm{Ei}\left(-\frac{l\Delta_\delta}{kT}\right) - \mathrm{Ei}\frac{l\zeta}{kT}\right) + \exp\frac{l\zeta}{kT}\left(\mathrm{Ei}\left(-\frac{l\Delta_\delta}{kT}\right) - \mathrm{Ei}\left(-\frac{lW_0\delta}{kT}\right) - 2\,\mathrm{Shi}\frac{l\zeta}{kT}\right)\right]\right\}; \tag{11}$$

for $-W_0\delta < \zeta < W_0\delta$

$$\overline{\sigma}(H) = \sigma_2 + \sigma_3(H), \tag{12}$$

where

$$\sigma_2 = \frac{128\pi e^2 m^{*2} a^3 \tau_1 \Delta}{h^6 kT} \times\left[\frac{2}{3}(\Delta_\delta^3 - W_0^3\delta^3) + 2W_0^2\delta^2\Delta_\delta - 2W_0\delta\Delta_\delta^2\right], \tag{13}$$

$$\sigma_3(H)=\frac{128\pi e^2 m^{*2}a^3\tau_1\Delta}{h^6 kT}$$
$$\times\sum_{l=1}^{\infty}(-1)^{l-1}h_l^{\sigma}\sinh\frac{l\zeta}{kT}\left\{\frac{kT}{l}\left[\Delta_\delta^2\exp\left(-\frac{1W_0\delta}{kT}\right)\right.\right.$$
$$-W_0^2\delta^2\exp\left(-\frac{l\Delta_\delta}{kT}\right)\Big]+2\left(\frac{kT}{l}\right)^2\Big[\Delta_\delta\exp\left(-\frac{l\Delta_\delta}{kT}\right)$$
$$-W_0\delta\exp\left(-\frac{lW_0\delta}{kT}\right)\Big]+2\left(\frac{kT}{l}\right)^3\Big[\exp\left(-\frac{l\Delta_\delta}{kT}\right)$$
$$-\exp\left(-\frac{lW_0\delta}{kT}\right)\Big]+W_0^2\delta^2\Delta_\delta\exp\left(-\frac{l\Delta_\delta}{kT}\right)$$
$$-W_0\delta\Delta_\delta^2\exp\left(-\frac{lW_0\delta}{kT}\right)+\frac{lW_0^2\delta^2\Delta_\delta^2}{kT}$$
$$\left.\times\left[\mathrm{Ei}\left(-\frac{l\Delta_\delta}{kT}\right)-\mathrm{Ei}\left(-\frac{lW_0\delta}{kT}\right)\right]\right\}; \tag{14}$$

for $W_0\delta<\zeta<\Delta_\delta$

$$\overline{\sigma}(H)=\sigma_4+\sigma_5(H), \tag{15}$$

where

$$\sigma_4=\frac{128\pi e^2 m^{*2}a^3\tau_1\Delta}{h^6 kT}\left[\frac{2\Delta_\delta^3}{3}+2W_0^2\delta^2\Delta_\delta+(\Delta_\delta^2+W_0^2\delta^2)\right.$$
$$\left.\times\zeta+W_0^2\delta^2\Delta_\delta^2\zeta^{-1}-\frac{4W_0^3\delta^3}{3}-4W_0\delta\Delta_\delta^2-\frac{\zeta^3}{3}\right], \tag{16}$$

$$\sigma_5=\frac{128\pi e^2 m^{*2}a^3\tau_1\Delta}{h^6 kT}$$
$$\times\sum_{l=1}^{\infty}(-1)^l h_l^{\sigma}\left\{2\left(\frac{kT}{l}\right)^2\zeta+W_0^2\delta^2\Delta_\delta^2\zeta^{-1}+\frac{kT}{l}\right.$$
$$\times\left[W_0^2\delta^2\sinh\frac{l\zeta}{kT}\exp\left(-\frac{l\Delta_\delta}{kT}\right)-\Delta_\delta^2\sinh\frac{lW_0\delta}{kT}\right.$$
$$\left.\times\exp\left(-\frac{l\Delta_\delta}{kT}\right)\Big]-2\left(\frac{kT}{l}\right)^2\Big[\Delta_\delta\sinh\frac{l\zeta}{kT}\exp\left(-\frac{l\Delta_\delta}{kT}\right)\right.$$
$$\left.+2W_0\delta\exp\left(-\frac{l\zeta}{kT}\right)\cosh\frac{lW_0\delta}{kT}\right]$$
$$+2\left(\frac{kT}{l}\right)^3\Big[\sinh\frac{lW_0\delta}{kT}\exp\left(-\frac{l\zeta}{kT}\right)-\sinh\frac{l\zeta}{kT}$$
$$\times\exp\left(-\frac{l\Delta_\delta}{kT}\right)\Big]+\frac{W_0^2\delta^2\Delta_\delta}{2}\Big[\exp\left(-\frac{1(\zeta+\Delta_\delta)}{kT}\right)$$
$$-\exp\frac{l(W_0\delta-\zeta)}{kT}-\exp\frac{l(\zeta-\Delta_\delta)}{kT}\Big]-\frac{W_0\delta\Delta_\delta^2}{2}$$
$$\times\exp\left(-\frac{l(\zeta+W_0\delta)}{kT}\right)+\frac{lW_0^2\delta^2\Delta^{\delta}{}_2}{2kT}\Big[\exp\left(-\frac{l\zeta}{kT}\right)$$
$$\left.\times\left(\mathrm{Ei}\left(-\frac{l\Delta_\delta}{kT}\right)-\mathrm{Ei}\frac{l\zeta}{kT}+2\ \mathrm{Shi}\frac{lW_0\delta}{kT}\right)\right.$$
$$\left.-\exp\frac{l\zeta}{kT}\left(\mathrm{Ei}\left(-\frac{l\Delta_\delta}{kT}\right)-\mathrm{Ei}\left(-\frac{l\zeta}{kT}\right)\right)\Big]\right\}; \tag{17}$$

for $\zeta>\Delta_\delta$

$$\overline{\sigma}(H)=\sigma_6+\sigma_7(H), \tag{18}$$

where

$$\sigma_6=\frac{128\pi e^2 m^{*2}a^3\tau_1\Delta}{h^6 kT}$$
$$\times\left(\frac{4\Delta_\delta^3}{3}-\frac{4W_0^3\delta^3}{3}+W_0^2\delta^2\Delta_\delta-W_0\delta\Delta_\delta^2\right), \tag{19}$$

$$\sigma_7=\frac{128\pi e^2 m^{*2}a^3\tau_1\Delta}{h^6 kT}$$
$$\times\sum_{l=1}^{\infty}(-1)^l h_l^{\sigma}\left\{\left(W_0^2\delta^2\sinh\frac{l\Delta_\delta}{kT}-\Delta_\delta^2\sinh\frac{lW_0\delta}{kT}\right)\frac{kT}{l}\right.$$
$$+2\left(\Delta_\delta\cosh\frac{l\Delta_\delta}{kT}-W_0\delta\cosh\frac{lW_0\delta}{kT}\right)\left(\frac{kT}{l}\right)^2$$
$$+2\left(\sinh\frac{lW_0\delta}{kT}-\sinh\frac{l\Delta_\delta}{kT}\right)\left(\frac{kT}{l}\right)^3+W_0^2\delta^2\Delta_\delta\cosh\frac{l\Delta_\delta}{kT}$$
$$-W_0\delta\Delta_\delta^2\cosh\frac{lW_0\delta}{kT}+\frac{lW_0^2\delta^2\Delta_\delta^2}{kT}$$
$$\left.\times\left(\mathrm{Shi}\frac{lW_0\delta}{kT}-\mathrm{Shi}\frac{l\Delta_\delta}{kT}\right)\right\}\exp\left(-\frac{l\zeta}{kT}\right). \tag{20}$$

In formulas (8)–(20) $\Delta_d=\sqrt{W_0^2\delta^2+\Delta^2}$, $\sinh(\ldots)$, $\cosh(\ldots)$, $\mathrm{Shi}(\ldots)$ and $\mathrm{Ei}(\ldots)$ are, respectively, the hyperbolic sine and cosine and the hyperbolic sine and exponential integrals.

For analysis of the results we take into account that for $W_0/\zeta_0=2$ and $\zeta=0$ the second equation of system (4) goes over to an identity, and consequently the order parameter is determined from the first equation. It follows from system (4) that charge ordering of the type described is possible only for $W_0/\zeta_0>1$, where for $W_0/\zeta_0<2$ the chemical potential ζ of the system of current carriers in the subcritical region, when $\delta>0$, is positive and increasing with temperature, and for $W_0/\zeta_0>2$ it is negative and decreasing with increasing temperature. Thus the behavior of the chemical potential is typically two-band. This circumstance has a substantial influence on the sign of the nonoscillatory part of the magnetoresistance. It follows from formulas (8)–(20) that: when $\zeta<0$ the nonoscillatory part of the magnetoresistance is positive in both the subcritical and supercritical regions, for $\zeta=0$ the nonoscillatory part of the magnetoresistance is zero in the subcritical and positive in the supercritical region, and for $\zeta>0$ the nonoscillatory part of the magnetoresistance is negative in the subcritical region and in part of the supercritical region. However, since the chemical potential ζ always decreases with increasing temperature in the supercritical re-

gion, the nonoscillatory part of the magnetoresistance then decreases in modulus, and at $\zeta=0$ it passes through zero and becomes positive.

Thus we see that for $W_0/\zeta_0=2$ the nonoscillatory part of the magnetoresistance of charge-ordered layered crystals suffers a temperature inversion, in which case the magnetoresistance is negative in the subcritical region and reaches a maximum absolute value at a temperature close to the critical. Since the critical temperature of the structural phase transition increases with increasing W_0/ζ_0, as follows from equation (4), the magnetoresistance of substances with low critical temperatures of the structural phase transitions should therefore be negative and undergo inversion in the supercritical region, while the magnetoresistance of substances with high critical temperatures should be purely positive. It follows from the system of equations (4) that the ''boundary'' transition temperature separating crystals whose magnetoresistance undergoes a temperature inversion from those that do not have this property is equal to $(\zeta_0/k)\ln 2$ in the approximation for $\Delta/W_0 \ll 1$.

Qualitatively comparing the results with the experimental data, we note that, as is shown in Ref. 3, the charge ordering arising at the structural phase transition has no effect on the density of states of the charge carriers, their low-temperature heat capacity, and the dynamic susceptibility. This is easily explained by considering that in the gap region between minibands, i.e., for $-W_0\delta<\varepsilon<W_0\delta$, the density of states of a system with energy spectrum (2) is constant and equal to $2m^*\pi/(ah^2)$, i.e., is independent of the order parameter δ. For $W_0/\zeta_0=2$ the density of states at the chemical potential level is equal to $2m^*\pi/(ah^2)$ in the entire subcritical region. Thus crystals whose density of states is independent of the order parameter should also have a small magnetoresistance, and as a consequence the main part of their electrical conductivity should be determined by formula (13).

We note that a decisive argument in favor of the intralayer charge ordering considered in Ref. 1 as opposed to the model proposed in Ref. 2, as a rule, is provided by the data of x-ray and neutron diffraction analyses, which show that displacements of the atoms in the direction perpendicular to the layers do not arise. However, a more detailed analysis made in Ref. 7 shows that such displacements should not be present if the electron–phonon coupling function is purely imaginary, i.e., if it is due to the interaction of electrons with vibrations of the layers as a whole relative to each other in the direction perpendicular to the plane of the layers. If there exists an interaction of electrons with bending oscillations of the layers, then even in the framework of the model considered here there should arise displacements of the atoms in the direction perpendicular to the layers.

The magnetoresistance inversion under discussion arises because the sign and magnitude of the magnetoresistance, as follows from formula (5), is determined by two competing processes of thermal promotion of current carriers: from the lower Landau subbands into the band near the chemical potential level, and from these latter bands into the higher-lying subbands. The first process increases the effective density of states at the chemical potential level and, consequently, leads to negative magnetoresistance, and the second process decreases the effective density of states at the chemical potential level and thus leads to positive magnetoresistance.

We also note that the results obtained in this paper are, at first glance, nonphysical, since the conductivity of the system formally is nonzero at $\delta=1$. But that is impossible in view of formula (1), from which it follows that in the case of complete ordering the conducting layers alternate with insulating layers, or layers of n type with layers of i or p type. Such systems do not conduct current in the direction perpendicular to the layers. However, this contradiction is only apparent, since it follows from Eqs. (4) that the state in which $\delta=1$ is realized only at $T=0$ and $\Delta=0$. If $\Delta\neq 0$, then $\delta<1$ even at $T=0$, since the interlayer motion of electrons tends to smooth out the nonuniformity of their layered distribution.

At finite temperatures far from the critical we have $\delta\approx 1$ if Δ/W_0 is small, and in that case, as follows from the general formula (5) together with (3), the conductivity of the system in the direction perpendicular to the layers tends toward zero by an asymptotic law $(\Delta/W_0)^3$. It is this circumstance that explains why, as a rule, the anisotropy of the conductivity in layered charge-ordered crystals is 2–4 orders of magnitude higher than the anisotropy of the effective masses.[4]

CONCLUSION

We have shown that the structural phase transition due to the interlayer charge ordering leads to a temperature inversion of the magnetoresistance in layered structures with low critical temperatures of the transitions. In the subcritical region the magnetoresistance of such structures is negative and reaches a maximum in absolute value at temperatures close to the critical. The magnetoresistance of structures with high critical temperatures of the structural phase transitions is positive. Structures for which the density of states at the chemical potential level and the low-temperature heat capacity are independent of the order parameter should have a close to zero value of the nonoscillatory part of the magnetoresistance.

At the transition to complete ordering the conductivity of layered structures in the direction perpendicular to the layers tends toward zero by a $(\Delta/W_0)^3$ law.

[a)]E-mail: public@cv.ukrtel.net

[1] A. I. Kononov and Yu. V. Kopaev, Fiz. Tverd. Tela (Leningrad) **16**, 1122 (1974) [Sov. Phys. Solid State **16**, 721 (1974)].
[2] E. A. Pashitskiĭ and A. Shpigel', Fiz. Nizk. Temp. **4**, 976 (1978) [Sov. J. Low Temp. Phys. **4**, 460 (1978)].
[3] J. M. Harper and T. H. Geballe, Phys. Lett. A **54**, 27 (1975).
[4] C. Zeller, G. M. T. Foley, E. R. Falardcau, and F. L. Vogel, Mater. Sci. Eng. **31**, 255 (1977).
[5] A. A. Mamalui and I. N. Sablin, Fiz. Nizk. Temp. **27**, 738 (2001) [Low Temp. Phys. **27**, 542 (2001)].
[6] P. V. Gorskii, Fiz. Nizk. Temp. **14**, 1229 (1988) [Sov. J. Low Temp. Phys. **14**, 679 (1988)] (Annotation of the manuscript, dep. VINITI 19 April 1988, No. 2981-V88).
[7] P. V. Gorskiĭ, Vestn. Kharkovsk. Univ., No. 227, 33 (1982).
[8] V. F. Gantmakher and I. B. Levinson, *Scattering of Current Carriers in Metals and Semiconductors* [in Russian], Nauka, Moscow (1984).
[9] P. V. Gorskiĭ, Fiz. Nizk. Temp. **12**, 584 (1986) [Sov. J. Low Temp. Phys. **12**, 329 (1986)].

Translated by Steve Torstveit

On the deviations from Matthiessen's rule in quasi-one-dimensional conductors

A. I. Kopeliovich*

B. Verkin Institute for Low Temperature Physics and Engineering, National Academy of Sciences of Ukraine, pr. Lenina 47, 61103 Kharkov, Ukraine

A. A. Mamalui,** L. G. Petrenko, and T. N. Shelest

(Submitted February 19, 2002; revised April 26, 2002)
Fiz. Nizk. Temp. **28**, 1078–1082 (October 2002)

An explanation is proposed for the large deviation from Matthiessen's rule observed experimentally in the quasi-one-dimensional metal $NbSe_3$, the Fermi surface of which contains several sheets which are isolated from each other. The deviation from Matthiessen's rule arises as a result of the nonadditive influence on the electron distribution function from processes of electron scattering on lattice defects (Se vacancies) and phonons. It is shown that the experimentally obtained temperature dependence of the electrical conductivity of $NbSe_3$ can be described satisfactorily in the framework of a simplified model of a one-dimensional Fermi surface in the form two pairs of symmetric points in quasimomentum space. Large deviations from Matthiessen's rule can be explained by the different character of the scattering on lattice defects and on phonons for electrons localized on different structural chains of the quasi-one-dimensional metal. © *2002 American Institute of Physics.*
[DOI: 10.1063/1.1521298]

In the presence of several scattering processes for current carriers in a conductor its electrical conductivity, generally speaking, differs from the sum of the resistances due to each of them—this effect is known as a deviation from Matthiessen's rule (DMR). The DMR effect is usually characterized by the relative quantity

$$\Delta = \frac{\rho - \rho_1 - \rho_2}{\rho},$$

where ρ is the resistivity of the sample in the presence of the two electron scattering processes, and ρ_1 and ρ_2 are the resistivities of the sample in the presence of only one of these processes.

In the framework of the quasiclassical theory of kinetic phenomena in conductors, two types of DMR should be distinguished. If the discussion is restricted to the scattering of electrons only on lattice defects and phonons, then the first type of DMR is due to the influence of defects on the elementary processes of electron–phonon scattering in the conductor (or to the influence of the electron–phonon interaction on processes of electron scattering on defects). A detailed theory of this type of DMR is developed in Ref. 1. The value of Δ characterizing a DMR of this type is, as a rule, small for good conductors, since the influence of defects on the electron–phonon scattering is proportional to the concentration of defects, and at not very high temperatures the probability of scattering of an electron on a phonon as it passes an impurity is also low. The value of Δ for the first type of DMR can be of either sign.

The second type of DMR (see, e.g., Refs. 2–4) is due to the interference of elementary scattering processes and the nonadditivity of their influence on the electron distribution function. This type of DMR, generally speaking, does not contain small parameters, and, as was noted in Ref. 4, the value of Δ is positive.

Large DMRs for the quasi-one-dimensional metal $NbSe_3$ were found in Ref. 5. We shall show that for one-dimensional metals with a Fermi surface consisting of several sheets, as is the case for the given compound, it is natural to expect large DMRs of the second type.

We write the kinetic equation for the nonequilibrium correction $-(dn/d\varepsilon)\chi_{\mathbf{p}}$ to the electron distribution function in the form

$$\hat{I}_d \chi_{\mathbf{p}} + \hat{I}_{\mathrm{ph}} \chi_{\mathbf{p}} = e\mathbf{E}\cdot\mathbf{v}_{\mathbf{p}}, \tag{1}$$

where $n(\varepsilon)$ is the equilibrium Fermi distribution function for the energy, $\mathbf{p}$ is the quasimomentum of the electron (we assume that this index also includes the number of the energy band), $\hat{I}_d$ and $\hat{I}_{\mathrm{ph}}$ are the collision operators for collisions of electrons with defects and phonons, respectively, e is the charge of the electron, $\mathbf{E}$ is the electric field, and $\mathbf{v}_{\mathbf{p}}$ is the electron velocity. The use of the standard kinetic equation may raise some doubt, since the electron–electron interaction in a one-dimensional system leads to the phenomenon of bosonization (see, e.g., Ref. 6), and the elementary excitations become electron density waves instead of individual electrons. Apparently, however, the degree of one-dimensionality of the electron spectrum of the compounds of the type considered (having a conductivity anisotropy of $\approx 10-20$) is not high enough for bozonization effects to appear: the electronic properties of these compounds have been discussed in the literature in the framework of the usual one-electron concepts.[7] The kinetic equation was used previously in Ref. 8 for describing the electrical conductivity of compounds of the TTF–TCNQ type, which have a higher degree of one-dimensionality than $NbSe_3$.

We note a difference in the theoretical treatment of DMRs of the first and second types: the first type of DMR is due to small corrections to the operator $\hat{I}_d$ due to the

electron–phonon interaction and to the operator $\hat{I}_p$ due to the presence of impurities; for the second type of DMR it is unnecessary to take these corrections into account.

Let us start by showing that in a one-dimensional conductor with the simplest Fermi surface the second type of DMR does not occur. In the simplest case the Fermi surface of a one-dimensional conductor consists of two symmetric points on the quasimomentum axis: p_F and $-p_F$ (they correspond to electron velocities v_F and $-v_F$). In the general case in the presence of a center of symmetry in the crystal, the Fermi energy can correspond to several pairs of symmetric points lying in one or several energy bands. If there is only one pair of such points, then Eq. (1) reduces to

$$\nu\chi_{pF}=eE\nu_F, \quad \chi_{-pF}=-\chi_{pF}, \quad \nu=\nu_d+\nu_p, \tag{2}$$

where ν is the only matrix element of the collision operator in this case. The conductivity of a one-dimensional conductor can be written in the form

$$\sigma=\sum \chi_{pFk}\nu_{Fk}\Pi_k/E,$$

where the summation is over pairs of symmetric points, and Π_k is the contribution of each such pair to the density of states. Since $\Pi_k \propto v_{Fk}^{-1}$, the conductivity

$$\sigma\propto\sum_k \chi_{pFk}. \tag{3}$$

In the case of the simplest Fermi surface, we obtain for the resistivity ($\rho=\sigma^{-1}$) from (2) and (3)

$$\rho\propto(v_d+v_p)/\nu_F.$$

Thus Matthiessen's rule is obeyed.

Let us consider the case of a one-dimensional conductor whose Fermi surface consists of two pairs of symmetric points in quasimomentum space—this example already gives sufficient information about the possible values of the DMR. Equation (1) in this case becomes

$$\begin{aligned} &v_1\chi_1+v_{12}(\chi_1-\chi_2)+\nu_{12}^*(\chi_1+\chi_2)=eE\nu_1;\\ &\nu_2\chi_2+\nu_{21}(\chi_2-\chi_1)+\nu_{21}^*(\chi_2+\chi_1)=eE\nu_2. \end{aligned} \tag{4}$$

Here the matrix elements ν_1 and ν_2 of the collision operator describe transitions of electrons within each of the pairs of symmetric points (transitions between p_1 and $-p_1$), ν_{12} describes transitions between points p_1 and p_2, and ν_{12}^* transitions between points p_1 and $-p_2$. Each of these matrix elements is equal to a sum of contributions due to defects and phonons. We obtain from (4) and (3)

$$\sigma=C^{-1}\times\frac{\nu_2v_1+\nu_1v_2+4\nu_{21}v_1}{\nu_1\nu_2+\nu_1(\nu_{21}+\nu_{21}^*)+\nu_2(\nu_{12}+\nu_{12}^*)+2\nu_{12}\nu_{21}^*+2\nu_{12}^*\nu_{21}}. \tag{5}$$

In the derivation of (5) we have used the relation $\nu_{21}v_1=\nu_{12}-v_2$, which follows from conservation of the number of particles in collisions; the coefficient C^{-1}, which is independent of the defect concentration and the temperature, does not appear in the expression for Δ, and we shall therefore not write out the expression for it here.

It is seen from Eq. (5) that even in the case of only two pairs of points, a complete analysis of the DMR is rather difficult. Therefore, we shall simplify the treatment even more by setting the off-diagonal elements of the collision integral to zero. We then have

$$\rho=C\left(\frac{v_1}{\nu_{d1}+\nu_{p1}}+\frac{v_2}{\nu_{d2}+\nu_{p2}}\right)^{-1}. \tag{6}$$

The resistivity corresponding to Matthiessen's rule is equal to

$$\rho_M=\rho_d+\rho_{\rm ph}=C\left[\left(\frac{v_1}{\nu_{d1}}+\frac{\nu_2}{v_{ds}}\right)^{-1}\left(\frac{v_1}{\nu_{p1}}+\frac{v_2}{\nu_{p2}}\right)^{-1}\right]. \tag{7}$$

It can be seen even from (6) and (7) that in the case of several pairs of points the maximum admissible values of the DMR $\Delta=1$ can in principle be achieved. Indeed, let $\nu_{d1}\to 0$ and $\nu_{p2}\to 0$, for example, while ν_{d2} and ν_{p1} remain finite. In other words, only the defects interact with electrons near the second pair of points, and only phonons near the first. Then it is obvious that in the presence of scattering only on defects or only on phonons, the resistivity tends toward zero, since the electrons near points which are noninteracting with the scatterer are accelerated without bound by the external field; the resistivity is nonzero in the presence of a combined action of defects and phonons. Thus the assumption of the largest possible difference in the effect on the electronic system from each of the two scatterers leads to the maximum possible DMR, which exceeds the values observed experimentally.[5]

The available published data on the structure and band spectrum of the quasi-one-dimensional metal $NbSe_3$ studied in Ref. 5 is consistent with the hypothesis of a substantially different scattering probability for the groups of carriers on lattice defects and phonons. It follows from the band calculations of Ref. 9 that the Fermi surface of this conductor contains five electron groups, which according to their association with each of the three different types of structural chains can be divided into two classes: electrons of groups 1, 4, and 5 (according to the classification of Ref. 9), which are localized mainly on the $NbSe_3$ chains I and II, and groups 2 and 3, on the III chain. According to Ref. 10, in the chains of different types there is a marked difference in the distances between Se atoms, and therefore the coupling energy of the Se atoms is different in them. Consequently, it is natural to assume that the Se vacancies (the main structural defect under the experimental conditions of Ref. 5) are formed predominantly in chains of one type and, accordingly, interact with electrons of one of the two classes. On the other hand, the difference in the strength of the interaction of the chains with phonons follows from the fact that the phase transition involving the formation of charge density waves occurs at greatly different temperatures in the different chains.[11] In the light of the data presented, a description of the electrical conductivity of $NbSe_3$ in the proposed one-dimensional model with two types of carriers appears quite justified.

Figure 1 shows the temperature dependence of the resistivity of $NbSe_3$ obtained in Ref. 5 on a quenched sample (curve *2*) containing Se vacancies and on an annealed sample (curve *1*) in which the defect concentration was considerably lower. Both curves are quite close to linear, as can be seen from their approximation by straight lines. The difference of these linear dependences from direct proportionality can be

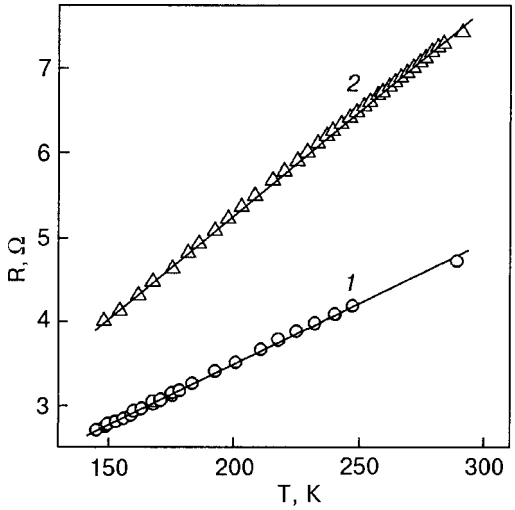

FIG. 1. Temperature dependence of the electrical resistance of a $NbSe_3$ sample in the quenched (from $T_q = 463$ K) state (*2*) and in the annealed state (*1*).

neglected within the experimental error and the accuracy of formula (6), i.e., it can be assumed that $\rho_{\text{ann}} = aT$ for the annealed sample and $\rho_q = bT$ for the quenched; the ratio of the resistivities of the quenched and annealed samples is $b/a = 1.724$. The ratio b/a here characterizes the value of the DMR:[a] $\Delta = 1 - a/b$. At temperatures of the order of Debye temperature and above, the dependence $\rho \propto T$ for the defect-free sample corresponds to the known asymptotic resistivity due to scattering on phonons. In this temperature region the electron–phonon relaxation rate behaves as follows: $\nu_{\text{ph1}} = A_1 T$ and $\nu_{\text{ph2}} = A_2 T$. The temperature dependence of the resistivity of the sample containing defects, according to Eq. (6), can be approximated by a direct proportionality (with a different coefficient of T than in the case of the pure sample) only in that temperature region where the following inequalities hold:

$$\nu_{d2} v_1 / v_2 \gg \nu_{d1}. \tag{8}$$

In this temperature region one has $\rho_q \approx C(A_1/v_1)T$, according to Eq. (6). This means that when condition (8) holds, the contribution to the current is mainly due to electrons of one of the two classes, while the contribution of the other is suppressed by frequent collisions with defects. Here for the ideal sample ($\nu_{d1} \to 0$ and $\nu_{d2} \to 0$) one has $\rho_{\text{ann}} = C(v_1/A_1 + v_2/A_2)^{-1} T$, i.e., $b/a = 1 + A_1 v_2 / A_2 v_1$. Thus in the ideal sample the contribution to the current comes from all the carriers, and that leads to a much smaller slope of the straight line $\rho(T)$ for the annealed sample than for the quenched. The ratio of the quantities appearing in inequalities (8) can, in principle, be found from an analysis of the deviations of the $\rho_q(T)$ curve from a direct proportionality, but such an analysis, in view of the smallness of the deviations, falls outside the limits of accuracy of the calculation done here.

In contrast to one-dimensional metals, in three-dimensional metals large DMRs are usually observed at low temperatures, when the differences in the electron–impurity and electron–phonon scattering are due to their different participation in umklapp processes.[2–4] At relatively high temperatures in an ordinary metal there are no reasons for groups of electrons to have large differences in the scattering efficiency on defects and phonons, and the DMRs are therefore small.

*E-mail: kopeliovich@ilt.kharkov.ua
**E-mail: mamalui@kpi.kharkov.ua

[a] We note the formal character of the introduction of the quantity Δ for $NbSe_3$: the resistivity ρ_d due to defects is determined by extrapolating ρ_q to zero temperature; this does not have a direct physical meaning, if for no other reason than the presence of phase transitions in the extrapolation region. Therefore, in the present case the ratio of b/a is a more adequate characteristic of the DMR than is Δ.

[1] Yu. M. Kagan and V. N. Flerov, Zh. Éksp. Teor. Fiz. **66**, 1374 (1974) [Sov. Phys. JETP **39**, 673 (1974)].
[2] A. I. Kopeliovich, Zh. Éksp. Teor. Fiz. **59**, 1273 (1970) [Sov. Phys. JETP **32**, 695 (1971)].
[3] Yu. M. Kagan and A. P. Zhernov, Zh. Éksp. Teor. Fiz. **60**, 1832 (1971) [Sov. Phys. JETP **33**, 990 (1971)].
[4] N. N. Bychkova and A. I. Kopeliovich, Fiz. Nizk. Temp. **3**, 458 (1977) [Sov. J. Low Temp. Phys. **3**, 221 (1977)].
[5] A. A. Mamaluĭ, T. N. Shelest, and Kh. B. Chashka, Fiz. Nizk. Temp. **26**, 176 (2000) [Low Temp. Phys. **26**, 130; 539 (2000)].
[6] B. Kramer (Ed.), *Quantum Transport in Semiconductor Submicron Structures*, Vol. 326 of NATO ASI Series E: Applied Sciences (1995).
[7] V. E. Fedorov, *Chalcogenides of Refractory Transition Metals. Quasi-One-Dimensional Compounds* [in Russian], Nauka, Novosibirsk (1988).
[8] L. P. Gor'kov, E. N. Dolgov, and A. G. Lebed', Zh. Éksp. Teor. Fiz. **82**, 613 (1982) [Sov. Phys. JETP **55**, 365 (1982)].
[9] N. Shima, J. Phys. Soc. Jpn. **51**, 11 (1982).
[10] J. L. Hodeau, M. Marezio, C. Roucau, R. Ayroles, A. Meerschaut, J. Rouxel, and P. Monceau, J. Phys. C **11**, 4117 (1978).
[11] P. Monceau (Ed.), *Electronic Properties of Inorganic Quasi-One-Dimensional Materials*, Vol. 2, Reidel, Dordrecht–Boston–Lancaster (1986), p. 139.

Translated by Steve Torstveit

QUANTUM EFFECTS IN SEMICONDUCTORS AND DIELECTRICS

Microscopic nature of Pr^{3+} optical centers in Y_2SiO_5, Lu_2SiO_5, and Gd_2SiO_5 crystals

Yu. V. Malyukin, P. N. Zhmurin, B. V. Grinev, and V. P. Seminozhenko

Institute of Single Crystals, Ukrainian National Academy of Sciences, pr. Lenina, 60, Khar'kov, 61001, Ukraine

N. V. Znamenskiĭ, É. A. Manykin, E. A. Petrenko, and T. G. Yukina

Russian Science Center "Kurchatov Institute" ul. Kurchatova, 1, Moscow, 123182, Russia
(Submitted May 16, 2002; resubmitted June 11, 2002)
Fiz. Nizk. Temp. **28**, 1083–1091 (October)

The results of investigations of the energy spectrum, energy relaxation channels, and dynamics of electronic excitations of Pr^{3+} optical centers in Y_2SiO_5, Lu_2SiO_5, and Gd_2SiO_5 crystals are reviewed. It is shown that the crystal field of the ligands of nonequivalent cationic sites in these crystals preserves the quasisymmetry of distorted octahedra and tetrahedra; the Pr^{3+} activator ions are nonuniformly distributed over the nonequivalent cationic sites in Y_2SiO_5. For high concentrations of activator ions (>1at.%) in Y_2SiO_5 crystals, the luminescence is quenched as a result of the migration and trapping of the electronic excitations energy of optical centers by traps. For $Y_2SiO_5:Pr^{3+}$ the low-temperature mechanism of dephasing of the optical transitions of Pr^{3+}, which is not characteristic for crystals and is due to the interaction of impurity ions with two-level systems of a multiwall adiabatic potential, is analyzed. [DOI: 10.1063/1.1521299]

1. INTRODUCTION

The crystal matrices of Y_2SiO_5, Lu_2SiO_5, and Gd_2SiO_5, which belong to the family of oxyorthosilicates with the general formula $RE_2(SiO_4)O$ (RE=Y,La–Lu), possess high optical quality and a wide transmission range. These matrices make it possible to introduce a quite high percentage of activator ions (up to 10 at.%) without degrading the structural or optical perfection.[1–5] Consequently, new laser and scintillation materials based on doped oxyorthosilicates are under intensive development. The high chemical and photochemical stability of oxyorthosilicates makes these materials promising for use in display technologies.[6] The following efficient oxyorthosilicate scintillating systems have been found recently: $Y_2SiO_5:Ce^{3+}$, $Gd_2SiO_5:Ce^{3+}$, $Lu_2SiO_5:Ce^{3+}$.[7–9]

Oxyorthosilicate crystals contain two types of cationic sites which differ by the specific volumes and coordination numbers and manifest different physical chemical properties.[1,5,10] These features make it possible to study the possibility of selective doping of cationic sites by rare-earth ions with different ionic radii and to stabilize different forms of the valence of the impurity ions. A deep study of the nature of optical centers in oxyorthosilicate crystals could make it possible to obtain unique solutions to technical problems in the development of laser materials with efficient upconversion schemes and scintillation materials based on fast f-d transitions in rare-earth ions.[11,12]

The optical and luminescence properties of impurity ions are determined primarily by the microstructure of their crystal environment and, to a lesser extent, depend on the macroscopic properties of the crystal. The following were established in a series of works:[13–24] the quasisymmetry of nonequivalent cationic sites in and the crystal-field parameters of Y_2SiO_5 (YSO), Lu_2SiO_5 (LSO), and Gd_2SiO_5 (GSO) crystals; the special features of the occupation of nonequivalent cationic sites in YSO by Pr^{3+} activator ions; the migration and trapping (in traps) of the electronic excitation energy at high density of Pr^{3+} activation centers; multiwell adiabatic potential of Pr^{3+} optical centers in a YSO crystal and thermally-stimulated tunneling transitions of a Pr^{3+} impurity ion between the minima of the adiabatic potential. The experimental results obtained taken together and the determination of the numerical values of a number of parameters make it possible to advance substantially in understanding the microscopic nature of Pr^{3+} activation centers in YSO, LSO, and GSO crystals and to develop the scientific foundations for further materials-science developments in optical materials based on oxyorthosilicates.

2. EXPERIMENTAL RESULTS AND DISCUSSION

The experimental setups and the experimental procedure are described in detail in Refs. 13–24. B. I. Minkov grew the $Y_2SiO_5:Pr^{3+}$, $Gd_2SiO_5:Pr^{3+}$, $Lu_2SiO_5:Pr^{3+}$ crystals at the Institute of Single Crystals at the Ukrainian National Academy of Sciences.

The main experimental results making it possible to determine more accurately the crystal-field structure of the cationic sites in YSO, LSO, and GSO and the special features of the flow of Pr^{3+} impurity ions into cationic sites are analyzed below. Secondary facts are omitted to avoid complicating the analysis with unnecessary details.

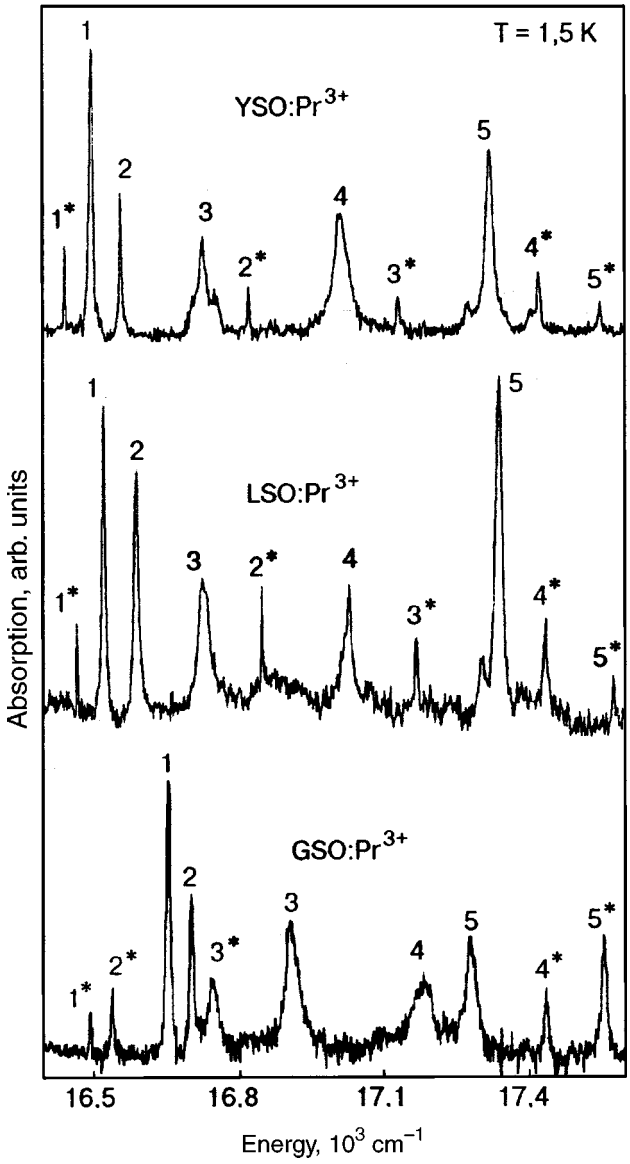

FIG. 1. Fragments of the absorption spectra of YSO:Pr^{3+}, LSO:Pr^{3+}, and GSO:Pr^{3+} crystals in the region of optical transitions with participation of the Stark components of the term $^1D_2$ of Pr^{3+} impurity ions.

A. Absorption spectroscopy and selective spectroscopy of Pr^{3+} optical centers in YSO, LSO, and GSO crystals

The special features of the splitting of the five-fold degenerate $^1D_2$ term of Pr^{3+} into Stark components by a low-symmetry crystal field were used as a probe to analyze the structure of the crystal field at the cationic sites in YSO, LSO, and GSO. The $^1D_2$ term is attractive primarily because it is well separated by substantial energy splittings from other terms of the Pr^{3+} ion.[14,18,20,22] This makes it possible to interpret reliably the spectral lines corresponding to optical transitions on the Stark components of $^1D_2$. In addition, the number of Stark components arising when the term $^1D_2$ is split is optimal in a certain sense. Thus, when the term with $J=1$ is split the number of Stark components produced is too small to follow the characteristic features of the crystal-field structure, while for $J>2$ the number is too large. Accidental degeneracy or very close spacing of the Stark components are possible; this makes it much more difficult to interpret the spectra.[18,20,21]

Figure 1 shows fragments of the absorption spectra of YSO, LSO, and GSO with participation of the Stark components of the $^1D_2$ term of Pr^{3+} ions.[20,21] Since the point symmetry of the cationic sites in YSO, LSO, and GSO is very low (C_1), the ground term $^3H_4$ of the Pr^{3+} ion should split into nine and the $^1D_2$ term into five Stark components.[18,20,21] We have indeed observed this experimentally.[20,21] At liquid-helium temperature, of the nine Stark components of the $^3H_4$ term only the bottom component is occupied; consequently, five spectral lines, corresponding to optical transitions on five Stark components of $^1D_2$, should be observed in the absorption spectrum. However, each fragment of the absorption spectrum in Fig. 1 contains ten spectral lines instead of five. They can be divided into two groups of lines, each with five lines (the lines are labeled by a number and a number with an asterisk). The spectral lines labeled by a number with an asterisk are much narrower at half-height than the spectral lines labeled only by a number.[18,20,21] The study of the selective luminescence of YSO, LSO, and GSO crystals has shown that these groups of spectral lines in Fig. 1 correspond to two different luminescence spectra. The time parameters of luminescence decay are also different.[20,21] On the basis of these facts it is concluded in Refs. 18, 20, and 21 that the distinguished groups of spectral lines belong to two different Pr^{3+} optical centers, which are formed as a result of the substitution of activator ions in two nonequivalent cationic sites in YSO, LSO, and GSO. The following notation is used below: spectral lines labeled by a number correspond to type-I Pr^{3+} optical centers and spectral lines labeled by a number with an asterisk correspond to type-II Pr^{3+} centers.

Interpretation of the structure of the spectra presented in Fig. 1 makes it possible to find the frequency ranges of the

TABLE I.

Splitting of the term $^1D_2$	YSO:Pr^{3+}		LSO:Pr^{3+}		GSO:Pr^{3+}	
	Type-I	Type-II	Type-I	Type-II	Type-I	Type-II
1	0 (16529.2)	0(16477.3)	0(16521.7)	0(16466.9)	0(16657.9)	0(16496.7)
2	59.6	364	66	373.7	42.1	43.8
3	224.9	667.9	202.2	688.4	248	248.7
4	501.2	948	498.2	951.7	525.9	940
5	801.3	1071.5	801.8	1091.4	621.8	1056.7

Splitting parameters of the term $^1D_2$ given in cm^{-1} relative to the position of the spectral lines 1 and 1*.

splitting of the term $^1D_2$ for two Pr^{3+} optical centers (see Table I). The large number of spectral lines associated with the term $^3H_4$, the close spacing of the lines, and the overlapping made it impossible to determine completely the analogous frequency intervals of the splitting of the term $^3H_4$.[20,21]

According to Table I the spectral lines 4, 5 and 4*, 5* in GSO crystals for both optical centers are separated from the triplet of spectral lines 1, 2, 3 and 1*, 2*, 3* by frequency ranges which greater the frequency ranges between the spectral lines 1, 2, 3 (1*, 2*, 3*) and 4, 5 (4*, 5*). For both Pr^{3+} optical centers in GSO crystals the spectral lines are clustered in the same manner (see Fig. 1). The character of the splitting of the $^1D_2$ term for ions occupying nonequivalent cationic sites in YSO and LSO crystals differ substantially (Table I). For type-I optical centers the smallest energy splitting between the spectral lines 1 and 2 is ~ 60 cm^{-1}. The spectral line 3 lies close to the lines 1 and 2. Next follow, after a large interval ~ 290 cm^{-1}, the spectral lines 4 and 5. For type-II optical centers in YSO and LSO crystals the spectral lines 4* and 5* are separated by the smallest energy interval. The spectral line 3* lies at a lower energy; it is followed by the spectral lines 1* and 2* separated by an interval ~ 300 cm^{-1}. This means that the reverse order of splitting of the term $^1D_2$ is observed for two optical centers in YSO and LSO crystals.

For a regular octahedral or tetrahedral symmetry of the crystal field at cationic sites, the five-fold degenerate term $^1D_2$ would be split into three- and two-fold degenerate states.[25,26] For octahedral symmetry, the three-fold degenerate state should lie at a lower energy, while for a tetrahedral symmetry it should lie at a higher energy.[25,26] Therefore, the crystal field of both cationic sites in a GSO crystal has the symmetry of a distorted octahedron.[22] In YSO and LSO crystals, the crystal field for type-I optical centers possesses the symmetry of a distorted octahedron, and for type-II optical centers the symmetry is that of a distorted tetrahedron.[22]

For quantitative analysis of the crystal-field structure of cationic sites, in Ref. 22 the model of a crystal potential of octahedral and tetrahedral symmetry[25–27] was used as a first step:

$$V_{\rm cr}=\sum_{i=1}^{2}\left\{\pm B_{4.0}\left\{Y_{4.0}(\theta_i,\varphi_i)+\sqrt{\frac{5}{14}}[Y_{4.4}(\theta_i,\varphi_i)+Y_{4,-4}(\theta_i,\varphi_i)]\right\}+B_{6,0}\left\{Y_{6,0}(\theta_i,\varphi_i)-\sqrt{\frac{7}{2}}[Y_{6.4}(\theta_i,\varphi_i)+Y_{6,-4}(\theta_i,\varphi_i)]\right\}\right\}, \quad (1)$$

where $B_{4.0}\geqslant 0$ and $B_{6,0}\geqslant 0$ are variable parameters and $Y_{l,m}(\theta_i,\varphi_i)$ are spherical harmonics. The plus sign in the relation (1) corresponds to octahedral and the minus sign to tetrahedral crystal-field symmetry. In the crystal field (1) the term $^1D_2$ splits into three- and two-fold degenerate states, which are separated by a frequency splitting $\Delta = 20B_{4.0}/7\sqrt{\pi}$. This corresponds to the positions of the centers of gravity of the spectral lines 1, 2, 3 and 4, 5 (1*, 2*, and 3*, 4*, 5*) of Pr^{3+} optical centers in YSO and LSO crystals and the centers of gravity of the spectral lines 1, 2, 3 and 4, 5 and 1*, 2*, 3* and 4*, 5* in GSO crystals (Fig. 1).[22]

TABLE II.

Parameter	YSO:Pr^{3+}		LSO:Pr^{3+}		GSO:Pr^{3+}	
	I Type	II Type	I Type	II Type	I Type	II Type
$B_{4.0}$	343	442	350	448	296	560
$A_{2.0}$	1104	–	1040	–	746	838.9
$B_{4.0}$	306	–	310	–	329	585.5
$B_{4.4}$	357	–	380	–	232	499.7
$B_{4.2}$; $A_{2.2}$	43.6	–	45	–	36.4	30.7

The parameters values are given in cm^{-1}.

The lowering of the symmetry of the cationic sites can be analyzed completely only for octahedral crystal-field symmetry, since there is a chain of distortions (tetragonal, trigonal, and rhombic) which result in complete splitting of the term $^1D_2$.[22] At each symmetry lowering step the model potential (1) becomes more complicated because of the appearance of additional terms.[22] For a tetragonal distortion three independently variable parameters $B_{4.0}$, $A_{2.0}$, and $B_{4.4}$ must be studied to describe the splitting of the term $^1D_2$; these parameters can be estimated from the experimental spectra (Table II).[22] Further lowering of the octahedral symmetry to rhombic symmetry (D_{2h}) completely lifts the degeneracy of the term $^1D_2$. Two additional variable parameters appear in the crystal potential: $A_{2.2}$ and $B_{4.2}$. Setting $B_{4.2}\approx A_{2.2}$, the numerical value of the parameters can likewise be obtained from experiments (Table II).[22]

Analyzing the data presented in Table II, which characterize the microstructure of the crystal field of the ligands of cationic sites in YSO, LSO, and GSO, shows that type-II Pr^{3+} optical centers in a GSO crystal are affected most by ligands (large values of $B_{4.0}$ and $B_{4.4}$). In this case, however, the octahedral symmetry of the cationic sites in a GSO crystal is distorted less than in YSO and LSO crystals. The values of the parameters $A_{2.0}$, $A_{2.2}$, and $B_{4.2}$ for YSO and LSO crystals are larger than for the GSO crystal.

B. Manifestation of concentration effects in the luminescence spectra and luminescence damping of activator ions in a YSO:Pr^{3+} crystal

The low-temperature optical spectra and the quenching of luminescence of YSO crystals with different activator-ion content—0.3, 0.6, and 1.8 at.%—were investigated to determine the distribution of Pr^{3+} ions over nonequivalent cationic sites.[21,23]

The total absorption intensity of two Pr^{3+} optical centers in YSO crystals increased as the change in the total concentration of activator ions.[21,23] However, the area under the spectral lines 1 or 1* changed differently (Fig. 1). As the total concentration of activator ions increased in the ratio

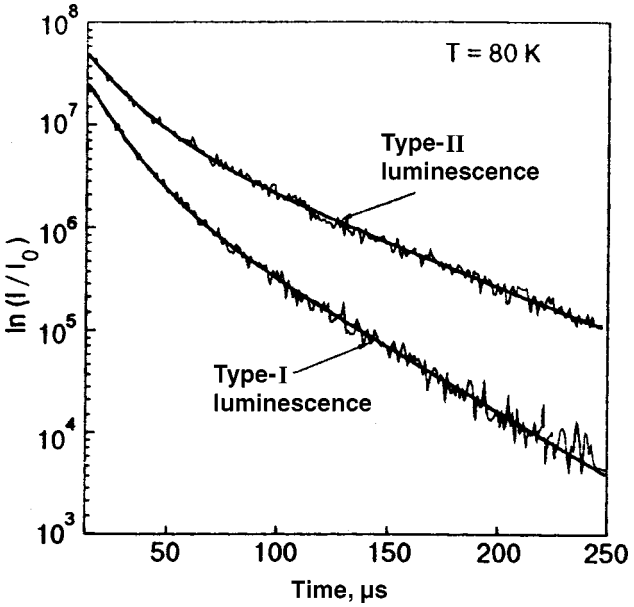

FIG. 2. Damping of the luminescence of two optical centers Pr^{3+} in a YSO crystal on optical transitions $^1D_2 \rightarrow {}^3H_4$ with total activator ion concentration 1.8 at.%.

1:2:6 the area of the spectral line 1 increased in the ratio 1:2.2:6.5 and that of the line 1* in the ratio 1:1.6:3.2. The nonuniform distribution of Pr^{3+} ions is explained by the different volume of nonequivalent cationic sites in the YSO crystal and by the different ionic radii of Y^{3+} and Pr^{3+} ions.[21,23]

The damping of the luminescence of optical transitions $^1D_2 \rightarrow {}^3H_4$ in YSO, LSO, and GSO crystals with activator ion concentration 0.3 at.% can be described by an exponential law.[20,21,23] But, even at activator ion concentration 0.6 at.% in a YSO crystal the damping of the luminescence of type-I optical centers deviated substantially from an exponential.[21,23] For 1.8 at.% activator ions the luminescence damping was nonexponential for both optical centers (Fig. 2). The deviation from an exponential law was strongest on the initial section of the experimental damping curve. At large times after the excitation pulse the luminescence decay curves can be described by an exponential law (Fig. 2). In addition, the luminescence decay constant in the exponent for a YSO crystal decreased with increasing temperature in the range 1.5–80 K.[21,23] The observed features of the luminescence decay curves were explained by migration (diffusion) and trapping of the excitation energy of Pr^{3+} activator ions by quenching centers.[20,23] The migration of electronic excitation energy is due to the dipole–dipole interaction between Pr^{3+} impurity ions.[21,23] Since optical transitions within the *f* shell of rare-earth ions are forbidden,[3,26,30] their dipole–dipole interaction is weak. Consequently, ordinarily, the transport of electronic excitation energy is incoherent; it is of a hopping character.[28,30] Energy transport along Pr^{3+} impurity ions is isotropic because the nonequivalent cationic sites in a YSO crystal form a three-dimensional lattice.[1,2] In this case the experimental luminescence damping curves of Pr^{3+} activator ions can be described by the function[28]

$$I_d(t) = I_0 \exp\left(-\frac{t}{\tau_0} - \alpha \sqrt{\frac{t}{\tau_0}} - \beta \frac{t}{\tau_0} \right), \tag{2}$$

$$\alpha = 7.4 R_0^3 c_{\mathrm{tr}}, \tag{3}$$

$$\beta = 8.6 R_0^{3/2} (D\tau_0)^{3/4} c_{\mathrm{tr}}, \tag{4}$$

where τ_0 is the luminescence decay constant of donors in the absence of quenching centers, R_0 is the critical transfer radius for electronic excitation energy, D is the diffusion coefficient of the electronic excitation energy; c_{tr} is the concentration of tunneling centers.

In Refs. 21 and 23, to fit the experimental luminescence damping curves using the relation (2) R_0 was estimated numerically from experimental data for a YSO crystal with intermediate activator ion concentration (0.6 at.%). In this case the luminescence damping of type-II optical centers is merely exponential and can be described by the relation (2)

TABLE III.

T. K	YSO 0.3 at. % Pr^{3+}		YSO 0.6 at. % Pr^{3+}		YSO 1.8 at. % Pr^{3+}	
	Type-I	Type-II	Type-I	Type-II	Type-I	Type-II
77	$\tau_0 = 108\times10^{-6}$ $\alpha = 0$ $\beta = 0$	$\tau_0 = 145\times10^{-6}$ $\alpha = 0$ $\beta = 0$	$\tau_0 = 108\times10^{-6}$ $\alpha = 0.4$ $\beta = 0.19$ $c_a = 3.1\times10^{19}$ $D = 6.2\times10^{-12}$	$\tau_0 = 145\times10^{-6}$ $\alpha = 0.14$ $\beta = 0$ $c_a = 10^{19}$	$\tau_0 = 108\times10^{-6}$ $\alpha = 2.3$ $\beta = 1.24$ $c_a = 1.8\times10^{20}$ $D = 6.9\times10^{-12}$	$\tau_0 = 145\times10^{-6}$ $\alpha = 1.98$ $\beta = 0.99$ $c_a = 1.5\times10^{20}$ $D = 3.5\times10^{-12}$
1.5	–	–	–	–	$\tau_0 = 108\times10^{-6}$ $\alpha = 2.3$ $\beta = 0.73$ $c_a = 1.8\times10^{20}$ $D = 5.7\times10^{-12}$	$\tau_0 = 145\times10^{-6}$ $\alpha = 1.98$ $\beta = 0.54$ $c_a = 1.5\times10^{20}$ $D = 2.5\times10^{-12}$

The parameters dimension are: τ_0 (s); c_a (cm^{-3}); D (cm^2/s).

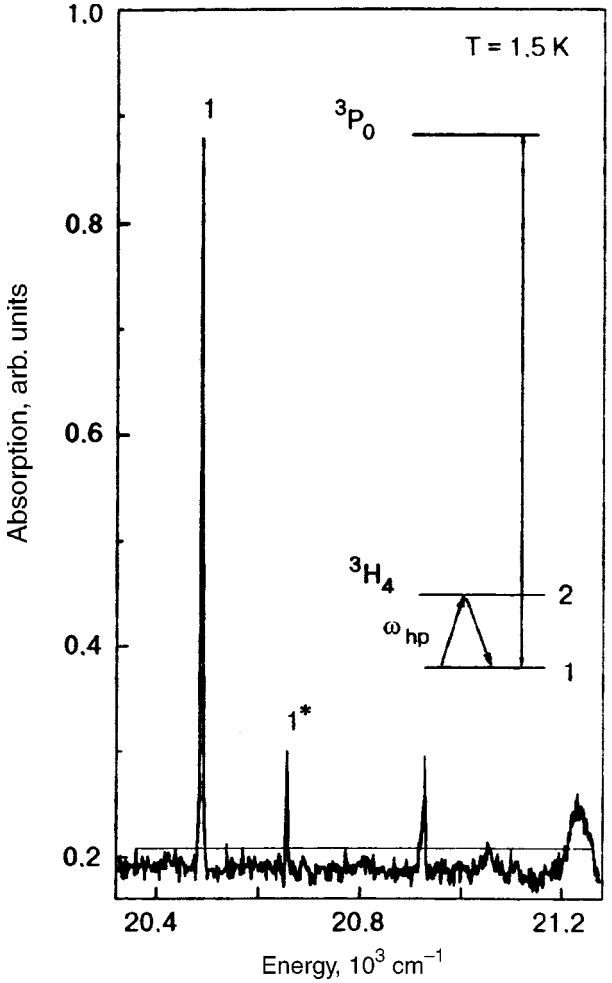

FIG. 3. Section of the absorption spectrum of a YSO:Pr^{3+} crystal in the region of optical transitions $^3H_4 \rightarrow {}^3P_0$.

with $\alpha = 0.14$ and $\beta = 0$, i.e. energy transfer to traps is very weak and there is no energy migration. Therefore the average distance between type-II optical centers can be taken as the critical energy transfer radius. For total activator ion concentration 0.6 at.% the concentration of type-II optical centers is $2.3 \cdot 10^{20}$ cm^{-3}, and the average distance between them is $R_0 \sim 12$ Å.[21,23] Taking $R_0 = 12$ Å and using the relation (3) for $\alpha = 0.14$, the trap concentration can be estimated as $c_{tr} \sim 1.3 \cdot 10^{19}$ cm^{-3}. It is shown in Refs. 21 and 23 that in a YSO crystal the traps for electronic excitation energy of Pr^{3+} activator ions are dimers of these ions.[21,23]

Table III gives the results of a fit of the experimental luminescence damping curves for YSO crystals with different activator ion concentration. The parameters α and β in the relation (2) were varied. The relations (3) and (4) were used to calculate the concentration of traps and the diffusion coefficient for the electronic excitation energy. For type-I Pr^{3+} optical centers the diffusion coefficients for the electronic excitation energy are virtually identical in samples with the maximum and intermediate activator ion concentrations. However, the diffusion coefficients are different for different optical centers. The diffusion of electronic excitation energy is of a thermal activation character, since the diffusion coefficient decreases with temperature.[28,29]

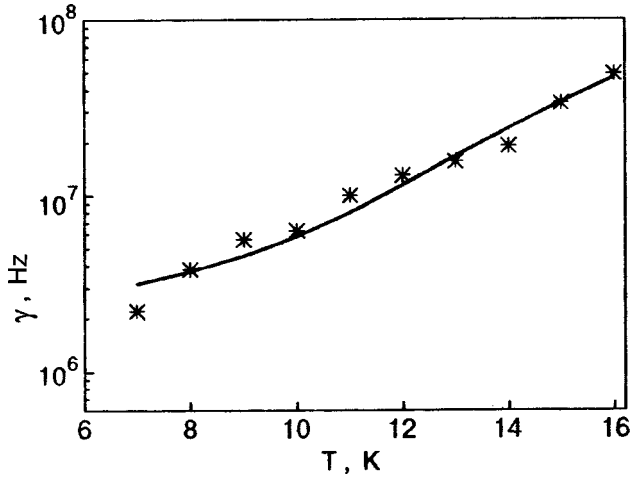

FIG. 4. Temperature dependence of the homogeneous width of the spectral line of Pr^{+3} optical centers in a YSO crystal on the transition $^3H_4 \rightarrow {}^3P_0$. The asterisks denote experimental points; the solid line is a fit using the relation (6).

C. Dynamics of electronic transitions of activator ions in a YSO:Pr^{3+} crystal

It is known[30,31] that the electron-phonon interaction determines the amplitude of photon echoes (PEs) on resonance optical transitions of impurity centers in crystals. Consequently, in contrast to stationary optical spectroscopy, information about the dynamical processes that contribute to the homogeneous width of spectral lines can be extracted from PE experiments. A double-pulse PE in a YSO:Pr^{3+} crystal was observed on resonance optical transitions $^3H_4 \leftrightarrow {}^3P_0$ in type-I Pr^{3+} optical centers.[13,15–17] To obtain the maximum amplitude of the PE signal the laser line ($\Delta\nu_{FWHM} = 0.2$ cm^{-1}) was scanned within the spectral line 1 (Fig. 3). The intensity of the PE signal varies nonmonotonically. Therefore the spectral contour of the line 1 is complicated and consists of unresolved several spectral lines.

We recall that the relation

$$I_{\text{echo}} \sim \exp(-2\gamma(T)\Delta t), \tag{5}$$

where $\gamma(T)$ is the homogeneous width of the spectral line ($\gamma(T) = \pi/T_2(T)$, $T_2(T)$ is the phase relaxation time of the optical transition), Δt is the time interval between the exciting laser pulses, and T is the temperature, determines the change in the amplitude of a double-pulse echo.[30,31]

The relation (5) makes it possible to determine directly from experiments the temperature dependence of the homogeneous width γ of a spectral line (Fig. 4). In Ref. 19 it is shown that the temperature dependence of the PE amplitude in a YSO crystal is determined by direct absorption and emission of phonons with the participation of the second Stark component of the term $^3H_4$ (see inset in Fig. 3) and by the interaction of a Pr^{3+} impurity ion with two-level systems of a multiwell adiabatic potential. The experimental results of Ref. 32 played the key role in explaining the temperature dependence of γ. In Ref. 32 hole burning was used to show that the spectral lines 1 and 1* (Fig. 1) consist of several spectral contours. The nonmonotonic variation of the PE amplitude when the laser line is scanned also indicates that the structure of the spectral line 1 is complex (Fig. 3). This

means that at a cationic site the Pr^{3+} impurity ions possess several closely spaced (in energy) states. These states can be represented in a multiwell adiabatic potential model. However, at the microscopic level it remains unclear which generalized nuclear coordinate engenders such an adiabatic potential. In Ref. 19 it is suggested that Pr^{3+} impurity ions in a YSO crystal can undergo thermally stimulated transitions between the minima of the adiabatic potential. At liquid-helium temperature only the bottom states in each minimum of a multiatomic adiabatic potential are occupied, so that the thermally-stimulated transitions are due to the interaction of Pr^{3+} impurity ions with two-level systems.[31] In Ref. 19 the additive contributions to the homogeneous width of a spectral line were summed to describe the function $\gamma(T)$ (Fig. 4). These contributions result from the interaction of the impurity center with phonons and two-level systems:

$$\gamma(T)=\gamma_{\rm ph}(T)+\gamma_{\rm TLS}(T)=\alpha\exp\left(-\frac{\Delta\varepsilon}{kT}\right)+\lambda\sinh^{-1}\left(\frac{\Delta}{kT}\right), \tag{6}$$

where α is the width at half-height of the second Stark component of the term $^3H_4$, $\Delta\varepsilon$ is the energy splitting between the first and second Stark components of the term $^3H_4$, λ is a parameter reflecting the phonon-tunneling interaction, $\Delta=\Delta_e\approx\Delta_g$ is the difference of the activation energies of the two-level systems in the ground and excited states of the impurity ions.

The parameters α and λ in the relation (6) were varied to obtain the best least-squares fit of the experimental points.[19] In so doing, $\Delta\varepsilon=89\ \text{cm}^{-1}$ and $\Delta=0.25\ \text{cm}^{-1}$.[19] The relation (6) with $\alpha=1.04\cdot10^{10}$ Hz and $\lambda=1.1\cdot10^{5}$ Hz fits well the experimental points in Fig. 4.

3. CONCLUSIONS

In summary, it has been shown that the nonequivalent cationic sites in YSO and LSO crystals retain the pseudosymmetry of a distorted octahedron and tetrahedron and in GSO crystals the distorted octahedron symmetry is observed for both cationic sites. The activator ions occupy nonuniformly the nonequivalent cationic sites in the YSO crystal lattice. At high activator ion concentrations (>0.6 at.%) a complicated luminescence decay law, due to two relaxation processes–migration and trapping (in traps)–of the excitation energy of the activator ions, is observed in YSO crystals. Dimers of the activator ions act as traps. At low temperatures Pr^{3+} impurity ions in a YSO crystal undergo thermally-stimulated transitions between several, closely spaced energy states, which are formed within cationic sites of the same type.

We dedicate this paper to the 70th birthday of Academician V. V. Eremenko with warm recollections of joint work.

[1] J. Felshe, "The crystal chemistry of the rare-earth silicates," in *Structure and Bonding*, Springer-Verlag, NY (1973), Vol. 13, p. 99.
[2] G. V. Anan'eva, A. M. Korovkin, T. I. Mirkulyaeva, A. M. Morozov, M. V. Petrov, I. R. Savinova, V. R. Startsev, and P. P. Feofilov, Neorganicheskie materialy **17**, 1037 (1981).
[3] A. M. Kaminskii, *Physics and Spectroscopy of Crystals*, Nauka, Moscow (1986).
[4] C. L. Melcher, R. A. Manente, C. A. Peterson, and J. S. Schweitzer, J. Cryst. Growth **128**, 1001 (1993).
[5] B. A. Maksimov, Yu. A. Kharitonov, V. V. Ilyukhin, and N. V. Belov, Kristallografiya **15**, 926 (1970).
[6] Yun Liu, Chao-Nan Xu, Hiroaki Matsui, Takeshi Imamura, and Tadahiko Watanabe, J. Lumin. **87–89**, 1297 (2000).
[7] C. L. Melcher and J. S. Schweitzer, IEEE Trans. Nucl. Sci. **39**, 502 (1992).
[8] P. Dorembos, C. W. E. van Eijk, A. J. J. Bos, and C. L. Melcher, J. Lumin. **60–61**, 979 (1994).
[9] H. Suzuki, T. A. Tombrello, C. L. Melcher, and J. S. Schweitzer, Nucl. Instrum. Methods Phys. Res. A **320**, 263 (1992).
[10] B. A. Maksimov, Yu. A. Kharitonov, V. V. Ilyukhin, and N. V. Belov, Dokl. Akad. Nauk SSSR **183**, 1072 (1968).
[11] P. Dorembos, J. Lumin. **87–89**, 970 (2000).
[12] R. T. Wegh, A. Meijerink, R.-J. Lamminmaki, and J. Holsa, J. Lumin. **87–89**, 1002 (2000).
[13] N. L. Pogrebnyak, Yu. V. Malyukin, and V. P. Seminozhenko, Fiz. Nizk. Temp. **20**, 610 (1994) [Low Temp. Phys. **20**, 483 (1994)].
[14] N. L. Pogrebnyak, P. N. Zhmurin, and B. I. Minkov, Ukr. Fiz. Zh. **40**, 178 (1995).
[15] N. L. Pogrebnyak, P. M. Zhmurin, V. P. Seminozhenko, and Yu. V. Malyukin, Ukr. Fiz. Zh. (Russ. Ed.) **39**, 791 (1994).
[16] Yu. V. Malyukin, N. L. Pogrebnyak, V. P. Seminozhenko, É. A. Manykin, D. V. Marchenko, D. V. Znamenskii, and E. A. Petrenko, Zh. Éksp. Teor. Fiz. **108**, 485 (1995) [JETP **81**, 260 (1995)].
[17] Yu. V. Malyukin, N. L. Pogrebnyak, É. A. Manykin, N. I. Znamensky, D. V. Marchenko, G. S. Katrich, and E. A. Petrenko, Proc. SPIE **3239**, 325 (1997).
[18] Yu. V. Malyukin, B. I. Minkov, R. S. Borisov, V. P. Seminozhenko, N. V. Znamenskii, É. A. Manykin, D. V. Marchenko, and E. A. Petrenko, Fiz. Nizk. Temp. **24**, 571 (1998) [Low Temp. Phys. **24**, 432 (1998)].
[19] R. S. Borisov, B. V. Grinev, Yu. V. Malyukin, B. I. Minkov, N. V. Znamenskii, É. A. Manykin, D. V. Marchenko, and E. A. Petrenko, Zh. Éksp. Teor. Fiz. **88**, 704 (1999) [JETP **88**(2), 385 (1999)].
[20] Yu. V. Malyukin, R. S. Borisov, P. N. Zhmurin, A. N. Lebedenko, N. V. Znamenskii, É. A. Manykin, Yu. V. Orlov, E. A. Petrenko, and T. G. Yukina, Fiz. Nizk. Temp. **26**, 1207 (2000) [Low Temp. Phys. **26**, 894 (2000)].
[21] Yu. V. Malyukin, R. S. Borisov, P. N. Zhmurin, A. N. Lebedenko, B. V. Grinev, É. A. Manykin, E. A. Petrenko, Yu. V. Orlov, and T. G. Yukina, Zh. Éksp. Teor. Fiz. **120**, 420 (2001) [JETP **90**, 370 (2001)].
[22] Yu. V. Malyukin, R. S. Borisov, P. N. Zhmurin, A. N. Lebedenko, B. V. Grinev, N. V. Znamenskii, É. A. Manykin, Yu. V. Orlov, E. A. Petrenko, and T. G. Yukina, Fiz. Nizk. Temp. **27**, 780 (2001) [Low Temp. Phys. **27**, 574 (2001)].
[23] Yu. V. Malyukin, P. N. Zhmurin, A. N. Lebedenko, B. V. Grinev, N. V. Znamenskii, É. A. Manykin, Yu. V. Orlov, E. A. Petrenko, and T. G. Yukina, Fiz. Nizk. Temp. **28**, 73 (2002) [Low Temp. Phys. **28**, 54 (2002)].
[24] Yu. V. Malyukin, P. N. Zhmurin, R. S. Borisov, M. Roth, and N. I. Leonyk, Opt. Commun. **201**, 355 (2002).
[25] K. Ballhausen, *Introduction to Ligand Field Theory* [Russian trans.], Mir, Moscow (1964).
[26] I. B. Bersuker, *The Electronic Structure and Properties of Coordination Compounds*, Khimiya, Leningrad (1986).
[27] N. A. Kulagin and D. T. Sviridov, *Introduction to the Physics of Activated Crystals*, Vishcha shkola, Khar'kov (1990).
[28] V. M. Agranovich and M. D. Galanin, *Electronic Excitation Energy Transfer in Condensed Matter*, North-Holland, Amsterdam (1982).
[29] M. J. Weber, Phys. Rev. B **4(9)**, 2932 (1971).
[30] A. A. Kaplyanskii and R. M. MacFarlane [Eds.], *Spectroscopy of Solids Containing Rare Earth Ions*, North-Holland, Amsterdam (1987).
[31] V. M. Agranovich and R. M. Hochstrasser [Eds.], *Spectroscopy and Dynamics of Excitations in Condensed Molecular Systems*, Nauka, Moscow (1987).
[32] K. Holliday, M. Croci, E. Vauthey, and U. P. Wild, Phys. Rev. **47**, 14741 (1993).

Translated by M. E. Alferieff

LATTICE DYNAMICS

Solitons in elastic plates

A. S. Kovalev* and E. S. Sokolova

B. I. Verkin Physicotechnical Institute of Low Temperatures, Ukrainian National Academy of Sciences, pr. Lenina, 47, Khar'kov, 61103, Ukraine

A. P. Mayer and C. Écki'

Institute of Theoretical Physics at Regensburg University, Regensburg, 93040, Germany
(Submitted February 13, 2002)
Fiz. Nizk. Temp. **28**, 1092–1102 (October 2002)

The nonlinear dynamics of elastic shear waves is investigated taking into account the interaction of the shear component of the displacements with low-amplitude sagittal components. Nonlinear evolutionary equations are derived for the shear-displacement field. These equations contain additional nonlinear dispersion terms due to the interaction with displacements in the sagittal plane. The soliton solutions of the equations obtained are studied and the possibility of the existence of exotic solitons—compactons and peakons—is discussed. © *2002 American Institute of Physics.* [DOI: 10.1063/1.1521300]

1. INTRODUCTION

The existence of periodic and localized nonlinear stationary waves is usually attributed to the competition between two factors: the nonlinearity of the system and the dispersion of linear waves. Recently, the role of dispersion has been investigated carefully and it was demonstrated that in weakly dispersive media nonlinear dispersion produces new types of solitons: ''compactons'' and ''peakons.'' Such excitations were first discussed for magnets[1] (see also Refs. 7–9) and then in hydrodynamics[2–4] and the theory of elasticity.[5,6]

In the theory of elasticity the nonlinear dynamics of elastic waves in one-dimensional systems is conventionally investigated on the basis of the Boussinesq equation (for longitudinal waves)

$$\rho v_{tt}-\lambda_0 v_{xx}-\tilde{\lambda}_0 a^2 v_{xxxx}-\Lambda_0 (v_x^2)_x=0, \tag{1}$$

or the modified Boussinesq equation (for transverse waves)

$$\rho u_{tt}-\lambda_1 u_{xx}-\tilde{\lambda}_1 a^2 u_{xxxx}-\Lambda_1 (u_x^3)_x=0, \tag{2}$$

where λ_i and Λ_i are linear and nonlinear elastic moduli, $\tilde{\lambda}_i \sim \lambda_i$, and a is the lattice constant.[10] For these equations wave propagates along the x direction (along an elastic chain) and $v(x)$ is the x and $u(z)$ the z component of the displacements. It is well known that the nonlinearity [the anharmonic terms in Eqs. (1) and (2)] and dispersion [the terms with the fourth spatial derivatives in Eqs. (1) and (2)] of the waves engender spatially localized waves—solitons. In the examples presented above the solitons are nonlinear localized waves with a stationary profile $v=v(x-ct)$, $u=u(x-ct)$. Soliton solutions of the Boussinesq equation exist for any sign of the dispersion ($\tilde{\lambda}_0$) and nonlinearity (Λ_0) For the modified Boussinesq equation solitons exist only if $\tilde{\lambda}_1\Lambda_1>0$. In reality, in most physical systems dispersion ordinarily has a definite sign ($\tilde{\lambda}_1>0$) and the nonlinearity of the shear waves is ''soft'' ($\Lambda_1<0$), i.e. the reverse equality holds: $\tilde{\lambda}_1\Lambda_1<0$. Moreover, in real crystals the characteristic dispersion of linear waves is negligibly small and in the long-wavelength approximation of the theory of elasticity, as a rule, it is neglected.[11] It results in the theoretical possibility of the existence of solitons, but in this case stationary nonlinear waves appear at long times when wave damping cannot be neglected.

For surface elastic waves, dispersion can be substantially increased by coating the surface of the elastic medium with a film consisting of a different material (Love surface shear waves[12] or Rayleigh waves in a medium with a coating[13]). For elastic waves in a plate, even with an ideal surface (no coating) Rayleigh–Lamb (RL) waves and the higher branches of surface shear waves also exhibit strong dispersion.[12] In these examples—Love surface waves in a half-space and Rayleigh–Lamb waves in plates, the dispersion relation in the long-wavelength approximation has the form

$$\omega^2=c^2k^2(1+bh^2k^2), \tag{3}$$

where c is the velocity of sound of the corresponding wave, h is the thickness of the coating or plate, and b is a constant of the order of 1. The dispersion law for linear waves for the ordinary modified Boussinesq equation differs from the expression (3) in that the lattice constant a replaces h. Thus, in the presence of a film with thickness much greater than one atomic layer or in a plate with finite the dispersion is greater to the extent of large parameter $(h/a)^2 \gg 1$. Under such conditions the formation of a nonlinear wave with a stationary profile is an experimentally observable effect.[14]

Nonlinear elastic surface waves and surface solitons were investigated theoretically in Refs. 15–19. The propagation of nonlinear waves in an elastic plate was discussed in

Refs. 20 and 21. In Ref. 20 the authors studied purely shear waves in an elastic plate and showed that the nonuniformity of a wave over the thickness of the plate makes solitons possible. In Ref. 21 the influence of the sagittal components on periodic nonlinear shear waves in an identical plate was taken into account and it was shown that there is a strong interaction between different components of the displacements.

In what follows we shall examine the propagation of almost transverse horizontal nonlinear shear waves and the corresponding solitons in a thin elastic plate of finite thickness. In an infinitely thin film the flexural rigidity is zero and only elastic displacements in two directions in the film plane are possible. The interaction arising between these components of the displacements results only in a change in the velocity of the longitudinal waves and renormalization (increase) of the constant Λ_1 in Eq. (2), since the characteristic dispersion of longitudinal waves is negligible, just as that of transverse waves. The situation is different in a plate of finite thickness, where all three components of the displacements are different from zero. In this case so-called Rayleigh–Lamb waves with displacement components in the sagittal plane, which are strongly dispersive, can appear. The nonlinear interaction of a shear wave with these waves increases the dispersion and results in a horizontal shear wave. But this dispersion is of a nonlinear character and the soliton solutions can have a substantially different profile—the solitons will acquire the exotic form of compactons and peakons. It is important to include in the analysis small displacements in the sagittal plane from a different standpoint also. As will be shown below, purely shear waves are unstable with respect to the emission of Rayleigh–Lamb waves and this interaction of waves with different polarization is nonlinear.

2. FORMULATION OF THE MODEL AND DERIVATION OF THE BASIC DYNAMICAL EQUATIONS

We shall consider the propagation of nonlinear elastic waves in the following geometry: an elastic plate of finite thickness $2h$, unbounded in the X and Y directions, occupies the volume $-h \leqslant z \leqslant h$. The wave is uniform in the Y direction and propagates along the X axis (Fig. 1). Let

$$u = u_{(y)}(x,z,t), \quad v = u_{(x)}(x,z,t), \quad w = u_{(z)}(x,z,t), \tag{4}$$

be the horizontal shear displacement $u_{(y)}$ and the displacements $u_{(x)}$ and $u_{(z)}$ in the sagittal plane, respectively.

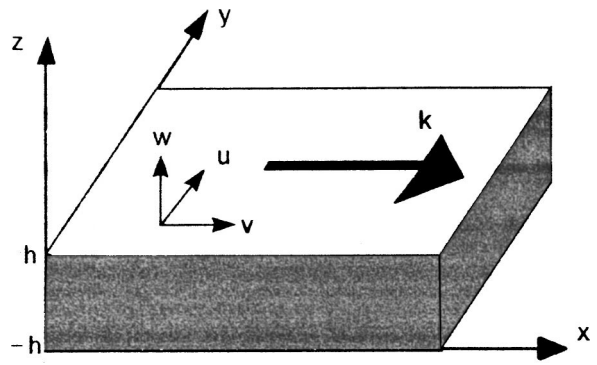

FIG. 1. Geometry of the problem.

For a crystal with cubic symmetry, the energy density in the harmonic approximation (taking account of the uniformity of the displacements in the Y direction) is

$$F_0 = \frac{1}{2} c_{11}(v_x^2 + w_z^2) + \frac{1}{2} c_{44}[u_x^2 + u_z^2 + (v_z + w_x)^2] + c_{12} v_x w_z, \tag{5}$$

where the subscripts for the components of the displacement denote differentiation with respect to the corresponding coordinate. In the notations of Ref. 11 $c_{11} = \lambda_{xxxx}$, $c_{12} = \lambda_{xxyy}$, and $c_{44} = \lambda_{xyxy}$.

Let the propagating nonlinear wave posess primarily horizontal shear polarization, i.e. $u \gg v, w$, and propagate with velocities close to that of linear shear waves. Consequently, we shall take account of the characteristic dispersion of the wave only for this component of the displacements:

$$F_{\text{dis}} = -\frac{a^2}{2} A(u_{xx}^2 + u_{zz}^2) - \frac{a^2}{2} B u_{xx}^2 \tag{6}$$

(in a cubic crystal with only nearest-neighbors interaction $B = 0$ and $A = c_{44}/12$).

The anharmonic part of the free energy can be written approximately (for the same conditions $u \gg v, w$ and $\partial/\partial y = 0$) as in:[19]

$$F_{\text{an}} \cong \frac{1}{2} s_{112121}(u_x^2 v_x + u_z^2 w_z) + \frac{1}{2} s_{332121}(u_x^2 w_z + u_z^2 v_x) + s_{132123}(v_z + w_x) u_x u_z + \frac{1}{24} s_{21212121} u_x^4. \tag{7}$$

We shall show below that in small-amplitude shear solitons moving with velocities c close to that of the velocity c_t of transverse waves the amplitude and region of localization in the direction of propagation are determined by the small parameter $\varepsilon = 1 - (c/c_t)^2 \ll 1$. Here $u \sim 1$, $v \sim w \sim \sqrt{\varepsilon}$, $\partial/\partial x \sim \partial/\partial z \sim \sqrt{\varepsilon}$, and all terms in Eq. (7) are infinitesimals of the order of ε^2. The dropped anharmonic terms containing triple products of derivatives of the functions $v(u,z)$ and $w(x,z)$ are infinitesimals of order the order of $\partial/\partial x \sim \partial/\partial z \sim \varepsilon^3$.

The dynamical equations corresponding to the total energy $F = F_0 + F_{\text{dis}} + F_{\text{an}}$ have the form, to the same degree of accuracy,

$$\rho u_{tt} = c_{44}(u_{xx} + u_{zz}) + Aa^2(u_{xxxx} + u_{zzzz}) + s_{112121}((u_x v_x)_x + (u_z w_z)_z) + s_{132123}((u_z v_z)_x + (u_z w_x)_x + (u_x v_z)_z + (u_x w_x)_z) + s_{332121}((u_x w_z)_x + (u_z v_x)_z) + \frac{1}{6} s_{21212121}(u_x^3)_x, \tag{8}$$

$$\rho v_{tt} = c_{11} v_{xx} + c_{44}(v_{zz} + w_{xz}) + c_{12} w_{xz} + s_{112121} u_x u_{xx} + s_{132123}(u_x u_z)_z + \frac{1}{2} s_{332121}(u_z^2)_x, \tag{9}$$

$$\rho w_{tt} = c_{11} w_{zz} + c_{44}(w_{xx} + v_{xz}) + c_{12} v_{xz} + s_{112121} u_z u_{zz} + s_{132123}(u_x u_z)_x + \frac{1}{2} s_{332121}(u_x^2)_z. \tag{10}$$

These equations must be supplemented by boundary conditions on the free surfaces of the plate $z=\pm h$:

$$c_{44}u_z+Aa^2u_{zzz}+s_{112121}u_zw_z+s_{332121}u_zv_x + s_{132123}u_x(v_z+w_x)=0,\quad z=\pm h, \tag{11}$$

$$c_{44}(v_z+w_x)+s_{132123}u_xu_z=0,\quad z=\pm h, \tag{12}$$

$$c_{11}w_z+c_{12}v_x+\frac{1}{2}s_{112121}u_z^2+\frac{1}{2}s_{332121}u_x^2=0,\quad z=\pm h. \tag{13}$$

We are interested in solutions in which in the leading approximation ($v,w=0$) a purely shear wave is independent of the z coordinate. Consequently, setting $u(x,z)=u^{(0)}(x)+u^{(1)}(x,z)$, where $u^{(1)}\ll u^{(0)}$, in the next approximation with $v,w\ll u$ and small anharmonic terms the function $u=u(z)$ must be taken into account only in the linear terms of Eqs. (8)–(13). Then, for waves with a stationary profile of the form $u=u(x-ct,z)$, $v=v(x-ct,z)$, and $w=w(x-ct,z)$ the equations of motion and the boundary conditions simplify as follows:

$$\left(1-\frac{c^2}{c_t^2}\right)u_{xx}^{(0)}+Aa^2u_{xxxx}^{(0)}+u_{zz}^{(1)}+Aa^2u_{zzzz}^{(1)}+\alpha(u_x^{(0)}v_x)_x + \beta(u_x^{(0)}w_z)_x+\xi u_x^{(0)}(v_{zz}+w_{xz})+r(u_x^{(0)3})_x=0, \tag{14}$$

$$v_{zz}+\kappa\mu v_{xx}+\nu w_{xz}+\alpha u_x^{(0)}u_{xx}^{(0)}=0, \tag{15}$$

$$\kappa w_{zz}+\varepsilon w_x+\nu v_{xz}=0, \tag{16}$$

$$u_z^{(1)}+Aa^2u_{zzz}^{(1)}+\xi u_x^{(0)}(v_z+w_x)=0,\quad z=\pm h, \tag{17}$$

$$v_z+w_x=0,\quad z=\pm h, \tag{18}$$

$$kw_z+(\nu-1)v_x+\frac{\beta}{2}u_x^{(0)2}=0,\quad z=\pm h', \tag{19}$$

where $\kappa=c_{11}/c_{44}$, $\nu=c_{12}/c_{44}+1$, $\varepsilon=1-(c/c_t)^2$, $\mu=1-(c/c_l)^2=1-(1-\varepsilon)/\kappa$, $\alpha=s_{112121}/c_{44}$, $\beta=s_{332121}/c_{44}$, $\xi=s_{132123}/c_{44}$, $r=s_{21212121}/6c_{44}$, $c_t=\sqrt{c_{44}/\rho}$ is the transverse speed of sound, and $c_l=\sqrt{c_{11}/\rho}$ is the longitudinal speed of sound. (We made the substitution $A/c_{44}\to A$.) Integrating Eq. (14) over the thickness of the plate and applying the boundary condition (17) easily yield a one-dimensional equation for shear displacements $u^{(0)}$ in the leading approximation:

$$(1-(c/c_t)^2)u_{xx}^{(0)}+Aa^2u_{xxxx}^{(0)}+r(u_x^{(0)3})_x + \left(u_x^{(0)}\frac{1}{2h}\int_{-h}^{h}dz(\alpha v_x+\beta w_z)\right)_x=0. \tag{20}$$

To find a closed-form equation for $u^{(0)}$ the functions v and w must be expressed in terms of the displacement $u^{(0)}$, using Eqs. (15) and (16), which comprise a system of inhomogeneous linear equations and can be solved using a Fourier transformation:

$$v=\int_0^\infty dk\sin kxV(k,z),\quad w=\int_0^\infty dk\cos kxW(k,z),$$

$$u_x^{(0)2}=2\int_0^\infty dk\cos kx\chi(k). \tag{21}$$

The solution of Eqs. (15) and (16) for the Fourier components of the sagittal displacements V and W have the form

$$V=V_1\cosh\gamma_1z+V_2\cosh\gamma_2z-\frac{\alpha\chi(k)}{\kappa\mu k},$$

$$W=W_1\sinh\gamma_1z+W_2\sinh\gamma_2z, \tag{22}$$

where

$$\gamma_i^2=k^2\varphi_i^2=\frac{k^2}{2}(p\pm\sqrt{p^2-4\mu\varepsilon}),\quad p=\kappa\mu+\frac{\varepsilon-\nu^2}{\kappa},$$

$$W_i=V_i(\varphi_i^2-\kappa\mu)/(\nu\varphi_i). \tag{23}$$

The dependences of V_i on $\chi(k)$ and k can be found from the boundary conditions (18) and (19):

$$V_{1,2}=\pm\chi(k)\left(\beta-\alpha\frac{\nu-1}{\kappa\mu}\right)\varphi_{2,1}\sinh(\gamma_{2,1}h) \times(\kappa\varphi_{1,2}^2+\varepsilon(\nu-1))G^{-1}, \tag{24}$$

where

$$G=\cosh(\gamma_1h)\cosh(\gamma_2h) \times\sum_{n=1}^{2}(-1)^n\gamma_n\tanh\gamma_nh(\kappa^2\mu-(\nu-\varepsilon)^2-\kappa(1-\varepsilon)\varphi_n^2). \tag{25}$$

Thus, the expressions (21)–(25) give the functions $v=v(x-ct,z)$ and $w=w(x-ct,z)$. If the function $\chi(k)$ corresponds to a soliton solution localized in the region $L\sim1/\sqrt{\varepsilon}$, then the solutions for v and w will also be localized in this region. The dependence of these solutions on the z coordinate can be different. For $c<c_t$ only solitons of one type with real γ_i occur. For $c>c_t$ there exist an infinite sequence of soliton solutions with different imaginary values of γ_2. However, in these solutions the displacement field oscillates as a function of the coordinate z, and these solutions do not satisfy the conditions under which the approximation used for the anharmonic energy (7) is adequate. Consequently, in what follows we shall consider only the main soliton solution. This solution corresponds to the following profile of the displacements: the deformations v_x, v_z, w_x, amd w_z are much smaller (as $\sqrt{\varepsilon}$) than the main shear deformation u_x, the displacements in a direction perpendicular to the plate are antisymmetric with respect to the center of the plate $w(z)=-w(-z)$ (i.e. the passage of a soliton is accompanied by a compression wave in the plate), and the longitudinal displacements are symmetric relative to the center of the plate ($v(z)=v(-z)$).

Substituting the solution (21)–(25) into Eq. (20) gives the final closed-form integrodifferential equation for $u^{(0)}$ (in what follows, to simplify the notation, we drop the index $^{(0)}$):

TABLE I. Elastic constants and parameters of a model for alkali-halide compounds.

Parameters	LiF	LicCl	NaF	NaCl	KF	KCl	RbCl	CsCl	CsI
K	13.78	4.65	12.1	4.09	0.46	6.59	17.53	41.19	27.54
p	−3.17	−2.58	−3.10	1.08	−1.60	1.66	3.37	6.14	4.47
C_1	−10.53	−6.69	−9.46	0.70	−2.18	0.80	1.12	1.34	0.21
C_3	−242.3	−82.05	−206.2	3.05	−17.57	5.28	10.59	116.8	81.03
ξ	16.84	31.62	18.21	−0.58	−69.90	−0.29	0.97	−2.37	−5.68
ρ	1.74	3.15	1.76	0.16	−4.34	0.16	0.15	0.12	0.02
$A\delta$	0.74	1.34	0.76	−1.59	−3.74	−2.55	0.36	−0.38	−0.24
Compacton	$\varepsilon<0$	$\varepsilon<0$	$\varepsilon<0$	–	–	–	$\varepsilon<0$	–	–
Peakon	–	–	–	$\varepsilon>0$	$\varepsilon>0$	$\varepsilon>0$	–	$\varepsilon>0$	$\varepsilon>0$

$\xi=2(C_1+C_3/(1-K))$, $\rho=2C_{1P}/(3(K-1))$, $A\delta=4C_{3P}/[3(1-K)^2(C_1+C_3/(1-K))]$.

$$\left(1-\frac{c^2}{c_t^2}\right)u_{xx}+Aa^2u_{xxxx}+\left(r-\frac{\alpha^2}{2\kappa\mu}\right)(u_x^3)_x + \kappa\sqrt{\mu\varepsilon}\left(\beta-\alpha\frac{\nu-1}{\kappa\mu}\right)^2\sqrt{p^2-4\mu\varepsilon} \times\left(u_x\int_0^\infty dk\cos kx\chi\frac{\sinh(\gamma_1 h)\sinh(\gamma_2 h)}{hG}\right)_x =0. \tag{26}$$

Since the waves which we are studying are almost purely shear waves, their velocity is close to c_t and the parameter ε is small ($\varepsilon\ll 1$). Under these assumptions Eq. (26) can be simplified:

$$\varepsilon u_{xx}+Aa^2u_{xxxx}+2C_1(u_x^3)_x +4C_3\left(u_x\int_0^\infty dk\cos kx\chi(k)M(k)\right)_x=0, \tag{27}$$

where the kernel of the integral operator $M(k)$ is given by

$$M(k)=\frac{\tanh(kh\sqrt{p})}{(kh\sqrt{p})-\tanh(kh\sqrt{p})sK\tanh s},$$
$$s=kh\sqrt{\frac{\varepsilon\mu}{p}} \tag{28}$$

and

$$C_1=\frac{1}{2}\left(r+\frac{\alpha^2}{2(1-\kappa)}\right),\quad p=\kappa-1-\frac{\nu^2}{\kappa}, \tag{29}$$

$$C_3=\frac{p}{4}\left(\alpha\frac{\nu-1}{1-\kappa}+\beta\right)^2,\quad K=\frac{(\kappa(\kappa-1)-\nu(\nu-1))^2}{\kappa(\kappa-1)} \tag{30}$$

The parameter p can also assume negative values (see Table I). In this case the substitution $p\to|p|$ must be made in all formulas.

If the characteristic spatial size of a solitary wave is of the order of L, then the function $\chi(k)$ makes the main contribution to the integral term in Eq. (27) in the wave number range $k<1/L$. Since ε is small in this range, the parameter s is small in the most interesting case $L\geqslant h$ and even for $L<h$. For $c<c_t$ we have $\varepsilon>0$ (s is real). Thus, we can set $s/\tanh s\simeq 1$ in Eq. (27) and rewrite the kernel of the integral operator in the form

$$M(k)\approx\frac{\tanh(kh\sqrt{p})}{kh\sqrt{p}-K\tanh(kh\sqrt{p})}. \tag{31}$$

The numerator in the kernel (31) vanishes at the critical value of the parameter k: $k_*\sim 1/h$. This pole of the kernel corresponds to the first symmetric Rayleigh–Lamb wave with phase velocity equal to the soliton velocity $c\simeq c_t$ (see below). Thus, a soliton consisting of a localized shear wave moving in a plate should emit Rayleigh–Lamb waves, and stationary motion of this soliton is, strictly speaking, impossible. For $c>c_t$ the parameter ε becomes negative, and in Eq. (28) $\tanh s$ must be replaced by $\tan s$. Then, the straight line $\omega=ck$ intersects the dispersion curve for Rayleigh–Lamb waves in an infinite sequence of additional points with $k_n\sim n/h\sqrt{|\varepsilon|}$. In this case a moving soliton emits the entire sequence of Rayleigh–Lamb waves with phase velocities close to the velocity of transverse waves. The emitted waves have the form $v,w\sim\Sigma_s A_s\sin[k_s(x-c_t t)]\chi(k_s)$, $\kappa_s=k_*$, k_1, k_2, ... The situation simplifies in the case of weakly localized solitons with spatial size $L\gg h$, when the Fourier transform of the soliton profile $\chi(k)$ is exponentially localized in the range $k<1/L\ll k_*$. Figure 2 shows the k-dependence of the kernel of the integral term M for $c<c_t$ (solid line) and the Fourier transformation of the squared distribution of the deformation field in the soliton χ (broken line), which in the limit of a standard soliton of a modified Boussinesq has the form $\chi(k)\sim k/\sinh(\xi k/\sqrt{\varepsilon})$, where $\xi\sim 1$. In this case the energy emitted in each RL wave is of the order of $E_*\sim\exp(-L/h)$, $E_n\sim\exp(-nL/h\sqrt{\varepsilon})$, i.e. the energy emitted by a small-amplitude soliton into all RL waves is finite and small, and it is determined primarily by the excitation of the main symmetric RL mode. Thus, for such weakly localized solitons the radiation effect can be neglected. Since the maximum value of the argument in the kernel M in this limit is of the order of $(kh\sqrt{\rho})_{\max}\sim h/L\ll 1$, the kernel simplifies and can be written as

$$M \approx \frac{1}{1-K} + \frac{pk^2h^2}{3(1-K)^2}. \tag{32}$$

In this limit Eq. (27) becomes a differential equation:

$$\varepsilon u_{xx} + Aa^2 u_{xxxx} + 2\left(C_1 + \frac{C_3}{1-K}\right)(u_x^3)_x - \frac{2pC_3}{3(1-K)^2} h^2 (\dot{u}_x (u_x^2)_{xx})_x = 0. \tag{33}$$

Substituting u_{tt} for the term $c^2 u_{xx}$, Eq. (33) becomes the modified Boussinesq equation (2)

$$\rho u_{tt} - \lambda_1 u_{xx} - \tilde{\lambda}_1 a^2 u_{xxxx} - \Lambda_1 (u_x^3)_x - Nh^2 (u_x (u_x^2)_{xx})_x = 0, \tag{34}$$

where

$$\lambda_1 = c_{44},\ \tilde{\lambda}_1 = A,\ \Lambda_1 = 2c_{44}(C_1 + C_3/(1-K))$$

and $N = 2pc_{44}C_3(3(1-K)^2)^{-1}$.

This equation contains a new nonlinear dispersion term $\sim h^2 (u_x (u_x^2)_{xx})_x$ in addition to the ordinary linear dispersion term $\sim a^2 u_{xxxx}$.

We note that an equation of this type can be derived from the equation of motion of a discrete anharmonic chain with a nonlinear interparticle interaction potential of the form $\sim (u_n - u_{n-1})^4$. Expanding these differences in a series, Eq. (2) acquires the additional term $-\Lambda_1 a^2 (u_x (u_x^2)_{xx})_x/8$. But, in Eq. (34) this term is proportional to not a^2 but rather h^2 and is much more important for real plates with $h/a \gg 1$. It changes the standard form of the soliton solution.

For shorter nonlinear localized waves with spatial size of the order of the plate thickness $L \sim h$ the form of the soliton should change substantially, since in the region of integration $k < 1/L \sim 1/h$ in Eq. (27) the argument $kh\sqrt{p}$ in the kernel (31) changes strongly. In this limit the emission of waves with sagittal polarization increases. But for a qualitative description of solitons with size $L < 1/k_* \sim h$, neglecting dissipation the kernel (31) can be replaced by the simplified expression

$$\tilde{M} = \frac{1}{(1-K) - (kh\sqrt{p})^2/3}. \tag{35}$$

which generalizes the expression (32) for $kh\sqrt{p} \sim 1$, has the correct asymptotic behavior for $k \ll 1/h$, and takes account of the main pole of the kernel of the integral operator at $k_* \sim 1/h$. (The expressions (31) and (35) behave differently as $k \to \infty$: $M \sim 1/k$ and $\tilde{M} \sim 1/k^2$. However, this difference is of no significance, since the function $\chi(k)$ truncates the integral at $k \sim 1/h$.) Making the substitution $M \to \tilde{M}$ in Eq. (27) and expanding (35) in the series

$$\tilde{M} = \frac{1}{1-K} \sum_{n=0}^{\infty} \left(\frac{k^2h^2p}{3(K-1)}\right)^n,$$

the integral part of Eq. (27) can be rewritten in the form

$$\frac{4C_3}{1-K}\left(u_x \sum_{n=0}^{\infty} \left(\frac{h^2p}{3(1-K)}\right)^n \frac{\partial^{2n}}{\partial x^{2n}} \frac{u_x^2}{2}\right)_x. \tag{36}$$

Integrating Eq. (27) with respect to x, dividing the result by u_x, and applying the operator

$$1 + \frac{h^2p}{3(K-1)} \frac{\partial^2}{\partial x^2},$$

give the nonlinear differential equation

$$\varepsilon u_x + Aa^2 u_{xxx} + 2\left(C_1 + \frac{C_3}{(1-K)}\right)u_x^3 - \frac{2C_1ph^2}{3(1-K)} u_x (u_x^2)_{xx} - \frac{Apa^2h^2}{3(1-K)} u_x \left(\frac{u_{xxx}}{u_x}\right)_x = 0. \tag{37}$$

This equation is similar to Eq. (33), but it is also applicable for $L \sim h$.

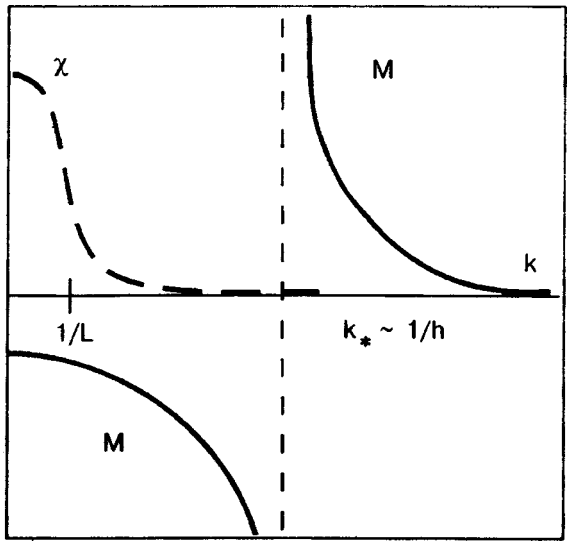

FIG. 2. The kernel M of the integral term in Eq. (27) versus the wave number k (solid line) and the Fourier transform of the soliton profile χ versus k (broken line).

3. LINEAR AND NONLINEAR PERIODIC WAVES IN A PLATE

Since resonance phenomena play an exceptionally important role in our problem, we shall examine first the possible linear waves in an elastic plate. In the linear limit Eqs. (8)–(10) decouple. The first equation describes shear waves with the dispersion relation $\omega = c_t k\sqrt{1 - Aa^2k^2}$.

The linearized equations (9) and (10) with the boundary conditions (12) and (13) possess a solution in a form of Rayleigh–Lamb waves. In this case the formulas (22) and (23) are correct [with $\chi = 0$ in Eq. (22)], if $\varepsilon = 1 - \omega^2/c_t^2k^2$ and $\mu = 1 - \omega^2/c_l^2k^2$, and the equality $G = 0$ with G determined by the formula (25) gives the dispersion relation for Rayleigh–Lamb waves in a plate consisting of a cubic crystal:

$$\frac{\varphi_1 \tanh(kh\varphi_1)}{\varphi_2 \tanh(kh\varphi_2)} \frac{\kappa^2\mu - (\nu - \varepsilon)^2 - \kappa(1-\varepsilon)\varphi_1^2}{\kappa^2\mu - (\nu - \varepsilon)^2 - \kappa(1-\varepsilon)\varphi_2^2} = 1. \tag{38}$$

Setting $v = \kappa - 1$ transforms this equation into the well-known expression[12] for the dispersion law of Rayleigh–Lamb waves in an isotropic material. In the short-wave limit

with $k \gg 1/h$, for the main symmetric RL wave and the lower antisymmetric flexural wave, an equation is obtained for the velocity of Rayleigh waves c_R in a half-space: $4\sqrt{\varepsilon\mu}=(\varepsilon+1)^2$, and in the long-wavelength limit with $k \ll 1/h$ the equality $4\mu=(\varepsilon+1)^2$ gives the limiting velocity of Rayleigh–Lamb waves $c_0=2c_t\sqrt{1-1/\kappa}$. In all cases, the Rayleigh velocity c_R is less than the shear-wave velocity $c_{sh}\simeq c_t$, and the maximum velocity of Rayleigh–Lamb waves is greater than c_t (but less than the velocity of longitudinal waves c_l). The dispersion curve $\omega=\omega(k)$ for the main symmetric RL waves changes slope from c_0 to c_R near wave numbers $k\sim 1/h$ and intersects the dispersion curve for shear surface waves at $k\sim 1/h$. For example, in the particular case of a "Poisson material" ($\kappa=3$) the intersection occurs at $k_*\simeq 0.53/h$. This point k_* corresponds to a pole of the kernel M, which we discussed in the preceding section. The dispersion relations considered are presented in Fig. 3a (see also Fig. 1 in Ref. 21).

For small-amplitude nonlinear periodic waves, an approximate solution of Eqs. (8)–(10) in the so-called "resonance approximation" can be represented in the form

$$u=u_0\sin\frac{1}{2}(kx-\omega t),$$

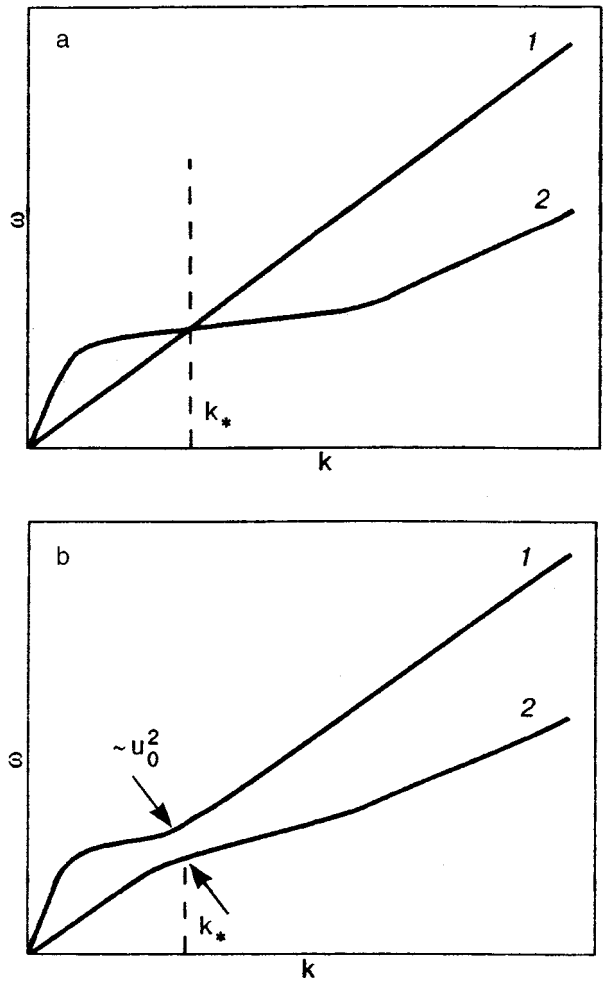

FIG. 3. Dispersion laws for the main branch of the shear waves (1) and the lower branch of symmetric Rayleigh–Lamb waves (2) in the linear approximation (a) and taking account of the nonlinear interaction of the waves (b).

$$v=V\sin(kx-\omega t)+qx,\quad w=W\cos(kx-\omega t), \tag{39}$$

where ω and k are, respectively, the frequency and wave number of the wave. Here $q=-\beta k^2u_0^2/16(\nu-1)$ is the average longitudinal deformation, which accompanies the propagation of a nonlinear periodic wave. Substituting the solution (39) into Eqs. (8)–(10) and the boundary conditions (11)–(13) gives an algebraic equation which plays the role of Eq. (26) for periodic waves:

$$\begin{aligned}\varepsilon-Aa^2\frac{k^2}{4}+\left(3r-\frac{\alpha^2}{2\kappa\mu}-\frac{\alpha\beta}{\nu-1}\right)\frac{\kappa^2u_0^2}{16}\\ -\kappa\sqrt{\mu\varepsilon}\left(\beta-\alpha\frac{\nu-1}{\kappa\mu}\right)^2\sqrt{p^2-4\mu\varepsilon}\\ \times\frac{\sinh(\gamma_1h)\sinh(\gamma_2h)}{hG}\,\frac{k^2u_0^2}{32}\\ =0.\end{aligned} \tag{40}$$

For an isotropic "Poisson material" ($\nu=1$, $\kappa=3$, $\gamma_1=k\sqrt{\varepsilon}$, $\gamma_2=k\sqrt{\mu}$) this equation becomes

$$\left(\varepsilon-\frac{\alpha^2k^2}{4}A\right)\Re=\frac{k^2u_0^2}{32}F(1-\varepsilon-J\Re), \tag{41}$$

where vanishing of the function

$$\Re=\frac{4kh\sqrt{\varepsilon}}{\tanh(kh\sqrt{\varepsilon})}-\frac{(1+\varepsilon)^2kh}{\sqrt{\mu}\tanh(kh\sqrt{\mu})} \tag{42}$$

corresponds to the dispersion law for Rayleigh–Lamb waves, $F=(\beta-\alpha/3\mu)^2$, $J=2(3r-\alpha\beta-\alpha^2/6\mu)/F$, and $\mu=(2+\varepsilon)/3$.

The corresponding dispersion curves for wave numbers $k\sim 1/h$ are presented in Fig. 3b. Now, two branches of the dispersion relation for a horizontal shear wave in the main symmetric Rayleigh–Lamb wave are separated and the degeneracy at the point $k=k_*$ is lifted.

For waves close to shear waves (near the point of intersection of linear shear waves and RL waves) the dispersion law is

$$\omega\cong c_tk-\frac{1}{8}c_tAa^2k^3-u_0^2\frac{k^3}{64c_t}F\left(\frac{1}{\Re}-J\right), \tag{43}$$

where the function $\Re\approx 4-kh/(\sqrt{\mu}\tanh(kh\sqrt{\mu}))$ varies from 2.5 at $k=0$ to 0 at $k_*\simeq 3.23/h$ and is negative for $k>k_*$. The stability of the nonlinear periodic wave close to a shear wave depends on the magnitude of the parameters A and $(J-1/\Re)$. Ordinarily, $A>0$ and $r<0$, and for $\mathrm{sign}(J)=\mathrm{sign}(r)<0$ we have $\partial^2\omega/\partial k^2<0$ for all k and $\partial\omega/\partial u_0^2<0$ for $k<k_*$ and $k>\varsigma(1+1/4|J|)k_*=\vartheta k_*$, $\varsigma<1$. For these values of k the nonlinear wave is close to a shear wave, and according to the Lighthill criterion[10] it is modulationally stable. However, in a narrow range of wavelengths smaller than the plate thickness with $k_*<k<\vartheta k_*$, such a wave becomes modulationally unstable. This instability can result in the formation of so-called envelope solitons. In the present work we shall not study nonlinear localized excitations of this type.

4. SOLITON EXCITATIONS IN AN ANHARMONIC PLATE

We shall consider the propagation of standard-profile solitons in a nonlinear plate. First we return to Eq. (33) for

long localized waves with $L \gg h$. For solitons with zero asymptotics for deformation at infinity, this equation for shear deformation $U = u_x$ is

$$a^2 U_x^2 = U^2 \frac{(c^2/c_t^2 - 1) - (C_1 + C_3/(1-K))U^2}{A + (4C_{3p}/(3(1-K)^2))(h/a)^2 U^2} \tag{44}$$

and can be solved in quadratures. It is obvious from Eq. (44) that soliton solutions exist only if

$$\operatorname{sgn}\left(\frac{c^2}{c_t^2} - 1\right) = \operatorname{sgn}\left(C_1 + \frac{C_3}{1-K}\right) = \operatorname{sgn} A. \tag{45}$$

Actually, this criterion corresponds to the standard conditions for the existence of solitons described by the modified Boussinesq equation taking account of the renormalization of the cubic anharmonicity coefficient as a result of the interaction with the sagittal components of the displacements. It is important that the effective anharmonicity constant $\xi = 2(C_1 + C_3/(1-K))$ can take on different signs (see Table I).

It is convenient to introduce the dimensionless coordinate η and the renormalized longitudinal deformation Q

$$\eta = \frac{x - ct}{a}\sqrt{\frac{c^2/c_t^2 - 1}{A}},$$

$$Q = U\sqrt{\frac{C_1 + C_3/(1-K)}{c^2/c_t^2 - 1}}, \tag{46}$$

and rewrite Eq. (44) in the form

$$Q_\eta^2 = Q^2 \frac{1 - Q^2}{1 + \gamma Q^2}, \tag{47}$$

where

$$\gamma = \frac{4C_3 p(c^2/c_t^2 - 1)}{3(1-K)^2(C_1 + C_3/(1-K))A}\frac{h^2}{a^2} = \delta\frac{h^2}{a^2}\left(\frac{c^2}{c_t^2} - 1\right). \tag{48}$$

The parameter δ in this formula is of the order of 1 and takes on different signs in different materials (see Table I).

For fixed parameters of the medium and plate thickness, all characteristics of the soliton depend only on its velocity (i.e. on the parameter ε) and therefore on the parameter γ. We shall show below that the size of the soliton approaches h as $\gamma \to \pm 1$ and the condition for applicability of Eq. (47) is violated in these limits. Nonetheless, we shall investigate the evolution of the form of the soliton solution (47) for all values of γ. We note that the parameter γ depends not only on the signs of the parameters ξ, A, and ε but also on the signs of C_3 and p (see Table I). Thus, under the conditions (45) for the existence of solitons the sign of γ can be different. This results in solitons of different form.

For $\gamma = 0$ $(c = c_t)$ the solution has the standard soliton form $Q = 1/\cosh\eta$. But in the initial variables $U = u_x(x)$ the amplitude of the soliton approaches zero as $\gamma \to 0$, and its region of localization approaches infinity. Therefore $\gamma = 0$ corresponds to a linear nonlocalized wave.

For positive values of γ the soliton solution (47) has the following implicit form:[7–9]

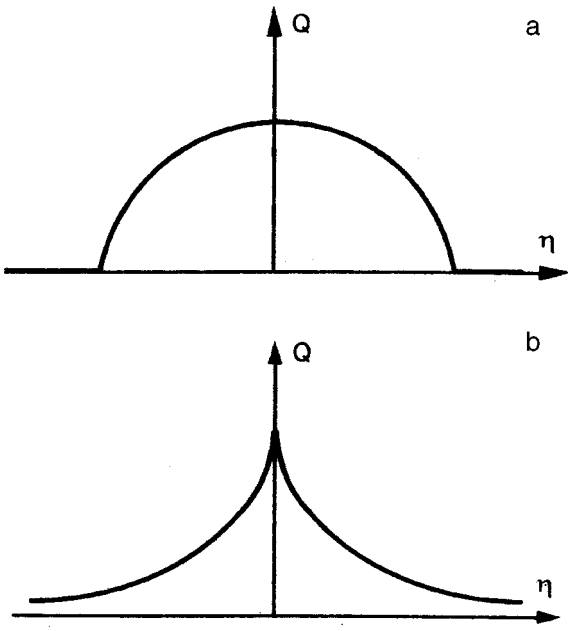

FIG. 4. Profile of the transverse deformation (in dimensionless variables) in a compacton (a) and peakon (b).

$$\ln\frac{\sqrt{1+\gamma Q^2} + \sqrt{1-Q^2}}{Q\sqrt{1+\gamma}} + \frac{\sqrt{\gamma}}{2}\arccos\frac{1 - \gamma + 2\gamma Q^2}{1+\gamma} = \eta. \tag{49}$$

For $\gamma \ll 1$ the soliton has a standard profile of size $L \sim \sqrt{A/(c^2 - c_t^2)}$, so that the characteristic dispersion A in this region is decisive and cannot be neglected.

For $\gamma \sim 1$, i.e. $c^2/c_t^2 - 1 \sim (a/h)^2 \ll 1$, the soliton solution (49) contains no parameters and thus the characteristic width of the soliton $\Delta\eta \sim 1$. Then, it follows from Eq. (46) that $\Delta x = L \sim h$, as indicated above.

As γ increases further, the second term in the numerator in the expression (47) becomes dominant and the characteristic dispersion plays a lesser role. (However, at large distances $|x| \to \pm\infty$, where $Q \to 0$, the role of characteristic dispersion and the sign of the parameter A are decisive.) In the limit $\gamma \gg 1$ the solution of Eq. (49) transforms into a so-called ''compacton'' (Fig. 4a):

$$Q = \cos\frac{\eta}{\sqrt{\gamma}}; \quad |\eta| > \pi\sqrt{\gamma}/2);$$

$$Q = 0; \quad |\eta| > \pi\sqrt{\gamma}/2). \tag{50}$$

It follows from Eqs. (46) and (50) that the soliton size remains of the order of the plate thickness $L \sim h$ for all $\gamma > 1$. From Eq. (50) in the initial coordinates for the shear displacements we have

$$u = h\sqrt{\frac{c^2}{c_t^2} - 1}\sqrt{\frac{A\delta}{C_1 + \dfrac{C_3}{1-K}}} \times \begin{cases} -1; & x < -\pi h\sqrt{A\delta/4}, \\ \sin\dfrac{x}{h}\sqrt{1/A\delta}; & |x| < \pi h\sqrt{A\delta/4}, \\ 1; & x > \pi h\sqrt{A\delta/4}. \end{cases} \tag{51}$$

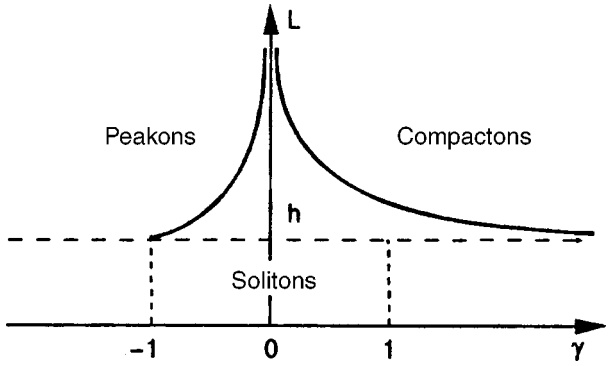

FIG. 5. Spatial size of a soliton versus the parameter γ.

Thus, the compacton solution describes a shear localized in a region whose size is of the order of the plate thickness. We note that for $\gamma \gg 1$ the soliton (51) does not contain the dispersion characteristic A, but satisfaction of the conditions (45) is mandatory.

For negative values of γ, in the range $-1<\gamma<0$ the soliton solution of Eq. (47) has the following implicit form:

$$\ln\frac{\sqrt{1-Q^2}+\sqrt{1+\gamma Q^2}}{Q\sqrt{1+\gamma}}-\sqrt{-\gamma}\times\ln\frac{\sqrt{-\gamma}\sqrt{1-Q^2}+\sqrt{1+\gamma Q^2}}{\sqrt{1+\gamma}}=\eta. \tag{52}$$

In the limit $\gamma\to-1$ this soliton transforms into a so-called ''peakon'' (Fig. 4b):

$$Q=\exp(-|\eta|). \tag{53}$$

To this solution there corresponds a completely definite soliton velocity c_*: $c_*^2/c_t^2-1=-(a/h)^2/\delta\ll 1$. The maximum deformation in the peakon is small $U_{\max}=(a/h)[\delta(C_1+C_3/(1-K))]^{-1/2}$ and its region of localization $\Delta x=L\sim h$, which follows from the form of the solution in the initial variables:

$$u(x>0,x<0)=\pm a\sqrt{\frac{A}{C_1+C_3/(1-K)}}\times\left[1-\exp\left(\mp\frac{x-ct}{h}\sqrt{1/A\delta}\right)\right]. \tag{54}$$

The dependence of the soliton width on the parameter γ for all values of γ is presented in Fig. 5.

Finally, in the region $\gamma<-1$ the soliton solution possesses a singularity at the center ($Q_\eta|_{\eta\to 0}\to\infty$). But all displacements and deformations remain finite and the soliton can be approximately represented as $Q\simeq\exp(-|\eta|)/\sqrt{-\gamma}$. For these values of γ the soliton size becomes much smaller than the plate thickness.

We note that in real substances the parameter δ can take on values in the range $[-10, 10]$. Consequently, compactons and peakons can correspond to positive and negative deviations of the soliton velocity from the velocity c_t of a transverse sound wave.

It is evident that in the most interesting range of soliton velocities ($\gamma\gg 1$ and $\gamma\simeq -1$), where the soliton assumes an exotic form, the soliton size L becomes comparable to the plate thickness. In this range, Eq. (33) is not satisfied and Eq. (37), which is also valid for $L\sim h$, must be used. As shown previously, for $\gamma\gg 1$ the characteristic linear dispersion is not important in this region and we can set $A=0$ in Eq. (37). Then, this equation assumes the form (33), but with a different coefficient multiplying the nonlinear term. The condition for the existence of solitons (45) changes and becomes

$$\operatorname{sgn}\left(\frac{c^2}{c_t^2}-1\right)=\operatorname{sgn}\left(C_1+\frac{C_3}{1-K}\right)=\operatorname{sgn}\frac{C_1 p}{K-1} \tag{55}$$

Introducing the new dimensionless coordinate

$$\zeta=\frac{x-ct}{h}\sqrt{\frac{3(C_1(K-1)+C_3)}{4C_1 p}}. \tag{56}$$

Eq. (37) for the deformation Q becomes

$$Q^2(Q_\zeta^2-Q^2+1)=0, \tag{57}$$

with the compacton solution

$$u_x=\sqrt{\frac{c^2/c_t^2-1}{C_1+C_3/(1-K)}}\times\cos\left(\frac{x-ct}{h}\sqrt{\frac{3(C_1(K-1)-C_3)}{4C_1 p}}\right). \tag{58}$$

For velocities in the range

$$1\gg\left(\frac{c^2}{c_t^2}-1\right)\gg A\left(\frac{a}{h}\right)^2-\left(\frac{a}{h}\right)^2 \tag{59}$$

and if the relations (55) are satisfied, compact small-amplitude solitons described adequately by the formula (58) can propagate in the plate. Table I illustrates the possibility of satisfying the relation (59). The table also shows for a number of specific substances the velocity ranges (signs of ε) where compactons can exist.

In order for peakons to exist in substances with the indicated signs of the parameters ξ and $A\delta$, an anomalous characteristic dispersion must be present ($A<0$). Consequently, they probably cannot be observed in alkali-halide compounds.

We thank A. M. Kosevich for his interest in this work and for variable remarks. This work was supported by INTAS as part of grant No. 99–0167.

*E-mail: kovalev@ilt.kharkov.ua

[1] A. M. Kosevich, B. A. Ivanov, and A. S. Kovalev, Phys. Rep. **194**, 117 (1990).
[2] P. Rosenau and J. Hymen, Phys. Rev. Lett. **70**, 567 (1993).
[3] P. Rosenau, Phys. Rev. Lett. **73**, 1737 (1994).
[4] R. Camassa and D. D. Holm, Phys. Rev. Lett. **71**, 1661 (1993).
[5] Yu. A. Kosevich, Phys. Rev. A **A173**, 257 (1993).
[6] Yu. A. Kosevich, Phys. Rev. B **47**, 3138 (1993).
[7] A. S. Kovalev, in *Nonlinear Physics: Theory and Experiment*, edited by E. Alfinito, M. Boiti, L. Martina, and F. Pampinelli, World Scientific, Singapore (1997), p. 508.
[8] A. S. Kovalev and M. V. Gvozdikova, Fiz. Nizk. Temp. **24**, 641 (1998) [Low Temp. Phys. **24**, 484 (1998)].
[9] A. S. Kovalev and M. V. Gvozdikova, Fiz. Nizk. Temp. **25**, 252 (1999) [Low Temp. Phys. **25**, 184 (1999)].
[10] A. M. Kosevich and A. S. Kovaleva, *Introduction to Nonlinear Physical Mechanics*, Naukova dumka, Kiev (1989).

[11] L. D. Landau and E. M. Lifshitz, *The Theory of Elasticity*, Nauka, Moscow (1987).
[12] J. D. Achenbach, *Wave Propagation in Elastic Solids*, North-Holland Publishing Co., Amsterdam (1973).
[13] H. F. Tiersten, J. Appl. Phys. **40**, 770 (1969).
[14] V. I. Nayanov, JETP Lett. **44**, 314 (1986).
[15] V. G. Mozhaev, Phys. Lett. A **319**, 333 (1989).
[16] G. A. Maugin and H. Hadouaj, Phys. Rev. B **44**, 1266 (1991).
[17] A. S. Kovalev and E. S. Syrkin, Surf. Sci. **346**, 337 (1996).
[18] C. Eckl, A. P. Meyer, and A. S. Kovalev, Phys. Rev. Lett. **81**, 983 (1998).
[19] A. P. Mayer, Phys. Rep. **256**, 237 (1995).
[20] Yu. S. Kivshar and E. S. Syrkin, Phys. Lett. A **153**, 125 (1991).
[21] A. P. Mayer, D. F. Parker, and A. A. Maradudin, Phys. Lett. A **164**, 171 (1992).

Translated by M. E. Alferieff

NEW METHODS OF LOW-TEMPERATURE EXPERIMENT

Measurement of the densities of liquids and gases under pressure using magnetic levitation of a standard sample

A. S. Panfilov* and Yu. Ya. Pushkar'

B. I. Verkin Physicotechnical Institute of Low Temperatures, Ukrainian National Academy of Sciences, pr. Lenina, 47, Khar'kov, 61103, Ukraine

(Submitted June 11, 2002)
Fiz. Nizk. Temp. **28**, 1103–1109 (October 2002)

A simple method is proposed for measuring the pressure dependence of the density of gases and liquids in a wide temperature range. The method is based on the principle of free suspension of a standard paramagnetic sample in a nonuniform magnetic field, when the magnetic force compensates the weight of the sample, taking account of the hydrostatic support of the medium. As an example of the application of the method, the density of helium gas up to pressure ~2.5 kbar at temperatures 20.4 and 77.3 K is determined. © *2002 American Institute of Physics.* [DOI: 10.1063/1.1521301]

1. INTRODUCTION

Hydrostatic weighing methods, used to determine the densities of gases and liquids at prescribed pressures and temperatures, are based on the change in the weight of a body (float) when it is immersed in the medium of interest. The apparatus used to measure the weight of the float determines the basic differences between the setups employed. The relative complexity of the mechanical devices, the difficulty of the measurement processes, and the need to take account of a large number of factors carefully in order to increase the measurement accuracy determined the specific nature of existing weighing methods (mechanical balances with different volumes of the arms, tensometric balances, and others).[1]

In the present paper we propose a comparatively simple method for measuring the density of gases and liquids. The method is based on studying the conditions of free suspension (levitation) of a standard paramagnetic sample in nonuniform magnetic field when the magnetic force compensates the weight of the sample, taking into account the hydrostatic support of the medium. As an illustration of the possibilities of this method, the results of an investigation of the density of helium gas up to pressures 2.5 kbar at temperatures 20.4 and 77.3 K are presented.

2. LEVITATION METHOD AND MEASUREMENT APPARATUS

Levitation in a nonuniform magnetic field can be achieved[2] if

$$\rho g = \chi H \frac{\partial H}{\partial z}, \tag{1}$$

where g is the acceleration of gravity, ρ is the density of the sample, H and $\partial H/\partial z$ are, respectively, the magnitude and vertical components of the gradient of the magnetic field, and χ is the volume susceptibility of the sample. If the sample is suspended in a medium with density ρ_0 and susceptibility χ_0, then the relation analogous to Eq. (1) is

$$g(\rho-\rho_0) = (\chi-\chi_0) H \frac{\partial H}{\partial z}. \tag{2}$$

Using as the standard sample a typical paramagnet (for example, a transition metal) with specific susceptibility $\chi_g = \chi/\rho \sim 10^{-5}$ emu/g magnetic fields sufficient to suspend the sample can be generated with a superconducting solenoid. Figure 1 shows a schematic distribution of the magnetic force $F_z \propto H\partial H/\partial z$ along the vertical axis z of a solenoid; the magnetic force is maximum at the edge of the solenoid at the point z_0. The procedure for measuring the levitation conditions consists of the following. Let the sample (a paramagnet) be suspended at the point z_2 (see Fig. 1) with current I_2 flowing through the solenoid, since the magnetic force compensates the weight of the sample precisely at this point (the vertical walls of the tube limit the lateral displacements rela-

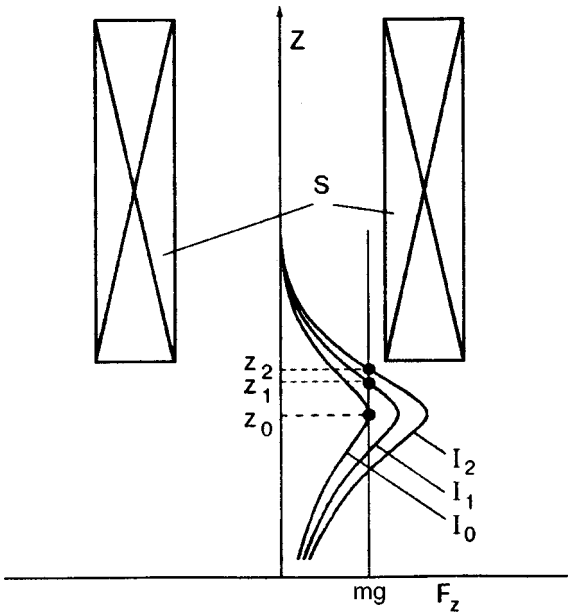

FIG. 1. Schematic distribution of the magnetic force $F_z \propto H\partial H/\partial z$ along the vertical axis of the solenoid S for currents $I_0 < I_1 < I_2$.

tive to which the equilibrium of paramagnets is unstable). As the current is decreased to I_1, the sample shifts to the point z_1 and, finally, for a current I_0 the condition (2) no longer holds and the sample falls out of the region of suspension at the point z_0. Thus, to determine the conditions for the magnetic suspension of a standard sample one need only fix the value of I_0, called in what follows the detachment current. The corresponding maximum value $(H\partial H/\partial z)_{\max}$ is found from the calibration curve of this quantity versus I. The absence of any mechanical "supports" for the sample and the high accuracy of the relative measurements of I_0 ($\sim 0.1\%$ in Gordon's experiment[2] at normal pressure) make it possible to use this method to identify reliably the contribution of the hydrostatic support of the medium under levitation conditions (2) and to determine the behavior of this contribution at high pressures in a wide temperature range (including low temperatures). An additional condition for achieving high accuracy in this method is that the magnetic susceptibility of standard samples must be isotropic. The samples can be substances with a cubic crystal lattice, where there is no susceptibility anisotropy because of the lattice symmetry. Substances with lattices of a different type should be fine-grained textureless polycrystals where the properties are isotropic because of averaging over crystallographic directions.

As follows from Eq. (2), setting $\chi_0=\chi_g^0\rho_0$ (χ_g^0 is the specific susceptibility of the medium), the expression

$$\rho_0(P,T)=\rho(P,T)\frac{1-\chi_g(P,T)g^{-1}H(\partial H/\partial z)}{1-\chi_g^0(P,T)g^{-1}H(\partial H/\partial z)} \tag{3}$$

gives the density ρ_0 of the medium for fixed P and T. For fixed temperature, the density ρ and susceptibility χ_g appearing in Eq. (3) for a standard sample can be found as a function of pressure using the relations

$$\rho(P)=\rho(0)(1+\kappa P),$$

$$\chi_g(P)=\chi_g(0)\left(1+\frac{\partial \ln \chi_g}{\partial P}P\right), \tag{4}$$

where the compressibility $\kappa=-\partial \ln V/\partial P$ of the sample and the derivative $\partial \ln \chi_g/\partial P$ of the pressure derivative of the susceptibility of the sample are assumed to be known. The susceptibility of the medium in most cases is small compared with that of the standard sample ($\chi_g^0 \ll \chi_g$), and to estimate its contribution the pressure dependence of χ_g^0 can be neglected, setting $\partial \ln \chi_g^0/\partial P=0$.

The measurement apparatus contains the following: a) a high pressure chamber made of a nonmagnetic material, b) a magnetic field source, c) a cryogenic system, and d) a high-pressure generator. The schematic form and relative arrangement of the main units of the apparatus are presented in Fig. 2.

The cylindrical vessel 5 of the high-pressure chamber is made of heat-treated beryllium bronze (BrB2). The vessel is 125 mm long and its inner and outer diameters are 3 and 7 mm, respectively. A capillary (omitted in the figure) connects the chamber with the high gas pressure generator, using a tightening nut 4 with right-left screw thread and an adapter 1. A shaft 7, containing an interior opening for the sample, is soldered to the adapter 1; the bottom of the shaft together

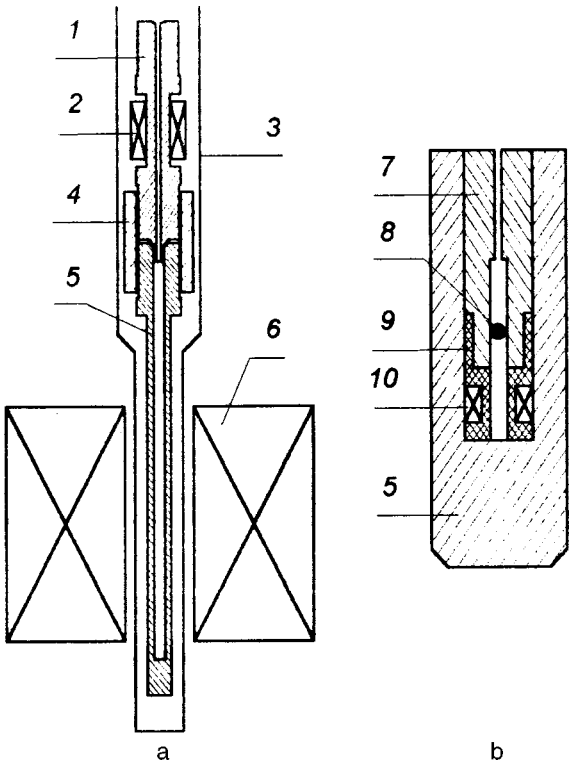

FIG. 2. Diagram of the levitation apparatus (a) and the bottom of the high-pressure chamber (b): *1*—adaptor; *2*—furnace; *3*—inner wall of the anticryostat; *4*—tightening nut; *5*—chamber vessel; *6*—superconducting solenoid; *7*—standard-sample holder; *8*—standard sample; *9*—coil frame; *10*—coil for detecting the detachment of the standard sample.

with the bottom of the chamber are shown in Fig. 2b. A coil *10*, consisting of 15–20 loops of PÉLSHO-0,1 wire wound on a insulator (teflon) frame *9*, which is secured to the shaft *7* by means of a threaded connection, is used to detect the motion of the sample *8*. The working channel in the shaft 7 and its continuation in the insulator *9* form the space where the sample moves. The coil wires are extracted from the high-pressure region through a longitudinal lateral slot in the shaft *7*, an axial opening in the adapter *1*, the pressure-delivery capillary, and standard high-pressure electric leads (see, for example, Ref. 1), placed outside the cryostat.

During the measurements the time when the sample detaches and falls into the coil is recorded according to the change in the resonance properties of the coil at frequency ~ 5 MHz, using an ac bridge whose output signal, after being detected, is observed on an oscillograph. To improve the reproducibility of the detachment current of the sample, special attention is given during fabrication of the measurement chamber to the quality of the working channel where the sample is suspended and whose surface is carefully polished to decrease its roughness. Great care is also taken, for the same reasons, in preparing a spherical sample and choosing the ratio of the diameter of the sphere (1 mm) and the diameter of the channel (1.2 mm), reducing lateral deflections of the sample away from the vertical axis to a minimum. To prevent displacements of the chamber axis, which can occur when pressure is applied, from the initial position, spring guides are used to secure the chamber relative to the inner channel of the anticryostat. Finally, light mechanical vibra-

tion of the chamber decreases the friction and the ''sticking'' of the sample to the channel walls.

A 50 mm long superconducting solenoid with inner and outer diameters 20 and 90 mm, respectively, is used to produce the magnetic field. The solenoid winding consists of a titanium–niobium alloy with critical current ~ 20 A. The maximum field at the center of the solenoid is 5 T. A high precision dc stabilizer powers the solenoid; the stabilizer enables fine discrete regulation of the current with a step of about 0.005%. The calibration curve $(H\partial H/\partial z)_{\max}$ is approximated by a linear function of the squared current,

$$\left(H\frac{\partial H}{\partial z}\right)_{\max} = \alpha I^2, \tag{5}$$

which is a consequence of the linear dependence of $H(I)$ of the solenoid. For this solenoid, the quantity α in Eq. (5), determined using the expression (1) from the magnitude of the detachment current in vacuum for samples with known susceptibilities, is $(1.216 \pm 0.010) \cdot 10^6$ Oe^2/(cm$\cdot$A^2).

The cryogenic system is mounted on the base of a standard metal helium cryostat to whose flange an anticryostat immersed in liquid helium is secured by means of a vacuum connection. The anticryostat consists of two coaxial thin-walled tubes made of nonmagnetic steel, the space between which is evacuated. The high-pressure measurement chamber with the pressure-delivery capillary is placed inside the anticryostat. The superconducting solenoid is located outside the anticryostat. Its position along the vertical axis relative to the high-pressure chamber is chosen so that the bottom of the cavity in which the sample moves is approximately 3–5 mm below the point z_0 corresponding to the maximum of the distribution of F_z of the solenoid (see Fig. 1).

A furnace 2, placed directly against the measurement chamber (Fig. 2), is used for thermostating the apparatus. This is required because of the temperature changes accompanying the pressure variations during the measurements. The temperature was monitored with a differential copper–constantan thermocouple, one end of which was placed in the high-pressure region at the bottom edge of the shaft *7*, i.e. directly againstthe sample; this minimizes the temperature measurement error due to temperature nonuniformities. To correct the indications U of the thermocouple, taking account of the effect of the pressure P on these indications, the function $U(P)$ was investigated for temperatures 20.4, 77.3, and 335 K. The data obtained show that the relative effect is essentially independent of temperature and is

$$\frac{1}{U}\frac{\Delta U}{\Delta P} = -(1.0 \pm 0.05) \cdot 10^{-3}\ (\text{kbar})^{-1}, \tag{6}$$

which is approximately 30% larger than the effect presented in Ref. 3 for a similar thermocouple at $T = 78$ and 362 K.

A membrane-type compressor[4] designed for studying the properties of gases was used as the high-pressure generator. Its principle of operation consists of increasing the gas pressure by compressing the gas in a closed volume using hydraulic oil pressure applied to a separating liquid and the gas membrane consisting of a special oil-resistant rubber. The initial pressure and volume of the gas are ~ 0.15 kbar and ~ 0.5 liters, respectively. The maximum gas pressure produced by this compressor reached 2.5 kbar. The pressure was measured to within 0.5% using a resistive sensor made of manganin wire, which was at room temperature; a standard piston-type nanometer was used to calibrate the sensor.

TABLE I. Density ρ, compressibility κ, magnetic susceptibility χ_g at $P = 0$ and the pressure derivative of the susceptibility $\partial \ln \chi_g/\partial P$ for certain standard samples with cubic (V, CeB_6) and hexagonal (Sc) crystal lattices.

Sample	T, K	ρ, g/cm^3	κ, Mbar^{-1}	χ_g, 10^{-6}emu/g	$\partial \ln \chi_g/\partial P$, Mbar^{-1}
V	20.4	6.119 [6]	0.626 [6]	5.95[a]	−0.9±0.06[b]
	77.3	6.118 [6]	0.627 [6]	5.92[a]	−0.9±0.06[b]
Sc*	300	2.985 [8]	2.3 [9]	6.4 [10]	−3.6 [5]
	77		1.7 [9]	7.2 [10]	
CeB_6	300	4.80 [11]	≃1.4 [12]	9.9 [13]	−0.7 [13]
	78			27.6 [13]	−1.1 [13]
	20.4			75.6 [13]	−1.3 [13]

Note: [a]this work (see text); [b]according to magnetostriction data from [7]; * for a polycrystalline sample.

To fabricate standard spherical samples ~ 1 mm in diameter the electric spark method was used to cut cubic blanks with approximately 1.3 mm edges from the initial material. The apparatus used in Ref. 5 was used to further work the samples in order to give them a spherical shape; in this apparatus, a sample moving in a circular channel under the action of a compressed air stream rubs against the lateral surfaces of the apparatus which are coated with an abrasive material.

3. EXPERIMENTAL RESULTS

To illustrate the possibilities of this method the pressure dependence of the density of helium gas (99.995% purity) up to 2.5 kbar at $T = 20.4$ and 77.3 K was investigated. The ''hard'' thermal stabilization method—pouring one of the cryogenic liquids (hydrogen or nitrogen) into the inner cavity of the anticryostat—was used to perform the measurements. Vanadium, whose physical charactersitics are presented in Table I, was chosen as the standard sample.

The zero-pressure values obtained for the magnetic susceptibility of vanadium using the method of suspending a sample in vacuum are in good agreement with published data.[10,14] The pressure derivative $\partial \ln \chi_g/\partial P$ of the susceptibility of vanadium, as follows from the magnetostriction data at $T = 4.2$ K,[7] is assumed to be weakly temperature-dependent, as is the susceptibility itself.[10] Finally, the value of χ_g^0 in Eq. (3) for helium is assumed to be $-(0.505 \pm 0.02) \cdot 10^{-6}$emu/g (Ref. 15) and temperature- and pressure-independent because of the atomic nature of this characteristic.

To determine the detachment current I_0 of a standard sample under prescribed conditions the levitation regime of the sample was established first by passing a quite high current through the solenoid. Next, I_0 was estimated approxi-

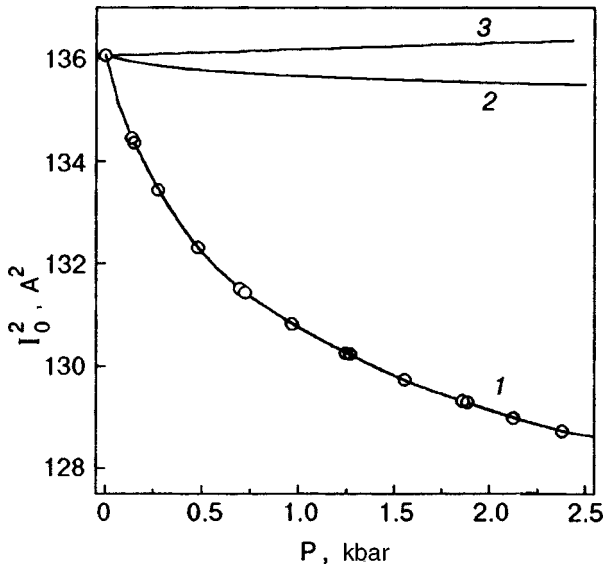

FIG. 3. Experimental pressure dependence of the squared detachment current on a standard vanadium sample in helium gas at $T=77.3$ K (curve 1). The curves 2 and 3 are partial contributions corresponding to the pressure change of the magnetic susceptibility of helium and vanadium.

mately by decreasing the current at a moderate rate. Finally, the final value of I_0 was refined by slowly decreasing the current as the estimated value was approached at a rate $\sim 0.02-0.05\%$ per minute. The characteristic measurement time of a single point did not exceed 10 min (the relaxation time of the thermal regime with the pressure varying by ~ 0.5 kbar was several minutes). The typical experimental pressure dependence of the squared detachment current $I_0^2(P)$ for a standard vanadium sample in helium gas is presented in Fig. 3. The dominant contribution to the magnitude of the effect is due to the change in the density of the medium (helium) under pressure, and the contributions due to the pressure-dependence of the magnetic susceptibility of the medium and the standard sample are not only relatively small but they partially compensate one another.

The values of the helium density for the pressure range 0.5 kbar$\leqslant P \leqslant$2.5 kbar, which follow from the expression (3), using Eq. (4) and fitting a fifth degree polynomial to the experimental data $I_0^2(P)$ obtained, are presented in Table II. These results agree well with existing average published data, taken from Ref. 16, for pressures up to 1 kbar and also with data at $T=77.3$ K for the pressure range 1–2.5 kbar, which were calculated by extrapolating the equation of state obtained for helium in Ref. 17 from experimental data for $T \geqslant 75$ K and $P \geqslant 3$ kbar to lower pressures. The observed agreement shows that the results obtained in this work are reliable.

Analysis of the error in measuring the density of the medium by the method being considered showed that the main contribution to this error is due to the statistical variance of the detachment current of the sample. The above-described measures for improving the reproducibility of the detachment current (high surface quality of the walls of the working chamber, spherical shape of the samples, mechanical vibration, and so on) made it possible to decrease the error in determining this current to $\sim 0.01\%$. The corresponding error in $H\partial H/\partial z$ is twice this value, i.e. $\sim 0.02\%$.

TABLE II. Values of the helium density at various pressures for temperatures 20.4 and 77.3 K.

P, kbar	Helium density, g/cm^3				
	T = 20,4 K		T = 77,3 K		
	a	b	a	b	c
0,5	0,2505	0,2499	0,1629	0,1632	
0,6	0,2622	0,2622	0,1788	0,1794	
0,7	0,2730	0,2728	0,1928	0,1934	
0,8	0,2827	0,2823	0,2052	0,2057	
0,9	0,2916	0,2909	0,2163	0,2166	
1,0	0,2996	0,2987	0,2264	0,2265	0,2308
1,1	0,3069		0,2357		0,2401
1,2	0,3137		0,2444		0,2486
1,3	0,3200		0,2525		0,2565
1,4	0,3259		0,2602		0,2639
1,5	0,3316		0,2675		0,2708
1,6	0,3372		0,2745		0,2773
1,7	0,3425		0,2812		0,2834
1,8	0,3477*		0,2877		0,2893
1,9	–		0,2938		0,2948
2,0	–		0,2996		0,3001
2,1	–		0,3051		0,3051
2,2	–		0,3103		0,3100
2,3	–		0,3152		0,3146
2,4	–		0,3198		0,3191
2,5	–		0,3241		0,3234

Note: a—results of this work; b—data from [16]; c—extrapolation of the data from [17]; * at pressures $P \geqslant 1.8$ kbar helium is in a solid state [16].

For the standard sample (vanadium) and medium of interest (helium gas) chosen for this work, the contribution of this source to the total error in determining the density of the medium in the pressure range 1–2 kbar is 0.3–0.4% at $T=20.4$ K and 0.4–0.5% at $T=77.3$ K (the lower values of the error correspond to higher pressures). The values presented for the error do not contain any appreciable contribution from the calibration curve of $H\partial H/\partial z$ versus I, because the fit of a linear function of the squared current to the calibration curve is reliable. This contribution does not exceed 0.05% for the above-presented error in determining the coefficient α in Eq. (5).

Another source of error is due to the fact that the pressure dependence of the magnetic susceptibility χ_g of the standard sample is taken into account in Eq. (3). For the values presented in Table I for the error in the pressure derivative $\partial \ln \chi_g/\partial P$ in vanadium the resulting error in determining the density of the medium in the same pressure range is 0.11–0.17% for $T=20.4$ K and 0.14–0.22% for T

$=77.3$ K (higher errors correspond to higher pressures). We also note that the contribution of the error presented above to the specific susceptibility of helium is $\sim 0.25\%$. Finally, the error in the pressure contributes an error of the order of 0.1%.

In summary, the total relative error in the measurements of the helium density performed by this method is 0.7–1% in the indicated pressure and temperature ranges. This falls within the typical error in similar measurements performed by other methods under conditions close to those used here (0.5–1%[16,17]).

4. CONCLUSIONS

The method developed in this work for measuring the density of gases and liquids made it possible to obtain information about the density of helium gas up to pressures ~ 2.5 kbar at $T=20.4$ and 77.3 K, filling the lacuna in the experimental data in this temperature range for pressures $P \geqslant 1$ kbar (see Table II). The data obtained could be helpful for refining the equation of state of helium in a wide range of pressures and temperatures and for technical applications, for example, in studying the influence of pressure on the magnetic susceptibility using the procedure examined in this work.

One feature of this method is the small volume of the measurement cavity ($\leqslant 0.3$ cm^3) together with reliable monitoring of the temperature using a copper-constantan thermocouple, to correct the indications of which a universal curve of the thermo-emf of the thermocouple versus the pressure is proposed. For this construction there is no need to thermostat comparatively large working volumes, which are used in other methods;[1,18–20] this is one of the advantages of the present method. Together with the short relaxation times of the temperature and the possibility of varying the pressure smoothly this substantially decreases the total time required to perform measurements by this method as compared with the standard piezometric methods in which the pressure must be regulated discretely. In addition, the measurement error due to temperature nonuniformity is smaller for a small working volume.

We note that the accuracy of measurements performed by this method increases as the role of hydrostatic support of the medium in compensating the weight of the standard sample increases. This can be achieved by using samples lighter than vanadium, for example, polycrystalline scandium (see Table I), for which the main contribution to the error due to the reproducibility of the detachment current is approximately two times smaller. For measurements on liquids whose density (~ 1 g/cm^3) is high compared with gases, the same contribution to the error decreases by a factor of ~ 5 and ~ 10 for vanadium and scandium, respectively, and is $\leqslant 0.1\%$.

The contribution due to the pressure dependence of the susceptibility of the sample behaves similarly. This makes it possible to decrease the total error of both contributions mentioned above, for example, in liquids, to a value of the order of 0.1% at moderate pressures (up to $\sim 2-3$ kbar). Against the background of this small error, the contribution due to the error in determining the specific susceptibility of the medium becomes appreciable. This error depends, first and foremost, on the ratio χ_g^0/χ_g of the susceptibilities of the medium and the sample and can be substantially decreased by using samples with higher susceptibilities than that of vanadium (or scandium). A suitable object is, in our opinion, the compound CeB_6, whose density falls between that of vanadium and scandium and which is a much stronger paramagnet with relatively weak pressure dependence of the susceptibility (Table I).

The fundamental possibilities noted above for substantially increasing the measurement accuracy by using the optimal standard sample and the relative simplicity of the proposed method make it promising for high-precision studies of $P-V-T$ diagrams of a wide class of gases and liquids.

We note that the upper limit of the pressures used in this work (2.5 kbar) can be substantially increased by using nonmagnetic chambers designed for higher pressure (up to 10–15 kbar[21]). A substantial increase in the viscosity of the medium, especially liquids, and an increase in the corresponding characteristic times of the measurement process up to acceptable levels could be an obstacle.

We thank I. V. Svechkarev for helpful remarks which he made after reading the manuscript. This work is dedicated to the 70th birthday of Academician Viktor Valentinovich Eremenko, with whom the authors had the honor of collaborating, fruitfully and happily, for many years.

*E-mail: panfilov@ilt.kharkov.ua

[1] D. S. Tsiklis, *Technique of Physical-Chemical Investigations at High and Superhigh Pressures*, Khimiya, Moscow (1965).
[2] R. G. Gordon, Rev. Sci. Instrum. **33**, 729 (1962).
[3] D. Bloch and F. Chaisse, J. Appl. Phys. **38**, 409 (1967).
[4] M. D. Bondarenko, Prib. Tekh. Eksp. **4**, 223 (1973).
[5] A. S. Panfilov, *Effect of Hydrostatic Pressure on the Magnetic Susceptibility of Transition Metals*, Candidate's Dissertation in Physical-Mathematical Sciences, Khar'kov (1973).
[6] D. I. Bolef, R. E. Smith, and J. G. Miller, Phys. Rev. B **3**, 4100 (1971).
[7] T. L. Tam, M. O. Steinitz, and E. Faweett, J. Phys. F: Met. Phys. **2**, L129 (1972).
[8] *Reference Data on the Physical-Chemical Properties of the Elements*, Naukova dumka, Kiev (1965).
[9] C. E. Monfort and C. A. Swenson, J. Phys. Chem. Solids **26**, 623 (1965).
[10] N. V. Volkenshteĭn and É. V. Galoshina, Fiz. Met. Metalloved. **20**, 368 (1965).
[11] M. I. Aivazov, S. V. Aleksandrovich, and V. S. Mkrtchyan, Phys. Status Solidi A **62**, 109 (1980).
[12] T. Goto, A. Tamaki, S. Kunii, T. Nakajima, T. Fujimura, T. Kasuya, T. Komatsubara, and S. B. Woods, J. Magn. Magn. Mater. **31–34**, 419 (1983).
[13] A. S. Panfilov, Yu. Ya. Pushkar, and I. V. Svechkarev, Fiz. Nizk. Temp. **19**, 96 (1993) [Low Temp. Phys. **19**, 69 (1993)].
[14] D. Z. Hechtfischer, Z. Phys. B **23**, 255 (1976).
[15] C. Barter, R. G. Meisenheimer, and D. P. Stevenson, J. Phys. Chem. **64**, 1312 (1960).
[16] R. D. McCarty, J. Phys. Chem. Ref. Data **2**, 923 (1973).
[17] R. L. Mills, D. H. Liebenberg, and J. C. Bronson, Phys. Rev. B **21**, 5137 (1980).
[18] D. S. Tsiklis, V. Ya. Maslennikova, and S. Ya. Gluvka, Dokl. Akad. Nauk SSSR, Ser. Fizika **216**, No. 4, 769 (1974).
[19] A. B. Bilevich and L. L. Pitaevskaya, Zh. Fiz. Khim. **45**, 2907 (1971).
[20] N. V. Tsederberg, V. N. Popov, and A. B. Kalenkov, "Properties of substances, cycles, and processes," *Trudy MÉI*, No. 234, 65 (1975).
[21] E. S. Itskevich, Prib. Tekh. Éksp. , No. 4, 148 (1963).

Translated by M. E. Alferieff